

THE UNIVERSITY OF HULL

Analysis-on-a-Roll Platforms Towards Automated and High Frequency In-Situ  
Sensing of Natural Geochemical Fluxes

being a Thesis submitted for the Degree of Doctor of Philosophy  
in the University of Hull

by

Aleksei Iurkov MSc (University of Hull)

May 2024

## Table of contents

1	Introduction .....	15
1.1	Project context .....	16
1.2	Research objectives .....	16
1.3	Project development objectives .....	16
1.4	Background.....	17
1.5	Previous work at Hull – The LIMPIDS project .....	18
1.5.1	Overview of LIMPIDS.....	18
1.5.2	In-situ river monitoring using laboratory instruments .....	19
1.5.3	LIMPIDS Microfluidic Lab-on-Chip In-situ Instrument Development .. .....	20
1.5.4	Evaluation of LIMPIDS project .....	22
1.6	Thesis structure.....	25
1.6.1	Chapter 2 – Literature review.....	25
1.6.2	Chapter 3 – System design development .....	25
1.6.3	Chapter 4 – System evaluation.....	26
1.6.4	Chapter 5 – Operational test of the System.....	27
1.6.5	Chapter 6 – Conclusion .....	27
2	Literature review .....	28
2.1	Climate change and carbon fluxes.....	28
2.1.1	Climate change problem.....	28
2.1.2	Carbon fluxes at the Earth surface .....	29
2.1.3	Karstlands and the carbon cycle.....	31
2.1.4	Forestry as a means of carbon sequestration.....	31
2.1.5	Proposed test site.....	32
2.2	In-Situ chemical measurement .....	34
2.2.1	Chemical analysis systems .....	34
2.2.2	Analysis methods .....	36
2.2.3	Microfluidic technology .....	42
2.2.4	Colorimetry .....	45
2.3	Frequency of water sampling .....	48
3	System design development.....	49

3.1	System concept .....	49
3.2	Carbonate PAD design .....	53
3.2.1	PAD chemistry .....	53
3.2.2	PAD structure and manufacture .....	54
3.2.3	PAD colour response.....	56
3.2.4	Manufacture of PAD roll.....	57
3.3	Colorimetry for PAD analysis .....	59
3.3.1	Analysis using a digital camera.....	60
3.3.2	Analysis using a colour sensor .....	61
3.4	Waterproof box.....	63
3.5	System design .....	65
3.5.1	Mechanical design and System assembly .....	65
3.5.2	Electronic design .....	70
3.5.3	Power budget.....	76
3.6	Sampling theorem in system design .....	79
3.6.1	Sampling processes .....	79
3.6.2	Minimum sampling frequency and signal spectrum .....	80
3.6.3	Water tank as a low-frequency filter.....	83
3.6.4	Example model.....	87
3.7	Error analysis .....	88
3.7.1	Aperture delay and uncertainty .....	88
3.7.2	Aperture skew.....	92
3.8	System software design .....	95
3.8.1	Automated measurement system (MATLAB) developed for phosphates PADs .....	95
3.8.2	AI PAD detection .....	96
3.8.3	Image processing platform .....	97
3.8.4	Evaluation example .....	99
3.8.5	Software overview.....	100
4	Sensing Evaluation.....	113
4.1	Initial experimental validation of carbonate PAD.....	113

4.2	Model-based comparison of camera and spectra sensor-based colour measurement .....	114
4.2.1	MATLAB simulation of optical sensing process.....	115
4.2.2	Paper optical properties .....	119
4.2.3	Comparison of camera and spectral sensor for pH measurement accuracy. ....	120
4.3	Experiment to evaluate carbonate concentration with paper analytical device .....	124
4.4	Comparison of side and back lightning.....	128
4.5	Experimental comparison of sensor and camera accuracy for measuring PAD device colour change.....	129
4.6	Calibration curve .....	131
5	Operational test .....	134
6	Conclusion .....	137
6.1	Project outcomes/ Results summary.....	137
6.2	Further work .....	138
6.3	Recommendations for the design of a LOAR platform .....	139
6.3.1	PAD and PAD roll production .....	139
6.3.2	LOAR instrument system.....	139
	References .....	141
	Appendix A - Sensor Board Schematic .....	148
	Appendix B – LED Board Schematic .....	149
	Appendix C – Analysis function .....	150
	Appendix D – Object detection function .....	156
	Appendix E - System limitations MATLAB code.....	161
	Appendix F – Carbonates BCG buffer solution preparation method .....	162
	Appendix G - Mechanical design.....	165
	Appendix H - LTSpice filter implementation .....	166
	Appendix I – Automated measurement system (MATLAB).....	171
	Appendix J – Camera and sensor comparison MATLAB code.....	176
	Appendix K – Mounting .....	185
	Appendix L – Motor coupling.....	186



## Table of Figures

Figure 1. Lab-on-a Roll System Concept.....	17
Figure 2. PAD Roll Concept .....	18
Figure 3. Photograph (taken 2010) of example river monitoring station: (a) River Enborne at Brimpton (b) The Cut at Bray .....	19
Figure 4. Measurement system block diagram .....	20
Figure 5. LoC trial at monitoring station on River Enborne at Brimpton: (a) setup, (b) failure due to blockage. ....	21
Figure 6. Proposed in-situ LoC chemical sensor instrument fluidic system using Electrodialysis and Capillary Electrophoresis .....	22
Figure 7. Earth's surface temperature and atmospheric carbon dioxide.....	28
Figure 8. Carbonate-silicate geochemical cycle .....	30
Figure 9. Poole's Cavern (February 2020): (a) Public walkway and speleothems (b) speleothems, (c) and (d) experimental equipment. Sensor network radio device (Tinytag Plus Radio) can be seen in (c) .....	33
Figure 10. a – pH sensor, b – electrical conductivity sensor, c – dissolved oxygen sensor.....	34
Figure 11. Portable autosampler for discrete surface water samples [51]. ....	35
Figure 12. A – diagram of a basic electrochemical liquid conductivity meter with 2 electrodes, b - electrochemical device with arrays of $4 \times 5$ cathodes and anodes with five flow channels on the cathode side. ....	37
Figure 13. Simple diagram of an optical spectrometer. ....	38
Figure 14. Typical appearance of the Absorption graph.....	39
Figure 15. Diffuse reflectance spectroscopy .....	39
Figure 16. A diagram of a basic capillary electrophoresis setup .....	40
Figure 17- Lab-on-a-chip for integrated clinical analysis made of plastic. ....	43
Figure 18. Paper-based analytical device for phosphates dissolved in water.....	44
Figure 19. Electrical conductivity measured weekly, daily, and hourly.....	48
Figure 20. Dipping System Concept .....	50
Figure 21. PAD roll concept design.....	50
Figure 22. System block diagram.....	51
Figure 23. PAD structure. ....	54
Figure 24. Optical image of the PAD surface subjected to laminate perforation using laser cutter. The easiest way to ensure water access to the reaction zone is to cut the lamination layer with scalpel before placing PADs on a roll. This method will be used for the production of PAD at the testing stage of the system, since no feasible solution has been found and this method also does not require any additional equipment. ....	56
Figure 25. Absorption spectra of bromocresol green dye in various pH buffer solutions.....	57

Figure 26. PAD device .....	57
Figure 27. Image analyses process from. ....	60
Figure 28. Example calibration curve (Phosphate concentration) from. ....	61
Figure 29. AS7262 spectral sensor spectral response curves .....	61
Figure 30. 3D system layout. ....	66
Figure 31. Front and side view of the system. ....	66
Figure 32. Motor connection.....	67
Figure 33. Tensioner. ....	68
Figure 34. Water scraper.....	68
Figure 35. Final laboratory version of the system (front).....	69
Figure 36. Final laboratory version of the system (side) .....	69
Figure 37. System block diagram.....	70
Figure 38. Motors connection. ....	71
Figure 39. Chart flow diagram of electronic system operation. ....	71
Figure 40. Sensors and LED boards positioning (a – top view, b – side view).....	73
Figure 41. Schematic for one sensor device. ....	73
Figure 42. PCB design for the sensor circuit. ....	74
Figure 43. PCB routing (red – top level, blue – bottom level) for LED circuit.....	74
Figure 44. LED PCB design.....	75
Figure 45. LED PCB placement (red – top level, blue – bottom level).....	75
Figure 46. Manufactured PCBs.....	76
Figure 47. Power consumption diagram .....	77
Figure 48. Digital signal processing.....	79
Figure 49. Top: Original waveform and sampling pulses, Middle: Sampled waveform, Bottom: Sampled and original waveforms shown together.....	80
Figure 50. Signal sampling intervals.....	81
Figure 51. Top: 1 KHz and 8 kHz sinewaves and sampled signal, Bottom: 1 KHz and 17 kHz sinewaves and sampled signal. ....	82
Figure 52. Water tank.....	84
Figure 53. Water tank diagram.....	85
Figure 54. Water tank residence time .....	86
Figure 55. Aperture jitter.....	89
Figure 56. Signal to noise ratio for various jitter values.....	91
Figure 57. Error Signal to noise ratio for various jitter values. ....	92
Figure 58. Skew due to PAD location in cluster.....	93
Figure 59. Skew due to roll alignment.....	93
Figure 60. Symmetrical cluster .....	94
Figure 61. Image before (left) and after (right) processing. ....	95
Figure 62. Graph of measurement results using Image J and Matlab program. ....	96
Figure 63. Chart flow diagram of object detection .....	98
Figure 64. Example of PAD devices images from the dataset .....	99

Figure 65. Screenshot of object detection application showing detection result (PAD, reference square and reaction zones).....	100
Figure 66. Chart flow diagram of the system operation. ....	101
Figure 67. Reaction zone detection diagram.....	107
Figure 68. An example of using a Telegram bot to manage the system (screenshots from the smartphone) .....	110
Figure 69. Photo of Carbonates detection PAD device (made by Samantha Richardson) .....	113
Figure 70. Results of the experiment (Based on a data obtained from Samantha Richardson). ....	113
Figure 71. Raspberry Pi Camera spectral response curves .....	114
Figure 72. AS7262 spectral sensor spectral response curves .....	115
Figure 73. Optical analysis diagram.....	115
Figure 74. BCG absorption spectra ( <i>ABCG</i> ) .....	116
Figure 75. Relative spectral emission ( <i>ELEDλ</i> ) of the LED .....	117
Figure 76. Spectral responsivity of the multichannel sensor ( <i>Resp</i> ).....	117
Figure 77.the BCG reflectance for different values of pH.....	118
Figure 78. Output values of the sensors vs pH .....	121
Figure 79. Output values of the camera vs pH.....	121
Figure 80. Experimental setup diagram .....	125
Figure 81. Experimental Setup.....	125
Figure 82. PAD image.....	126
Figure 83. Coloure intensity measurement results for various buffer pH values .	127
Figure 84. All measurement results on one plot .....	128
Figure 85. Images of PADs obtained at Back (a) and side (b) illumination conditions. ....	129
Figure 86. Artificial devices (not carbonate measuring) .....	130
Figure 87. Calibration curves for pH measurements. ....	132
Figure 88. Start of the analysis.....	134
Figure 89. PAD before dipping.....	135
Figure 90. PAD analysis .....	135
Figure 91. Pictures before and after analysis. ....	136
Figure 92. Result saved in database .....	136
Figure 93. Sensor board schematic .....	148
Figure 94. LED board schematic .....	149
Figure 95. Mechanical design .....	165
Figure 96. Water tank.....	165
Figure 97. Filtering schematic.....	166
Figure 98. Filters response .....	167
Figure 99. Schematic without anti-aliasing filter.....	167



Figure 100. Results without the aliasing signal (source V2 set to 0.0 V amplitude). .....	168
Figure 101. With the aliasing signal at 0.3V (30% of the amplitude of the non-aliasing signal).....	169
Figure 102. Schematic with anti-aliasing filter .....	170
Figure 103. Results with the aliasing filter .....	170

## **List of abbreviations**

ADC - Analog-to-digital converter

AI – Artificial intelligence

CD - Capillary Electrophoresis

C4D - Capacitively Coupled Contactless Conductivity Detection

DSP – Digital signal processing

ED - Electrodialysis

GPU - Graphics processing unit

HSL - Hue, Saturation, Lightness (colour model)

IC – Integrated Circuit

PAD - Paper-based analytical device

pH - Acid level of water

LIMPIDs - Linking Improved Modelling of Pollution to Innovative Development of Sensors

LoC - Lab on a Chip

LOAR - Lab-on-a Roll

PSU - Power supply unit

RGB – Red, Green, Blue (colour model)

RTC – Real Time Clock (electronic device)

MilliQ - Water that has been purified using an ion exchange cartridge

YOLO - You Only Look Once (object detection algorithm)

## **Chemical formulas**

BCG - Bromocresol green

$\text{CO}_3^{2-}$  - Carbonate ion

$\text{CaCO}_3$  - Calcium carbonate

$\text{Ca}_2^+$  - Calcium ions

$\text{CO}_2$  - Carbon dioxide

$\text{CaCl}_2$  - Calcium chloride

$\text{HCO}_3^-$  - Bicarbonate ion

$\text{H}_2\text{CO}_3$  - Carbonic acid

HCl - Hydrogen chloride

His - l-histidine

$\text{H}_2\text{O}$  - Water

MES - 2-(N-morpholino) ethanesulfonic acid

NaOH - Sodium hydroxide

$\text{NH}_4$  - Ammonium

$\text{NO}_2$  - Nitrite

$\text{NO}_3$  - Nitrate

P - Phosphorous

PDADMAC - Polydiallyldimethylammonium chloride

## **Abstract**

In the context of the rapidly intensifying crisis of climate change, the intricate dynamics of Earth's ecosystems have assumed a paramount significance. The carbon cycle plays a significant role in the dynamics of the earth's ecosystem, and anthropogenic emissions of CO<sub>2</sub> into the atmosphere have a significant effect on it. It is the geological part of the carbon cycle that is the least studied because measuring the content of carbonates in groundwater is a difficult task and consequently there is little data on high-frequency changes in the concentration of carbonates over a long period of time. Unlike traditional laboratory analyses, on-site measurements involve collecting data directly in the natural habitat of a water body, which allows information to be received in real time and taking into account a specific context (temperature, humidity, weather etc.). This approach not only reduces the risk of contamination of samples during transportation, but also allows capture of dynamic changes occurring over a short period of time, which otherwise could be missed due to sporadic sampling.

This thesis presents the design and development of an innovative device capable of overcoming the obstacles that have prevented comprehensive measurements of the chemical composition of water in-situ, especially with regard to the content of carbonates. Previous attempts at in-situ chemical measurement with devices based on microfluidic lab-on-a-chip technology have proved difficult due to issues such as the lack of reliability of the complex fluidic system and the need to use bulky and possibly short-lived liquid reagents. The system developed in this work is based on another type of microfluidic sensors known as Paper Analytical Devices (PADs), which are more suited to use in challenging locations. These have been previously applied to environmental monitoring but typically via manual sampling using single devices. This thesis describes a development of fully automated in-situ measurement system using a continuous roll of PADs (LOAR – Lab on a Roll). This provides a platform with a potential for wide applicability in water chemistry analysis, but this work focus use of carbonate PADs based on colorimetry detection. Two approaches to detection are investigated: one based on embedded system digital cameras and the other one using low-cost spectral sensors. These approaches are compared via modelling and experimental evaluation. The camera-based approach is shown to be more efficient and offers greater flexibility through use of machine learning to assist the measurement process. The accuracy of water chemistry measurement is potentially impacted by sampling errors (e.g. aliasing and jitter) and this is discussed and possible mitigations considered. The thesis also describes the design (mechanical, electronic and software) of an in-situ LOAR prototype and an its evaluation which demonstrates its feasibility. The experience gained leads to detailed recommendations for development of future versions.



## **Acknowledgment**

I would like to thank everyone who took part in the work in one way or another. First of all, I would like to express my gratitude to my supervisor Dr. Ian Bell for his comprehensive help, support and contribution throughout my studies at the University of Hull.

I would also like to thank my second supervisor, Dr. Dmitry Kuvshinov, for his guidance and support, and my third supervisor, Michael Rogerson, for his help and expertise in geoscience.

I would also like to thank all the members of the Analytical Research Group at the University of Hull, especially Samantha Richardson and Nicole Pamme for their help and expertise in chemistry and manufacturing of microfluidic devices.

I also wanted to thank my wife and my parents for their love and support, and my daughter for motivation and inspiration.

## 1 Introduction

Climate change and global temperature changes are already a significant problem for everyone today. And as Prof. Gideon Henderson said for BBC Radio 4 “I think it’s actually carbon change, not climate change, and climate - the fact that it has changed - that’s the symptom of the fact that we have changed the carbon cycle.”[1]. Some studies show that these processes may increase and some trends (for example, rising ocean levels) cannot be reversed in the coming centuries. However, in order to confront inevitable changes, it is necessary to understand the causes and impacts of these changes, as well as methods that are proposed to stop them or neutralize their consequences. For example, the effect of carbon sequestration (capturing and storing atmospheric carbon dioxide) on carbon fluxes (movement of carbon between different parts of the environment) has not yet been fully studied, and geological sequestration has long been considered insignificant compared to other types of sequestration.

In order to study the phenomenon of carbon fluxes, it is necessary to periodically take material for study (typically of natural water in rivers, streams and caves), but this is often very challenging, since samples are often required from hard-to-reach places (caves for example)[2]. If the sampling is not frequent enough, some of the information may be lost or misleading (the Nyquist-Shannon theorem - see chapter 2.3). Furthermore, during transportation, samples can change their characteristics over time and under the influence of external factors. It may be impossible to economically achieve meaningful measurements over a sustained period, with either manual or automated sample collection. Thus, there is a need for a device that will not only take the samples but will also carry out in-situ measurements.

Previously, use of standard laboratory instruments for in-situ water chemistry measurements was investigated (pollutants in river water), but it turns out to be expensive, requires significant maintenance and is very limited in usable locations[3]. Therefore, small, low-power, low-cost autonomous devices for measuring the content of ions in natural water were developed (LIMPIDS project – see chapter 1.4). The method for determining ions concentration was the Lab-on-a-chip (LoC) technology using glass or plastic microfluidic devices (see chapter 2.2.2). This technology is potentially highly accurate but lacks robustness, devices may not perform well with repeated use, and reagents may be unstable[4].

An alternative to using LoC can be to use Paper-based Analytical Devices (PADs). Such devices are easier to manufacture and easier to use, but they are less accurate. This work proposes that the usability of PADs outweighs the potential accuracy of LoC for in-situ water chemistry measurement. That is, accuracy can be sufficient, and with appropriate design, it is proposed that robust in-situ measurement platform can be developed. Typically, existing PADs are manufactured and used as

individual devices (for single-time measurement). A salient feature of the proposed approach is to employ a roll of PADs to provide a Lab-on-a Roll (LOAR) platform in which a sequence of devices can be exposed to the sample source at predetermined intervals (sampling rate). The LOAR concept has potential application to a wide range of chemical measurements, but this project will use carbonate measurement as an example due to the importance and challenges of these measurements, as discussed above.

### **1.1 Project context**

This project was a part of a larger multi-disciplinary PhD cluster project at the University of Hull on water; “Sensing and Safeguarding the Water Environment”, led by Prof. Nicole Pamme (now at the Department of Materials and Environmental Chemistry (MMK) at Stockholm University). The aim of the cluster project was to make breakthrough in developing a deep understanding of water quality, pollution dynamics and wider environmental geochemistry by harnessing expertise in computer sciences, microfluidics and novel sensing technologies. This specific project was part of an effort to develop automated in-situ measurement of carbonate in Karst cave water in collaboration with Prof. Michael Rogerson (now at Northumbria Department: Geography and Environmental Sciences) and Prof. Nicole Pamme’s group.

### **1.2 Research objectives**

The aim of this project is to develop a system by which it will be possible to test the effectiveness of the use of PAD devices for autonomous measurement of carbonates and also to compare different methods of optical analysis of PAD devices. Below is a list of the objectives of this study

1. Define the requirements and evaluate the potential capabilities of the LOAR platform concept for in-situ natural water chemistry measurement.
2. Develop and evaluate optical sensing techniques suitable for colorimetry based LOAR PADs
3. Develop and evaluate a demonstration system for an in-situ LOAR platform targeted at carbonate chemistry of water in karst landscape caves.

### **1.3 Project development objectives**

The following objectives should be achieved in the development of this project:

- Develop the electro-mechanics of a laboratory-based lab-on-roll prototype “dipping” system for purposes of evaluation and development.
- In collaboration with chemists, develop carbonate-measurement PAD designs and processes for manufacturing PAD rolls for use in the laboratory prototype.
- Analyse the impact of the aliasing and other potential errors on LOAR based sampling and use this to inform design requirements and limitations.



- Develop electronic hardware and associated control software for control of the laboratory prototype in order to facilitate automated measurements.
- Develop sensor hardware systems and analysis algorithms and software for automated measurement using the carbonate PADs.
- Evaluate and optimise the performance of full “dipping” measurement system in the laboratory.
- Further develop the mechanical, electronic and software subsystem to produce a prototype capable of deployment in caves.
- Evaluate the in-situ measurement system in field trials.

#### 1.4 Background

The LOAR proposed system concept is illustrated in 3.1. When a sample is to be taken the PAD roll is advanced to expose the next unused PAD to the sample source. The response of the PAD to the sample is detected using a sensing system (e.g. colour change response, electrochemical measurement) to provide a reading of the concentration of the chemical species of interest in the sample.

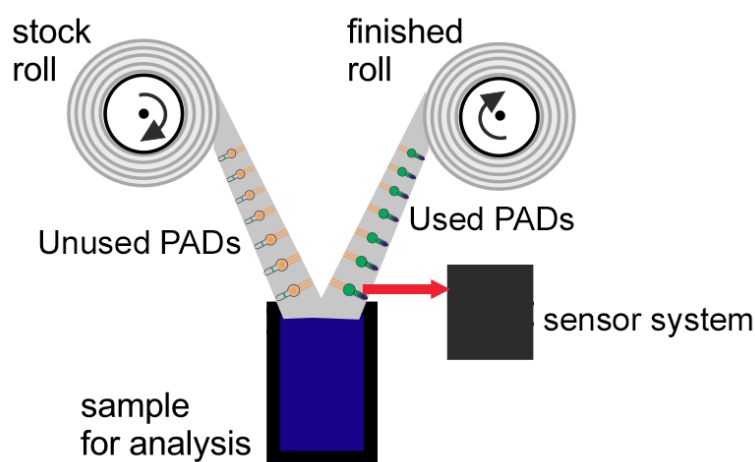


Figure 1. Lab-on-a Roll System Concept

The PAD roll does not have to comprise single type of PAD devices that are used one per sample. The proposed system can use a cluster of similar or different PADs (see Figure 2) which are exposed to the sample at the same sample time. The multiple PADs can provide measurement of different target chemical species or parameters, extending the measurement range for single species beyond that feasible with a single PAD and potentially assist calibration.

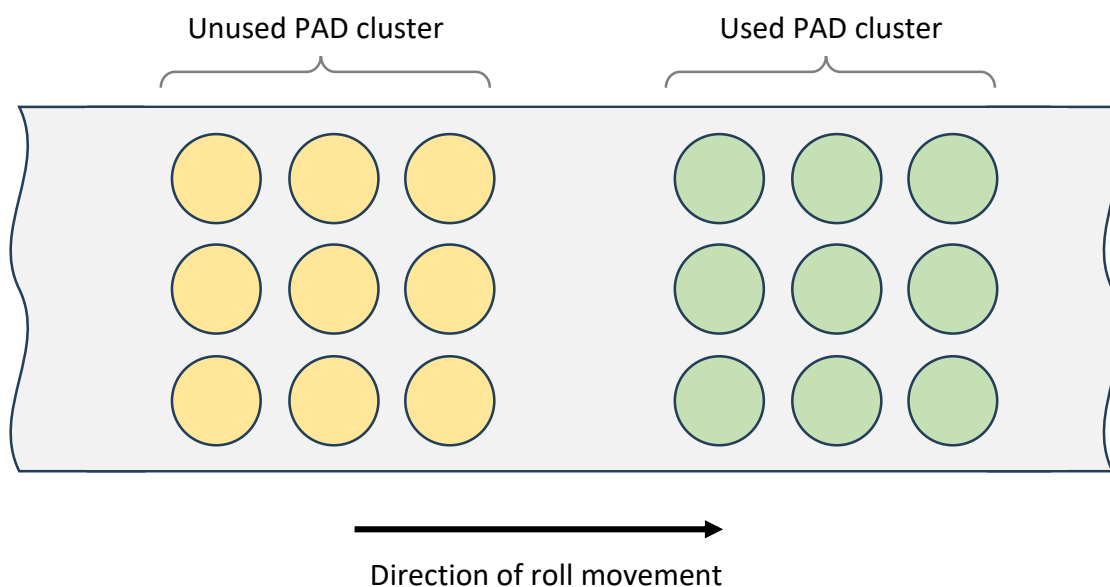


Figure 2. PAD Roll Concept

## 1.5 Previous work at Hull – The LIMPIDS project

### 1.5.1 Overview of LIMPIDS

Investigation of use of PADs for in-situ measurement of water chemistry was inspired by experiences gained in a previous project at Hull [3-6]. This project was titled “Novel technologies for in situ environmental monitoring: linking sensor development to improved pollutant transport models” (EP/G014221/1 (Hull) EP/G019967/1 (Reading)), but also referred to as “Linking Improved Modelling of Pollution to Innovative Development of Sensors” (LIMPIDS). It was funded by the Engineering and Physical Sciences Research Council (EPSRC) and was a collaboration between University of Hull Departments of Chemistry and Engineering, University of Reading School of Human and Environmental Sciences, Centre for Ecology & Hydrology (UKCEH), Wallingford, and the Environment Agency. The EPSRC funded project ran from 2009 and 2013, but further work continued in the Department of Chemistry at Hull until 2015.

The work was motivated by the importance of rivers as a source of water and the high level of impact on river water quality by both local human activities (domestic, industrial and agricultural) and the global influence of climate change [7]. The changes in water chemistry of rivers are difficult to predict due to the variety of complex factors (geographical, chemical and biological) involved [8]. This implies a need for models capable of predicting the impacts of land management and climate changes on water quality. However, to fully understand the processes which link hydrology and stream water chemistry within a catchment, chemical measurement frequencies must be based on the timescale of the catchment’s hydrologic response, which is often on the order of minutes or

hours. Long term water quality monitoring also allows the capture of extreme events, which can provide useful information on the characteristics of the water systems being studied. LOAR project will potentially solve these problems.

LIMPIDs project included both development work on a novel in-situ microfluidic sensor-based instrument and an attempt to deploy existing laboratory-based technologies in the field. In both cases the aim was to achieve high frequency (sub-daily, for example, hourly) monitoring to facilitate advancements in the science of hydrochemistry leading to improved models of catchment pollutant transport. More typically, monitoring requires the manual collection of samples which have to be stabilised and transported to a laboratory for analysis. The procedure is slow, costly and samples can degrade. It cannot be done at high frequency for extended periods due manpower constraints.

### 1.5.2 In-situ river monitoring using laboratory instruments

The existing instruments deployed in the project measured ionic pollutants: phosphorous (P), nitrate ( $\text{NO}_3$ ), ammonium ( $\text{NH}_4$ ) and nitrite ( $\text{NO}_2$ ) plus turbidity, chlorophyll-a, dissolved oxygen, conductivity and pH. Three monitoring sites were established in the catchment of the River Thames (southern and eastern England), specifically Enborne at Brimpton, the Kennet at Clatford and The Cut at Bray. Experience from using the existing instruments in situ was that installation and ongoing maintenance of the monitoring stations was laborious and expensive. Installation size (typically a shed or trailer), the need for mains power, and other considerations such as security limited possible monitoring sites. Instruments were visited each week for calibration and real time data were reviewed daily to identify issues with the equipment, such as pump failures. Failures resulted in the need for detailed data quality control, which required significant expertise and was time consuming and difficult. Fuller details can be found in [3].



Figure 3. Photograph (taken 2010) of example river monitoring station: (a) River Enborne at Brimpton (b) The Cut at Bray [3].

### 1.5.3 LIMPIDS Microfluidic Lab-on-Chip In-situ Instrument Development

The work on the novel in-situ instrument aimed to develop a self-contained system for field deployment of analytical microfluidic Lab on Chip (LoC) device(s) capable of detecting a range of ionic pollutants, including, but not limited to, those being monitored by the existing laboratory instruments in the other part of the project. The system (Figure 4) would integrate chemical sensing, power supply (batteries), power management, control of sampling and measurement processes, signal processing, communications and data logging. The system was based around a microcontroller with analogue signal processing and PC-based software for instrument configuration.

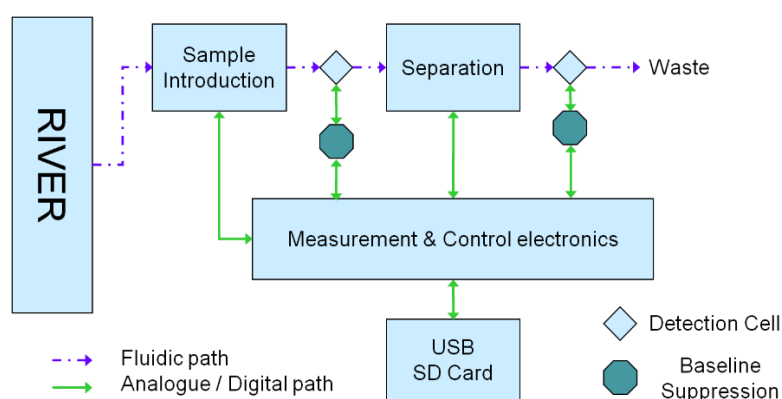


Figure 4. Measurement system block diagram

The chemical analysis (of ionic species concentration) was based on ion separation, with Capillary Electrophoresis (CE) [9] and Capacitively Coupled Contactless Conductivity Detection (C4D) [10] being identified as the preferred method. The signal from the C4D comprises small variations on a large offset. To improve sensitivity and limit of detection an electronic baseline suppression system was developed. The full system was not deployed in situ, but operation of key functions was verified and assessed in the laboratory. Full details can be found in [4].

Some testing was performed on the handling of river water by a LoC device [4, 6]. Water from the River Enborne environmental monitoring station (Figure 5) near the village of Brimpton was pumped continuously through a device with a 1mm channel (Figure 5a) for over two and half months before failure occurred due to blockage (Figure 5b). This indicated that a LoC-based measurement system could be feasible in terms of the useable time in situ, but also illustrated that failures were likely to occur at some point. It should also be noted that the channel in this device was larger than is often used in LoC analytical systems.

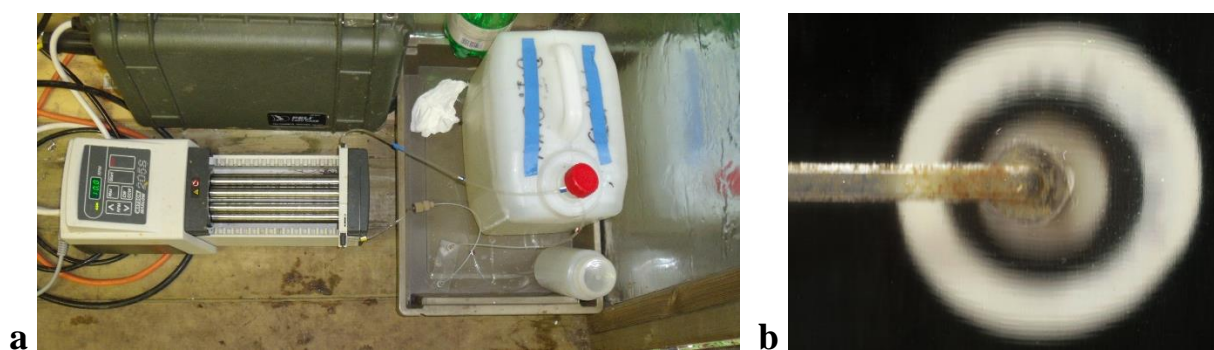


Figure 5. LoC trial at monitoring station on River Enborne at Brimpton: (a) setup, (b) failure due to blockage.

Similar to the laboratory instruments measurement failures, would be expected due temporary extreme conditions (e.g. freezing). Also as just discussed the operating life of LoC devices limited. Therefore, to facilitate identification of rogue data, provide overall data robustness, and alert users of actual or pending failures self-test capabilities were investigated [4, 6].

Work on the chemistry and fluidics aspects of the instrument continued after the end of funded LIMPIDs project [5]. A main area of this work was an investigation of Electrodialysis (ED) as a possible sample introduction method because it can be combined with CE for rapid pre-treatment and the subsequent determination of inorganic ions in river water [11]. An instrument fluidic system was proposed (Figure 6), but not fully developed. In this system water is pumped from the river to the sample reservoir from where it is introduced to an ED LoC device by a peristaltic pump. This pump circulates passes the sample through the ED chip for long enough to extract sufficient ions for the measurement.

On the other side of ED chip's ion exchange membrane, a fluidic loop is filled with a buffer solution (buffer solutions are used as a means of keeping pH at a nearly constant value in a wide variety of chemical applications). The buffer is MES/His (2-(N-morpholino) ethanesulfonic acid (MES), l-histidine (His)) which is commonly used in CE. To start a new measurement, the loop is flushed to the waste container and new buffer is loaded from the reservoir. After ion extraction from the sample the ions in the buffer loop are transferred to the CE chip by applying a voltage to force the ions to move to the CE separation channel. An ion bridge [12] is suggested to isolate the fluid flows in the CE chip extraction loop. The CE chip is also filled with fresh buffer for each measurement. The ions are electrokinetically injected into the main CE channel between the two short side channels, using their respective electrodes. A voltage is then applied to the long channel causing the ions to move towards the C4D detector. Different ions move at different speeds in the applied field so separate, reaching the detector at different times and producing detection peaks corresponding to their concentrations.

Detection is managed by the system described in [4]. Full details of the proposed system can be found in [5].

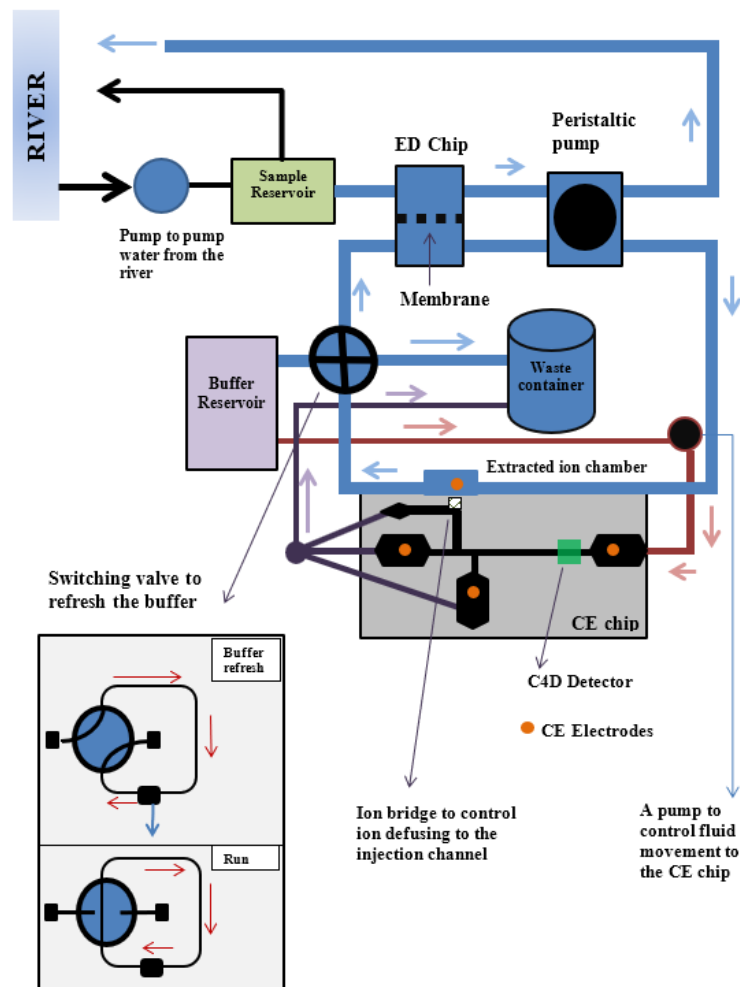


Figure 6. Proposed in-situ LoC chemical sensor instrument fluidic system using Electrodialysis and Capillary Electrophoresis (based on fig 7.1 in [5])

#### 1.5.4 Evaluation of LIMPIDS project

The proposed fluidic system in Figure 6 is complex and may be prone to failure particularly when operated in situ. In situ operation is likely to produce more stress on the instrument than running in the lab, for example, temperatures are likely to be more extreme and subject to more rapid changes. Freezing may potentially damage the fluidic system. This could be averted by providing by heating the system enclosure, however this may significantly increase the power budget.

Experience of working with LoC devices in the laboratory indicates that problems, such as blocked channels and bubbles, are quite common. Self-test was investigated [4, 6] to help identify these issues in an autonomous system, which may reduce their impact, but will not prevent data loss or increase reliability. Fault detection techniques included impedance-based bubble detection [13], chromatography baseline profile analysis [14], and pump noise observation.

The tubing used in peristaltic pumps is subject to wear and has a lifetime of 24 to 1000 hours [15], however in the instrument flow rates are likely to be lower than in [15] so lifetimes may be extended. Despite this possible tube failure is a concern.

Both the lab instruments (some of them) and the proposed LoC system require liquid reagents (in the case of the LoC system the MES/His buffer). The reagent consumption of standard instrument system is 100 L every two weeks [3] whereas for the LoC system it is 1.5 L every two weeks [5].

The experiment with pumping river water through a LoC device highlights issues that are likely to occur with continuous or frequent exposure to natural waters, such as biofouling, mineral deposits, blockages by particulates, and degradation of materials. This is potentially exacerbated by the relatively low robustness of the miniaturised fluidic system.

The need for liquid reagents is a difficulty due to their weight, possibility of leaks damaging other parts of the system or contaminating the environment, and reagent degradation over time. Buffer usage in the proposed LoC instrument is about 1 ml per measurement (with a wash step included in the measurement process). The design objective was for below 2L of reagents, which implies about 2000 measurements, which is acceptable. Neither of the compounds in the MES/His buffer are generally regarded as hazardous in solution ([15] referenced in [5]). Buffer stability was analysed and [5] recommends a measurement run of less than 4 months.

Overall, the experience from the LIMPIDS project indicates that use of microfluidic LoC devices for in-situ chemical monitoring has great potential but may be practically difficult to achieve due to reliability issues and with microfluidic channels on chip and other fluidic components such as pumps and valves (both on and off chip). Furthermore, the need to use liquid reagents, and possibly storage of liquid waste, may limit severely operational time and contributes to system complexity. Liquid reagents and waste may leak into the environment if the system is catastrophically damaged. Maintenance is potentially complex - reloading liquid reagents and possibly flushing the fluidic system - and may be difficult to achieve in situ. The whole fluidic and LoC subsystem may only be suitable for single use due to potential clogging and fouling issues.

In comparison, the proposed LOAR system does not require complex fluidics and each PAD is operated as first and only use, which should provide better reliability and lower susceptibility to drift in performance. PADs store all reagents in dry form, which should provide longer operating life for comparable chemistries. The electro-mechanical system for PAD roll transport has the potential to be

significantly more robust than a microfluidic subsystem and maintenance by roll change should be relatively easy to perform, particularly in situ.



## **1.6 Thesis structure**

### **1.6.1 Chapter 2 – Literature review**

This chapter provides an exploration of the multifaceted problem of climate change and its correlation with carbon movement. It highlights the importance of carbon movement in the context of climate change. The dynamic interplay of natural and human activities that affect carbon mobility is central, as understanding this complex process is paramount to developing effective mitigation strategies.

The rest of Chapter 2 delve into contemporary approaches and technologies developed to combat climate change and manage carbon movement by analysing the implementation carbon capture and storage technologies. Demonstrating their role in removing greenhouse gases from the atmosphere and mitigating their adverse effects. These innovative methods present promising opportunities for limiting carbon emissions.

This chapter also describes the various methods used to accurately measure the concentration of carbonates in water. Among these techniques, the PADs method stands prominent, as it provides a cost-effective and relatively simple means to measure carbonate concentration using colorimetry. Adding a water sample on a PAD, produces a visible colour change occurs, indicating the endpoint of the reaction and enabling the calculation of carbonate levels.

Ultimately, through its brief analysis of carbon concentration measurement methods, this chapter presents the arguments for the need to use the on-site carbonate measuring instrument developed in this work.

### **1.6.2 Chapter 3 – System design development**

The chapter commences with top-level overview of the system concept. Providing with a clear understanding of the core principles and fundamental architecture.

This chapter also describes detailed design of the LOAR system and carbonate measurement process. This starts with the carbonate PADs and PAD roll design and manufacturing process, including the preparation of reagents.

Colorimetry is a widely utilized analytical technique based on the measurement of absorbance or transmittance of light by a coloured solution. Part of this chapter outlines how this technique can be applied to the carbonate PADs in the context of the LOAR instrument.

This is followed with a description of the hardware, both the electromechanical design of the “dipping” system and the electronic hardware to provide control, sensing, data handling, and power management.

The next part of this chapter discusses the application of the Nyquist-Shannon theorem to water sampling. This fundamental theorem in signal processing is highly relevant in assessing water quality as it may have a significant impact on the accuracy of measurements. The implications for the LOAR instrument, and other aspects of sampling accuracy, are discussed.

Finally, the system software is described in detail with emphasis of the AI based location of critical areas of PAD for analysis and the colorimetric analysis process itself.

### **1.6.3 Chapter 4 – System evaluation**

Chapter 4 discusses the process of evaluating the system, which is necessary to ensure the efficiency and reliability of its operation. This chapter contains several key components that together contribute to a comprehensive assessment of the performance and functionality of the system.

**Initial Experimental Validation of Carbonate PAD:** This section describes initial experimental tests to confirm the device's ability to measure and analyse carbonate levels in various samples.

**Model-based comparison of camera and spectra sensor-based colour measurement:** One of the main aspects discussed in this section is the comparison of two different measurement methods: colour measurement using a camera and a low-cost spectral sensor. The section examines the advantages and limitations of each method to determine which one is may be most suitable for accurately assessing colour changes in the PAD device.

**Experimental to evaluate carbonate paper analytical device:** This section presents the results of experiments specifically designed to evaluate the effectiveness of PAD.

**Comparison of side and back lighting:** Lighting plays a crucial role in the accuracy of colour measurement. A comparison of side and rear lighting methods helps to determine the optimal lighting setting for consistent and reliable results.

**Experimental comparison of sensor and camera accuracy for measuring PAD device colour change:** Another key point of this chapter is to determine the accuracy of both sensor and camera when evaluating PAD colour changes.

**Calibration curve:** Calibration is an integral part of any analytical system. This describes the process of constructing a calibration curve for a PAD. This curve serves as a guideline for translating colour measurements into meaningful values of carbonate concentration.

#### **1.6.4 Chapter 5 – Operational test of the System**

Operational test: The final stage of the system development includes performance tests. The results of these tests provide key parameters and how well the device works for its intended purpose.

#### **1.6.5 Chapter 6 – Conclusion**

This chapter contains outcomes in respect to the stated objectives of the project and presents the conclusions obtained in the course of this work. This section also contains further recommendations for the design of the system, which will help to speed up the production process and improve the result. The final part of this chapter contains future work, where further directions of work on the system are discussed.

## 2 Literature review

### 2.1 Climate change and carbon fluxes

#### 2.1.1 Climate change problem

Climate change on Earth is one of the most interesting and frightening natural phenomena that worries all of humanity. The warming trend in global temperatures, which is visible from all independent methods for calculating global temperature changes, is also accompanied by other observations, such as the melting of mountain glaciers on all continents, a decrease in snow cover, earlier flowering of plants in spring, a short ice season on lakes and rivers, a decrease Arctic ice and sea level rise [16]. In addition to changes in temperature, changes in annual precipitation and an increase in the number of climatic disasters such as hurricanes, storms and floods are also recorded [17-19]. Figure 7 shows of Earth's surface temperature and carbon dioxide (CO<sub>2</sub>) in the atmosphere.

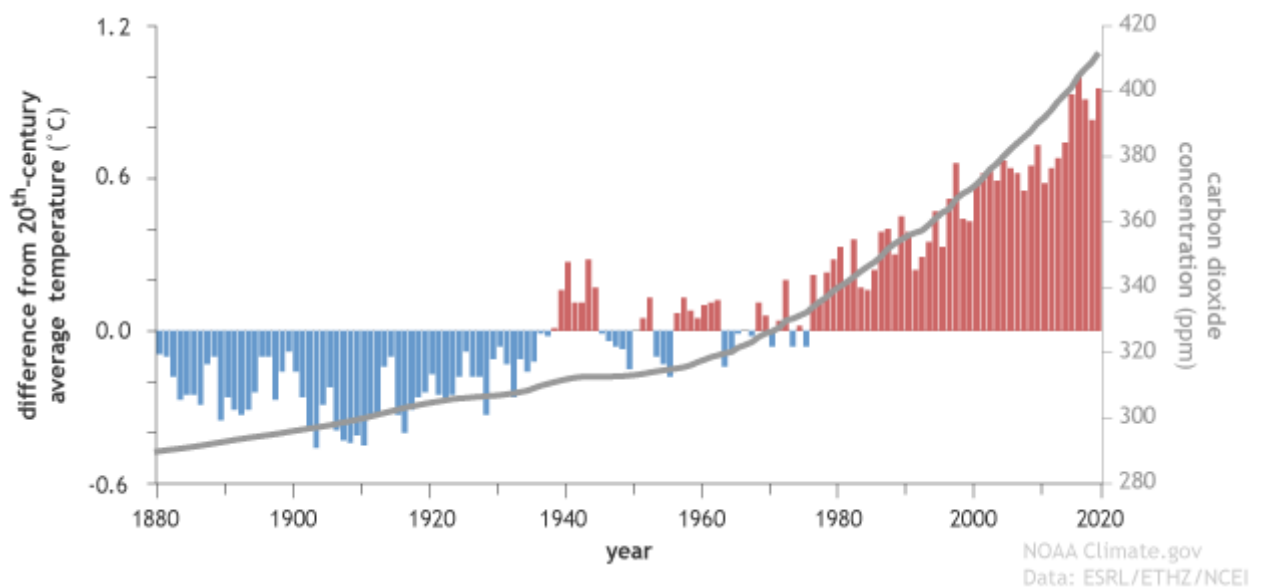


Figure 7. Earth's surface temperature and atmospheric carbon dioxide [20].

There are many causes of climate change, but it is well established that the main culprit for the rise in temperature on Earth is human [21]. The significant increase in CO<sub>2</sub> in the atmosphere is caused by booming industry and the emergence of a large number of cars around the world. A large amount of CO<sub>2</sub> in the atmosphere decreases the loss of heat from the surface of the Earth via short-wavelength infrared radiation, increasing the average temperature of the Earth surface. The increase in the temperature of the surface layer of the atmosphere leads to a shift in climatic zones, causing melting of the Arctic and Antarctic ice, as well as permafrost, which leads to an increase in the level of the World Ocean [22].

Global warming has a great impact on various aspects of the life of living organisms. Especially significant changes have occurred in the phenology (cyclical or seasonal timing) of plants and animals [23, 24]. These changes lead to the

desynchronization of seasonal interactions between species, which has a significant impact on the biodiversity and primary productivity of ecosystems. Changes in phenology cause disturbances in the structure of the eco-system due to the difference in the phenological reactions of species to these changes. For example, the phenology of species growing in cold regions is more sensitive to temperature increases than the phenology of species in warm regions [25]. Thus, changes in the phenological synchronicity of interactions between plants and animals can significantly transform the structure of plant communities. Climatic changes are also affecting the animal kingdom. Many species are dying out, others are changing their traditional habitats [26]. In addition, in humans, warming can lead to an increase in the incidence of intestinal infections, asthma, allergies and respiratory diseases [27].

There is an urgent need to understand the likely changes to climate and ecosystems which will arise from ongoing CO<sub>2</sub> emissions. However, there is a parallel need to also understand naturally occurring transports of carbon through the Earth's systems to identify potential solutions for removal atmospheric carbon for stable storage where it will do least harm.

### **2.1.2 Carbon fluxes at the Earth surface**

The dynamics of terrestrial ecosystems depend on interactions between biogeochemical cycles that have recently undergone anthropogenic modification. This is especially true for carbon, nitrogen and water cycles. Terrestrial ecosystems, where carbon is stored in living biomass, decomposing organic matter, and soil, play an important role in the global carbonate-silicate geochemical cycle. The cycle diagram is shown in Figure 8 Carbon is exchanged between these reservoirs and the atmosphere through photosynthesis, respiration, decomposition and combustion. Human intervention in this process occurs through changes in the structure of land cover, contamination of the surface of water basins and soil areas, as well as through direct emission of CO<sub>2</sub> into the atmosphere [28]. Thus, human activity introduces an imbalance, and the carbon emitted exceeds that absorbed. It follows from this that in order to restore the balance, it is necessary either to reduce the amount of carbon released or to increase the amount of absorbed carbon.

One of the methods of carbon absorption can be the carbonate minerals weathering. Carbonate rocks, such as limestone and dolomite, are composed primarily of carbonate minerals, which contain the carbonate ion, CO<sub>3</sub><sup>2-</sup>. Limestone is composed of calcite or aragonite, which are different crystalline forms of calcium carbonate, CaCO<sub>3</sub>.

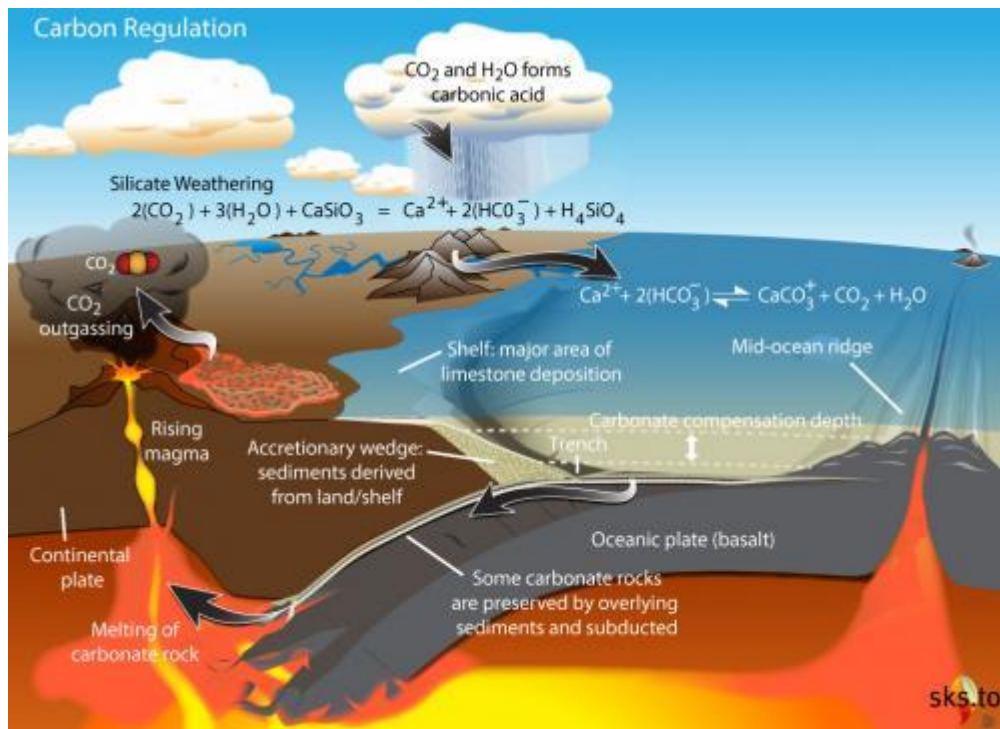
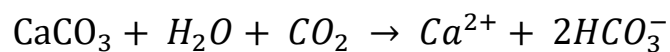
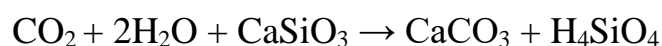


Figure 8. Carbonate-silicate geochemical cycle [29]

The carbonate weathering process is a potential sink for atmospheric CO<sub>2</sub> [30]. The general equation for carbonate weathering can be represented as follows:



In this reaction, carbon dioxide dissolves in water to form carbonic acid, which reacts with calcium carbonate to produce calcium ions (Ca<sup>2+</sup>) and bicarbonate ions (HCO<sub>3</sub><sup>-</sup>). These ions are transported by rivers and streams to the oceans, where they contribute to the formation of carbonate minerals in marine sediments. Over geological timescales, these sediments can become buried and form limestone rocks, effectively sequestering the carbon in solid form [31]. The effect of weathering of carbon minerals on carbon cycles is often underestimated and only silicate weathering is considered. Silicate weathering primarily involves the breakdown and alteration of silicate minerals, which are abundant in the Earth's crust. Silicate minerals are composed of silicon and oxygen, often in combination with other elements like aluminium, iron, calcium, magnesium, and potassium. The process of silicate weathering occurs through various chemical reactions, including dissolution, hydrolysis, and oxidation. During silicate weathering, atmospheric CO<sub>2</sub> is converted to bicarbonate, which is then transported to the ocean:



The resulting solid carbonates are then precipitated as carbonate minerals. Nevertheless, carbonate rocks are more susceptible to weathering than silicate rocks, and they significantly affect the concentration of dissolved inorganic carbon

in almost all freshwater catchments. Increased concentrations of dissolved inorganic carbon can also enhance photosynthetic carbon uptake by aquatic organisms [32]. If carbon is stored as a solid, it will be removed from the short-term carbon cycle, and the carbon balance will be shifted towards consumption. The relationship between the weathering of carbonate minerals and aquatic photosynthesis is called coupled carbonate weathering (CCW). It is assumed that this process may have previously been underestimated, and the impact on carbon cycles is 3 times greater than expected [33]. The weathering of carbonate minerals is responsible for about 94% of atmospheric CO<sub>2</sub> uptake, while silicate weathering is only 6%. Therefore, atmospheric carbon absorbed by coupled carbonate weathering can have a significant impact on both short- and long-term climate changes.

### **2.1.3 Karstlands and the carbon cycle**

Karstlands form when water-soluble carbonate rocks, such as limestone, are exposed to water at the Earth's surface, and weathered. They are characterised by a lack of surface water and consequently weak soil development, complex and efficient subsurface water drainage generally through caves and a range of characteristic landforms such as sinkholes, dolines, pavements, fissures and towers [34].

Karstlands are involved in the global carbon cycle and participate in various biogeochemical processes. During the formation of carbonate rocks, CO<sub>2</sub> is converted from gas to solid carbonate minerals, thereby binding carbon and slowing down the processes of climate change [35-37].

Rocks that dissolve as a result of chemical dissolution form karst aquifers. The karstification process occurs under the influence of rain or melt water passing through the soil and then through cracks and fractures in the carbonate rock.

Understanding the carbon fluxes in underground water systems within limestone caves will allow better understanding of global carbon cycles in nature. More data on carbon dissolved in water will allow for a better understanding of carbon processes and, as a result, climate change [38]. This field is rapidly developing, but sampling technologies, which facilitate the data collection required to progress the research are significantly limited at the moment.

### **2.1.4 Forestry as a means of carbon sequestration**

Forests play a major role in the global carbon cycle. They are a reservoir containing more than 20% of the global land carbon stock in the phytomass (living plant biomass) and upper soil layer [39]. Young growing forests quickly accumulate associated carbon in wood, branches and roots of trees, but

deforestation releases accumulated carbon for years, which leads to carbon imbalance in nature [40].

Woodland Trust Northern Forest Project is developing rapidly in the north of England [41]. The goal of the project is to promote the idea of creating forests as a means of reducing carbon dioxide in the atmosphere. This project is about to plant 50 million trees in northern England. In general, both projects are aimed at popularizing the idea of planting trees in order to restore the carbon balance.

Studying the influence of forests on climate at spatial and temporal scales as well as assessing the impact of changing climatic conditions on the functioning and dynamics of forest vegetation are extremely difficult [42]. This is primarily because of the complex system of direct and reverse relationships formed between forest vegetation and climate.

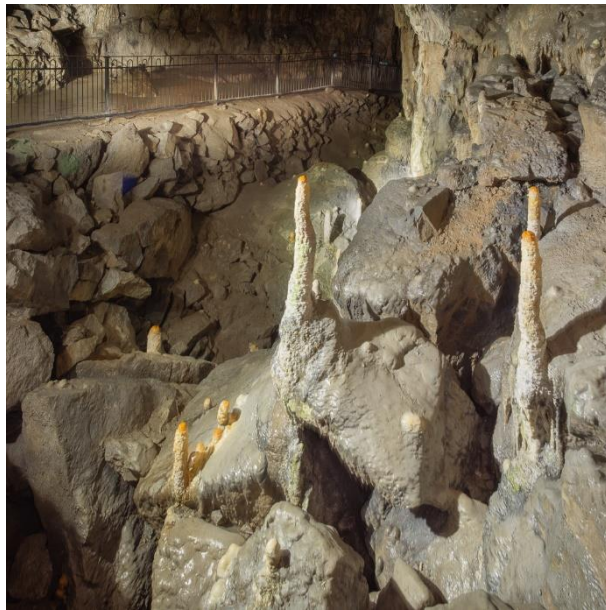
Since the full impact of trees on the carbon cycle is not fully understood, studying the effects of planted trees on karst waters and the ecosystem as a whole will help to better understand the mechanisms of climate change.

One way to study this relationship is to study changes in the concentration of carbonates in groundwater. As previously mentioned, regular sampling of water samples is a laborious task, and for karst water systems sampling would often need to be carried out in caves. Often caves are difficult to access, and researchers have no way to take samples as frequently as is required to obtain sufficient data. This method also has several disadvantages. Manual approaches are often quite expensive and samples may degrade during the time taken to transport them for analysis. Thus, there is a need for an automatic monitoring system measuring the concentration of carbonates in ground water. Automatic sampling systems exist, but such systems do not analyse samples [43], again leading to the possibility of sample degradation. This provides the motivation for this work to develop a low cost instrument for in-situ measurement to carbonates in water, which is suitable for deployment in caves.

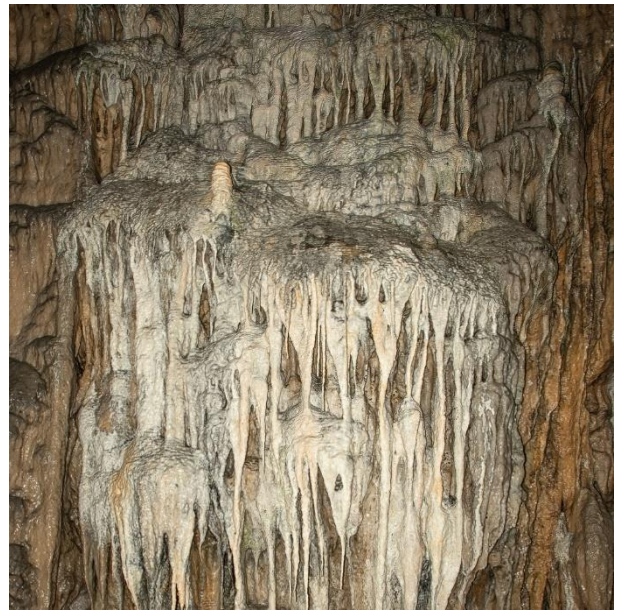
### **2.1.5 Proposed test site**

Poole's Cavern (cave on the edge of Buxton in the Peak District, in the county of Derbyshire, England) cave was chosen as a place for evaluation of the measurement system. The cave is open to the public and therefore it has easy access via a walkway from which visitors can view the karst rock formations (speleothems) (see Figure 9 a,b). This choice was made on the basis of the fact that several studies in the field of geosciences are already being carried out in this cave (see Figure 9 c,d), there is already some equipment (such as a radio sensor network), and there are also qualified personnel who can help with research.





(a)



(b)



(c)



(d)

Figure 9. Poole's Cavern (February 2020): (a) Public walkway and speleothems (b) speleothems, (c) and (d) experimental equipment. Sensor network radio device (Tinytag Plus Radio) can be seen in (c)

## 2.2 In-Situ chemical measurement

### 2.2.1 Chemical analysis systems

In the field of water parameter analysis, there is a wide range of solutions, ranging from basic sensor technologies to complex systems with multiple sensors capable of continuous monitoring in real time. Therefore, it is necessary to investigate options that can potentially be used to automatically monitor the concentration of carbonates in water on site.

The simplest and cheapest solution for analysis is to use ready-made electronic sensors (that would be easy to integrate into a computer system) like pH, conductivity, dissolved oxygen and etc. (shown in Figure 10) [44-46]. The electrical interface of the electronic sensors allows to relatively quickly design complex measurement systems based on them and provide for continuous monitoring in real time. This instant feedback is crucial in situations requiring rapid response to changing conditions. Process automation through sensor integration simplifies measurements, reducing the need for constant manual monitoring [47, 48].



Figure 10. a – pH sensor, b – electrical conductivity sensor, c – dissolved oxygen sensor.[44-46]

Although the initial development and configuration costs of integration sensors from different manufacturers or using different technologies can be significant can lead to compatibility issues, but the long-term benefits of sensor integration often result in significant savings.

The accuracy and reliability of sensor data is crucial. Any malfunction of one or more sensors can compromise the integrity of the entire system, which underscores the importance of regular calibration and quality assurance measures [49]. Often, sensor outputs may depend on external conditions, and may also change their characteristics over time [44-46]. It should also be noted that there are no electronic sensors for analysing the concentration of certain substances (e.g carbonates) [50]. This fact makes it impossible to build carbonates measurement system based only on electronic sensors.

There are also systems that only collect samples, but do not perform analysis. Such automatic sampling systems are devices that collect water samples on site without performing analysis (see Figure 11). They provide continuous sampling in real time, reducing the need for manual intervention [51, 52]. The analysis of the collected water samples takes place later in the laboratory.



Figure 11. Portable autosampler for discrete surface water samples [51].

The integration of precision sampling mechanisms provides a complete set of data in the samples, since in laboratory conditions it is possible to completely eliminate the influence of foreign impurities, which increases the accuracy of the analysis.

Electricity consumption is a critical factor, especially in remote or energy-limited environments where energy efficiency is of paramount importance. In some cases, an on-site analysis may be required, as samples may change their characteristics over time.

There are commercially available automatic measurement systems. These automated on-site analysis systems are generally excellent at measuring certain sets of impurities (but not carbonates) present in water [53, 54].

However, such systems often have a higher price, primarily due to the integration of advanced technologies and sophisticated instrumentation. In addition, it is important to note that although these on-site analysis systems are capable of measuring several impurities in water, there is a gap in their ability to measure certain components such as carbonates.

The reliability of automatic sampling systems is crucial, and any malfunction or malfunction in the sampling mechanisms can compromise the integrity of the entire analysis process.

There is no system on the market that would analyse the concentration of carbonates in water on-site. Thus, there is a need for a system that would be flexible enough to be configured to measure various impurities in water, but also relatively cheap.

### 2.2.2 Analysis methods

There are many methods for analysing of the chemical composition of water. The following are the methods that are potentially most suitable for the analysis of carbonate content and can be implemented on site.

#### 2.2.2.1 Electrochemical analysis

The first and most widespread type of measurement of water impurities is electrochemical analysis. These methods usually involve applying an electrical potential to electrodes immersed in a solution (a diagram of electrochemical device is shown in Figure 12a). Changes in current, voltage, or impedance are then measured, which provide information about the concentration or properties of the specific substances being analysed. There are various electrochemical methods, including potentiometry, amperometry and voltammetry, each with its own principles and fields of application (example of advanced electrochemical device is shown in Figure 12b). The choice of the method depends on the specific requirements of the analysis and the properties of the target analytes [55].

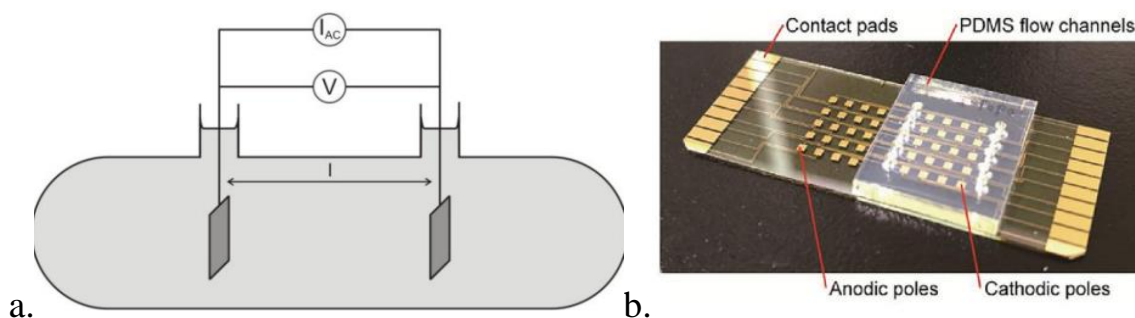


Figure 12. A – diagram of a basic electrochemical liquid conductivity meter with 2 electrodes, b - electrochemical device with arrays of  $4 \times 5$  cathodes and anodes with five flow channels on the cathode side [56].

One of their key strengths is their high sensitivity, which makes it possible to detect the smallest concentrations of ions or molecules in water samples. In addition, electrochemical methods have a high degree of selectivity. They can be adapted to measure specific ions or compounds, allowing for accurate and targeted analysis. This selectivity is especially important for distinguishing closely related species and ensuring the accuracy of the results [56-58].

Economic efficiency is a significant advantage associated with certain electrochemical methods. The simplicity of the equipment and lower maintenance requirements contribute to lower overall costs compared to some alternative analytical methods.

Portability is a key feature of many electrochemical devices, allowing for on-site analysis in the field. This feature is especially useful for environmental monitoring in remote or difficult locations where transporting samples to a laboratory may be time consuming.

Despite these advantages, electrochemical methods come with their own set of problems. Interference from other substances in the water is a common problem that can affect the accuracy of measurements [59, 60].

Calibration is another aspect that needs attention. Electrochemical sensors often need regular calibration to maintain accuracy, and the process can be sensitive to environmental conditions. Incorrect calibration can compromise the reliability of the results [59].

Often, the physical data of the measured liquid depends not only on the targeted analyte, but also on many other impurities, which in turn requires additional purification / filtration of the liquid. The presence of third-party substances can lead to false positive or negative results, requiring careful consideration and confirmation of the results. Contamination of the electrode is a common problem that occurs as substances accumulate on the surface of the electrode over time. This contamination can reduce sensitivity and impair the operation of the electrochemical system, which requires regular maintenance and cleaning [55]. Another limitation is that the data obtained by this method requires complex analysis and interpretation [55, 61].

### **2.2.2.2 Spectrometry**

Another method which potentially can be used for chemical analysis is optical spectrometry. In laboratory spectrometers, the principle of measuring optical absorption is most often used. The basic diagram of such a spectrometer is shown

in Figure 13. The measurement principle consists in comparing the spectrum of two beams of light coming from the same source, one of which passes through a sample and the second one probes a reference sample. Sometimes a comparison is made with distilled water. The difference is the absorbed light, the intensity of which depends on its physico-chemical characteristics (example of absorption of a sample as function of analyte concentration is shown Figure 14).

Also, the diffuse reflection spectroscopy method can be used for analysis, the diagram of which is shown in Figure 15. In this method, the light reflected from the object is measured, thus this method is more suitable for opaque samples that do not transmit or transmit a small amount of light.

But for on-site measurements, it is necessary to use portable spectrometers. Portable spectrometry is a powerful tool for chemical analysis of water, providing convenience and flexibility for on-site testing. One of the key advantages of portable spectrometry is its ability to provide fast measurements of various water parameters in real time. This includes the analysis of key elements, ions and molecules present in water samples. [For example, portable spectrometers are capable of measuring the iron content in a liquid in the range from 0.01 to 1000 mg/l [62]. The portability of these spectrometers allows for field testing in various environmental conditions, allowing instant information on water quality [63, 64]. Modern spectrometers can detect very low concentrations of analytes [65, 66]. However, the exact limit of detection varies depending on the specific instrument and the conditions of the measurement.

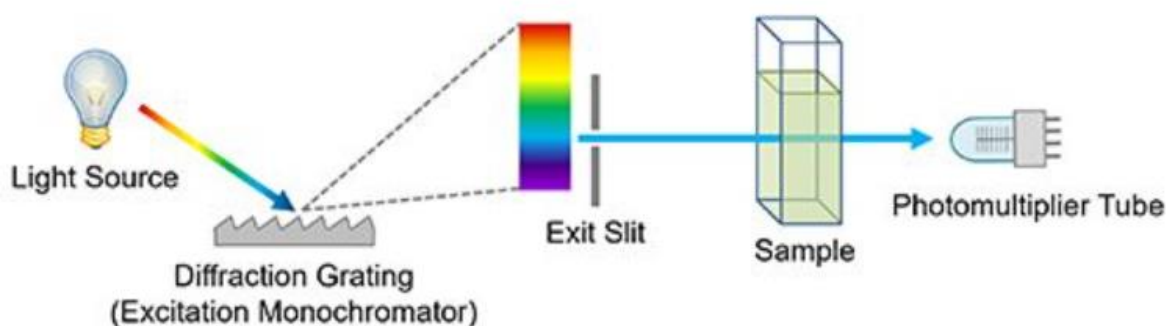


Figure 13. Simple diagram of an optical spectrometer[67].

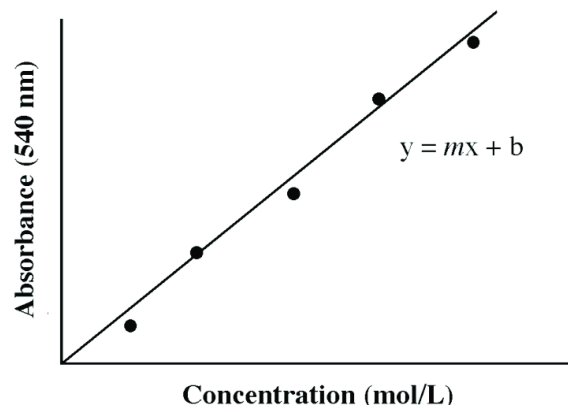


Figure 14. Typical appearance of the Absorption graph [68].

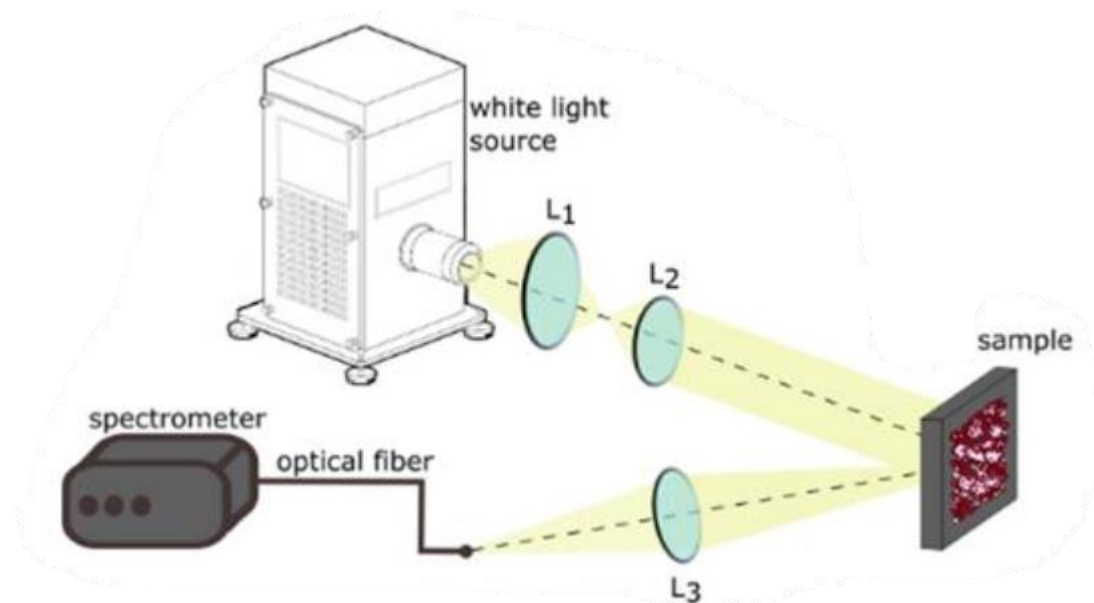


Figure 15. Diffuse reflectance spectroscopy [69].

The compact and lightweight design of these devices increases their practicality in the field, making them suitable for water sensing applications.

However, like any technology, portable spectrometry has its limitations. One notable disadvantage is the compromise in sensitivity and accuracy compared to traditional benchtop laboratory spectrometers. Miniaturization and simplification of the instrument often leads to a decrease in analytical characteristics, limiting its use in scenarios where high-precision measurements are of paramount importance [66].

Spectrometers can be used to analyse carbonates, but the initial cost of portable spectrometers can be significantly higher compared to other methods, and the delivery and storage of liquid reagents for analysis can be a serious challenge to development, which in turn also increases the cost of the system being developed.

### 2.2.2.3 Capillary Electrophoresis

Another method is Capillary Electrophoresis. It is an analytical technique that separate and analyse ions, molecules, or particles based on their electrophoretic mobility in a capillary filled with an electrolyte (diagram is shown in Figure 16) [70]. Capillary Electrophoresis (CE) has proven to be an invaluable technique for water chemistry analysis, offering a unique set of advantages in terms of speed, efficiency, and precision (can be up to  $10^{-21}$  mol) [70, 71]. One of the primary benefits of CE is its ability to separate and analyse ions, molecules, and particles in a highly efficient manner. The technique relies on the movement of charged species through a narrow capillary under the influence of an electric field, enabling the rapid separation of components based on their charge-to-size ratio. CE provides a high degree of resolution, allowing for the precise quantification of various water constituents, including ions and organic compounds. CE may require careful sample preparation and optimization to account for these effects. The initial setup costs and maintenance demands may be higher compared to simpler analytical methods, requiring careful consideration of the specific analytical needs and resources available [71, 72]. Thus, capillary electrophoresis is not suitable for analysis in an autonomous carbonic measurement system.

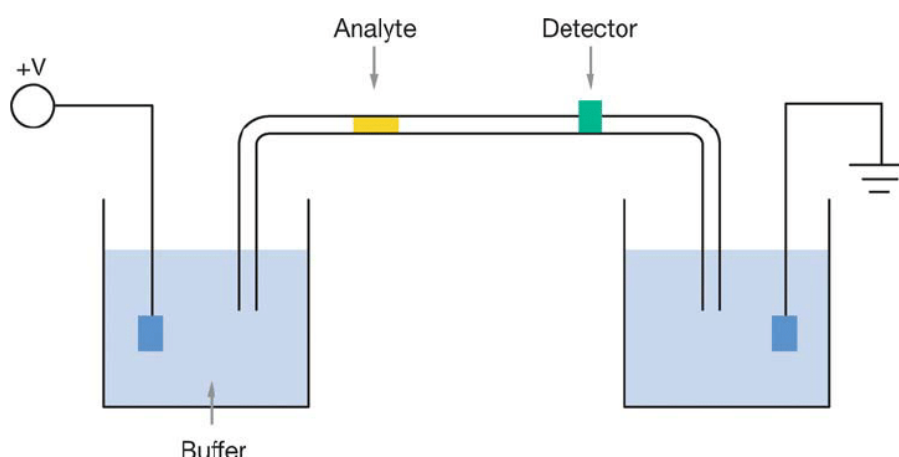


Figure 16. A diagram of a basic capillary electrophoresis setup[73].

### 2.2.2.4 Enzymatic methods

Another potential way to analyse water composition is to use enzymatic methods. Enzymatic methods of chemical analysis of water are based on the catalytic activity of enzymes to obtain measurable signals such as colour changes or fluorescence, proportional to the concentration of the target substance [74-76].

A significant advantage is the sensitivity of enzymatic methods which can reach several mM for heavy metals for example. Enzymes can be used to analyse various water parameters, including nutrients, organic compounds, and ions. This adaptability makes enzymatic methods applicable to a wide range of environmental monitoring scenarios.



However, enzymes can be sensitive to environmental conditions, including temperature and pH. Maintaining optimal conditions for enzyme activity is crucial to obtain reliable results, and deviations from these conditions can lead to inaccuracies in the analysis [75-77].

Another disadvantage is the stability of enzymes, especially during prolonged monitoring or when exposed to harsh environmental conditions. Storage and handling conditions should be carefully monitored to maintain enzyme stability and activity over time [77, 78].

This method is not suitable for this project, as it is difficult to integrate it into an autonomous system and will require temperature control module which will significantly reduce duration of operation on a single battery charge.

#### **2.2.2.5 Biochemical methods**

There are also biochemical methods of chemical analysis of water that involve the use of biological reactions and biomolecules to determine the composition of water samples. These methods use interactions between living organisms or biological molecules and target analytes present in water. Biological reactions stimulated by microorganisms often exhibit high selectivity towards certain substances, which allows for targeted analysis with minimal interference from other components [79, 80].

The adaptability of biochemical methods should be noted, since they can be applied to a wide range of water parameters.

Despite these advantages, biochemical methods have certain limitations. The influence of other substances in the water sample may be a problem affecting the accuracy of measurements. Careful consideration of potential interference and validation of results are important steps in ensuring the reliability of biochemical analysis.

Biochemical methods can also be sensitive to environmental conditions such as temperature and pH. Changes in environmental parameters can affect the activity of living organisms or biomolecules, which leads to potential inaccuracies in the analysis [79, 81]. Similar to the enzyme method, this method is difficult to integrate, and the measurement results are difficult to digitize automatically

#### **2.2.2.6 Ion-membrane methods**

Ion-membrane methods of chemical analysis of water involve the use of selective membranes that allow certain ions to pass through, blocking others. These methods are based on the principle of ion-selective membranes, which allow direct measurement of ion concentrations in water samples. Ion-membrane methods have a wide dynamic range, allowing the analysis of a wide range of ion concentrations

in water samples [82-84]. For example this method can detect up to 0.001M NaCl concentration in water [85].

One significant disadvantage is the potential interference from other ions, which can cross-react with the membrane. Careful checking and accounting of the water composition is necessary to eliminate these interferences and ensure the accuracy of measurements.

Maintenance of ion-selective electrodes is also a disadvantage. Over time, the characteristics of these electrodes may deteriorate, which affects their sensitivity and accuracy. Regular calibration and proper storage conditions are necessary to maintain the functionality of the electrodes and ensure the long-term reliability of the method [83, 86]. This method requires expensive equipment and special skills for the production of sensors, which does not meet the objectives of the project.

### **2.2.3 Microfluidic technology**

For this project, a microfluidics technology/platform was chosen for implementation of the chemical analysis within this project, due to its potential for achieving high frequency in-situ monitoring, as discussed in chapter 1.5. Specifically, the choice of this method of analysis was due to the relatively low cost of the devices, the speed of the analysis, and the possibility of on-site analysis due to their small size and potential for low power consumption. This method also potentially can provide suitable accuracy and concentration range.

#### **2.2.3.1 Lab-on-a-chip**

One of the possible microfluidic methods for water chemistry analysis is lab-on-a-chip (LoC) devices [5, 87, 88]. It is a miniature device that allows one or several multistage chemical processes to be carried out on a single glass or plastic chip with an area of several mm<sup>2</sup> to several cm<sup>2</sup> and uses microliter or nanoliter amounts of samples. The samples and reagents move through various miniature channels, pumps, valves, reaction chambers and detection systems to achieve the analytical process (see Figure 17).

The LoC technology finds potential application in many areas of environmental monitoring [89]. For example, use in water quality assessment, to detect pollutants and pathogenic microorganisms in various water bodies. Moreover, the technology has potential application in biosensing, enabling to track biomarkers and biological indicators that give an idea of the state of the environment and the presence of harmful organisms. These devices provide a relatively high speed of analysis and provide high performance, but there are significant practical challenges for in-situ environmental use, as identified by the LIMPIDS project (like low reliability and see chapter 1.5.3). LoC devices are typically more suited to lab-based use.

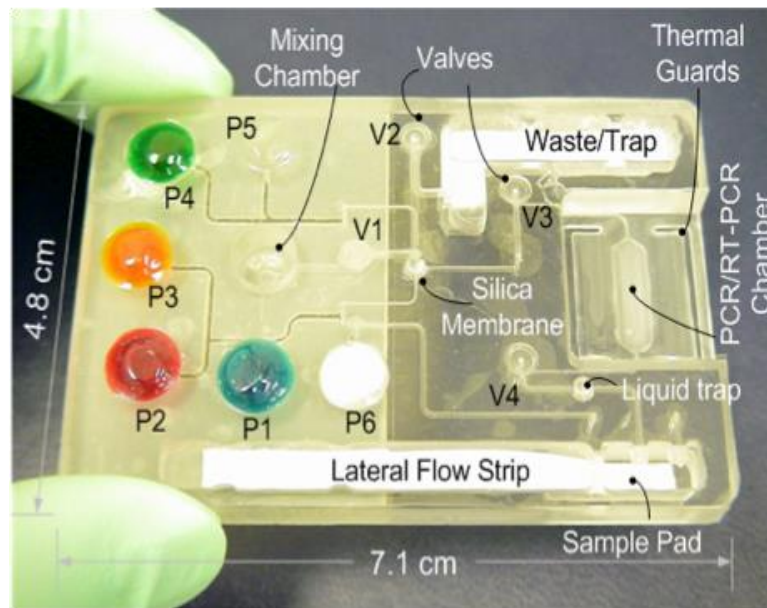


Figure 17- Lab-on-a-chip for integrated clinical analysis made of plastic [90].

### 2.2.3.2 Electrokinetic microfluidics

Another microfluidic method is Electrokinetic microfluidics based on the use of electric fields to manipulate liquids and particles inside microchannels. In the field of chemical analysis of water, electrokinetic microfluidics is characterized by high accuracy and control, providing the ability to separate charged particles and manipulate them with high accuracy [91, 92].

However, electrokinetic microfluidics has its own set of problems [93, 94]. . The influence of other ions or pollutants in the water poses a risk to the accuracy of measurements, which requires careful verification procedures. The complexity associated with manufacturing microfluidic devices with precise characteristics can limit availability, especially in resource-constrained environments [95].

### 2.2.3.3 Centrifugal microfluidics

There is also a centrifugal microfluidics based on the controlled rotation of a disc-shaped microfluidic platform to ensure the movement of liquid. This rotation creates centrifugal forces that guide liquids through pre-defined channels and chambers. The disk usually contains several compartments for loading, processing and detecting samples. Centrifugal microfluidic devices are designed to automate various analytical tasks, which makes them suitable for assessing water quality [96, 97].

Centrifugal microfluidic devices provide a high degree of automation. The rotation of the disc sequentially controls the stages of loading, processing and sample determination without the need for external pumps, valves or manual intervention [98].

Centrifugal microfluidics allows the integration of several analysis stages within a single device. This includes sample preparation, mixing, reaction and detection, simplifying complex analyses of the chemical composition of water.

This method also has its drawbacks. Making centrifugal microfluidic devices with precise characteristics and cameras can be a difficult task. The manufacturing process involves several layers and may require specialized equipment [98].

#### 2.2.3.4 Paper-based Microfluidic Devices

Another type of devices are microfluidic Paper-based Analytical Devices (PADs) [99]. These use reaction zones and channels in paper, delineated by hydrophobic wax impregnation, to control liquid sample movement, which occurs by capillary action. Reagents pre-absorbed on different layers or channel locations facilitate multi-step reactions with the sample being analysed. The paper layers are typically protected by an outer layer of plastic lamination on both sides, through which inlets can be cut to facilitate sample introduction.

An example of a PAD device and analysis process is shown in Figure 18. It shows the simplified design and manufacturing process of the device. At the first stage, the device is printed (i), then reagents are added (ii). Next, the device is folded (iii) if several layers are used and holes are cut for water access (iv) [100, 101].

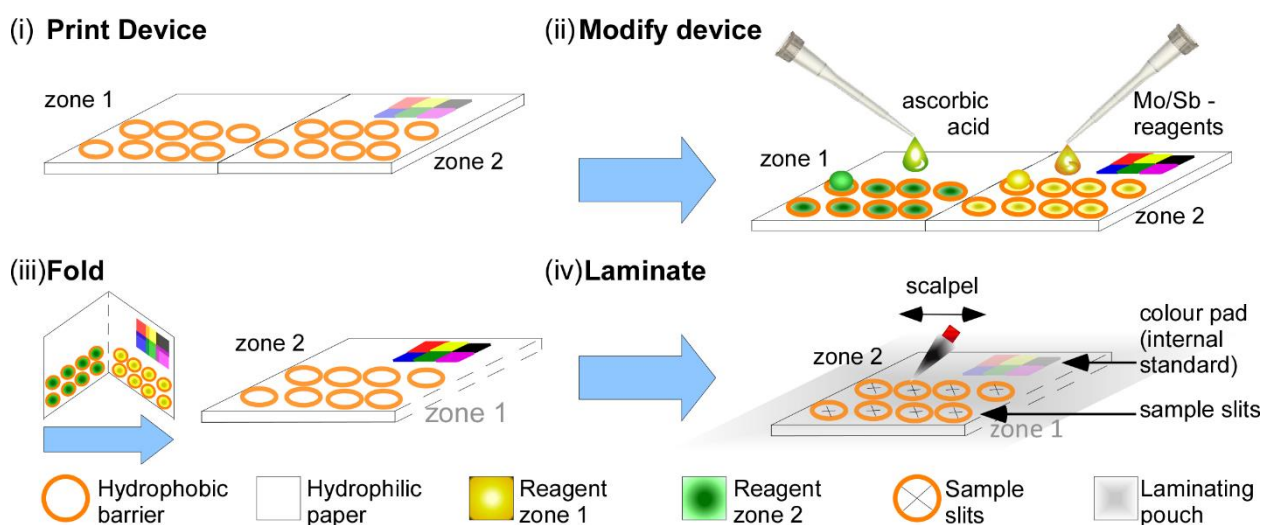


Figure 18. Paper-based analytical device for phosphates dissolved in water [100, 101].

Despite limitations in accuracy and sensitivity, paper-based microfluidic sensors are simple, inexpensive, portable, and disposable analytical instruments for many analytical applications including clinical diagnostics, food quality control, and environmental monitoring [102, 103]. For example PADs can measure phosphates in water with an accuracy of 1 mg/L [101].

PADs are a great alternative to LoC for in-situ analysis since they are much easier to produce. Liquids can move through them by capillary forces, so no pumps are required. Reagents are embedded in the paper in dry form, so there is no need to store and manipulate liquid reagents. They are lightweight and the use of paper leads to the possibility of producing the devices on a roll, potentially in large numbers, as proposed for the LOAR system. PADs were selected for this work taking into account all the advantages and disadvantages.

The chemistry of the carbonate PADs, used in this project to determine the concentration of dissolved inorganic carbon in fresh water, was developed by Prof. Nicole Pamme's Group at University of Hull (and now Stockholm University). A later development, using the same basic chemical reaction, but different PAD structure, is described in [104]. Both dry and wet reagents can be used in PADs. In dry chemistry, the reagents are pre-applied to paper, which ensures a stable and longer shelf life. Wet chemistry involves adding liquid reagents to paper on demand, which provides greater flexibility in terms of analysis design and multiplexing capabilities.

There are many ways to produce microfluidic paper sensors such as photolithography, wax printing, cutting out the desired shape of the sensor, and others [105]. All these methods allow PAD devices to be produced with the same reliability, but it is wax printing that is the fastest.

Comparing all the methods discussed in this chapter, it can be concluded that microfluidic devices are most suitable for measuring carbonates, but it is PAD devices that meet the requirements of the project, since they are the simplest and cheapest to produce, and the potential accuracy allows measurements to be made with sufficient accuracy to track carbonate fluxes. PAD devices are also widely used in other studies within the cluster, which also allows you to use the experience of using them in this project.

#### **2.2.4 Colorimetry**

Colorimetry is a technology used to quantify and describe the colour characteristics of an object, including changing the colour of objects/solutions and analysing their spectral properties. Colorimetry has similar principles to spectroscopy and uses common methods for analysing the interactions of light and an object. For example, diffuse reflectance is measured in both cases. This involves measuring the amount of light reflected by a sample over a range of wavelengths.

The principles of colorimetry are based on absorption of light passing through liquids, but measurement of colour intensity can also be implemented using reagents embedded in solid substrates such a paper. In the latter case, colour changes, or intensity changes at specific wavelength, of absorbed light is related to

concentration. These approaches are referred to as reflectance colorimetry or reflectance spectroscopy and are applicable to readout for PADs [106-108]. As part of this work, the evaluation of the analysis results will be carried out using various methods of digital image processing and special light-sensitive sensors.

The fundamentals of chemical methods of analysis using colorimetry are based on the Beer-Lambert law, which states that the intensity of solution coloration depends on the concentration of a coloured substance in the solution and on the thickness of the liquid layer [109, 110]. It follows that the intensity of coloration at a suitable specific wavelength, using a fixed illuminating intensity, can be calibrated to measure concentration.

With the help of various colorimetric techniques, it is possible to estimate the quantitative content of certain substances in a solution with a fairly high accuracy. This accuracy is not inferior to the accuracy with which concentrations are determined as a result of much more complex and expensive chemical analyses and is sufficient for many scientific, production and even medical tasks.

Colorimetric methods can determine concentrations of substances up to 1 mg/L (for phosphates and heavy metals, but it always depends on analyte) [101, 111].

Colorimetric methods use visual comparison or comparison using special devices. The comparison is made by direct or compensatory methods [109, 112].

The direct method involves comparing the colour of the test solution at a certain temperature and in a certain liquid layer with the reference solution (or calibration values). The standard contains an exactly known amount of colouring agent at the same temperature and in the same liquid layer.

The accuracy of the hardware measurement is higher than the human comparison to colour reference standards since the hardware can quantify the colour of the light reflected from an object and more accurately measure its changes.

A visual comparison method is used to compare the colour intensity of the solution with reference solutions, the concentration of the substance in which is known.

The compensation method is based on bringing the colour of the test sample to the reference [109]. Solutions, with the help of various optical devices, are placed in the device in such a way that they are combined in the field of view of the researcher. The eye is able to fix the similarity of the colour of two samples with high accuracy. In some devices, the task is facilitated by the fact that when the colour intensity coincides, the visual boundary that initially separates the solutions disappears.

In order to bring the solution to the reference, a transparent solvent is added to it or the height of the liquid layer is increased. Then, from the value of the added diluent

or the height of the solution layer, a quantitative characteristic of the concentration of colouring substances in the solution is derived. Compensation methods are used in visual colorimeters and in photolorimeters. They are the most practical, since they are not affected by extraneous factors such as temperature.

### 2.3 Frequency of water sampling

Often, collecting water samples is a labor-intensive and time-consuming process, since sampling is carried out from hard-to-reach places, which does not allow it to be done with a sufficiently high frequency. In this regard, the spectral-temporal characteristics of changes in the concentration of chemicals in water are often not taken into account. But since the designed analytical system is aimed at carrying out automatic sampling and analysis, it is necessary to consider the application of selection theory in the process of concentration change signal reconstruction [113-115].

The phenomenon of insufficient sampling leading to missed rapid changes also occurs in the context of water measurements. In such situations, if water samples are not taken frequently enough, relatively rapid variations in certain parameters may be undetected (da Silva et al., 2019). An illustrative example of this is depicted in Figure 19. In this experiment, it is shown how the frequency of measuring the conductivity of water affects the reconstructed signal. The lower the sampling frequency, the more information is lost.

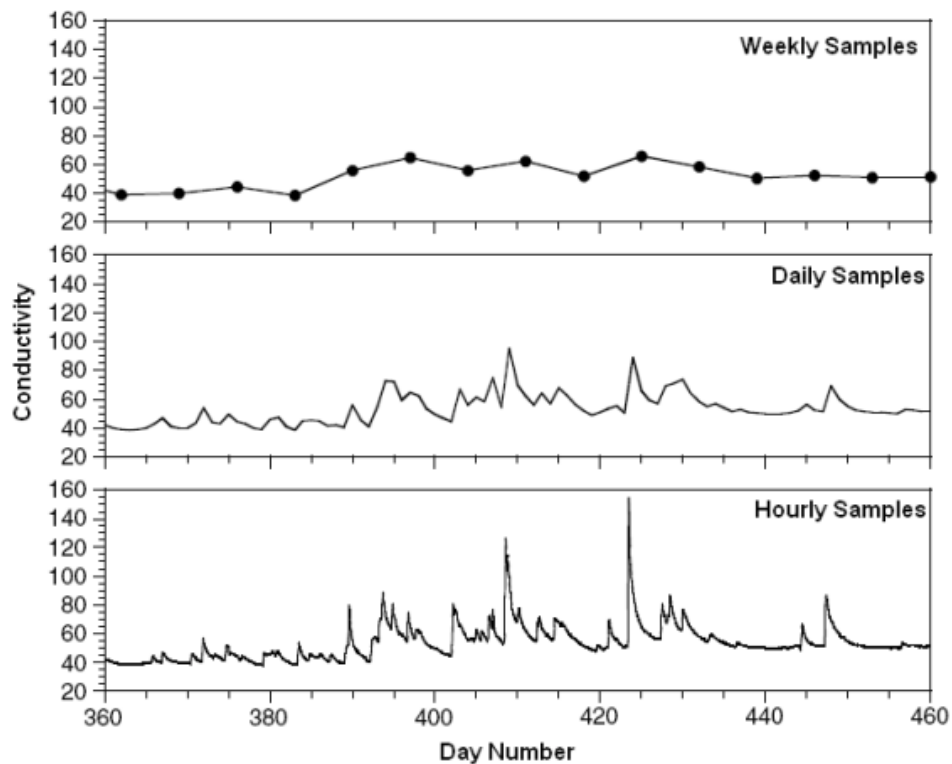


Figure 19. Electrical conductivity measured weekly, daily, and hourly [116]

Water sampling in cave environments is a unique challenge due to the unknown variation rate of the carbonates concentration in the water. Therefore, the frequency of sampling is very important to obtain complete information about changes in the concentration of the measured substance in water.



### **3 System design development**

This chapter discusses the development of a new automatic water analysis system. Existing water sampling systems, have proven to be effective, but they lack on-site analysis capabilities. The goal of the current project is to develop a system that not only eliminates this limitation, but also prioritizes the cost-effectiveness and productivity of its components.

#### **Design specification**

The system should take measurements at least twice a day to ensure that the data is collected frequently enough for analysis. The duration of the system's autonomous operation is crucial to ensure continuous monitoring. It is necessary to set up the system to work offline for at least two weeks. This will allow us to reliably assess the dynamics of changes in the concentration of carbonates over a significant period. The system should also measure the concentration of carbonates in water within the range of changes in the concentration in tap water, which ranges from 50 mg/l to 300 mg/l an error not exceeding 50 mg/l.

Given that the system will be installed in a cave, it is necessary to protect it from excessive humidity, which can affect its performance. The system will be placed in a waterproof case to ensure its protection from external influences. However, it should be noted that this limits the available volume for the placement of equipment, and it is estimated that the dimensions of the case will be approximately 30 by 50 by 50 cm.

In addition, it is necessary to ensure that information can be transmitted to external devices. This includes the possibility of wireless data transmission, which allows to receive and analyse data without direct access to the system.

#### **3.1 System concept**

In order to make measurements automatically, it is necessary to develop a system that will dip paper devices into water, take measurements using an optical method and then analyse obtained results. Figure 20 shows the basic mechanical set-up of the concept. The system will consist of one or two motors that will drive the roll of paper devices, which will be read by (potentially) two sensors (spectral sensors, camera or any other optical devices that capable to do optical measurements) before (if needed) and after dipping.

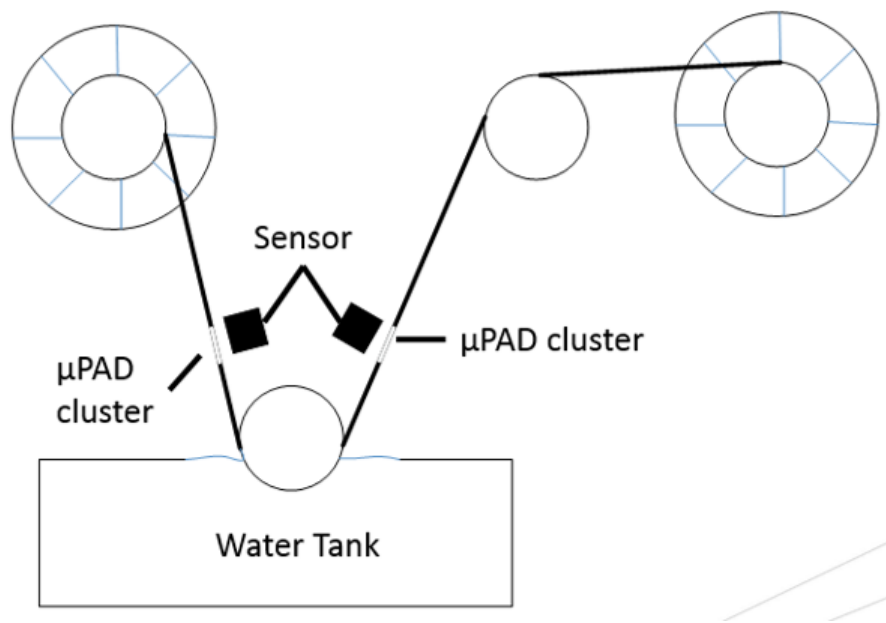


Figure 20. Dipping System Concept

The appearance of PAD devices plays a large role in system operation and optical analysis (the chemistry and manufacturing process are discussed in chapter 3.2). A possible PAD roll design is shown in Figure 21.

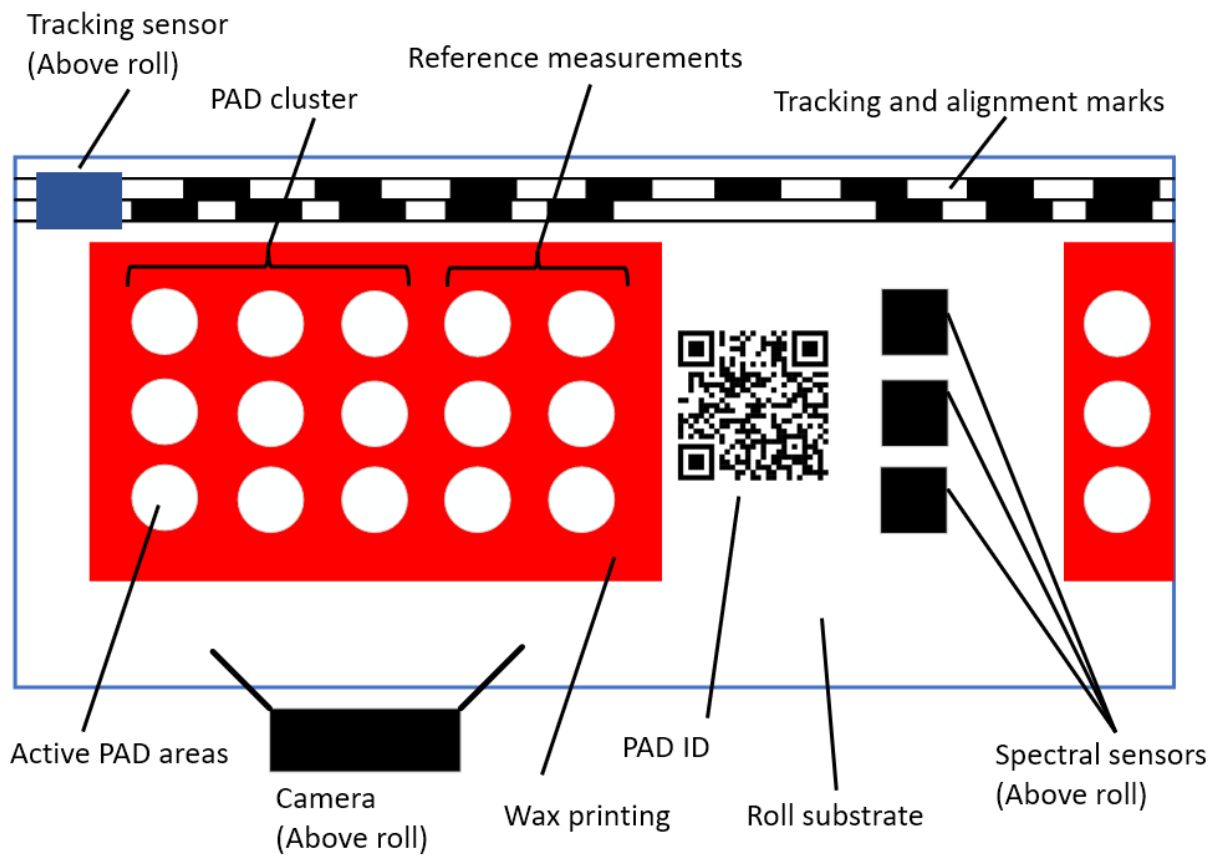


Figure 21. PAD roll concept design

The device has two sections. PAD cluster directly measures the concentration of carbonates in the sample. One PAD is capable of measuring a relatively small concentration range of carbonates, therefore each device has a number of active concentration measurement zones. Reference PADs are used to normalize the measurement results and to determine the pH of the sample water. The camera is mounted where it can image a complete PAD and ID code. The spectral sensors require accurate positioning with respect to the PAD position and roll surface. Tracking and alignment marks are used to control the speed and position of the device.

The design of the system is shown in more detail in the section 3.5. Section 3.5.1 contains a system assembly developed based on the one shown in the Figure 20. The electrical system, the block diagram of which is presented in Figure 22. System block diagram, will consist of a microcomputer system that will operate the entire system, including actuating the motors and processing the sensor results to provide concentration measurements. The system comprises sensors, motor drivers, data storage and interfaces for data exchange and power management. The system may use several communications protocols, including wireless ones for transmitting information and receiving commands. Potential interfaces include standard USB, Bluetooth and WiFi as well as sensor network radio, such as that used in Poole’s Cavern (see chapter 2.1.5) and Low Frequency (LF) ground-penetrating “Cave Radio” for ground to surface communications. However full development of all potential communications is not a priority for the initial prototype.

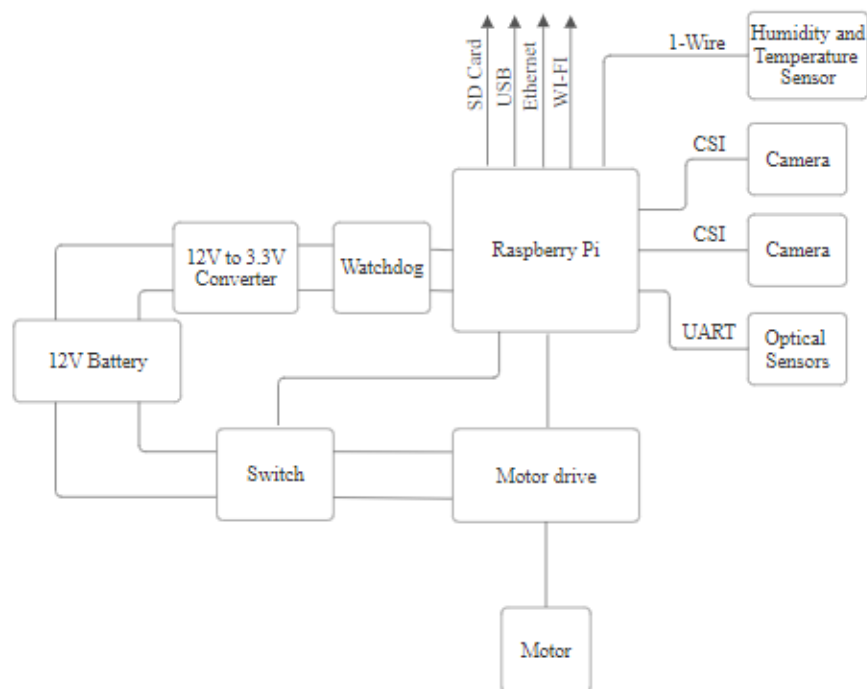


Figure 22. System block diagram

The time parameters and sampling frequency that potentially affect the accuracy of the system are discussed in the section 3.6.

Section 3.7 describes the process of developing software that is responsible for managing the system, measuring and analysing the results

Summing up, the concept of the system is based on the automation of the measurement process using paper devices. By immersing the paper devices into water, leveraging optical methods for measurement, and data analysis through a microcomputer system, this setup may deliver accurate and reliable results. With its diverse interfaces, the system ensures seamless communication and efficient power management, which in theory can lead to increased efficiency and productivity of measurements using paper devices.

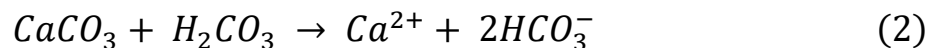
## 3.2 Carbonate PAD design

### 3.2.1 PAD chemistry

Although the LOAR platform concept is potentially applicable to detection of a wide range of chemical species in natural water, as highlighted in chapter 2.1, this project aimed to develop and evaluate a PAD for detection of carbonates in water in karst cave systems. The PAD chemistry was developed by Prof. Nicole Pamme's group at Hull (chemistry), in particular by Dr Samantha Richardson, in collaboration with Prof. Michael Rogerson (geoscience). The basic principle of the PAD is to react the carbonate with an acid after which the resulting pH will depend on the amount of carbonate in the sample, which can be detected using an indicator.

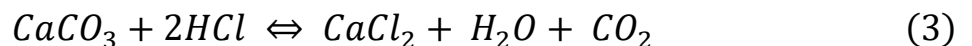
The process of dissolution of karst rocks primarily depends on the effect of carbonic acid, which is formed as a result of the absorption of carbon dioxide by rainwater when passing through the Earth's atmosphere. Subsequently, during the passage through the soil, the water additionally absorbs carbon dioxide produced by vegetation. Consequently, carbon dioxide combines with water molecules to form a dilute solution of carbonic acid. This slightly acidic solution enters into a chemical reaction with karst rocks, leading to their dissolution.

The solubility of carbon dioxide in water significantly increases the reactivity of rainwater, allowing it to act as a solvent for carbonate-rich karst formations. Over time, the repeated interaction of carbon dioxide solution with karst rocks leads to the gradual removal of mineral components from the rock. This dissolution process leads to the release of soluble ions and solid particles into the water, effectively destroying the karst structure and forming characteristic landforms such as sinkholes and caves. The primary reaction sequence in limestone dissolution is the following:



Measurement of the carbonates concentration is based on the fact that they react with hydrogen chloride (HCl), and change the pH level [117]. In general, this reaction for detecting carbonates in water consists of two steps.

The first step is the reaction of sodium carbonate with hydrogen chloride. The reaction equation is as follows.



The reaction between sodium carbonate and hydrogen chloride also occurs in two steps. First, carbonates are neutralized with hydrogen chloride, resulting in carbonic acid. Then, since carbonic acid is unstable in aqueous solutions, it decomposes into water and carbon dioxide. Depending on the amount of carbonate and hydrogen chloride dissolved in water, the carbonates either all dissolve (the solution will remain acidic), or only a part will dissolve (the solution is more alkaline).

The second step is to use an indicator to determine the pH and hence the carbonate concentration. The colorimetric method for measuring pH is based on the property of certain substances (indicators) to change their colour depending on the pH value of the solution. The coloration is compared with the colour of the same indicator in a solution with a known pH.

Bromocresol green (BCG) has been identified as a suitable indicator for carbonate measurement in PAD device. It changes colour depending on the acid level of water (pH). If all the carbonates dissolve and the solution is more acidic, it will turn yellow. If the carbonates are not all dissolved and the solution is alkaline, it will turn blue. After Bromocresol green has changed its colour, the concentration of carbonates in water can be estimated using colorimetric methods [118].

In order to stabilize the solution, it is required to use buffer that prevent pH changes. PDADMAC (Polydiallyldimethylammonium chloride) was added for this purpose. It electrostatically interacts with negative charged ions (that may lead to pH changes like sulphate ions) and absorbs and binds on neutral organic and inorganic particles, leading to stabilization [119].

To adjust acidity level either sodium citrate can be used to make the solution more alkaline, or citric acid to make it more acidic.

### 3.2.2 PAD structure and manufacture

The structure of the PAD is shown in Figure 23. It comprises a single paper layer, patterned with hydrophobic wax barriers and laminated on both sides with plastic. A sample entry hole is cut in the laminate to facilitate sample entry.

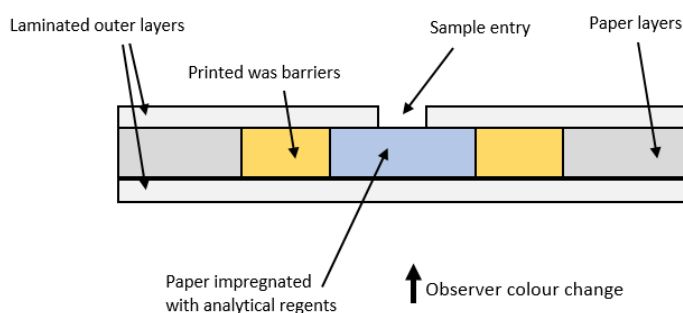


Figure 23. PAD structure.

To protect the device from getting wet, it is necessary to laminate the PADs (individual devices or the whole roll for the LOAR approach). There are two types of lamination: hot lamination and cold lamination. During hot lamination of images, the laminator shafts are heated to the required temperature, depending on the material used. Films for hot lamination are glued to the material under the influence of temperature. Films for cold lamination have an adhesive layer. The laminator shafts remain cold and create the pressing pressure necessary for bonding.

Within the framework of this project, it was decided to use hot lamination as it is the cheapest roll laminator on the market. GBC Ultima 35 Ezload A3 Heavy Duty Roll Laminator was purchased specially for PAD manufacturing. This laminator more suites for PADs on a roll manufacturing than typical single sheet laminator as it allows to produce a long roll of PADs without gluing devices together.

In order for the PAD device to show the result, it is necessary that the water passes into the layer(s) of paper impregnated with reagents. A hole is required in the laminate for sample entry into the first layer. Typically, this is achieved by manual cutting, which may mean the holes are not consistent in size and shape. A relatively large central inlet also tends to cause an uneven response over the PAD area. Furthermore, the holes are typically cut well in advance of use. But leaving the PAD device open, there is a possibility of moisture ingress and evaporation of reagents, which in turn can affect the accuracy of the result. Thus, in order to prevent evaporation of reagents and increase the shelf life of the devices, it may be preferable if the perforation is carried out immediately before the measurement and immersion in water.

One of the options for perforating is to use a laser. By removing the top lamination layer with multiple small holes covering the entire area of the reaction zone, it is possible to produce a more even response and, by creating the inlets just before use, to prevent degradation of the reagents.

To investigate the possibility to use a CO<sub>2</sub> laser cutter with 9.3 μm wavelength to perforate the 42.5-micron laminate, an experiment was carried out in which the PAD device was perforated using a laser device. Figure 24 shows the result of this initial experiment conducted with 15% laser power (maximum power is 100W) and 0.01 s radiation time. The contrast spots on the PAD surface indicate a perforation, however no additional experiments were conducted to prove it. It is expected that the suitable laser power level can be selected in series of such experiments, so that only the top layer of lamination will be burned, leaving the active PAD material intact.

The use of a laser in a cave is theoretically possible, but practically presents a rather difficult task, since the laser requires a powerful energy source and special

conditions (temperature, humidity, etc.). All this would significantly increase the size and weight of the entire system. Hence, the laser perforation root has not been pursued further on.

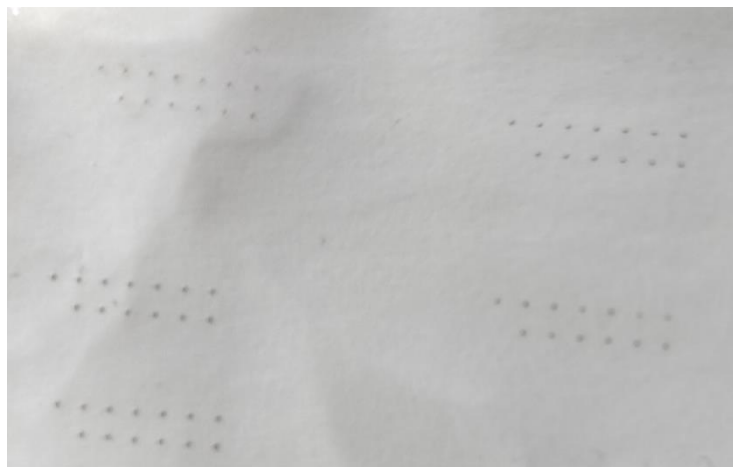


Figure 24. Optical image of the PAD surface subjected to laminate perforation using laser cutter. The easiest way to ensure water access to the reaction zone is to cut the lamination layer with scalpel before placing PADs on a roll. This method will be used for the production of PAD at the testing stage of the system, since no feasible solution has been found and this method also does not require any additional equipment.

### **3.2.3 PAD colour response**

The PAD is impregnated with HCl and BCG solutions. When the water sample enters the carbonate reacts with the HCl. The concentration of carbonate in the sample relative to the concentration of the deposited HCl determines the pH of the liquid in the PAD. The BCG changes colour in accordance with the final pH after the HCl-carbonate reaction and hence the carbonate concentration.

BCG is yellow in lower pH (more acidic) conditions and blue in higher pH conditions (less acidic). At an intermediate point it is green (typically the carbonates PAD will look green before use). If the sample contains a relatively large amount of carbonate this will react with most or all of the deposited HCl, removing the acidity and resulting in a blue colour when the sample moves into the BCG layer. If there is relatively little carbonate in the sample the HCl will remain in the water that moves into the BCG layer causing it to turn yellow. Absorption spectra of bromocresol green is shown in Figure 25.



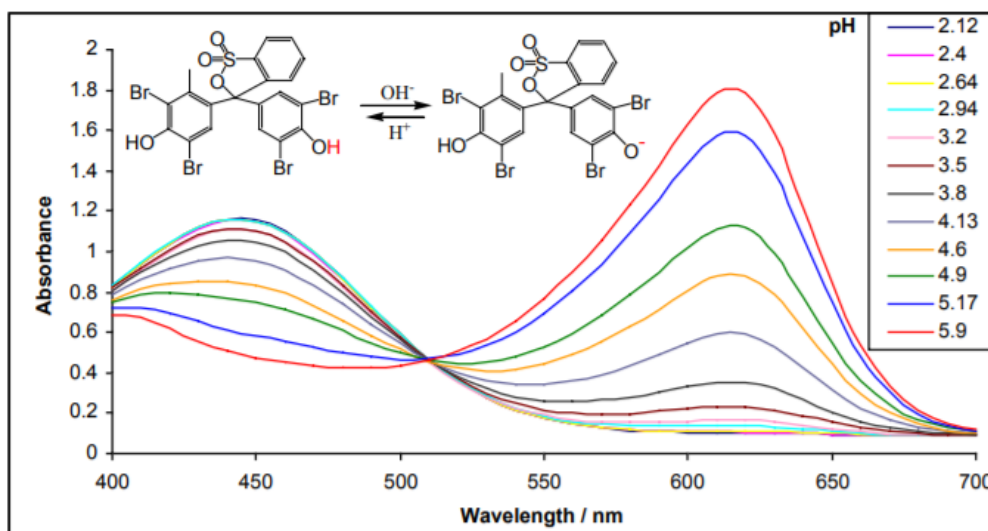


Figure 25. Absorption spectra of bromocresol green dye in various pH buffer solutions [117].

There is a point (515nm) on the graph when the absorption value is the same for all pH values. This is an isosbestic point. This is the wavelength at which two compounds capable of turn into each other, have the same light absorption [120]. This point can be used to adjust the sensor. Since for all pH the sensed value at the isosbestic point should be the same, it is possible to estimate the amount of reflected light using this point for calibration. Thus, it will be possible to correlate the values at the output of the sensors and the pH of the solution.

### 3.2.4 Manufacture of PAD roll

CAD layout design: The process begins with the creation of a detailed CAD layout (computer-aided design system). This layout serves as the basis for a paper-based device. An example of a PAD is shown in Figure 21 for PAD roll or Figure 26 for single device.

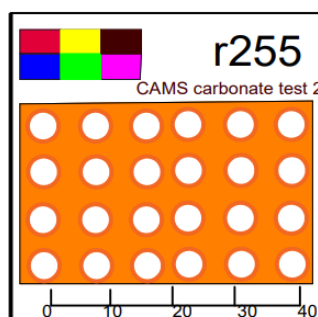


Figure 26. PAD device

1. Printing with a wax printer: The CAD layout is then used to print the design on filter paper using a wax printer. This printer uses wax-based ink to transfer the drawing to paper with high precision.

2. Wax Melting: To activate the melt wax and create a waterproof barrier, the printing paper is heated. This can be done with a heat gun or any other suitable heating device.

3. Pipetting reagent: After melting the wax, the reagents are pipetted to specially designated areas of the paper-based device (see Appendix F – Carbonates BCG buffer solution preparation method).

4. Drying: After applying the reagents, the paper-based device should dry.

5. Cutting and gluing: Then the dried paper is cut into separate strips. These spacer strips are then glued together to form a continuous roll.

6. Lamination: Next, the roll must be laminated using roll laminator if making a roll.

Cut Holes: Holes are required to facilitate water access to reaction zone. These holes are precisely cut into the lamination layer using a scalpel or laser (can be done during manufacturing).

### 3.3 Colorimetry for PAD analysis

Previous work on PAD colorimetry has shown that consumer digital cameras, such as those in smartphones can be used to quantify chemical concentrations detected by PADs [101, 106, 107]. Digital camera images are represented by standard numeric colour models such as RGB (Red, Green, Blue) or HSL (Hue, Saturation, Lightness). These numerical values provide a quantifiable representation of the observed colour changes, forming the basis for further analysis.

The initial step in the quantification process is to create a calibration curve. This curve establishes the relationship between the intensity of colour change and the known concentrations of the analyte and this is required for any optical device such as a camera, optical sensor, etc. To construct this curve, a series of standard solutions with precisely measured concentrations of the analyte is prepared. Then each standard solution is applied to separate paper devices containing a colorimetric indicator. Under controlled conditions, the paper devices change colour, and these colour changes are documented using consistent methods (e.g. photography or scanning under laboratory conditions).

The calibration curve serves as a graphical representation of the relationship between the colour intensity and the concentration of the analysed substance. The form of this dependence can be linear, logarithmic, or correspond to other mathematical functions. Deciphering the nature of this relationship is of paramount importance for accurate quantification.

In the presence of a calibrated system, it becomes possible to analyse unknown samples. A sample of unknown concentration is exposed to the same colorimetric parameters and experimental conditions as standard solutions. Then the colour change observed in the sample can be compared with the calibration curve. Using interpolation or extrapolation, the concentration of the analyte in the sample is determined based on the corresponding colour intensity.

However, achieving an accurate and reliable quantitative assessment is fraught with certain difficulties. Factors such as lighting conditions, camera calibration, and differences in colour perception among different people can lead to variability in colour measurements. Careful verification of the accuracy of the method is necessary, including repetition of standard solutions and comparison with actual concentrations to ensure reliable results. The proposed LOAR in-situ instrument will have an advantage over manual PAD analysis using a camera in that it will be able to provide consistent lighting, camera calibration, and will not depend on human perception.

### 3.3.1 Analysis using a digital camera

To measure concentration using a camera, the process involves capturing an image of a paper device. Once the image is received, it needs to be analysed through a series of steps to determine the concentration [100, 101]. This method was performed manually using the Java-based image processing freeware application ImageJ (National Institutes of Health, USA). For the LOAR in-situ instrument all steps in the process will need to be automated.

The image is inverted and divided into three colour channels: red, green and blue (RGB colour model). Subsequently, the average colour intensity values for the pixels in the analytical areas of the image for each channel are calculated. This involves summing up the colour intensity values of all relevant pixels (analysis circles) in each channel and dividing them by the total number of pixels involved. The resulting average values for each RGB colour channel provide information about the intensity of the colours present in the image.

To accurately determine the concentration, taking the possibility of variable lighting conditions into account, these average values of colour intensity are compared with a pre-determined reference value obtained by applying the same averaging process to the pixels in a coloured reference square printed on the PAD. An average relative intensity (ARI) is calculated by dividing the average intensity of the analysis circle pixels by the average intensity a selected reference square. Choice of RGB channel and reference square colour for ARI calculation depends on the colours exhibited by the PADS, which may be different for different analytes. Comparing measured ARI values with a calibration curve (see Figure 28), it is possible to calculate the concentration of the target substance.

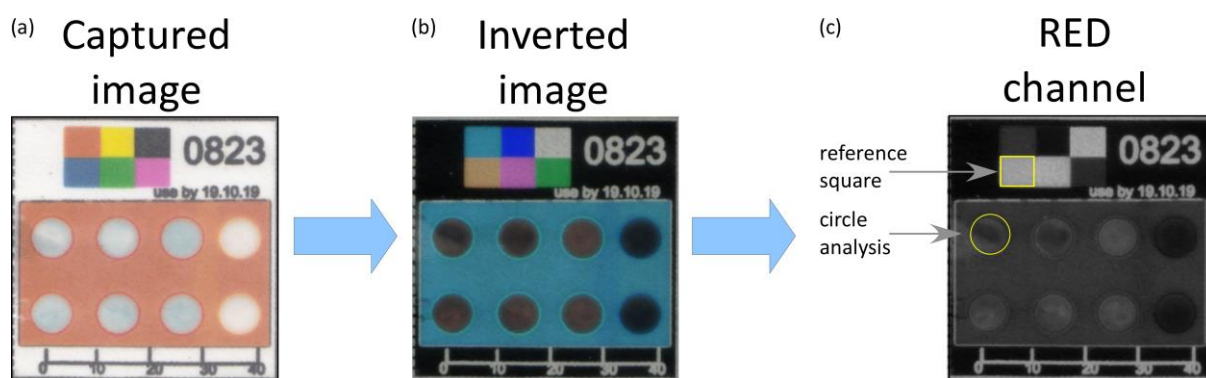


Figure 27. Image analyses process from [100, 101].

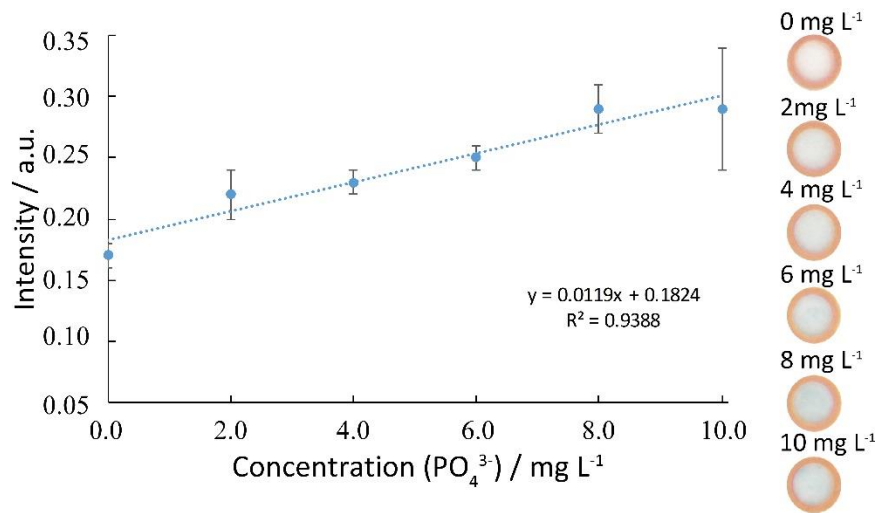


Figure 28. Example calibration curve (Phosphate concentration) from [100, 101].

### 3.3.2 Analysis using a colour sensor

Less than two years prior to the start of this project a number of low-cost Integrated Circuit (IC) based spectral/colour sensors were launched by Austriamicrosystems (AMS, now AMS Osram) [121]. Costs are comparable with embedded systems camera modules, and they potentially provide better separation of more wavelengths and hence possibly better accuracy, so these devices were considered as a possible alternative to using cameras for PAD colour sensing.

The IC spectral sensors sensor work on a different principle than the camera. The sensor consists of several channels, each of which is designed to capture certain wavelengths of light. To do this, the light wavelengths are separated using optical Gaussian filters integrated into standard CMOS silicon chip [122]. These provide a narrow bandwidth for each channel, isolating the desired wavelength range. The response of the AS7262 "6-Channel Visible Spectral ID Device with Electronic Shutter and Smart Interface" is shown in Figure 29.

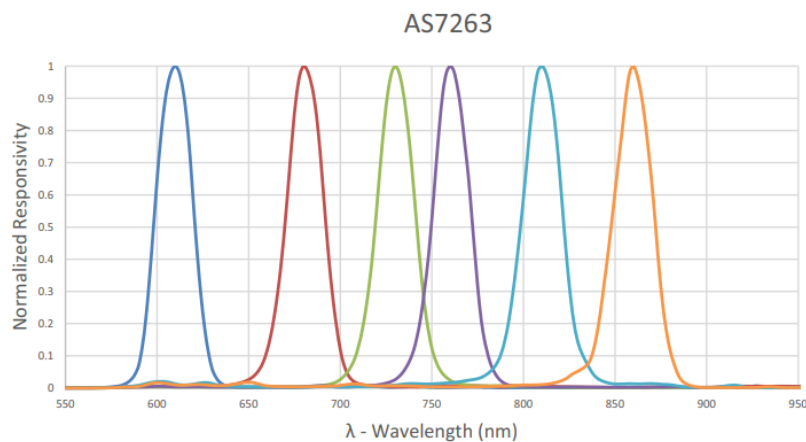


Figure 29. AS7262 spectral sensor spectral response curves [122].

After the filtration process, the light is directed to the photodiode associated with each channel. This photodiode is used to detect and quantify the intensity of light within a given wavelength range. The sensor measures the light intensity for each channel by integrating the received value over a pre-programmed time interval, providing an estimate of the light intensity within this interval.

The sensor requires the creation of a controlled environment devoid of extraneous objects and light sources in the field of view. This is crucial to ensure the accuracy and reliability of measurements. Thus, the location of the sensor is of paramount importance to achieve accurate and consistent measurement results (while the camera is not so demanding on positioning, it is enough just to have the PAD in the camera's field of view). Proper alignment and optimal positioning of the sensor (the sensor needs to be in front of reaction zone, see Figure 21 and Figure 40) in the environment ensures an unobstructed view and minimizes any interference, contributing to the overall accuracy and efficiency of the measurement process.

### 3.4 Waterproof box

The main factor that limits the mechanical characteristics of the system is the waterproof box in which the system will be placed. This must be practical for carrying and installation at the site of interest (e.g. in a cave) and limits the size (diameter) of the PAD roll. It is possible to calculate the length of the PAD roll using the following expression if the maximum outer diameter of the roll is known.

$$L = \frac{t * (D^2 - d^2)}{4\pi}$$

Where L is length of the roll, t is the thickness of the paper, D is outer diameter, d is inner diameter.

The number of measurements can be calculated as the ratio of the tape length to the distance between groups of PADs. It's also important to calculate how long it takes to take this number of measurements. This value should not exceed the lifetime of the devices.

Table 1 shows initial parameters and results of calculations (see Appendix E).

Table 1 – System parameters

	Value	Units
PAD life time	30	day
Sample interval	30	min
Gap between DAP group	10	cm
Weight per unit area of paper	80	g/m <sup>2</sup>
Weight per unit area of lamination	175	g/m <sup>2</sup>
Wheel weight	100	g
PAD width	8	cm
Diameter of roll core	5	cm
Lamination thickness	0.125	mm
Paper thickness	0.1	mm
Length of waterproof case	55	cm
Height of waterproof case	50	cm
Total thickness	0.45	mm
Length of a LOAR	20944	cm
Number of samples	1397	
Diameter of a PAD roll	35	cm
Total weight of a roll	8645.13	g

These calculations are not final, but the starting point for the development of the system. The main limiting factor will be the waterproof case and the final dimensions of the system will depend on it. Chemical reagents, battery capacity,

sample degradation, etc., can also affect these calculations. In the future similar calculations could be provides to users configuring a system for deployment.



### **3.5 System design**

The main task of the system is to dip paper analytical devices (PADs - which measure water chemistry) into the water tank and measure the PAD response. Motors move the devices through the water tank from the first roll to second one to make the measurement. Devices are analysed by optical sensors before and after dipping. Water is pumped, or gravity-fed, into the tank and flows out over a lip to ensure a constant water level in the tank.

The system will eventually be housed in a waterproof case, but at testing stage the system is designed without taking into account the restrictions that the case will impose. The part of the case through which the roll passes is important and will be included in the open frame design as a “baseplate”.

In order to take many measurements over a certain period of time, PAD devices should be located on a long tape wound in a roll. The roll is a strip of plastic-laminated paper, a few centimetres wide, with small holes on one side of the lamination to allow water to enter the PADs. The PADs are arranged in groups, which are used together for each measurement sample. The next group of PADs to be used must remain wholly inside the case (above the baseplate) to avoid being exposed to moisture prior to use. After “dipping” the PAD group must be moved wholly inside the case (above the baseplate). This implies a blank section of roll between PAD groups. Ideally the length of the blank section is as short as possible to reduce size of the roll.

It is important to remove water from the surface of the roll (plastic laminate surface) after it exits the water – a “squeegee” type arrangement on the baseplate may achieve this. The mechanical design of the system is shown in Appendix G.

#### **3.5.1 Mechanical design and System assembly**

The development process of the system took a significant step forward with the creation of a detailed assembly drawing. This drawing serves as a blueprint, providing precise instructions and guidelines for the assembly of the first prototype.

In order to ensure practicality and cost-effectiveness, a 3D printing approach was applied to most components of the system. Polylactic acid was used as the printing material, it is suitable for prototyping and is sufficiently rigid and strong. This solution not only speeds up the production process, but also provides the flexibility to create complex geometries and non-standard shapes that would otherwise be difficult or expensive with traditional production methods.

With the help of a 3D printer, a functional mechanical layout of the entire system was created. This 3D layout, illustrated in Figure 30 (front and side view of the system is shown in Figure 31), offers an in-depth visualization of how all the

individual mechanical parts interconnect and complement each other to form a system. The visual representation allows to assess the design's integrity, before moving forward with the physical assembly.

The 3D layout contains the motor that rotates the rolls with PAD devices, the tensioner that prevents spontaneous rotation of the rolls under gravity, and the water scraper that removes water droplets from PAD devices. All components of the system except the motor and aluminium struts (the basis of the system) are produced by 3D printing.

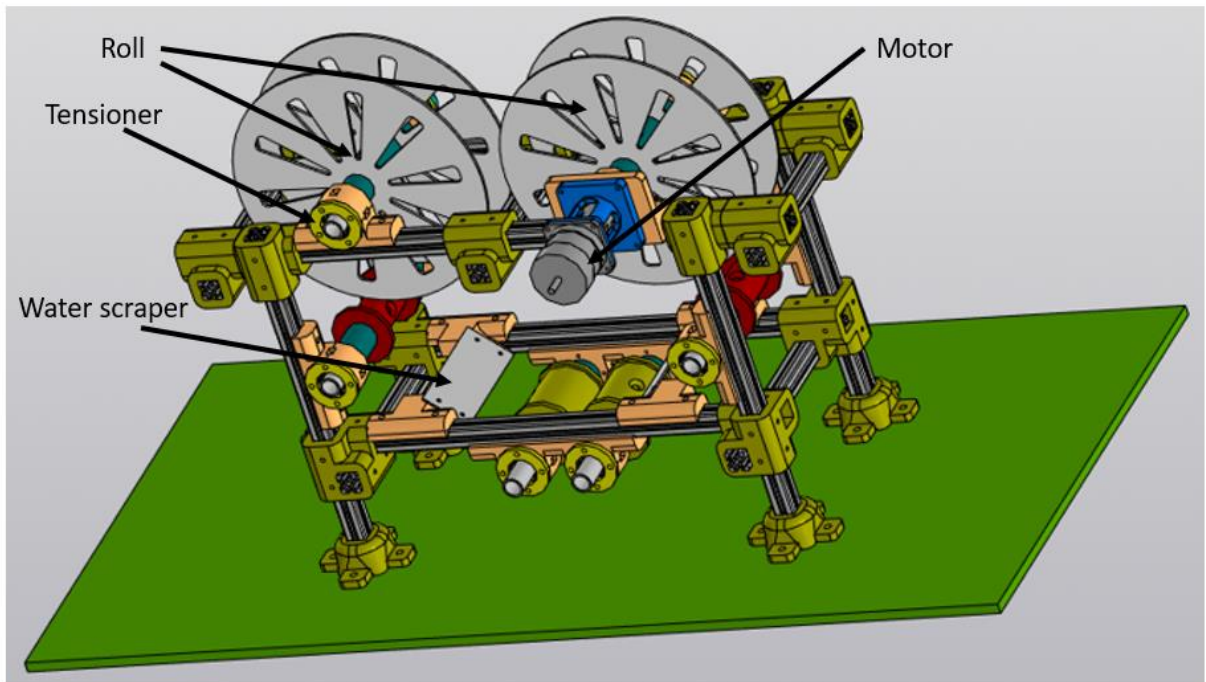


Figure 30. 3D system layout.

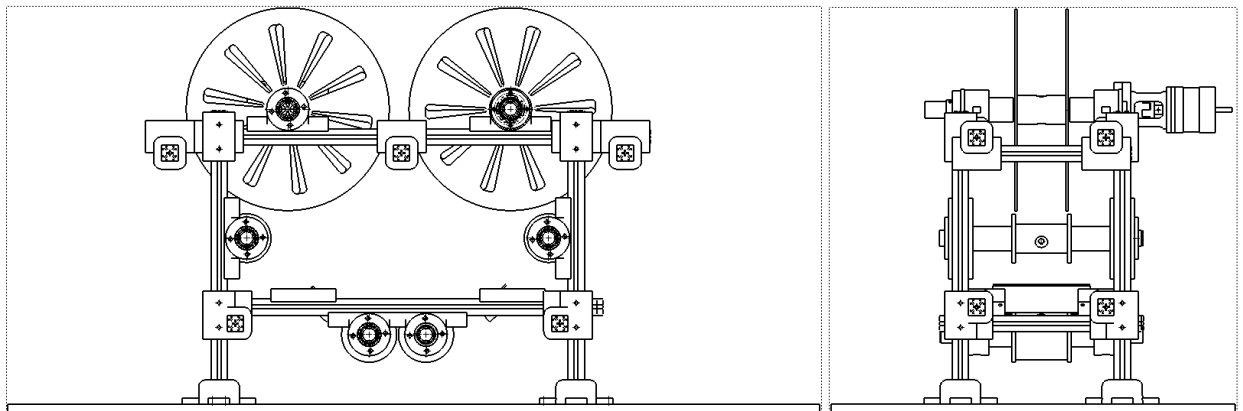


Figure 31. Front and side view of the system.

The integration of the motor into the system ensures the efficient functioning of the entire setup, driving the PADs roll. Figure 32 illustrates connection of the motor to the system. To achieve this, a mounting system that securely holds the motor in place, preventing any unwanted vibrations or misalignments during operation was designed (see Appendix K). This is ensured by means of a strong attachment to the frame of the system. The coupling mechanism is used to connect the motor output shaft to the corresponding input shaft of the system (see Appendix L). This coupling ensures smooth and reliable transmission of rotational energy, maximizing efficiency and reducing energy losses. This is achieved through precise tooth coupling, ensuring a tight fit and facilitating smooth power transfer without excessive friction or slippage.

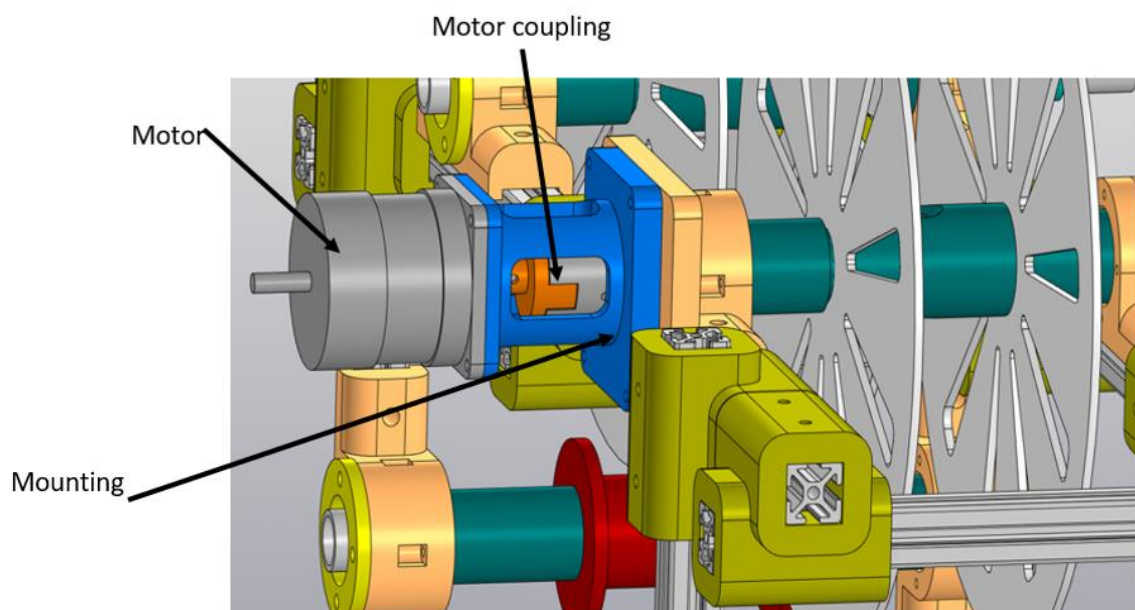


Figure 32. Motor connection

A special tensioner (shown in Figure 33) is installed on the other shaft to prevent the rolls from turning and ensure tension. The teeth create some tension (getting into the grooves), which is enough to prevent the roll from turning under gravity, but not enough to prevent the shaft from spinning when the motor is running. Since the tensioner is made of polylactic acid, the teeth may wear out over time, so it is necessary to monitor their condition.

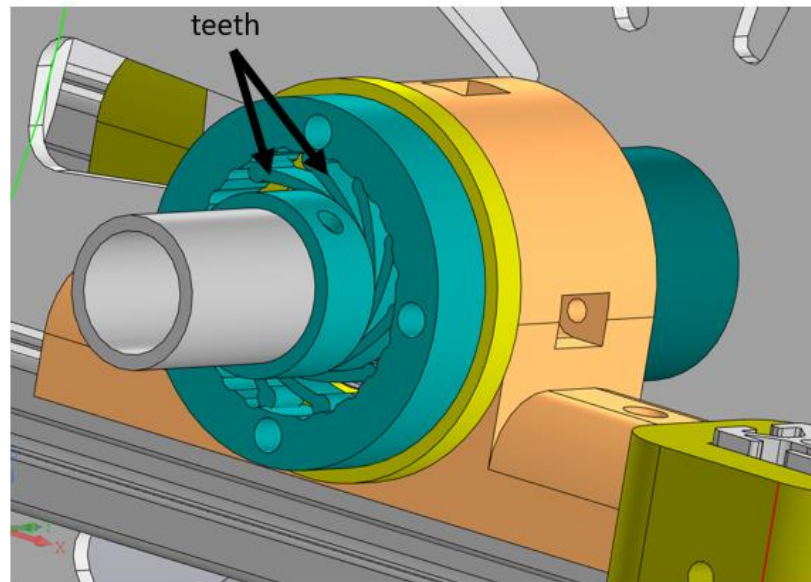


Figure 33. Tensioner.

The water scraper, shown in Figure 34, plays a crucial role in maintaining measurement accuracy by effectively removing water from the surface. Its purpose is to eliminate potential interference caused by the presence of water, which could otherwise affect the accuracy of the measurement. It also eliminates or reduces the amount of water carried inside the main instrument housing. Use of windscreen wiper blades was considered for this role, but not evaluated.

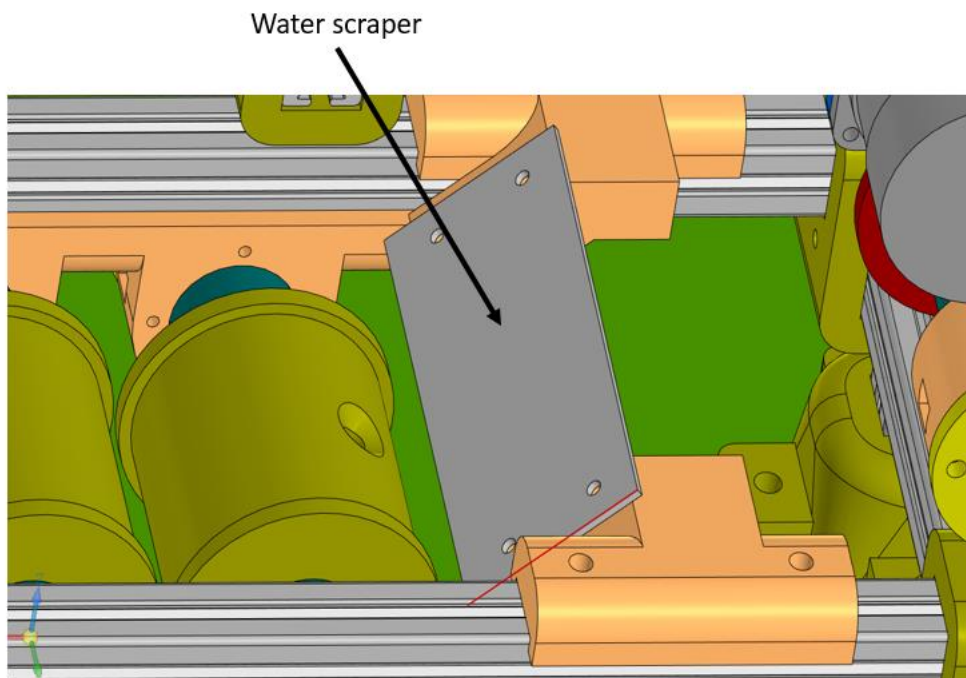


Figure 34. Water scraper.

Final laboratory version of the entire system using cameras for measurements is shown in Figure 35 and Figure 36. Raspberry Pi and motor driver are placed on the

stand because during laboratory tests it was necessary to constantly disconnect them for debugging and have an access to the Raspberry Pi memory card. The rolls are made according to the calculations in Chapter 4.3, but more space is left between the parts of the system for the convenience of conducting tests. Wooden stand is used to hold Raspberry Pi. Also, there is no scraper in this version.

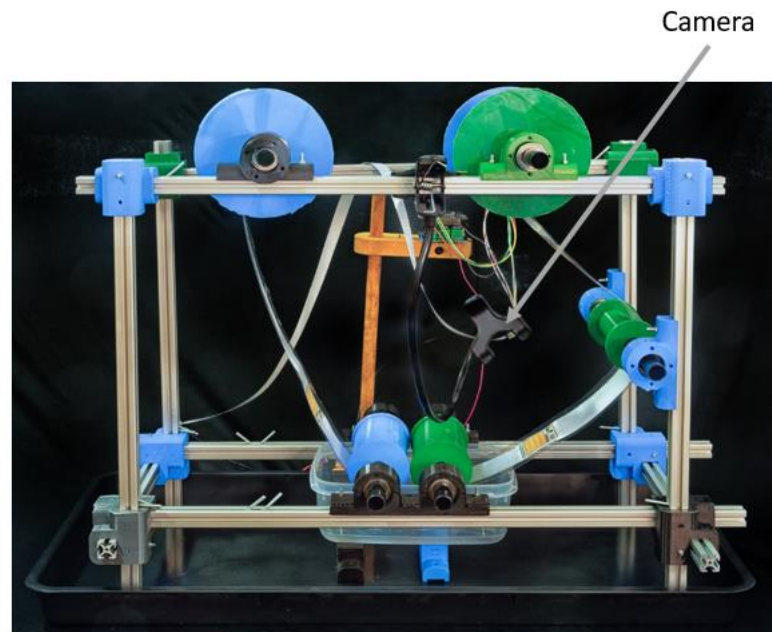


Figure 35. Final laboratory version of the system (front)

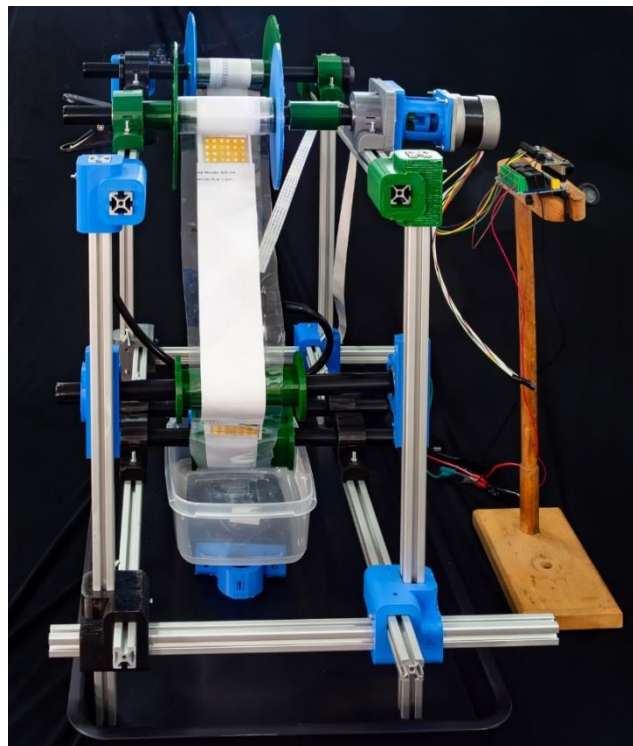


Figure 36. Final laboratory version of the system (side)

### 3.5.2 Electronic design

The electronic and electrical part of the system should be designed to achieve minimum power consumption and the performance level of chemical analysis and data processing stated in Section 3.

The control system is based on Raspberry Pi 4. The choice of this version of Raspberry Pi is due to the fact that it gives quite high performance while remaining quite compact and energy efficient compared to other Raspberry Pi and microcontrollers. The Raspberry Pi takes on a key role in controlling the motors, the key mechanical components that determine the functionality of the system. These motors (RS PRO 0.49Nm Hybrid Stepper Motor) are controlled by a driver (Adafruit DC & Stepper Motor Bonnet for Raspberry) that generates pulse-width modulated signals for the motors. A block diagram of the system is shown in Figure 37.

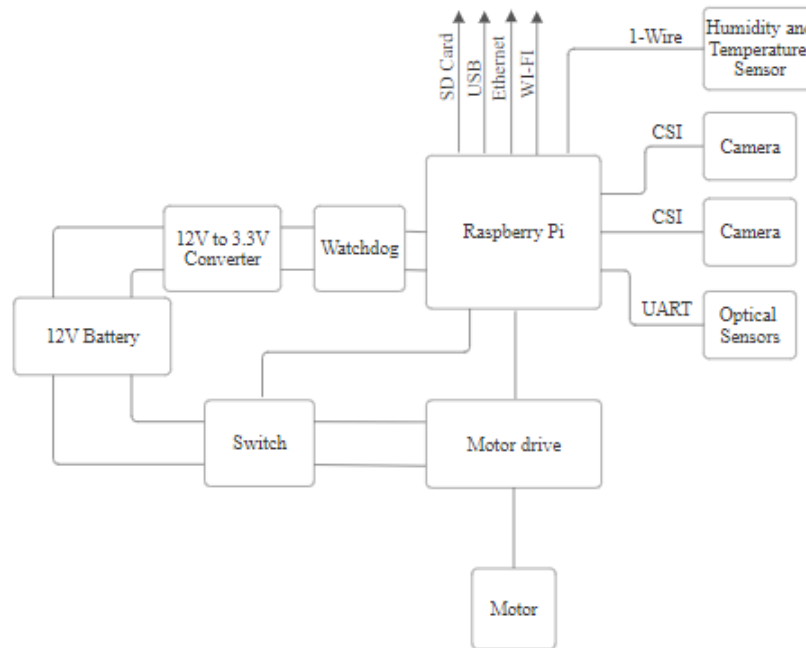


Figure 37. System block diagram

The motor connection schematic is shown in Figure 38. It needs to be noted that positioning and alignment control for spectral sensors has not been implemented in the system for a number of reasons discussed in Chapters 4 and 6 and therefore the motor connection diagram does not contain feedback. For the camera, positioning is performed using an object detection method (see Chapter 3.8).

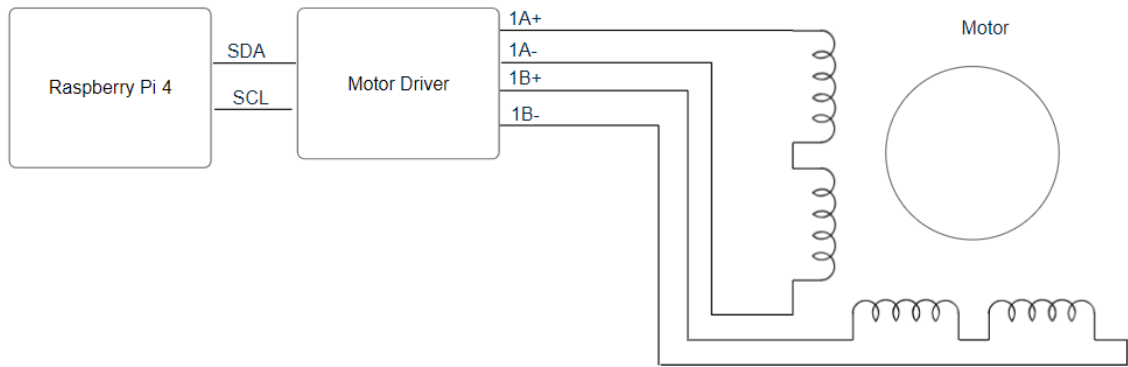


Figure 38. Motors connection.

Figure 39 shows simplified chart flow diagram of the system operation. After power up Raspberry Pi moves the motor to place PAD in the field of view of the camera/sensor, then do measurements/analysis and save the result and send it over if required. After whole cycle is complete watchdog power down the Raspberry Pi and wait until next measurement cycle.

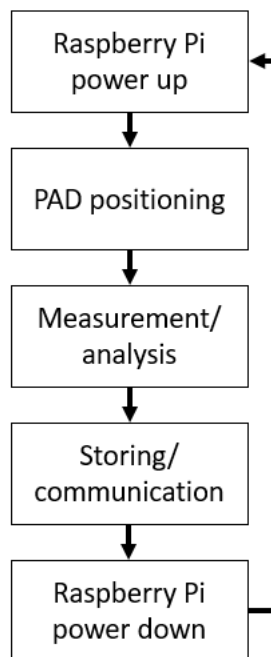


Figure 39. Chart flow diagram of electronic system operation.

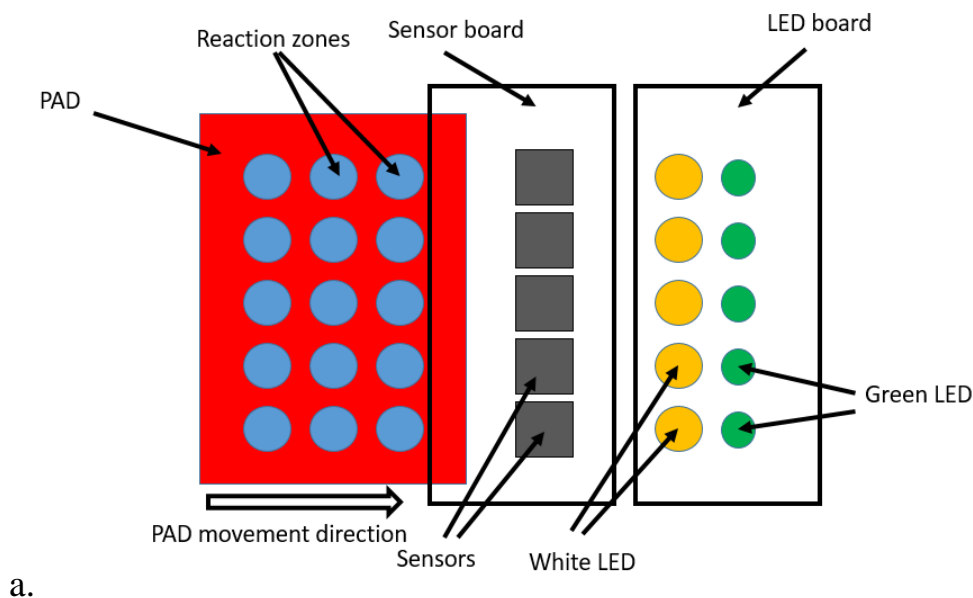
The whole system is powered by a 12-volt 288 Wh battery, which serves as the main source of energy. Motor and motor driver directly powered by 12 volts. To power Raspberry Pi, a voltage converter is used, generating 3.3 volts. Raspberry Pi Watchdog (operating timer) is used for power management to switch off the Raspberry Pi when the system is inactive.

Raspberry Pi also performs analysis using cameras or sensors (either can be used for optical analysis) to obtain PAD images before and after chemical reaction (“before” camera is not always required, but might be used to detect spoiled devices). Raspberry Pi Camera Module 2 has selected as a camera type colour sensor, which was chosen due to the fact that various Raspberry Pi libraries support this camera. AS7263 6-Ch NIR Spectral Sensing Module has been chosen as an alternative colour sensor because its 6 channels have a good coverage of the bromocresol green absorbance spectrum. After analysing the PAD image (calculating concentration), Raspberry Pi will save the results of the analysis on a memory card (SD). This storage method provides a compact, portable and efficient means of archiving analytical results.

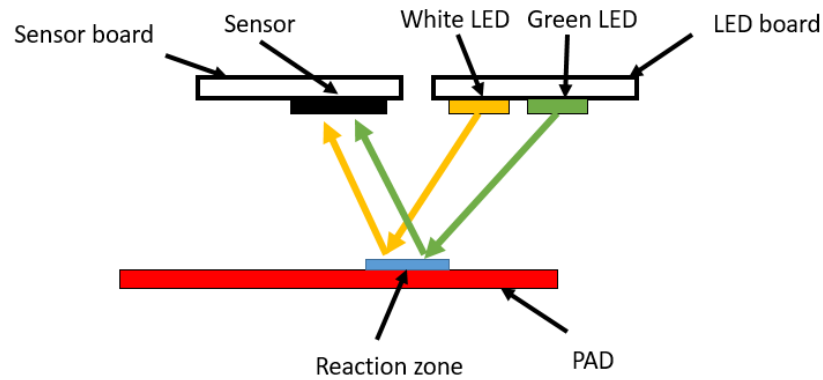
In addition, Raspberry Pi has a rich range of connectivity options. These include the usual wired connection via Ethernet, wireless data transmission via Wi-Fi and data exchange via the universal serial bus (USB).

### 3.5.2.1 Sensor Board

A custom-designed board was developed to accurately position the AC7676 sensors, in alignment with the reaction zones on the paper (the placement distances between optical sensors, LEDs and reaction zones are the same). PADs and boards positioning diagram is shown in Figure 40.







b.

Figure 40. Sensors and LED boards positioning (a – top view, b – side view).

Board schematic for one sensor device is shown in Figure 41 (full schematic in Appendix A). AS7262 communicates with Raspberry Pi via the UART interface and connected to AT25 flash memory for storing results. Simplified schematic is shown in Figure 41. .Figure 42, Figure 43 show the layout of the sensor PCB.

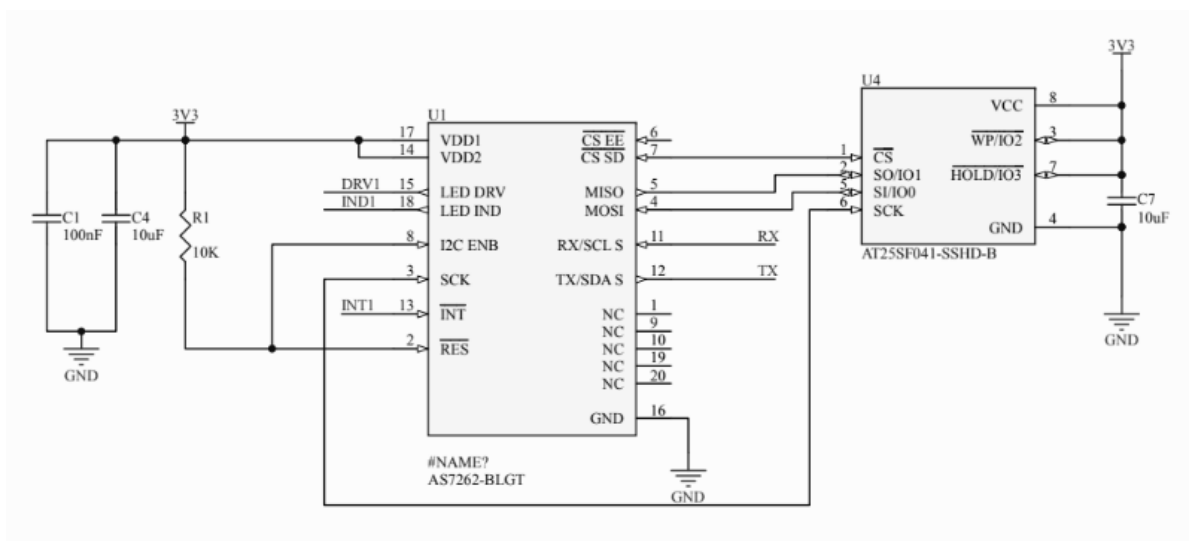


Figure 41. Schematic for one sensor device.

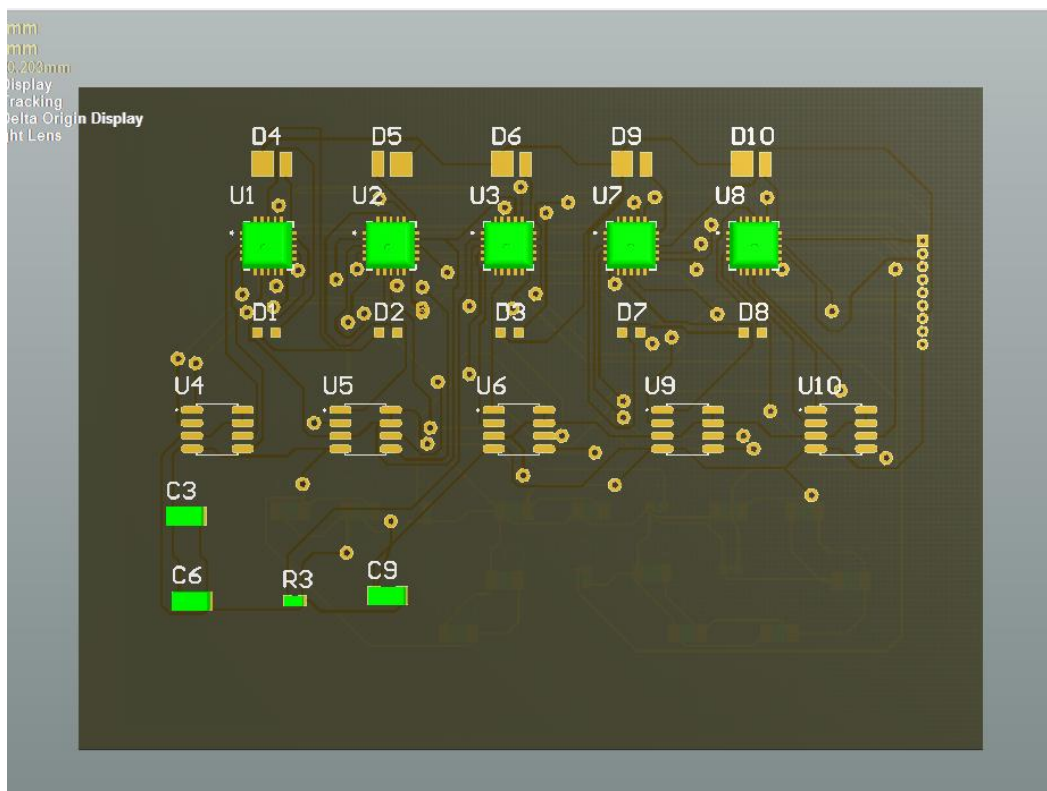


Figure 42. PCB design for the sensor circuit.

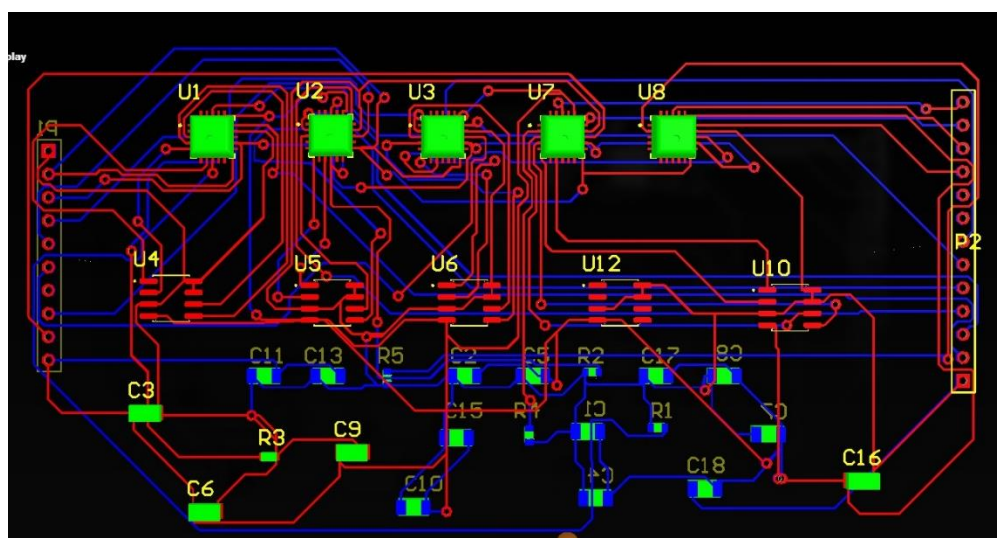


Figure 43. PCB routing (red – top level, blue – bottom level) for LED circuit.

Another board that used for lighting (PCB - Figure 44 and Figure 45, schematic – Appendix B) are equipped with a total of 10 LEDs – 5 white LEDs and 5 green LEDs connected to the main board over connector P2. The white LEDs provide a uniform illumination of the reaction zones over the entire surface of the paper (PAD). The choice of white LEDs with a wide emission spectrum is required to cover entire absorption spectrum of BCG (colouring agent). LED board may be place either next to sensor board or behind the paper device, each LED directly

behind each reaction zone. A wide spectrum is crucial for obtaining reliable and consistent absorption data as a result of reactions occurring on a paper.

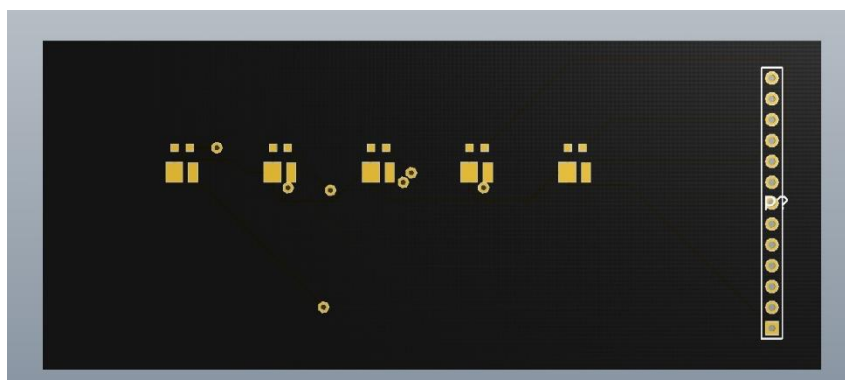


Figure 44. LED PCB design.

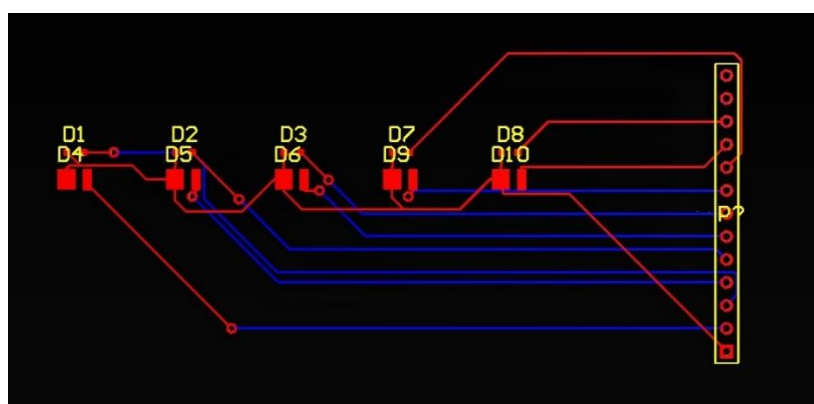


Figure 45. LED PCB placement (red – top level, blue – bottom level).

There are also 5 green LEDs installed on the board, and the wavelength of these LEDs has been carefully selected in accordance with the isosbestic point of the bromocresol absorption spectrum which is used as a reference (see chapter 3.2.3). Having a narrow emission spectrum covering essentially the isosbestic point only, green LEDs provided a stable reference point in the absorption spectrum analysis. This feature allowed to compensate for any potential fluctuations in lighting conditions, ensuring that measurements were accurate and reliable. This is due to the fact that the absorption of BCG at this point is the same for all pHs (see section 3.2.3). Photos of manufactured PCBs are shown in Figure 46.

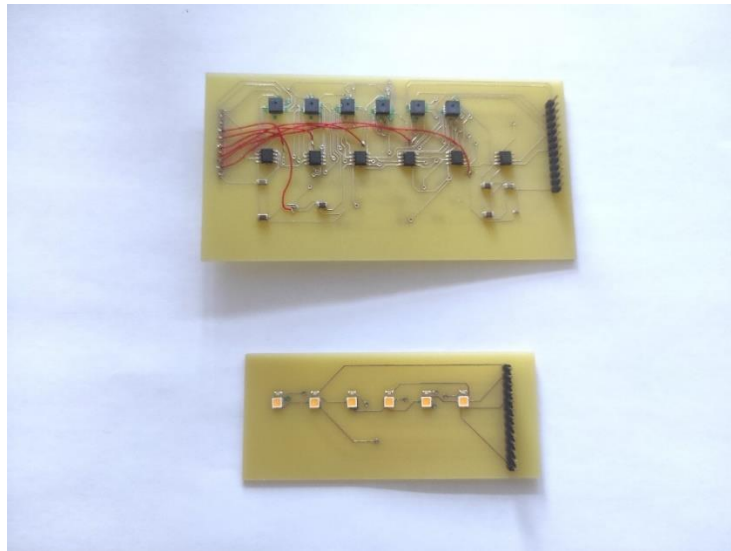


Figure 46. Manufactured PCBs.

### 3.5.3 Power budget

In order to determine the system's autonomous operational duration accurately, a thorough calculation of its total power consumption is necessary. As presented in Table 2, all system elements and their respective current consumption have been carefully listed, forming the foundation for the analysis.

**Table 2 – Power budget**

Component name	Quantity	Power consumption Max	Power consumption Idle
Raspberry Pi	1	5W	1.4W
Optical sensor AS7262	6	15mW	1.5mW
High Power White LEDs	6	330mW	0mW
Standard LEDs (green)	6	100mW	0mW
Raspberry Pi camera	2	1W	0W
MikroElektronika MIKROE-2101 Temperature & Humidity Sensor	1	5mW	1.5mW
Hybrid Stepper Motor	1	7.2W	0 W
Watchdog	1	20mW	5mW
		Total max power: 14W	Total idle power: 1.4W
*All data taken from official datasheets			

Considering that the system remains active for approximately 60 seconds per hour (assume that it required to make 2 measurements per hour, with each measurement lasting around 30 seconds including Raspberry Pi booting time. It depends on many factors such as hardware configuration, software, boot configuration, etc. This booting time was obtained experimentally). This value reflects the energy required to sustain the system's operation during the active state.

To ensure long-term autonomy, a high-capacity battery of 288 Wh (watt-hour) was purchased to power the system. Using the capacity of this battery to store energy and taking into account the specified power consumption, the expected duration of the system's autonomous operation can be calculated. Figure 47 shows power consumption diagram which includes Raspberry Pi booting time, time for moving rolls and processing time, where the latter one includes the time period for image/spectrum acquisition.

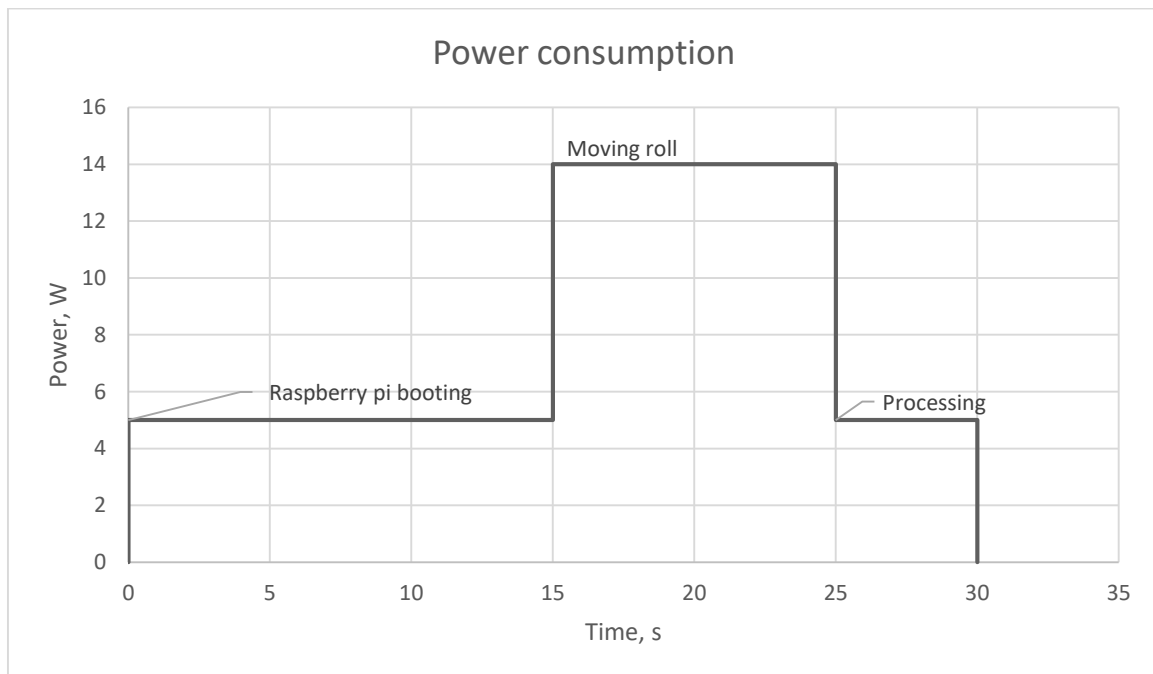


Figure 47. Power consumption diagram

According to the graph, the average power when system is active is 8 W. Thus, if the system makes 2 measurements per hour (active for 1 minute out of 60), then in one hour the average power is 0.13W.

Using the formula:

$$\text{Autonomy (hours)} = \text{Battery Capacity (Wh)} / \text{Average Power Consumption (W)},$$

$$\text{Autonomy (hours)} = 288\text{Wh} / 0.13\text{W} \approx 2215 \text{ hours.}$$

Consequently, the system is projected to function autonomously for an impressive 2215 hours, equivalent to approximately 92 days, before requiring a recharge or battery replacement. It also necessary to take self-discharge effect into account.

Assuming it will be about 20% [123], the total time will be 73 days. It is crucial to note that this calculation provides an initial estimation and serves as a valuable guideline for system planning.

It is essential to recognise that real-world scenarios may introduce variations, and more accurate values will be obtained after thorough testing under different conditions. Factors like temperature, environmental variations, and specific usage patterns can influence power consumption and subsequently affect the system's operational duration. Nonetheless, this rough calculation offers valuable insights and a foundation for system optimisation.

## 3.6 Sampling theorem in system design

### 3.6.1 Sampling processes

Changing of chemical concentration in natural water is an ongoing and dynamic process, influenced by various environmental factors and human activities. Water sampling plays a crucial role in monitoring and understanding these fluctuations, much like the process of digitizing analogue electronic signals using an analogue-to-digital converter (ADC).

In this analogy, the chemical concentration itself can be seen as the sampled signal, and just like any sampling process, the measurements are susceptible to errors inherent to non-idealities in the sampling implementation.

Similar to electronic systems, where sampling errors can lead to signal distortion, erroneous water sampling can lead to inaccurate assessment of the chemical composition.

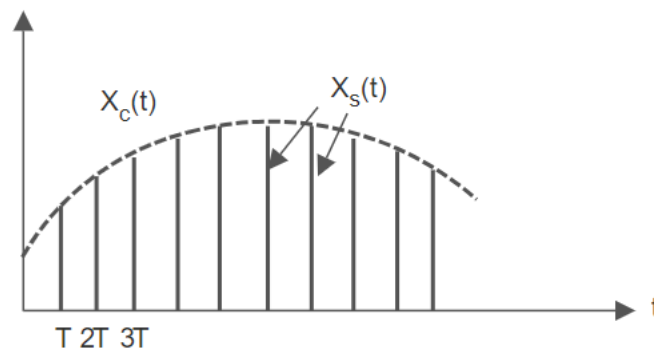


Figure 48. Digital signal processing

The process of signal sampling involves converting an original continuous signal (denoted as  $X_c(t)$ ) and represented by a dashed line, into its sampled version (labelled as  $X_s(t)$ ) which is shown as a series of pulses (see Figure 48). This conversion is achieved by capturing discrete data points at regular intervals of time, referred to as the sampling interval ( $T$ ). The frequency at which these samples are taken is known as the sampling frequency ( $f_s$ ), which is mathematically equivalent to the inverse of the sampling interval ( $f_s = 1/T$ ).

In an ideal scenario, each pulse in the sampled signal (has a duration  $\tau$ ) which is infinitesimally short ( $\tau \rightarrow 0$ ). However, in practical implementations,  $\tau$  is chosen to be very small compared to the variation time scale of the signals being sampled to minimize distortion and accurately capture the signal's characteristics.

The sample index ( $n$ ) is used to count samples. It is a positive integer starting from 0 and increasing for each subsequent sample. This means that the value of the sample  $X_s(nT)$  occurs at a time instant  $nT$  in the sampled signal  $X_s(t)$ . The samples occur at uniformly distributed points in time,  $t = 0, T, 2T, 3T$ , and so on.

Figure 49 shows an example of a sinusoidal signal, denoted as  $X(t)$ , which has a frequency of 0.001 Hz (1 cycle per 1000 seconds). This continuous signal is sampled to obtain its sampled version,  $X_S(t)$ , using the form of the sampling pulse  $p(t)$ .

The sampling pulse waveform  $p(t)$  is characterized by a frequency of 0.01 Hz (1 cycle per 100 second), making it significantly higher than the frequency of the original sinusoidal signal. This high-frequency pulse is used to extract discrete samples from the continuous signal  $x(t)$ .

The pulse duration of 10s is selected to provide an acceptable visual representation of the selected waveform on the graph.

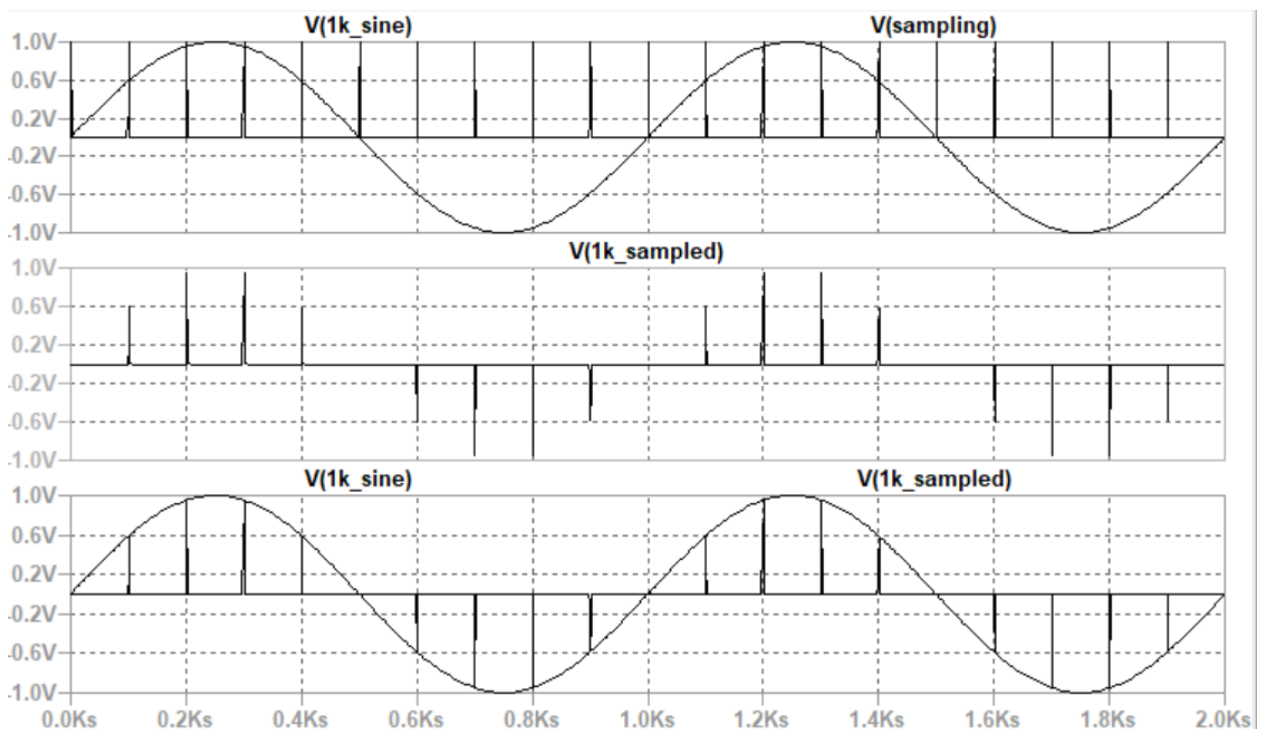


Figure 49. Top: Original waveform and sampling pulses, Middle: Sampled waveform, Bottom: Sampled and original waveforms shown together.

### 3.6.2 Minimum sampling frequency and signal spectrum

**Nyquist theorem.** In order to accurately reproduce a sinusoidal signal from its samples, it is extremely important to adhere to the Nyquist theorem, which states that the sampling frequency must be more than twice the frequency of the signal. This condition ensures that all the necessary information is collected during the sampling process. This theorem is also referred to as the "sampling theorem" or the "Nyquist-Shannon theorem" [124, 125].

While Nyquist's theorem is important for sinusoidal signals with a single frequency, real signals are often more complex and contain many frequencies.



These signals can be characterized by their frequency spectrum, which is the magnitude of all frequencies present in the signal. The spectrum provides valuable information about the frequency components and distribution within the signal.

The theorem is as follows: “If a function  $x(t)$  contains no frequencies higher than  $B$  hertz, it is completely determined by giving its ordinates at a series of points spaced  $1/(2B)$  seconds apart”. Figure 50 illustrates the concept of Nyquist's theorem, demonstrating the requirement for appropriate sampling intervals to represent the original continuous signal.

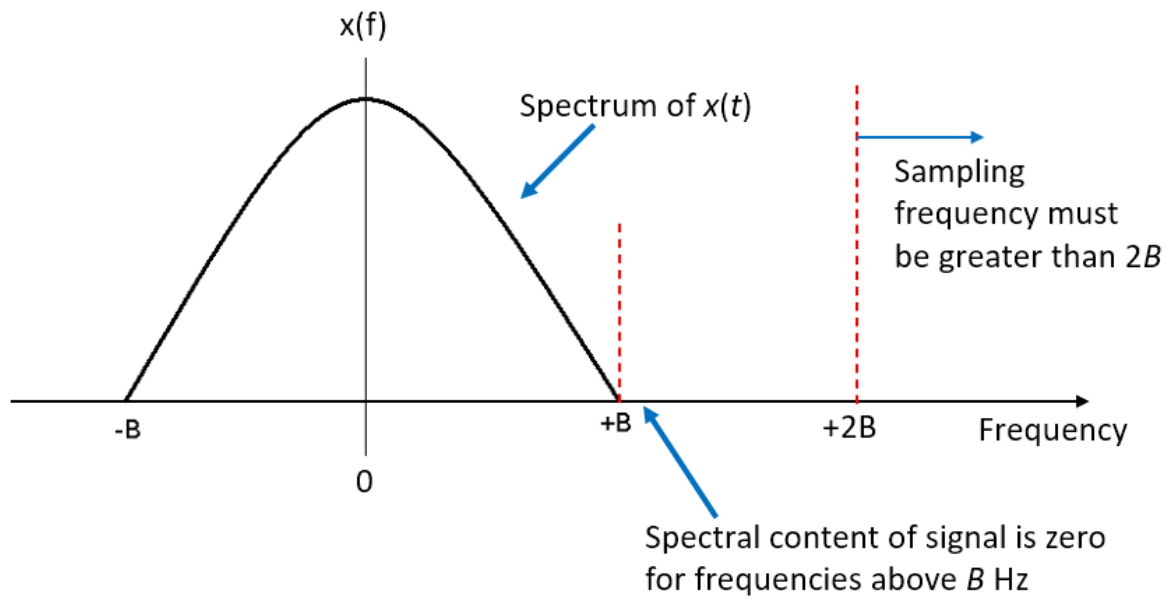


Figure 50. Signal sampling intervals

The concept of the Nyquist frequency or Nyquist rate is a fundamental principle in signal processing, governing the minimum sampling frequency required to accurately capture and reconstruct a continuous signal from its discrete samples. The Nyquist frequency is defined as twice the maximum frequency present in the original signal.

**Aliasing.** When a signal sample's frequency lower than the Nyquist frequency, a phenomenon known as aliasing occurs. Aliasing leads to errors during the reconstruction process, as the sampled data lacks sufficient information to faithfully represent the original continuous signal. The consequence of aliasing is the appearance of false frequencies or distortions in the reconstructed signal – in the case of water sampling erroneous representation of the variation with time the species concentrations being measured.

To understand why aliasing occurs, one can consider a scenario where the original signal contains frequency components beyond the Nyquist frequency. When the signal is sampled at a rate lower than twice the highest frequency present, these higher frequencies "fold back" into the lower frequency range during

reconstruction, causing frequency overlap. As a result, the reconstructed signal contains non-existent frequencies, making it significantly different from the actual continuous signal. In order to avoid aliasing and ensure accurate signal recovery, it is extremely important to adhere to the Nyquist frequency. When this sampling condition is met, the sampled data has enough information to accurately reconstruct the original continuous signal without any distortion or false frequencies.

An example of aliasing is shown in Figure 51. Consider two continuous signals with frequencies of 8 kHz and 17 kHz, respectively. To accurately capture and reconstruct these signals, the Nyquist theorem tells that the sampling frequency should be at least twice their respective frequencies. In this case, the Nyquist rates for the 8 kHz and 17 kHz signals would be 16 kHz and 34 kHz, respectively.

Now, let's assume that both of these signals are mistakenly sampled at a fixed rate of 9 kHz, which is below their corresponding Nyquist rates. When sampling the 8 kHz signal at 9 kHz, the sample values will match with the sample points of a 1 kHz signal. Similarly, when sampling the 17 kHz signal at 9 kHz, the sample values will match with the sample points of a 1 kHz signal as well.

As a result, the sampled data for both the 8 kHz and 17 kHz signals will appear to be a 1 kHz signal when viewed at the fixed sampling rate of 9 kHz. This means that the information contained in the original signals at 8 kHz and 17 kHz is lost due to the insufficient sampling rate, and the reconstructed data resembles a 1 kHz signal instead.

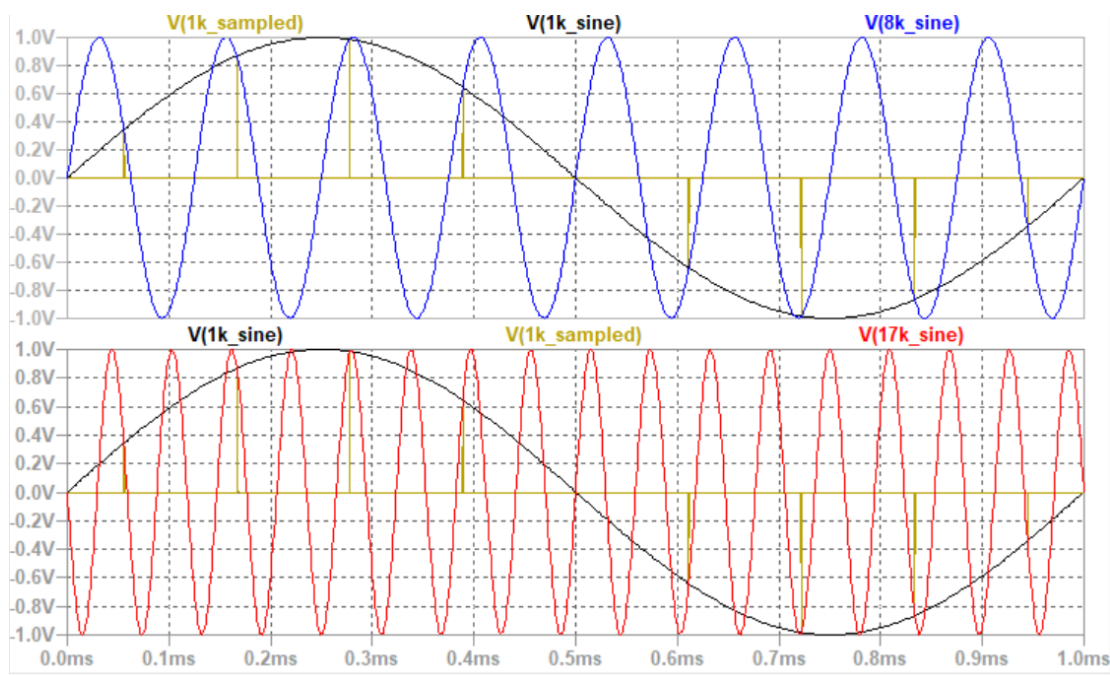


Figure 51. Top: 1 KHz and 8 kHz sinewaves and sampled signal, Bottom: 1 KHz and 17 kHz sinewaves and sampled signal.

The phenomenon of aliasing can lead to serious misinterpretations and inaccuracies in signal processing applications. To avoid aliasing and reconstruct the original signals, the sampling frequency should meet or exceed the Nyquist rate for each signal. In this example, the sampling frequency should be at least 16 kHz for the 8 kHz signal and 34 kHz for the 17 kHz signal to obtain accurate and reliable data.

**Low-pass filtering.** When dealing with situations where it is physically or practically challenging to achieve a sufficiently high sample rate to prevent aliasing, an effective solution is to implement an antialiasing filter. The purpose of the antialiasing filter is to remove all frequency components in the input signal that are above the Nyquist frequency, thereby eliminating any potential aliasing effects.

The antialiasing filter is typically a low-pass filter designed to attenuate or suppress frequencies above the Nyquist frequency, allowing only the essential frequency components to pass through. By filtering out the unwanted higher frequencies, the antialiasing filter ensures that the signal does not contain any information that would cause aliasing during the sampling process.

In scenarios where an analogue output is required, the reconstruction filter is used. The reconstruction filter serves a similar purpose to the antialiasing filter and is designed to have the same cut-off frequency requirement. This means that the reconstruction filter should have the same filtering characteristics as the antialiasing filter, ensuring that any high-frequency components from the digital-to-analogue conversion process are appropriately filtered out before producing the analogue output.

As a consequence, defining the filtering requirements for digital-to-analogue conversion or choosing a mathematical model for fitting the sampled data can become a nontrivial task. One of the key input parameters for that analysis is a filtering action of the measurement system itself.

In the designed system, the water tank acts as a low-pass filter that affects rate of variation of the concentration of chemicals in the water. This filtration effect can significantly affect the dynamics of measurements of the chemical composition of water, since it can weaken certain frequency components, while passing others.

### **3.6.3 Water tank as a low-frequency filter**

In the proposed system, PADs are used to sample the target chemical species in the water at regular intervals (sample period  $T$ ). This involves dripping the pad into a water tank, or reservoir, fed from the natural water source. In a karst cave this could be a natural flow, such as drip from a rock formation, or the tank could be fed from a body of water (e.g. stream or lake) using a pump.

The tank design (see Figure 52) includes an overflow lip or pipe which ensures a constant fluid level, required for consistent automated dipping, and means that the flow rates in and out of the tank are equal (assuming the tank remains full).

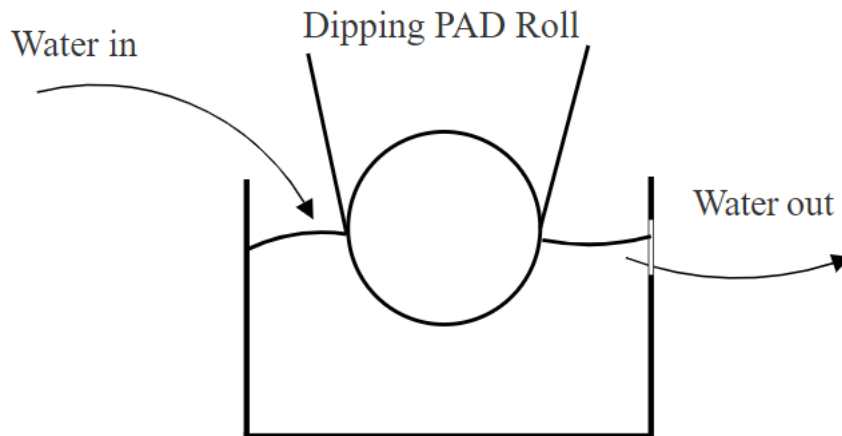


Figure 52. Water tank

It is important to understand that the tank has some inertia and prevents the capture of high-frequency fluctuations of chemical species. This is due to the fact that in the case when the concentration of a certain species in the tank itself and the water entering it is different, it takes some time for these values to become equal.

As discussed in section 2.3, the sampling process must meet the Nyquist requirement to produce valid results, which implies frequencies components of the concentration signal above the Nyquist rate should be filtered out if necessary. In general, an antialiasing filter is not required if aliasing frequencies are not present in the sampled signal. However, for the case of carbonate measurement in karst caves the dynamics of the water system being measured may not be well known and the spectral content may be subject to significant variation with time (for example fast dynamics in response to rainfall events) [126]. Therefore, the water sample feed and tank volume should (when possible) be designed to act as an antialiasing filter for the relevant species-concentration signals. The response of a water tank to a chemical concentration signal can be analysed using the box model.

### 3.6.3.1 Box Model of Water Tank

Consider a model system of the water tank characterized by a constant volume and constant rates of inflow and outflow of water. In the case of a change in the concentration of a certain element in the incoming water, it becomes necessary to understand the reaction of the entire system to this change (see Figure 53).

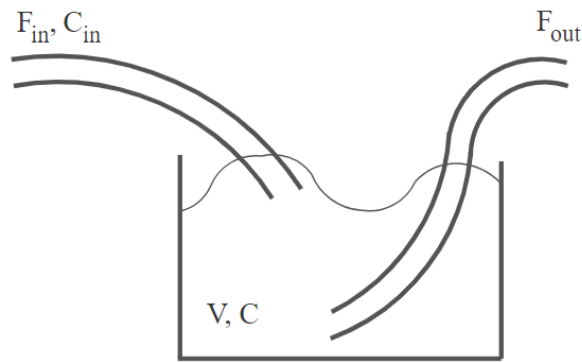


Figure 53. Water tank diagram

Below are the variables for such a system:

- $V$  represents the volume of water the container can hold, measured in cubic centimetres ( $\text{cm}^3$ ).
- $C$  represents the concentration of the element inside the container, measured in moles per cubic centimetre ( $\text{mol}/\text{cm}^3$ ).
- $C_{in}$  is the concentration of the element in the incoming water.
- $F$  indicates the flow rate at which water enters/leaves the container, measured in cubic centimetres per second ( $\text{cm}^3/\text{s}$ ).

Next, the equation of the change in the concentration of an element in the system over time can be defined. This equation relates the water flow and the discrepancy between the concentration in the incoming water ( $C_{in}$ ) and the concentration in the retention system ( $C$ ).

$$V \frac{dC}{dt} = C_{in}F_{in} - CF_{out} \quad (4)$$

When the flow rate of water in and out of the container remains same and equal  $F$  (stationary condition for the water level in the tank), the equation may be simplified:

$$\frac{dC}{dt} = \frac{F}{V} (C_{in} - C) \quad (5)$$

This differential equation provides invaluable insights into the dynamic behaviour of the element's concentration within the containment system over time. It demonstrates that the rate of change of the concentration is directly proportional to the flow rate and inversely proportional to the volume of the system and the difference between the incoming concentration and the concentration within the system.

To determine the concentration of an element at a certain point in time, the differential equation can be integrated:

$$C(t) = C_{in} \left( 1 - e^{-\left(\frac{F}{V}\right)t} \right) \quad (6)$$

This equation shows that the concentration of the element within the system tends to approach the concentration in the incoming water ( $C_{in}$ ). The speed at which this occurs depends on the flow rate of water ( $F$ ) and the volume of the system ( $V$ ). Over time, the concentration of the element in the retention system increasingly corresponds to the concentration in the incoming water.

A graphical representation of the solution is shown in Figure 54. Over time, the concentration of the element in the system gradually changes, approaching its limit value. This asymptotic behaviour is shown on the Figure 54 where the concentration asymptotically converges to its final value, marked as  $C_f$ .

To determine the time required to establish concentration, the term residence time is used. The residence time is determined by the stationary state in which the concentration of the element no longer changes with time ( $dC/dt = 0$ ). In this stable state, the concentration reaches its final value  $C_f$ , and remains constant over time. In fact, the system reaches a harmonious equilibrium, while the concentrations of inflow and outflow are equal to each other ( $C_f = C_{in}$ ).

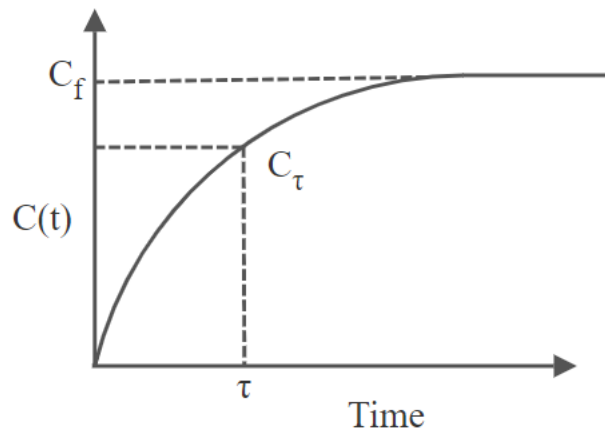


Figure 54. Water tank residence time

Thus, the residence time  $\tau$  is defined as concentration at steady state over inflow rate or the volume of water contained in the system ( $V$ ) divided by the water flow rate ( $F$ ).

$$\tau = \frac{V}{F} \quad (7)$$

Therefore, after one residence time ( $\tau$ ), the concentration can be found as:

$$C_{\tau} / C_{in} = (1 - e^{(-F / V * \tau)}) = 1 - e^{(-1/\tau * \tau)} = 1 - e^{-1} = 0.63 \quad (8)$$

Thus, the residence time, or renewal time, essentially represents the time required for 63% of the initial concentration to be replaced by the new concentration.

It is important to note that this behaviour of filters is characterized by a parameter known as the time constant (residence time in the box model), denoted as  $\tau$ . As discussed above, the time constant is influenced by two factors: the volume of the water tank ( $V$ ) and the rate at which water flows into the tank per unit of time ( $F$ ).

For a low-pass filters of the first order, the parameter determining their performance is the cut-off frequency, which corresponds to the point at which the signal level is attenuated by -3 dB. This key cut-off frequency is expressed using the settling time (tau) as follows:

$$f_c = \frac{1}{2\pi\tau} = \frac{F}{2\pi V} \quad (9)$$

Remarkably, this correlation discloses that lower flow rates result in a reduction of the cut-off frequency.

It should be noticed that the dimensions of the tank also play a key role in determining the cut-off frequency. Larger volume tanks tend to provide lower cut-off frequencies. The important assumption embedded in this model is the assumption of ideal mixing in the tank. This assumption may be less applicable in larger tanks, where the probability of non-ideal mixing scenarios becomes higher.

Thus, it can be confirmed that the tank acts as a low-frequency filter for which the maximum sampling frequency can be calculated, provided the flow rate remains constant. It is also worth noting that this process may be influenced by additional factors such as fluid density, etc. which may affect the process of mixing liquids and the behaviour of the system as a whole.

#### 3.6.4 Example model

. The purpose of this model is to reproduce the behaviour of a 1.5-litre tank with a flow rate of 1 millilitre per second (estimated flow rate in the Pool's Cavern cave), providing a residence time ( $\tau$ ) of 1500.0 seconds, which is equivalent to 25 minutes.

For this particular scenario, the cut-off frequency is calculated using the ratio  $f_c = F / (2\pi V)$ , resulting in a value of 106.1  $\mu$ Hz. This parameter determines the maximum frequency that can be accurately represented in the system. With a minimum sampling frequency ( $f_s = 2f_c$ ) of 212.2  $\mu$ Hz, corresponding to a maximum sample period of 78.5 minutes.

The electronic analogue will be a filter with a time constant ( $\tau$ ) equal to 1500 seconds, which is the result of a capacitance (C) equal to 1 Farad and a resistance (R) equal to 1500 ohms. This approach makes it easier to model the tank's response to changing input data.

Taking into account the sampling interval (T) equal to 3600 seconds (which is equivalent to one hour), we calculate the sampling frequency ( $f_s$ ) equal to 277.8  $\mu$ Hz. This frequency determines the rate at which data points are collected, reflecting the temporal granularity of our model.

Appendix H represents examples of signals with a frequency multiple of the sampling frequency, in particular, with a frequency of 0.864x (240.0  $\mu$ Hz) and 0.08333x (23.15  $\mu$ Hz)  $f_s$ .

### **3.7 Error analysis**

#### **3.7.1 Aperture delay and uncertainty**

Aperture Uncertainty, or aperture jitter, is the sample-to-sample variation in sampling time (Brannon, Kester, Kester). This is particularly important in some high-speed electronic systems, where jitter requirement may be in the sub picosecond range. However, it is potentially an issue in any sampling system (at relevant timescales). Each sample should occur at integer multiples of the sample period ( $nT$ ) but in a real system there will be timing errors and each sample will deviate from the ideal timing (actual time  $nT + \Delta t_n$ , where  $\Delta t_n$  is the error in cycle  $n$ ). The timing error is a random process, with potentially a number of factors in the system contributing, thus the overall expected error can be expressed as the root mean squared (RMS) sum of these contributions ( $\Delta t_{\text{RMS}}$ , the RMS average of  $\Delta t_n$ ). The timing noise (the jitter,  $t_j = \Delta t_{\text{RMS}}$ ) results in corresponding measurement errors due to the change in signal value in the time between the ideal and actual sample times (Figure 55). The measurement errors result in an RMS noise ( $\Delta c_{\text{RMS}}$ ) added to the measurement.



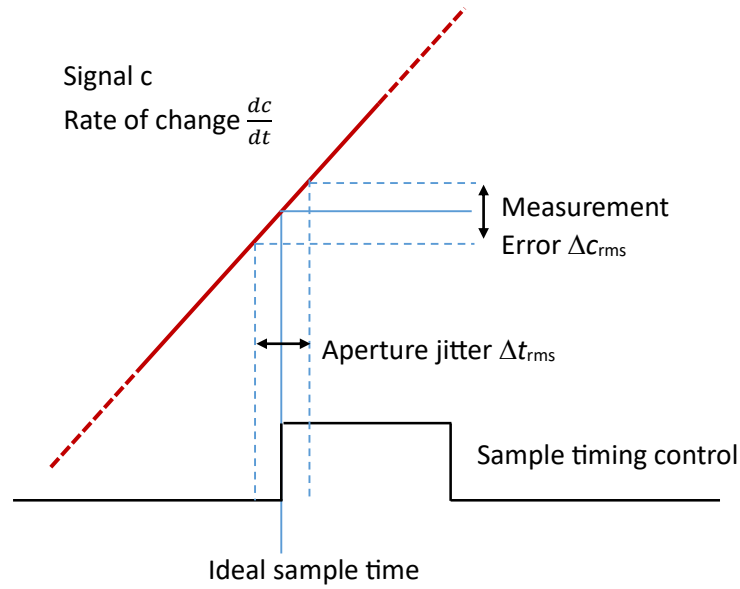


Figure 55. Aperture jitter

The value of  $\Delta c_{RMS}$  is obtained by multiplying rate of change of the measured signal  $\frac{dc}{dt}$  by the jitter

$$\Delta c_{RMS} = \left. \frac{dc}{dt} \right|_{RMS} \Delta t_{RMS} = \left. \frac{dc}{dt} \right|_{RMS} t_j \quad (10)$$

For the case of sinusoidal (that is considering a specific frequency of signal,  $f$ ) the signal is

$$c(t) = A \sin(2\pi f t) \quad (11)$$

where  $A$  is the amplitude. The rate of change is

$$\frac{dc}{dt} = 2\pi f A \cos(2\pi f t) \quad (12)$$

The RMS value of a sinusoidal is obtained by dividing its amplitude by  $\sqrt{2}$

$$\left. \frac{dc}{dt} \right|_{RMS} = \frac{2\pi f A}{\sqrt{2}} \quad (13)$$

So using the equation above for  $\Delta c_{RMS}$  the error due to jitter is

$$\Delta c_{RMS} = \frac{2\pi f A}{\sqrt{2}} t_j \quad (14)$$

The RMS signal to RMS error ratio is

$$\frac{\frac{A}{\sqrt{2}}}{\frac{2\pi f A}{\sqrt{2}} t_j} = \frac{1}{2\pi f t_j} \quad (15)$$

In electronics this is typically expressed as signal to noise ratio (SNR) in dB.

$$SNR = 20 \log_{10} \left( \frac{1}{2\pi f t_j} \right) = -20 \log_{10}(2\pi f t_j) \quad (16)$$

When considering converting signals to digital Effective Number of Bits (ENOB) can be a useful equivalent to SNR. This indicates the number of bits in an ideal Analogue to Digital Converter (ADC) which would have the same quantisation noise as the SNR (in dB) of interest.

$$ENOB = \frac{SNR - 1.76}{6.02} \quad (17)$$

The error relative to the signal amplitude can also be expressed as percentage

$$\%Error = 100 \times 2\pi f t_j \quad (18)$$

Errors are larger for faster signals and higher jitter.

**Numerical example:** using the same setup as the aliasing example above and using the highest signal frequency 138.9  $\mu$ Hz (an hourly (277.8  $\mu$ Hz) sample rate). With a jitter of 1 second the error is 0.087%. This can also be expressed as SNR of 61 dB or an ENOB of 10 bits. These values can be used to compare with errors or noise in other parts of the measurement, data capture and processing performed by the system (e.g. number of bits in ADCs, accuracy of PAD measurement).

A range of SNR and ENOB values are shown in Figure 56 for concentration signal (this figure determines noise level for various jitters and frequencies when signal amplitude and frequency remains the same, for example for signal frequency 0.001 Hz and jitter 1 second SNR will be 50 dB) cycle times in the range 15 minutes to 28 hours approximately (specifically frequencies in the range 10  $\mu$ Hz to 1000  $\mu$ Hz). This implies minimum measurement sample periods approximately in the range of 8 minutes to 14 hours to conform with the Nyquist rate. This is in line with the expected usage of the Lab on Roll Platform. As jitter errors are higher at higher signal frequencies the minimum sample time expected in system usage should be used to determine the jitter specification. The system should ideally be specified to achieve a jitter error significantly less (e.g. tenfold) than the expected error from the chemical measurements obtained from the PADs.

For example, if the PAD has an accuracy of 10% the jitter error should be less than 1%, implying a jitter time of less than 1 second for signals of 15 minutes period or longer (see Figure 57). Achieving 1 second timing accuracy within an embedded system controller is straightforward, but the electromechanical and fluidic aspects of the PAD roll and dipping system may introduce greater uncertainty to the actual sample timing.

10  $\mu\text{Hz}$   $\Rightarrow$  16.7 minutes period.

100  $\mu\text{Hz}$   $\Rightarrow$  2.78 h period.

1000  $\mu\text{Hz}$   $\Rightarrow$  27.8 hours period.

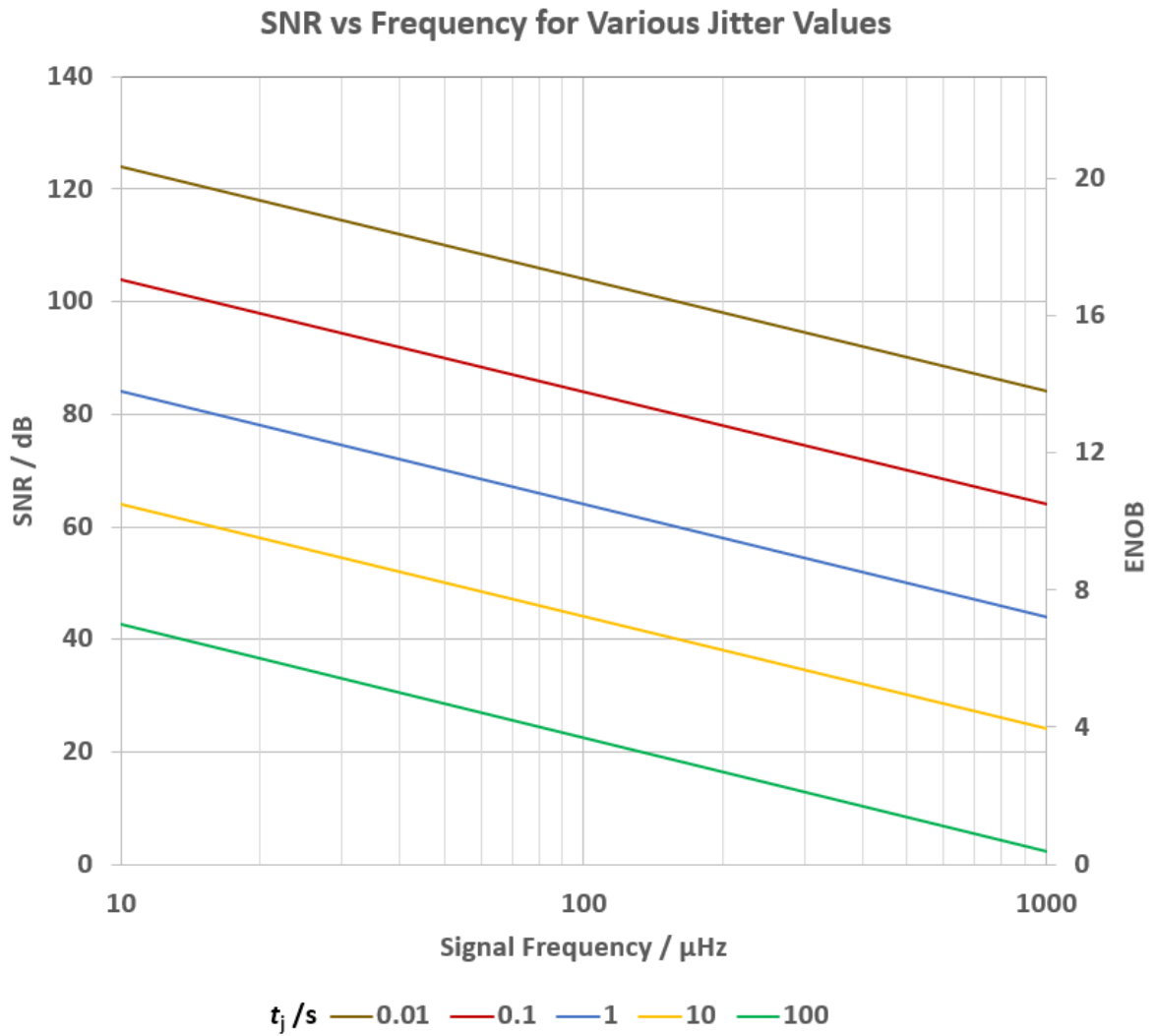


Figure 56. Signal to noise ratio for various jitter values.

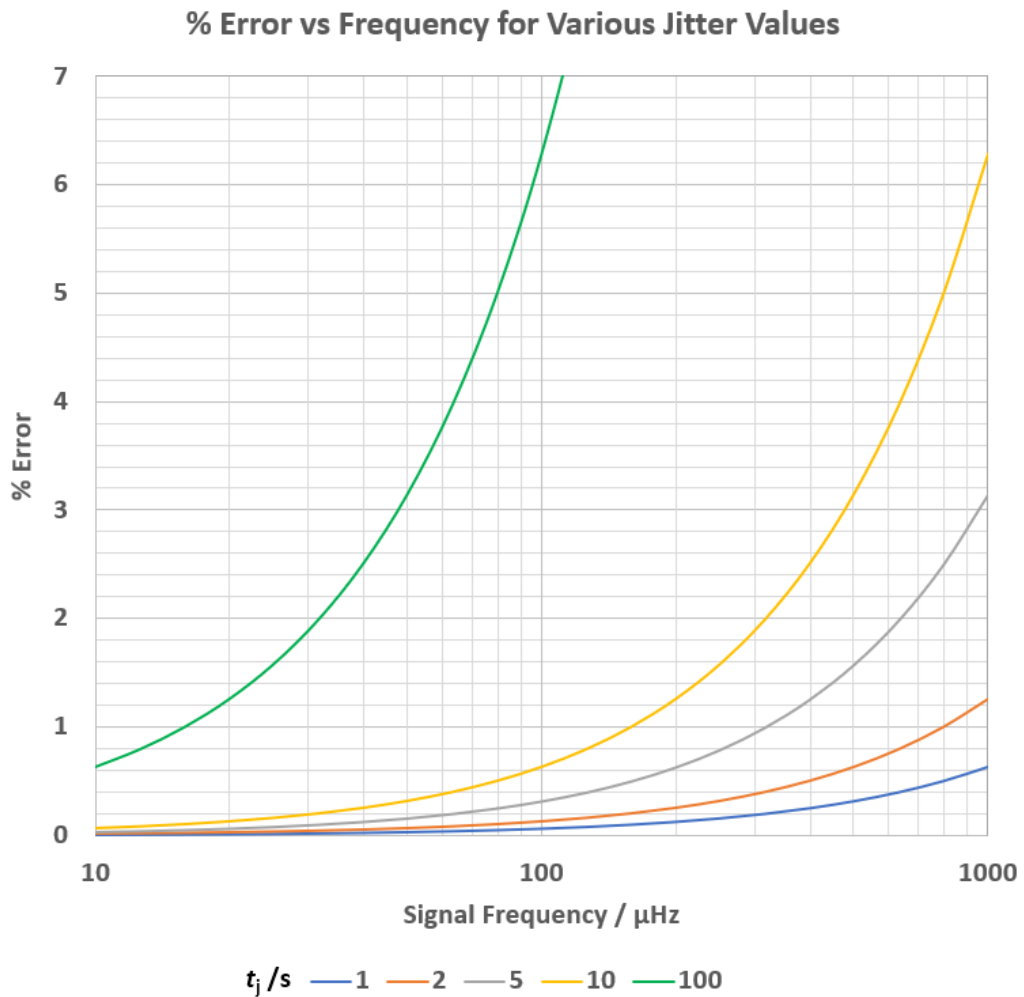


Figure 57. Error Signal to noise ratio for various jitter values.

For the developed system using camera sensing method, the time noise is approximately 1 second. Thus, at a signal frequency of 0.001 Hz, the error will be approximately 0.6%. In case of spectral sensor implementation, the jitter can be higher but not expected to go above 1.5 second, accordingly the error will be 1.2%. This evaluation shows that the jitter error will contribute a relatively small part to the overall system error, compared to the PAD error.

### 3.7.2 Aperture skew

In electronics, in systems with multiple ADCs sampling at the same or, or interleaved to obtain higher throughput, however mismatch between the channels in terms of offset, gain, timing and bandwidth introduce errors into the sampled data which results in spurs in the spectrum of the sampled signal. A similar situation occurs with PADs clusters as they do not enter the sample tank simultaneously (Figure 58) – this will occur due to the layout of the cluster resulting in sequential entry into the water sample based on location in the cluster, which cannot be avoided if multiple PAD rolls are used. It may also occur if the roll is not perfectly aligned with the water surface (Figure 59) so that a given PAD

roll enters the water at the same time. This could be due to misalignment of the PAD transport, due to the tank not being level. It should be possible to minimise misalignment with good mechanical design and in-situ installation. Means to level the tank should be provided.

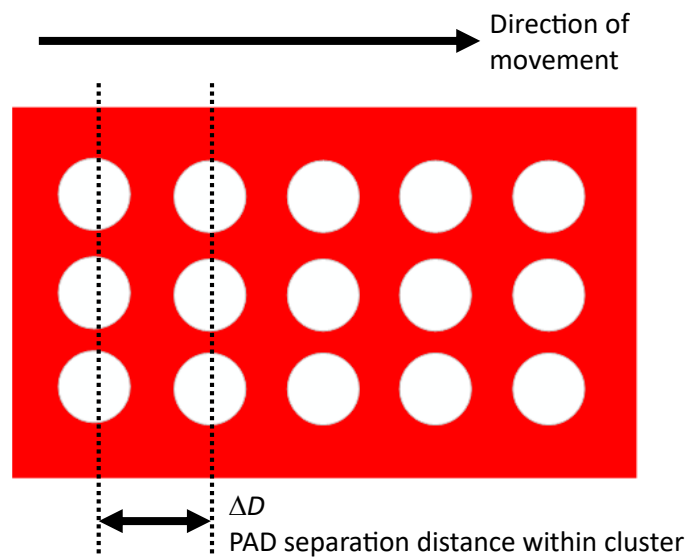


Figure 58. Skew due to PAD location in cluster

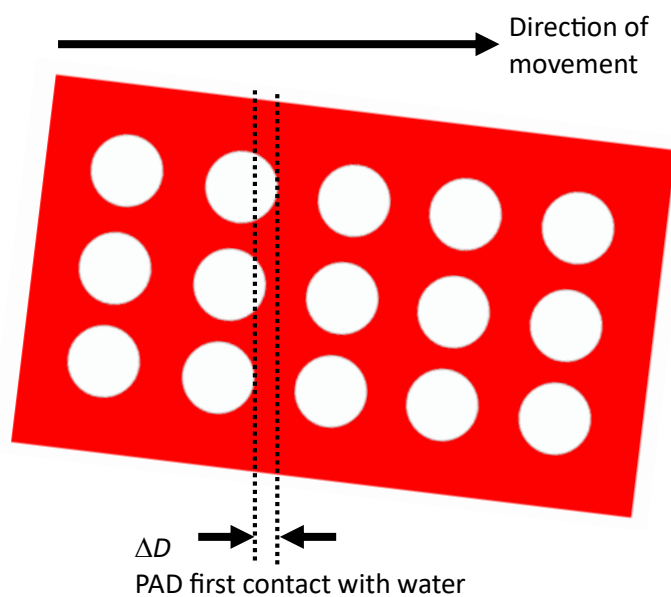


Figure 59. Skew due to roll alignment

For a PAD separation, or alignment skew distance of  $\Delta D$  and a roll speed of  $s$  the time skew is  $\Delta T = s\Delta D$ .

For skew due to PAD position  $\Delta D$  is known. The skew should be very small when compared to the sampling period (around 1:1800 for seconds order of magnitude

skew in half hour sampling). The errors can be calculated in a similar way to jitter but are fixed rather than random variations.

A symmetrical cluster – equivalent PADS at equal distance either side of the nominal ideal sample position (and hence time) – the centre of the cluster would allow linear interpolation to be used to correct for skew if needed (Figure 60).

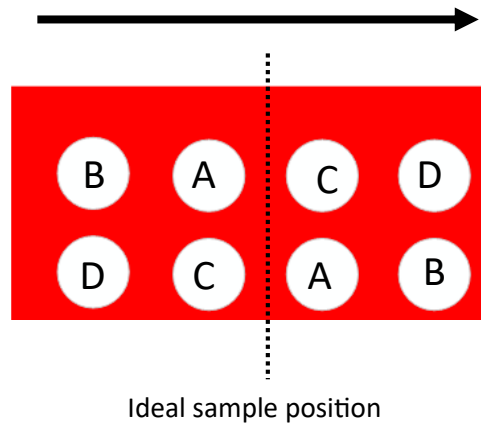


Figure 60. Symmetrical cluster

The error due to PAD skew for  $\Delta D$  equals to 5 mm at signal frequency of 0.001 Hz (expected skew and signal frequency) will be less than 0.1% which will also be relatively small part to the overall system error. To avoid the influence of the skew error, it is necessary that the rate of change of the signal after mixing (filtering) in the water reservoir be slower than the time difference between immersing the reaction zones in water. This design uses a 1.5-liter water tank, which eliminates this error (since the water reservoir filters rapid changes in concentration, it does not affect the final measurement accuracy, see chapter 3.6.4).

In conclusion, it is also worth noting that the system allows to take measurements with a maximum frequency of 2 measurements per minute or 0.03Hz.

### 3.8 System software design

#### 3.8.1 Automated measurement system (MATLAB) developed for phosphates PADs

Optical analysis can be performed using a sensor or a camera. As suggested, spectral sensor analysis may give more accurate results as the sensor has a greater spectral resolution (this is later evaluated in more detail in chapter 4.2.3). With development work constrained by COVID19 pandemic lockdowns, it was decided to focus on using a camera, since this method does not require precise optical alignment.

In order to prove the concept of software-based analysis of PAD images, an application was developed in the MATLAB development environment. The program automatically analyses photos of samples of existing PADs developed to detect phosphates [101]. The aim was that some techniques tested in this program environment will be used later in developing software for the system. MATLAB allows rapid exploration of techniques which will be ported to the embedded system (code in Appendix I).

The program is a combination of two functions. The first is a function that calculates areas of all the connected pixels of a preset colour in the image. The second is the function that converts the image into a new binary image which contains merely connected components of areas greater or less than the threshold intensity? (the threshold was selected in advance experimentally). Result of circles identification is shown in Figure 61. Right figure contains only reactions zone of PAD device (rest of pixels are removed). Note that the right figure aspect ratio has been distorted as a result of the resolution change (for simplicity to resolution 800x600); and number of pixels was reduced for better performance as original photos have high resolution and processing may take up to 5 minutes (due to high number of pixels).

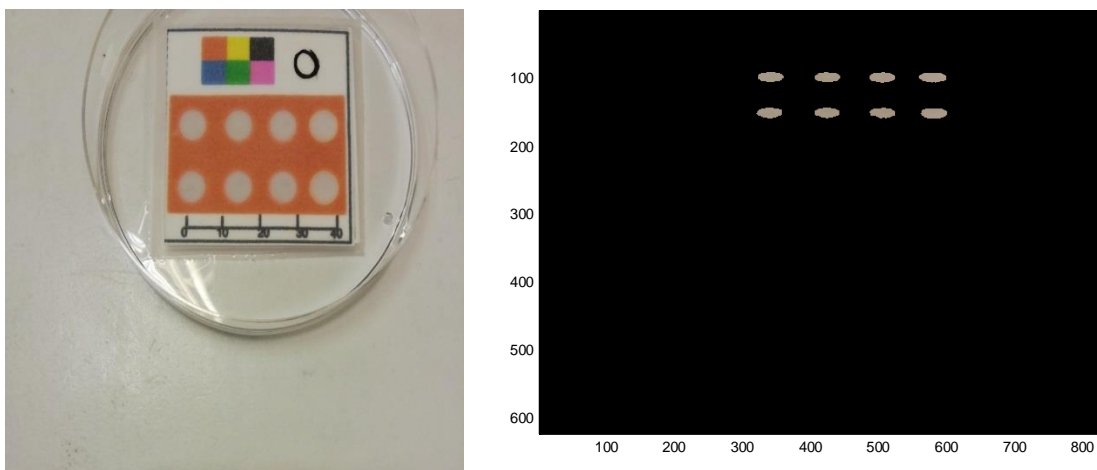


Figure 61. Image before (left) and after (right) processing.

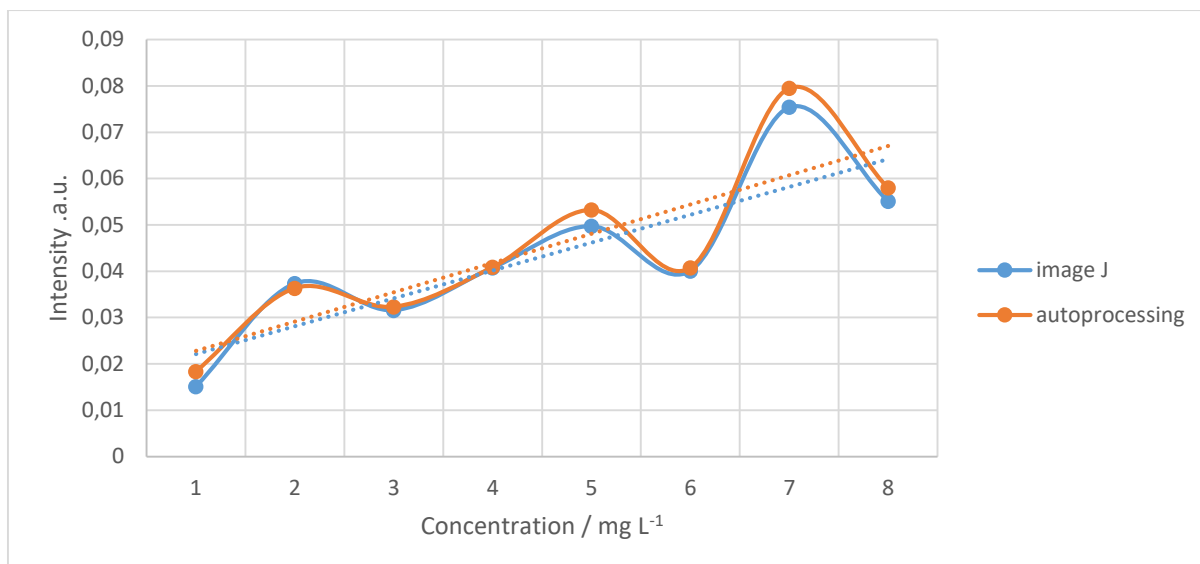


Figure 62. Graph of measurement results using Image J and Matlab program.

Figure 62 shows graphs of blue channel colour intensity of the PAD devices on the concentration of phosphates for images used for laboratory experiment. These results were obtained as a result of experiments to measure the concentration of phosphates in the laboratory conducted by a group of chemists at the University of Hull. The graph compares the results obtained manually using same algorithm (as described earlier in chapter 3.3.1) not automated image editor/processing software (e.g ImageJ) and the results obtained using the MATLAB analysis software. According to the graph, it can be concluded that the difference between the results of automatic and manual measurement methods does not go beyond 5%.

### 3.8.2 AI PAD detection

All subsequent work described in sections 3.8 has been done on the system using a camera-based optical analysis.

The first stage of the analysis is the detection of all the PAD devices within the relevant section of PAD roll, after which chemical colorimetry can be applied using the relevant pixel data from each individual PAD. Given the fixed camera location and accurate pad roll positioning within the instrument, one would assume that the devices will always be in the same location within the image, and then the need for automatic PAD position detection would not be avoided. But on the other hand, some variability is expected, and the analysis result may have an error if the device is not accurately located in the image. Furthermore, automatic PAD location is more adaptable to different PAD roll layouts without requiring significant additional data or software changes. Thus, it was decided to use an artificial neural network-based image processing to recognize the PADs within the camera image.

Image processing is an important application for Machine Learning technologies. Globally, all images of some object make up a library of unstructured data. Using



neural networks, machine learning and artificial intelligence, this data can be structured and used for detection and recognition tasks.

In order to recognize an object, a neural network must first be trained on the data. The picture is divided into small sections, up to several pixels, each of which will be an input neuron. With the help of synapses, signals are transmitted from one layer to another. During this process, hundreds of thousands of neurons with millions of parameters compare the received signals with already processed data. At some point, increasing the number of layers leads to simply memorizing the sample, not learning [127].

When training, it is important to teach the network to determine not only a sufficient number and values of features to give good accuracy in new images. It is also important not to overfit, not to "adjust" unnecessarily to the training set from images. After completing the correct training, the network should be able to identify objects (of the same classes) which were not used in the training process [128].

It is necessary to take into account that the initial data for the neural network must be unambiguous and consistent, so that situations do not arise when the neural network will give out high probabilities that one object belongs to several classes.

It should also be noted that using AI to detect PAD is not the most energy efficient solution in terms of resources spent, but this solution is one of the easiest to implement and quite flexible.

### **3.8.3 Image processing platform**

Before starting to develop the AI software, many machine learning libraries were examined. The Tensorflow Lite library turned out to be the most suitable [129]. The model created using this library has the lowest object recognition accuracy, but the model has the smallest size and the shortest image processing time [130, 131]. These factors are important given the power, memory and processing constraints applicable to the in-situ monitor.

TensorFlow is an open-source library created for Python. TensorFlow compiles many different algorithms and models, allowing the user to implement deep neural networks for use in tasks such as image recognition and classification.

The Tensorflow library uses the YOLO algorithm to detect objects. YOLO transforms an object detection task into a regression task. It goes from the pixels of the image to the coordinates of the bounding boxes and the probabilities of the classes. Thus, a single convolutional network predicts several bounding boxes and probabilities of classes for the content of these areas.

Since YOLO needs only one look at the image, the sliding window method is not suitable in this situation (this method was used in earlier object detection algorithms) [132]. Chart flow diagram of object detection is shown in Figure 63. Instead, the image will be divided into a grid with cells of size  $S \times S$ . Each cell can contain several different objects for recognition.

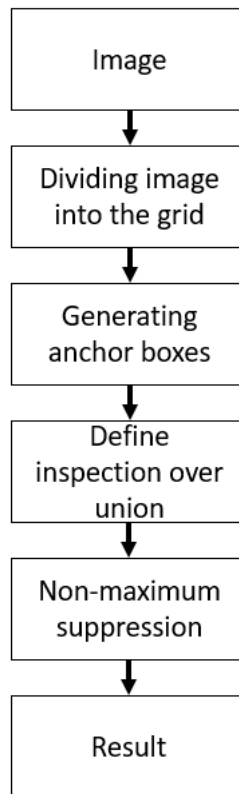


Figure 63. Chart flow diagram of object detection

Firstly, each cell is responsible for predicting the number of bounding boxes (rectangular region surrounding an object). Also, each cell predicts a confidence value for each area bounded by the bounding box. In other words, this value determines the probability of finding an object in a given area. That is, if some grid cell does not have a specific object, it is important that the confidence value for this area is low. Thus, a map of objects and frames ordered by confidence value may be built by visualizing all the predictions.

Secondly, each cell is responsible for predicting the probabilities of classes of detecting objects. This does not mean that some cell contains some object, only the probability of finding the object. For example, if a cell predicts a car, it does not guarantee that the car is actually present in it. This only means that if an object is present, then this object is most likely a car.

Anchor boxes (anchor frames / fixed frames) are used to predict bounding boxes. The idea of anchor boxes encapsulates into the preliminary definition of two

different forms. Thus, each cell predicts 4 coordinates for each bounding boxes, one "object error" and a certain number of class probabilities.

For the next step, it is important to define the IoU metric (Intersection over Union). This metric is equal to the ratio of the area of the intersecting areas to the area of the combined areas. Next, to get rid of duplicates, it is necessary to use “non-maximum suppression” (non-maximum suppression). The algorithm takes the bounding box with the highest probability of belonging to the object, then among the other bounding boxes bordering the given area, takes the one with the highest IoU and suppresses it.

A GPU is required to create a model, so the training of the model took place on the Google Cloud platform. This environment allows training the model on the server using its resources.

### 3.8.4 Evaluation example

To start the machine learning process, a dataset from images of PAD devices (Figure 64) must be created (a certain amount of source data). On this dataset, the detection algorithm will learn to process requests. To do this, it is necessary to determine the position of the entire PAD, the square sector of the reference value and each reaction zone on each image.

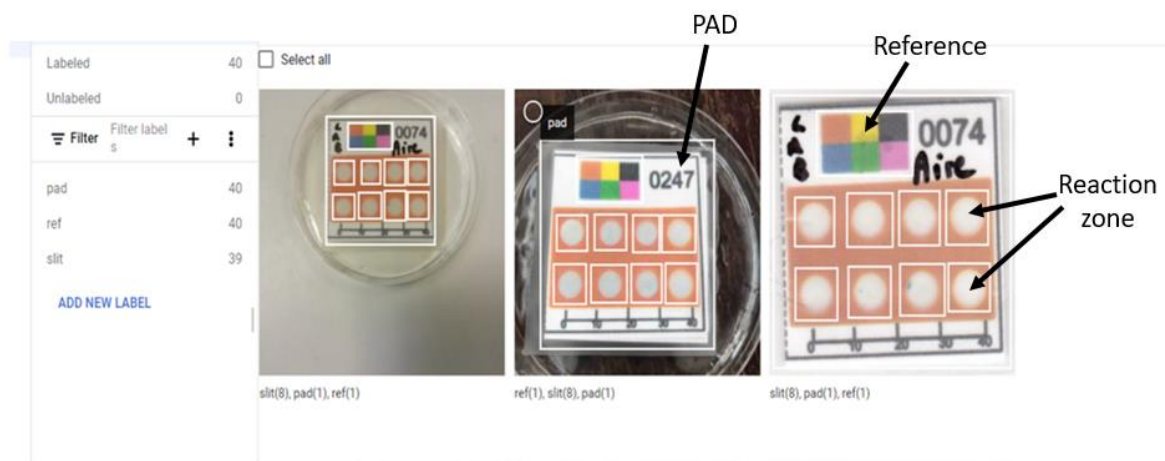


Figure 64. Example of PAD devices images from the dataset

The dataset includes about 50 photos of the PADs in various positions and at various angles. Usually more data is required, but this is enough to detect devices on a neutral background. Then, based on the sample, a model is created with the *tflite* file extension using Google Cloud platform, which can then be used on mobile devices for detection. When using this file, an android application project was developed, an example of which is shown in Figure 65 (this model is used for

Raspberry Pi software). This figure shows that the app detects PAD, reference square and all reaction zones.



Figure 65. Screenshot of object detection application showing detection result (PAD, reference square and reaction zones).

Thus, this model can be used by the android application for fast analysis of PAD devices, Raspberry Pi for automatic analysis, as well as for the analysis of any other PAD with a similar form.

### 3.8.5 Software overview

This section provides an overview of a complex Raspberry Pi software system designed to automate a complex procedure for quantifying the concentration of

carbonate in water samples using PADs. The main functionality of the system includes image capture, colour analysis, data processing and hardware configuration, which provides an effective and accurate solution for assessing the concentration of carbonates. Chart flow diagram of the system operation is shown in Figure 66.

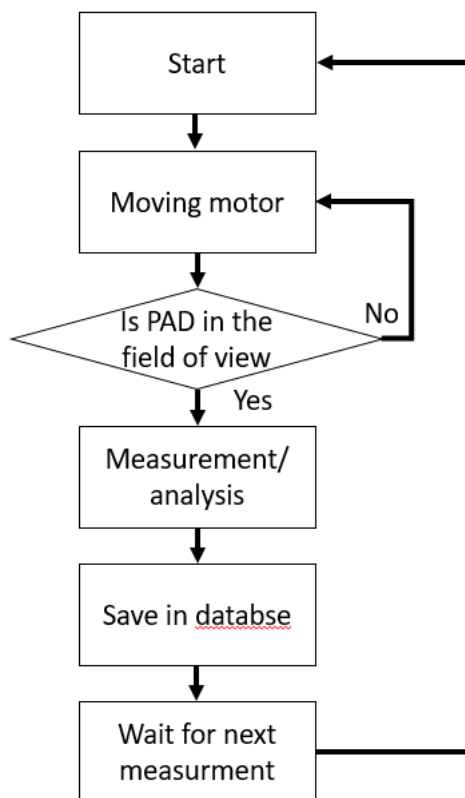


Figure 66. Chart flow diagram of the system operation.

The system uses the capabilities of the OpenCV library (cv2) to obtain high-resolution images of paper devices decorated with reaction spots [133]. Subsequently, the images are subjected to processing procedures, including the detection of specific areas in which a chemical reaction of colour change occurs.

After successful detection of reaction spots, the system uses the NumPy (np) library to perform complex analysis of colour variations [134]. The software carefully compares the colour characteristics before and after chemical reactions. The degree of colour change serves as an empirical marker of the presence and concentration of carbonates in the water sample.

Using the established correlations between colour changes and carbonate concentration levels, the system determines the quantitative concentration of carbonates in a water sample. This process involves converting colour data into a concentration indicator.

The system easily interacts with peripheral components, which is facilitated by libraries such as board library and adafruit\_motorkit[135]. These integral components, including motorized mechanisms to optimise PADs placement, ensure precise alignment during image capture and analysis.

Using the capabilities of the thread library, the system manages parallel tasks. Dedicated streams are allocated to perform individual functions, including image acquisition, colour analysis, and mechanical system operation. Such a parallelized workflow significantly increases the efficiency of the system and responsiveness.

The system provides optimized user interaction using the argparse library [136]. This allows users to enter specific parameters and options through the command line interface, thereby increasing the adaptability of the system and customizable functions.

### **3.8.5.1 Operational process**

The operational process begins with the launch of the “image.py” script (provided in Appendix D). This script acts as the control centre, guiding the system through its successive phases. When executed, the script starts two separate threads, each of which serves an important purpose.

The Object Detection thread is responsible for detecting objects, in particular, for identifying paper devices with reaction spots. Using the techniques describe above, this stream carefully scans the field of view in search of distinctive features of paper-based devices.

The Motor Control thread is dedicated to motor control. It manages the motorized mechanism responsible for dipping the PADs and moving the paper-based devices within the camera's field of view. By precisely adjusting the positioning of the devices (Raspberry Pi moves the role until a PAD appears in the field of view of the camera), this thread optimizes the object detection process, ensuring thorough coverage and accuracy.

Upon achieving an optimal position, the system initiates a processing function. This function performs a colour change analysis on the reaction spots of the paper-based device. By analysing colour attributes, the software quantifies the extent of colour changes, correlating these changes to the concentration of carbonates in the water sample.

Once the colour analysis is complete, the system captures an image of the processed paper-based device. This image serves as visual evidence of the colour changes detected during the chemical reaction. Simultaneously, the analysis results, including calculated carbonate concentrations and timestamps, are documented.

The results of the analysis are systematically stored in an SQLite library. This database serves as a repository for historical and real-time data related to carbonate concentration measurements. The structured storage ensures data integrity and facilitates subsequent search and analysis.

After the analysis is completed and the data is saved, the system enters standby mode. This waiting period is set by the user to ensure a controlled repetition of the entire workflow. The waiting time can be adjusted depending on the desired frequency of analyses.

After that time interval, the process recommences. The object detection thread resumes scanning the environment for new paper-based devices, and the cycle repeats, enabling the system to perform periodic analyses and accumulate a comprehensive dataset.

### **3.8.5.2 Arguments**

The `image.py` script takes advantage of a range of command-line arguments to facilitate flexible and customized usage. Each argument serves a specific purpose, enabling users to tailor the behaviour of the software according to their needs and preferences.

#### 1. `--modeldir`:

- Specifies the directory containing the TensorFlow Lite (TFLite) model file required for object detection. Allows users to define the location of the TFLite model that defines the object detection capabilities of the system.
- Example Usage: `--modeldir /path/to/model/directory`

#### 2. `--graph`:

- Indicates the filename of the TFLite model to be used for object detection (if different from the default `detect.tflite`). Provides flexibility to choose a specific TFLite model for detection, enabling compatibility with various models.
- Example Usage: `--graph custom_model.tflite`

#### 3. `--labels`:

- Specifies the filename of the label map used to interpret the detection results (if different from the default `labelmap.txt`). Offers the capability to use label maps other than the default one for a diverse range of detection tasks.
- Example Usage: `--labels custom_labels.txt`

#### 4. --threshold:

- Sets the minimum confidence threshold for displaying detected objects during the analysis. Allows users to fine-tune the confidence level required for an object to be displayed as a detection result.
- Example Usage: --threshold 0.5

#### 5. --image:

- Specifies the filename of a single image on which object detection will be performed. Enables users to execute detection on a single image, aiding in quick analysis and testing.
- Example Usage: --image sample\_image.jpg

#### 6. --imagedir:

- Specifies the name of a directory containing multiple images for batch object detection. Facilitates bulk analysis by detecting objects across multiple images within the specified directory.
- Example Usage: --imagedir /path/to/image/directory

#### 7. --edgetpu:

- Activates the use of the Coral Edge TPU Accelerator to accelerate object detection. Enhances detection speed by leveraging specialized hardware acceleration, specifically the Coral Edge TPU.
- Example Usage: --edgetpu

#### 8. --sampling\_frequency:

- Specifies the frequency at which the system performs object detection and analysis in seconds. This parameter determines the time interval between successive analyses. This argument is optional. It allows to control the rate at which the system captures images, detects objects, and performs analysis.
- Example: --sampling\_frequency 300 (for a sampling frequency of 300 seconds, or every 5 minutes)

### 3.8.5.3 Software description

Main file is pad\_analysis.py (provided in Appendix C) and it starts with establishing a connection to an SQLite database file named "pads.db". The connect() function from the sqlite3 library is used for this purpose. If the database file does not exist, it will be created. The relevant part of the code is shown below:

```
conn = sqlite3.connect('pads.db')
```



```

cur = conn.cursor()
cur.execute("""CREATE TABLE IF NOT EXISTS pad(
    id INTEGER PRIMARY KEY,
    name TEXT,
    avrint INT,
    ref INT);
""")
conn.commit()

```

The cursor "cur" is used to execute SQL commands and interact with the SQLite database. Then code executes an SQL statement to create a table named "pad" if it doesn't already exist, which will store all information about analysis results.

Then object detection function is called:

```
TFcam.padfinder(last_row[0])
```

This is code from Appendix B. It is responsible for finding PADs and moving motors simultaneously.

```

def padfinder(pic_id):
    global stop_threads
    global picid
    picid = pic_id
    stop_threads = False
    t1 = Thread(target=objectdetection)
    t2 = Thread(target=motormove)
    t1.start()
    t2.start()
    while True:
        #print(stop_threads)
        if stop_threads:
            t1.join()
            t2.join()
            break

```

Thread t1 (target=objectdetection) analysing video stream. Thread t2 (target=motormove) run motors to move PAD roll.

```

def __init__(self,resolution=(1280,720),framerate=30):
    self.stream = cv2.VideoCapture(0)
    ret = self.stream.set(cv2.CAP_PROP_FOURCC,
        cv2.VideoWriter_fourcc(*'MJPG'))
    ret = self.stream.set(3,resolution[0])
    ret = self.stream.set(4,resolution[1])

```

This initializes a video capture object using OpenCV (cv2) for accessing a camera with resolution 1280, 720 and framerate 30. The 0 passed as an argument indicates the default camera (usually the first camera). The third line sets the codec format to

MJPEG ('MJPG'). cv2.CAP\_PROP\_FOURCC is a property related to the codec format. The fourth line sets the width of the captured frames (the resolution's width). The fifth line sets the height of the captured frames (the resolution's height).

The following code stops executing object detection function if a PAD is detected

```
if take_picture:
    cv2.imwrite('images/img' + str(picid) + '.jpg', frame)
    stop_threads = True
    cv2.destroyAllWindows()
    videostream.stop()
    break
```

Next, the image analysis stage begins by calling function analysis.

```
detected_objects, slit_list, ref= analysis(image, labels, interpreter)
```

The following code calculate average blue intensity of reference square. All pixels outside reference square are ignored using a threshold based on maximum blue and minimum red intensity of reference square  $\pm 80$ . The threshold was obtained experimentally. Pixels outside the reference square are set zero to facilitate visualising the processed image. Variables minred is a threshold for red channel, maxblue for blue channel. Variables xmin, xmax, ymin, ymax are coordinates of detected reference square. Variable ref\_all is a total sum of all pixels, ref\_num its total number:

```
if object_name == 'ref' :
    minred = 255
    maxblue = 1
    ref_all = 0
    ref_num = 1
    for m in range (ymax-ymin):
        for n in range (xmax-xmin):
            if image[m+ymin,n+xmin,2] < minred:
                minred = image[m+ymin,n+xmin,2]
            if image[m+ymin,n+xmin,0] > maxblue:
                maxblue = image[m+ymin,n+xmin,0]
    for m in range (ymax-ymin):
        for n in range (xmax-xmin):
            if image[m+ymin,n+xmin,0]<maxblue-90 or
            image[m+ymin,n+xmin,2]>minred+90:
                image[m+ymin,n+xmin] = (0, 0, 0)
            else:
                ref_all += image[m+ymin,n+xmin,2]
                ref_num += 1
    ref_avr = ref_all/ref_num
```

This code calculates average intensity of reaction area. All pixels outside the reaction zone circle are ignored using a threshold based on the colour of the reaction zone ( $\pm 20$  in the code below). The threshold was obtained experimentally. Pixels outside the reaction zone are set zero to facilitate visualising the processed image. Variable `image_ref` is a middle pixel red channel threshold, which used to remove background. Diagram is shown in Figure 67 Variables `xmin`, `xmax`, `ymin`, `ymax` are coordinates of detected reference square. Variable `slit_all` is a total sum of all pixels, `slit_num` its total number:

```

if object_name == 'reactionzone' :
    slit_all = 0
    slit_num = 0
    image_ref = image[ymin+int((ymax-ymin)/2),xmin+int((xmax-xmin)/2)]
    for m in range (ymax-ymin):
        for n in range (xmax-xmin):
            if image[m+ymin,n+xmin,0]>image_ref[0]+20 or
            image[m+ymin,n+xmin,0]<image_ref[0]-20:
                image[m+ymin,n+xmin] = (0, 0, 0)
            else:
                slit_all += image[m+ymin,n+xmin,1]
                slit_num += 1

slit_list.append([ymin,xmin,slit_all/slit_num, label])

```

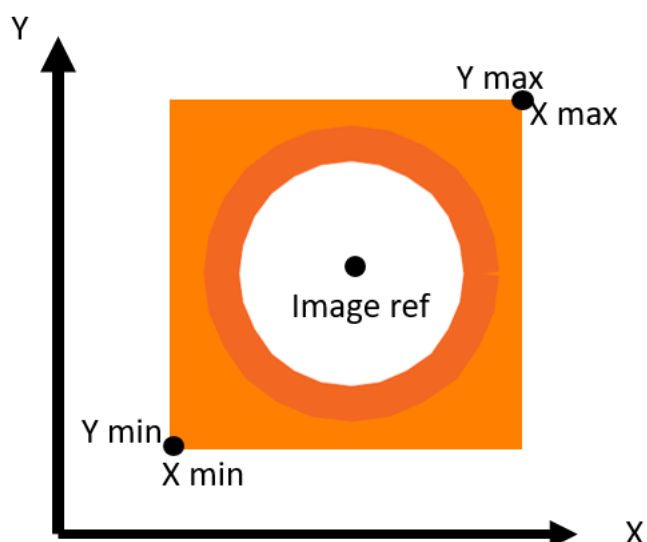


Figure 67. Reaction zone detection diagram

After all the results of the analysis are stored in the database.

```

sqllex = "INSERT INTO pad(id, name, avrint, ref) VALUES(NULL, '%s', '%s', '%s')"
%(image, re, str(ref))
    cur.execute(sqllex)
    conn.commit()

```

### 3.8.5.4 Sensor software

Data from the spectral sensor is read either via UART or via the I2C interface (depending on the sensor connection). It is also necessary that the lighting does not change or also use reference values (i.e. it is assumed the LEDs are providing an even illumination not changing in time) . The code for communication with the sensor and obtaining the values of 6 channels is presented below:

```

import time
import board
from adafruit_as726x import AS726x_UART

uart = board.UART()
sensor = AS726x_UART(uart)
sensor.conversion_mode = sensor.MODE_2
print("\n")
print("V: " + sensor.violet * "=")
print("B: " + sensor.blue * "=")
print("G: " + sensor.green * "=")
print("Y: " + sensor.yellow * "=")
print("O: " + sensor.orange * "=")
print("R: " + sensor.red * "=")

```

### 3.8.5.5 User interface

During the discussion of the interface development, it was decided to conditionally divide this development into two parts. The first part is the development of the interface for the testing of the system. The main requirement for this stage is the speed and ease of development of the interface. For the system testing stage, it is possible to minimise the usability of the user interface.

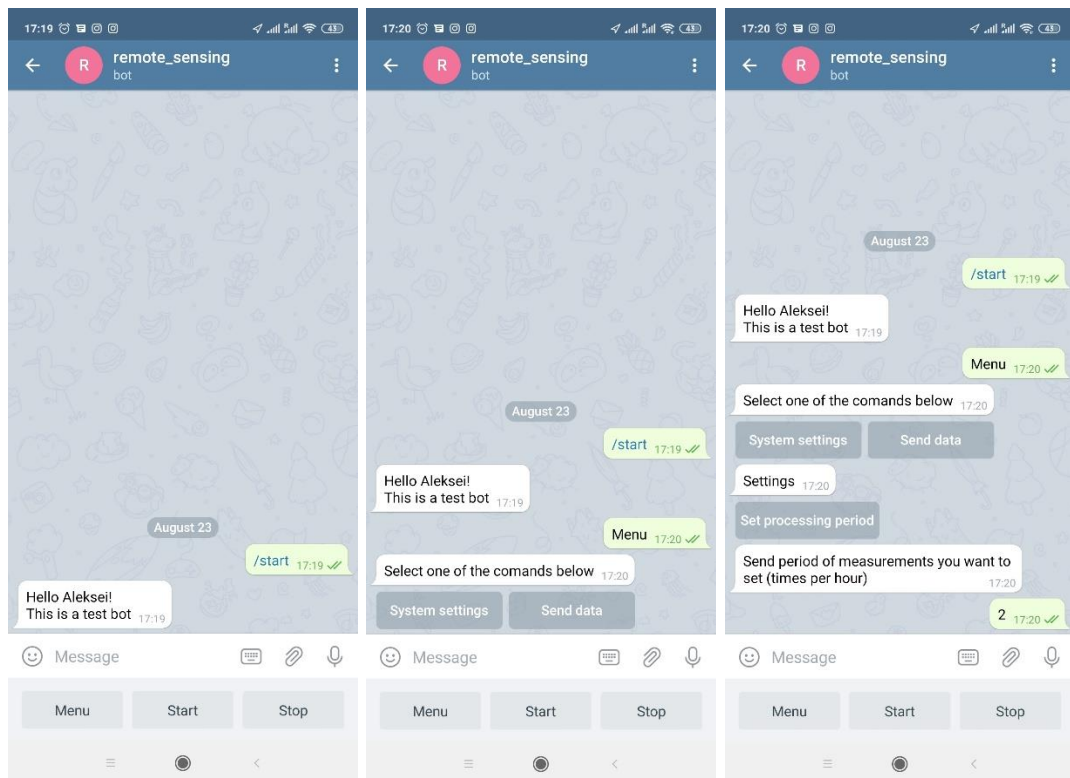
The second stage is the development of an interface that will be as convenient and understandable as possible for anyone

Taking into account all the requirements for the first stage it was decided to use the Telegram messenger to implement a user interface for managing the system. Telegram will allow management of all the components of the system, collect data, display data in the form of tables and graphs.

In order to manage the Telegram bot, a special Telegram API library was used. This library is an HTTP interface for working with bots in Telegram.

Figure 68 shows an example of using a telegram bot to manage the system. The interface is intuitive, but since the bot does not show the current state of the system. Thus, errors may occur when the system is used by several users. This problem can be solved by drawing up an action plan, following which each user must to check the state of the system before use. However, this problem is unlikely to occur during testing, since at this stage the system will not be used by more than one user at a time.

Another significant limitation is that the system must have Internet access during operation. This will not be a problem at the testing stage, but it will be a significant problem for the device running in a cave (where there will most likely be no Internet connection).



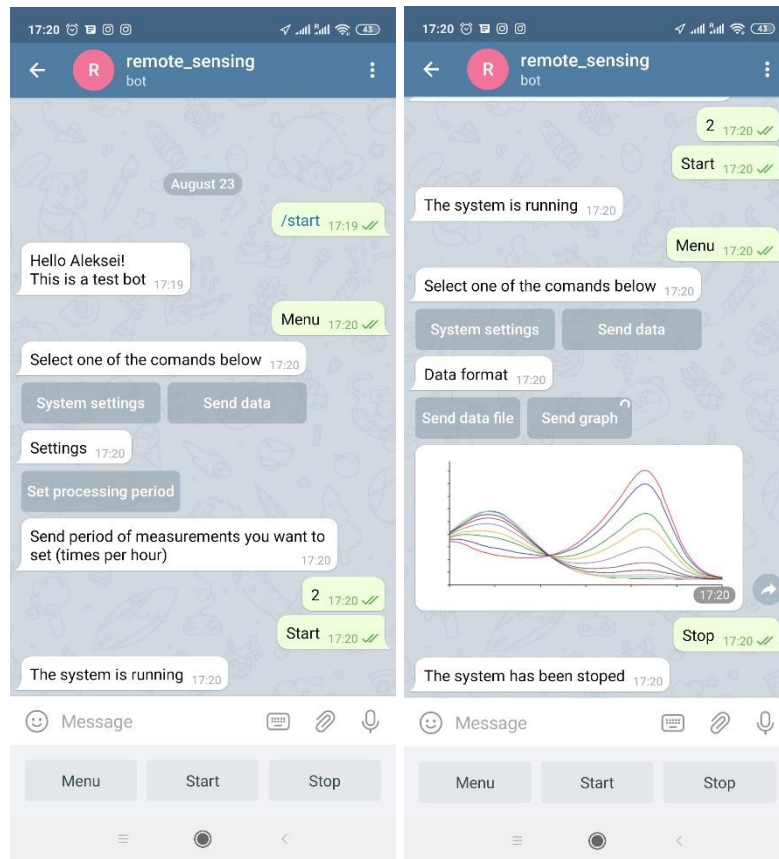


Figure 68. An example of using a Telegram bot to manage the system (screenshots from the smartphone)

Code below shows the libraries that are required for the script to work. the first Library is directly Telegram API. It is used to control the bot. The conf file contains a unique bot token that is not required for connection. Lines 4, 5 and 6 are required to run the program on the server. At this stage, the program was launched on the server for debugging. In the future, the program will work on Raspberry Pi. The code lines below show imported library telebot and token conf:

```
import telebot
import conf
```

Following code illustrates the initialization of reply keyboard buttons and a welcome message that will contain basic information about the bot.

```
from telebot import types

bot = telebot.TeleBot(conf.TOKEN)

@bot.message_handler(commands=['start'])
def welcome(message):

    markup = types.ReplyKeyboardMarkup(resize_keyboard=True)
    item1 = types.KeyboardButton("Menu")
    item2 = types.KeyboardButton("Start")
    item3 = types.KeyboardButton("Stop")
```

```
markup.add(item1, item2, item3)
```

```
bot.send_message(message.chat.id, "Hello!\nThis is a test  
bot".format(message.from_user, bot.get_me()), reply_markup=markup)
```

The code below describes how the bot responds to reply keyboard buttons clicks.

```
@bot.message_handler(content_types=['text'])  
def resp(message):  
    if message.chat.type == 'private':  
        if message.text == "Menu":  
  
            markup = types.InlineKeyboardMarkup(row_width=2)  
            item1 = types.InlineKeyboardButton("System settings",  
callback_data='settings')  
            item2 = types.InlineKeyboardButton("Send data", callback_data='data')  
  
            markup.add(item1, item2)  
  
            bot.send_message(message.chat.id, "Select one of the comands  
below".format(message.from_user, bot.get_me()), reply_markup=markup)  
            elif message.text == "Start":  
                bot.send_message(message.chat.id, "The system is running")  
            elif message.text == "Stop":  
                bot.send_message(message.chat.id, "The system has been stoped")
```

The code below describes how the bot responds to inline keyboard buttons clicks.

```
@bot.callback_query_handler(func=lambda call: True)  
def callback_inline(call):  
    try:  
        if call.message:  
            if call.data == 'settings':  
                markup = types.InlineKeyboardMarkup(row_width=2)  
                item1 = types.InlineKeyboardButton("Set processing period",  
callback_data='period')  
  
                markup.add(item1)  
  
                bot.send_message(call.message.chat.id,  
"Settings".format(call.message.from_user, bot.get_me()), reply_markup=markup)  
                elif call.data == 'data':  
                    markup = types.InlineKeyboardMarkup(row_width=2)  
                    item1 = types.InlineKeyboardButton("Send data file",  
callback_data='file')  
                    item2 = types.InlineKeyboardButton("Send graph",  
callback_data='graph')  
  
                    markup.add(item1, item2)  
  
                    bot.send_message(call.message.chat.id, "Data  
format".format(call.message.from_user, bot.get_me()), reply_markup=markup)  
  
                    elif call.data == 'period':
```

```
        bot.send_message(call.message.chat.id, "Send period of
measurements you want to set (times per hour)")

elif call.data == 'file':
    bot.send_message(call.message.chat.id, "file is not found")

elif call.data == 'graph':
    sti = open('BCG.png', 'rb')
    bot.send_photo(call.message.chat.id, sti)
```



## 4 Sensing Evaluation

### 4.1 Initial experimental validation of carbonate PAD

To validate the PAD design, the series of test has been conducted by a professional chemist on the ingestion of carbonates in water at the Department of Chemistry[101, 137]. A photo of the PAD devices used in these tests is shown in Figure 69.

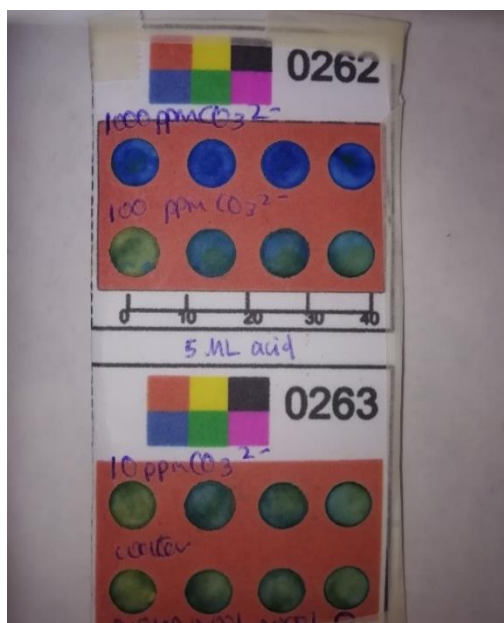


Figure 69. Photo of Carbonates detection PAD device (made by Samantha Richardson)

Figure 70 shows carbonate concentration obtained without using same algorithm described in section 3.3.1 and any software developed within this project. This graph shows how reaction zone colour intensity depends on carbonates concentration. The different coloured bars represent HCl concentration, as stated on the graph.

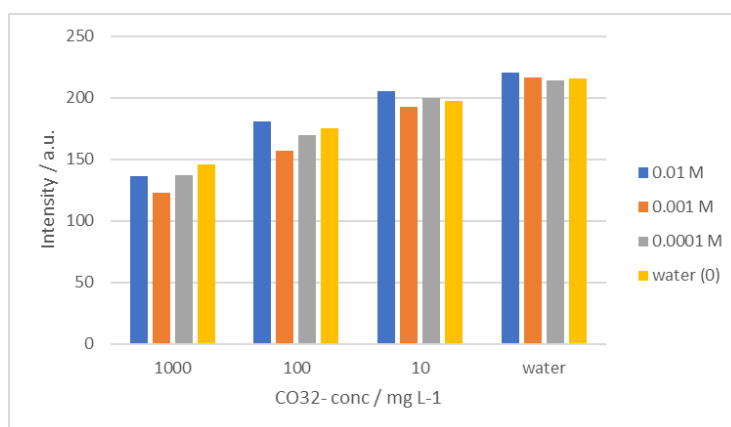


Figure 70. Results of the experiment (Based on a data obtained from Samantha Richardson).

The experiment proved that the PAD device can be used to determine carbonates in water, but the main limitation is that the measurement range is small (0 – 300 mg/L). But this problem can be solved by increasing the number of measurement areas with different concentrations of HCl.

## 4.2 Model-based comparison of camera and spectra sensor-based colour measurement

A camera is the most affordable tool for optical analysis.. The spectral response of a typical camera is shown in Figure 71.

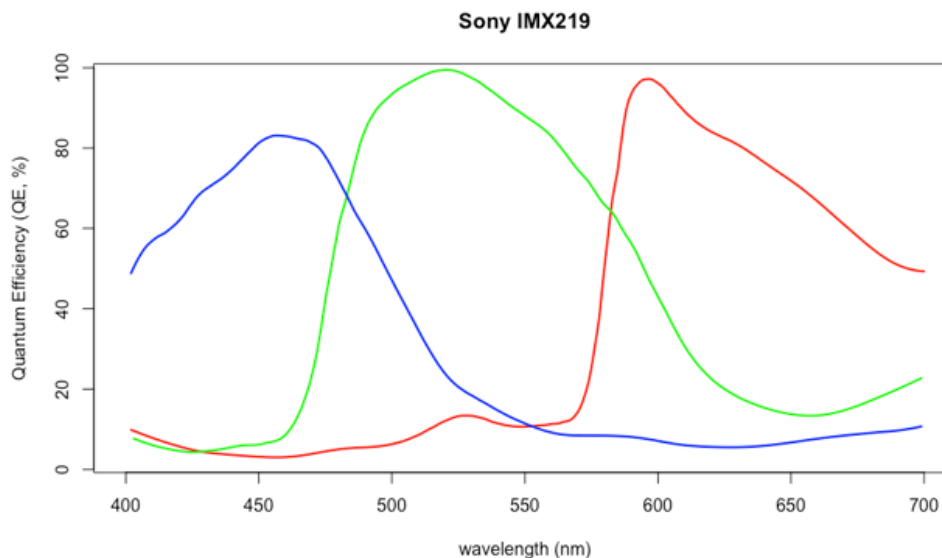


Figure 71. Raspberry Pi Camera spectral response curves[138]

As can be seen in Figure 71, the spectral response curves are not uniform in the wavelength band and overlap each other significantly. This adds to the error and subsequently reduces the accuracy of the measurements. Signal to noise ratio for Raspberry Pi camera (IMX219) is not published, but for similar module (IMX179) it is 34dB[138]

As mentioned in chapter 3.3 low cost spectral sensors are a potential good alternative to cameras. For example, the AS7262 spectral sensor has six sensing elements, the spectral response curves of which are distributed throughout the visible light band (Figure 72) [122].

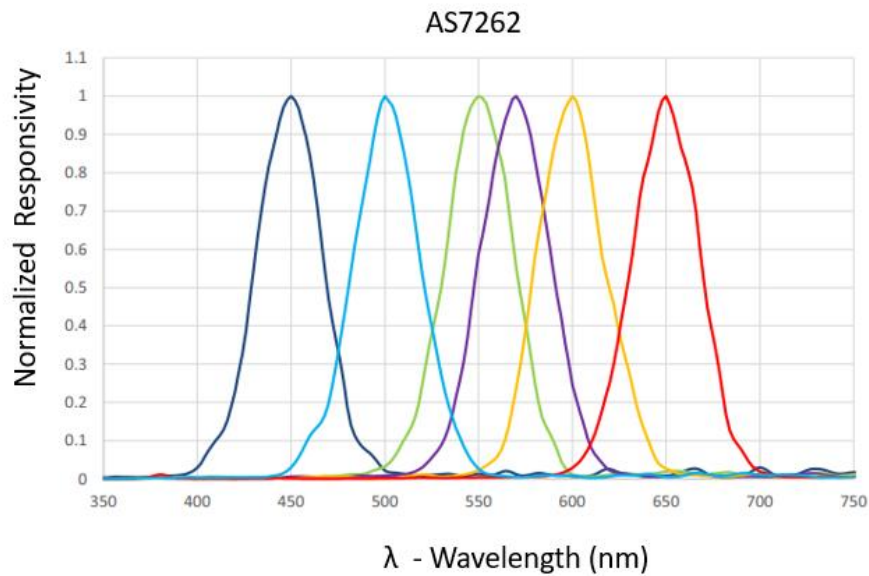


Figure 72. AS7262 spectral sensor spectral response curves

The six-channel sensors allow to build a more complete light absorption chart (6 points on the graph versus 3 on the camera). Their small size is also advantageous. The accuracy of each channel is  $\pm 12\%$  [122].

#### 4.2.1 MATLAB simulation of optical sensing process

To theoretically check the operation and evaluate the relative performance of the camera and spectral sensors, a mathematical model was built. In the process of optical analysis, 3 objects can be distinguished: a light source, an object and a detector. Figure 73 represents this process.

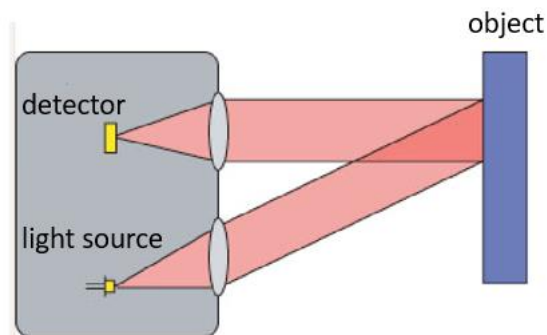


Figure 73. Optical analysis diagram.

The result of the analysis will depend on three parameters: the spectral emission of the LED, the reflection spectrum of the BCG and the spectral sensitivity of the detector. Since the value of all variables varies from 0 to 1, we can assume that these values are coefficients proportional to the output value. Thus, the output signal will be equal to the integral of the product of these three values:

$$Sens_{output} = \int_{350nm}^{750nm} E_{LED}(\lambda) R_{BCG}(\lambda) Resp(\lambda) d\lambda \quad (20)$$

Where:

$E_{LED}$  is relative spectral emission of LED,  $R_{BCG}$  is a diffuse reflectance spectra of bromocresol green and  $Resp$  is spectral responsivity.

Reflectance spectra of bromocresol green is approximated as:

$$R_{BCG} = 1 - A_{BCG} \quad (21)$$

Where  $A_{BCG}$  is its absorption spectra.

BCG absorption spectra graphs are shown in Figure 74. The spectra were only available in graphical form (see Figure 25), so to provide numerical data for the model all graphs were digitized and plotted manually (based on Figure 25).

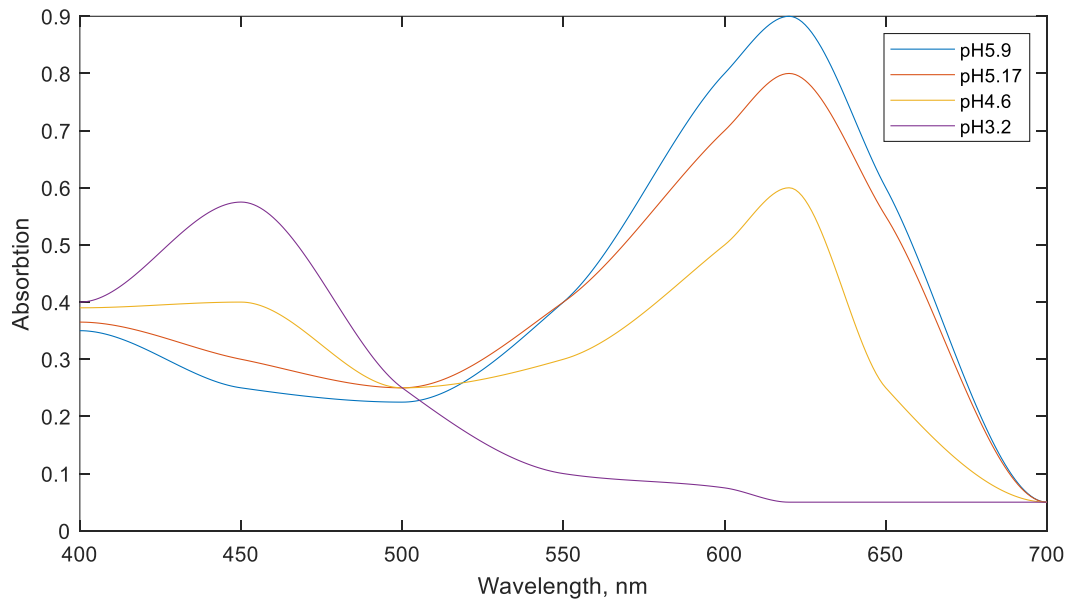


Figure 74. BCG absorption spectra ( $A_{BCG}$ ) (recreated from Figure 25).

In order to make measurements, a light source with the widest possible spectrum is required. A white LED (ams-OSRAM Durius S 5 Horticulture) selected for this purpose [139]. Figure 75 shows a graph of the relative spectral emission of the LED, which was constructed by the same digitization method.

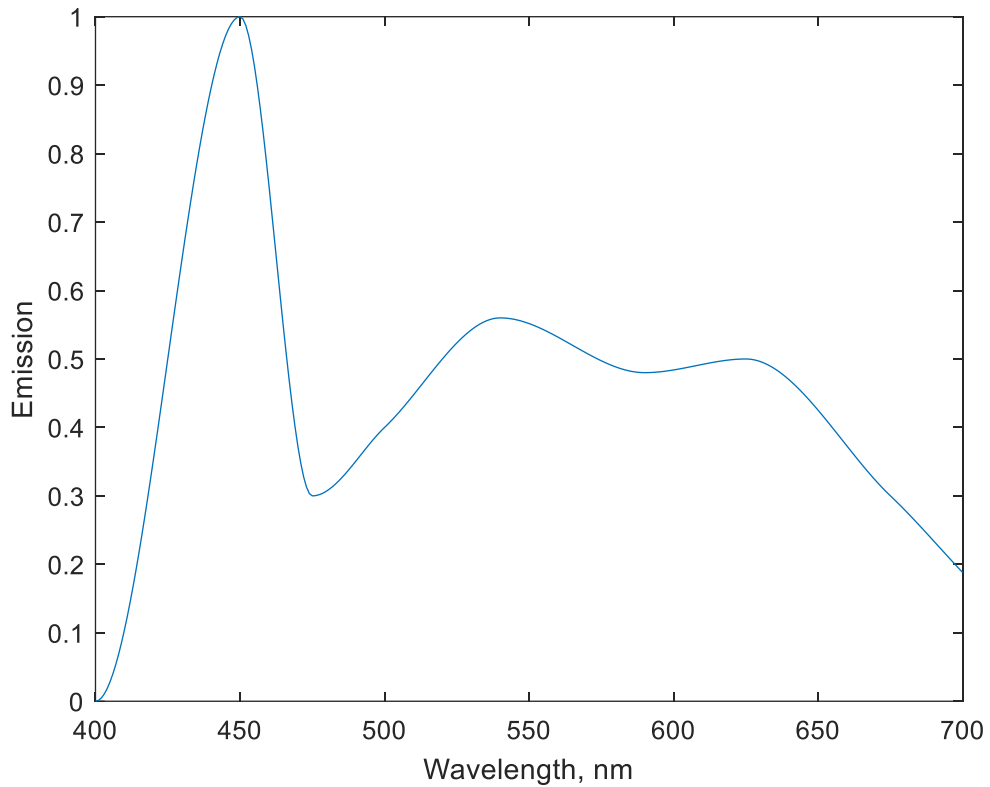


Figure 75. Relative spectral emission ( $E_{LED}(\lambda)$ ) of the LED[139]

The graphs of spectral responsivity of the 6-channel sensor is shown in Figure 76. This graph was obtained using data points from Figure 72 exported to MATLAB and interpolated using polynomial interpolation(the graph has some inaccuracies, since the data is obtained by superimposing the graph on a grid).

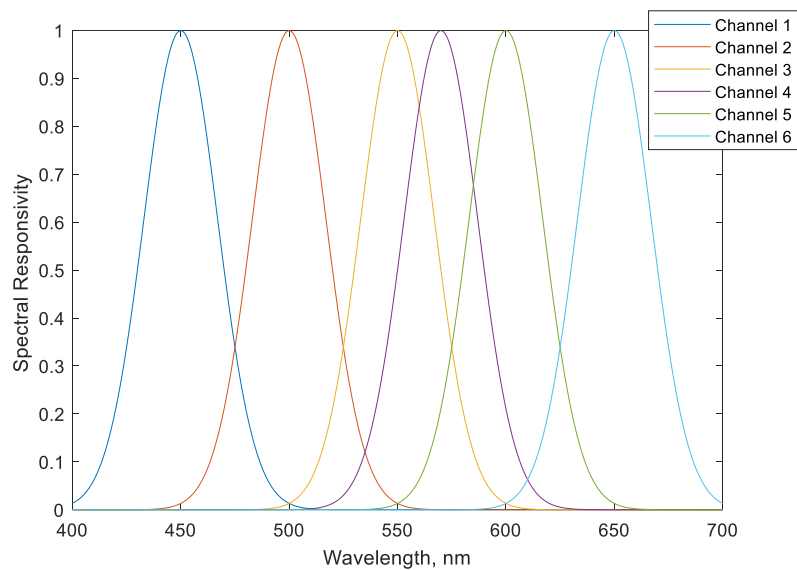


Figure 76. Spectral responsivity of the multichannel sensor ( $Resp$ ) [122].

Figure 77 shows the graphs of the multiplication of these three functions ( $A_{BCG}$  - Figure 74,  $E_{LED}$  - Figure 75,  $Resp$  - Figure 76). Graphs are arranged in descending order of pH.

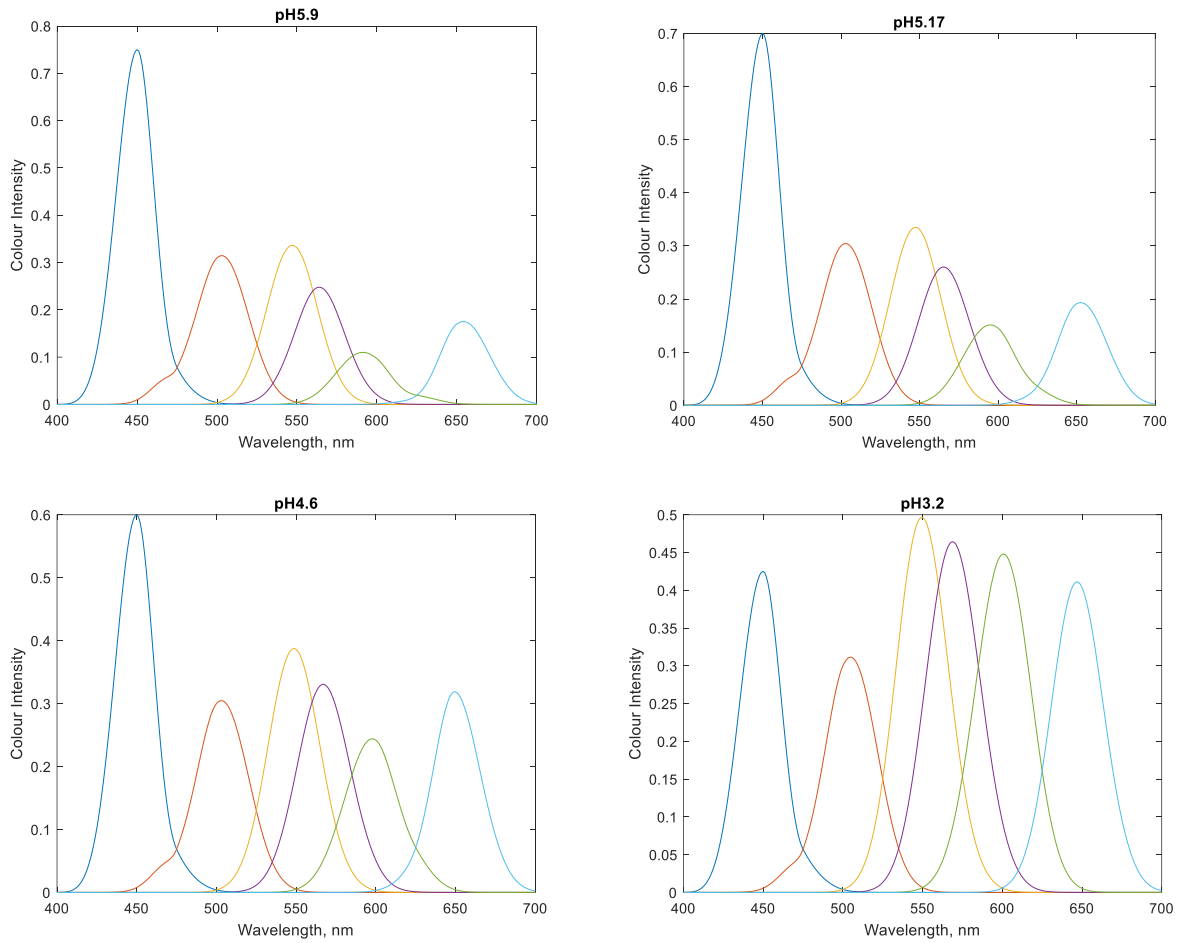


Figure 77.the BCG reflectance for different values of pH.

After that, it is necessary to integrate the graphs to obtain relative values at the sensor output. The calculated data are presented in Table 3.

Table 3. Calculated integrated output of each channel (arbitrary units)

	Channel 1	Channel 2	Channel 3	Channel 4	Channel 5	Channel 6
pH5.9	22.82	13.42	13.31	9.8	4.74	6.67
pH5.17	21.42	12.97	13.47	10.67	6.57	7.68
pH4.6	18.75	12.93	15.71	13.79	10.60	12.08
pH3.2	14.03	13.06	20.27	19.84	19.37	16.72

### 4.2.2 Paper optical properties

Ideally, the paper is supposed to be perfectly white, but in reality its parameters are not perfect and will add some error in measurements. In general, there are three properties of paper that will affect the measurement results. These parameters include whiteness or colour, gloss (reflectivity), transparency or light transmission [140].

In the paper industry, when considering the optical properties of paper, the concepts of light transmission and transparency are distinguished [140]. The ability of a body to transmit light is called light transmittance and is expressed by the coefficient of light transmittance. A particular case of light transmission is transparency - light transmission without scattering. An example of a transparent material is glass. For paper, light transmission is more characteristic of light scattering due to its multiple refraction in the dispersive-porous structure of the paper. Thus, this parameter determines how clearly the objects behind the paper are visible, and these objects, in turn, will affect the colour of the measured PAD.

Whiteness is the property of paper to reflect most of the light incident on it scattered and evenly over the entire visible part of the spectrum. Due to the rough surface, the paper scatters the reflected light in different directions. And when reflected, the spectral composition of the light does not change much via the visible part of the spectrum. Thus, when illuminated by natural sunlight, the reflected light is taken as achromatic.

Quantitatively, whiteness is expressed by the reflection coefficient, that is the ratio of the amount of reflected light to the incident one. The difference in the reflection coefficients in different areas of the spectrum indicates a deviation from whiteness. A colour shade occurs if there is a certain deviation [141].

The most common off-whiteness in printed papers is yellowness, which appears as reduced reflection in the blue region of the spectrum.

. This zone shows the greatest differences in the reflection curves of different types of paper, and also the greatest changes occur during fading [142].

Gloss is the third optical characteristic of paper. It shows the ratio between the intensity of the light reflected specularly from the surface and the light scattered in all directions (diffuse reflection). This parameter affects the amount of light that the sensor will capture.

Thus, in order to minimize the influence of the paper on the final measurement result, it is required to use similar paper and lighting condition. Also, if the illumination of the PAD devices is from a stationary light source, then the error added by the paper will be constant.

### 4.2.3 Comparison of camera and spectral sensor for pH measurement accuracy.

In order to understand the accuracy of measurements using various devices and techniques, a model that simulates the measurement process and artificially adds an error to the input data was built (see Appendix J). The results of Chapter 4.2.1 are used as input data. This program plots the dependence of the sensor/camera output signal on the pH level of the green bromine. Then it artificially adds a random error and calculates the output value for the sensor/camera taking into account the error. Next, the potential measurement results with and without error are compared, and based on these results, the theoretical measurement error for the sensor and camera is calculated.

Following steps describes the calculation procedure:

1. The input data are interpolated using a shape-preserving piecewise cubic interpolation. It was experimentally established that this method provides the greatest accuracy compared to other methods investigated in MATLAB.

```
dat1 = interp1 (pH,sens_out(:,1),ppH, 'PCHIP');
dat2 = interp1 (pH,sens_out(:,2),ppH, 'PCHIP');
dat3 = interp1 (pH,sens_out(:,3),ppH, 'PCHIP');
dat4 = interp1 (pH,sens_out(:,4),ppH, 'PCHIP');
dat5 = interp1 (pH,sens_out(:,5),ppH, 'PCHIP');
dat6 = interp1 (pH,sens_out(:,6),ppH, 'PCHIP');

camera_blue = (pH,camera(:,1),ppH, 'PCHIP');
camera_green = (pH_v,camera(:,2),ppH, 'PCHIP');
camera_red = (pH,camera(:,3),ppH, 'PCHIP');
```

These data are converted into graphs of the dependence of the sensor/camera output values on the sample pH. Figure 78 show how the values at the output of the six AS7262 sensors and camera RGB pixels depend on the pH value. These graphs are not linear, which means that when the acidity changes, the output values change at different speeds. If the final pH value is calculated using the average of all values (six for the sensor, three for the camera), then the values of the sensors, where the function grows relatively slowly, will add a sufficiently large error. Therefore, weight coefficients must be used to quantify the significance of the measurement results and thereby minimize the measurement error. In order to directly link the coefficients to the rate of rise or fall of the function, the derivatives of these functions at the points of the obtained values can be used as the coefficients.



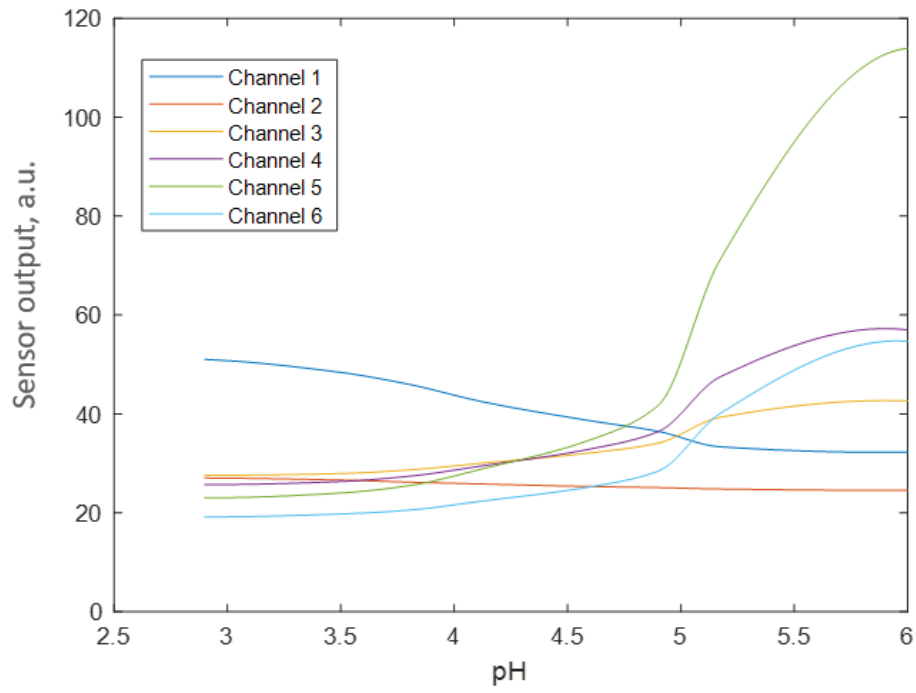


Figure 78. Output values of the sensors vs pH

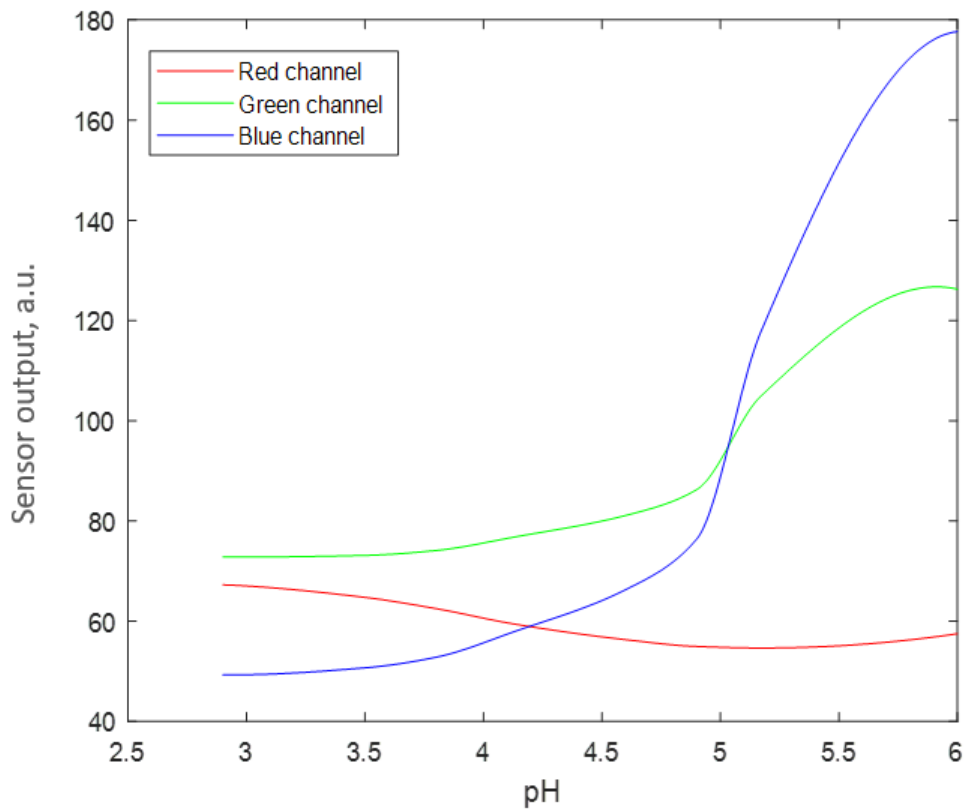


Figure 79. Output values of the camera vs pH.

2. The program generates a random value of pH in the range of values from 3.2 to 5.5. The range was narrowed to avoid errors when interpolating values close to the boundaries of this range. From the graphs in Figure 78 and Figure 79, it is necessary to find the values of the sensors that correspond to the generated pH value. The following code shows data points interpolation for spectral sensor and camera:

```
for i = 1:10000
    pH_val = 2.2*rand+3.25;
    %pH_val = [4.12555065153409];
    sens_1 = interp1 (ppH,dat1,pH_val, 'PCHIP');
    sens_2 = interp1 (ppH,dat2,pH_val, 'PCHIP');
    sens_3 = interp1 (ppH,dat3,pH_val, 'PCHIP');
    sens_4 = interp1 (ppH,dat4,pH_val, 'PCHIP');
    sens_5 = interp1 (ppH,dat5,pH_val, 'PCHIP');
    sens_6 = interp1 (ppH,dat6,pH_val, 'PCHIP');
    camera_b = interp1 (ppH,camera_blue,pH_val, 'PCHIP');
    camera_g = interp1 (ppH,camera_green,pH_val, 'PCHIP');
    camera_r = interp1 (ppH,camera_red,pH_val, 'PCHIP');
```

3. Following code shows the part of the code in which the error is stimulated, which is in the range of 2% of the sensors value.

```
sens_1_real = sens_1 + sens_1*(0.5 - rand)*0.02;
sens_2_real = sens_2 + sens_2*(0.5 - rand)*0.02;
sens_3_real = sens_3 + sens_3*(0.5 - rand)*0.02;
sens_4_real = sens_4 + sens_4*(0.5 - rand)*0.02;
sens_5_real = sens_5 + sens_5*(0.5 - rand)*0.02;
sens_6_real = sens_6 + sens_6*(0.5 - rand)*0.02;
camera_b_real = camera_b + camera_b*(0.5 - rand)*0.02;
camera_g_real = camera_g + camera_g*(0.5 - rand)*0.02;
camera_r_real = camera_r + camera_r*(0.5 - rand)*0.02;
```

4. Then again, the pH value is calculated for the obtained sensor values.

```
pH_sens1 = interp1 (dat1,ppH,sens_1_real, 'PCHIP');
pH_sens2 = interp1 (dat2,ppH,sens_2_real, 'PCHIP');
pH_sens3 = interp1 (dat3,ppH,sens_3_real, 'PCHIP');
pH_sens4 = interp1 (dat4,ppH,sens_4_real, 'PCHIP');
pH_sens5 = interp1 (dat5,ppH,sens_5_real, 'PCHIP');
pH_sens6 = interp1 (dat6,ppH,sens_6_real, 'PCHIP');
pH_camera_b = interp1 (camera_blue,ppH,camera_b_real, 'PCHIP');
pH_camera_g = interp1 (camera_green,ppH,camera_g_real, 'PCHIP');
pH_camera_r = interp1 (camera_red,ppH,camera_r_real, 'PCHIP');
```

5. The simplest and most obvious way to calculate the acidity value is the arithmetic mean method.

```
pH_av = (pH_sens1 + pH_sens2 + pH_sens3 + pH_sens4 + pH_sens5 + pH_sens6)/6;

if pH_val < 4.5
    pH_camera_av = (pH_camera_g + pH_camera_r)/2;
else
    pH_camera_av = (pH_camera_b + pH_camera_g + pH_camera_r)/3;
end
```

the graph of the blue camera sensor is not monotonic and split into two part (before pH=4.5 and after). Therefore, if the value of the blue sensor is below the pH value of 4.5, it is not taken into account in the calculation.

6. Following code shows the identification of the nearest pH values for finding weight coefficients at these points

```
[~, ind_1] = min(abs(dat1-sens_1_real));
[~, ind_2] = min(abs(dat2-sens_2_real));
[~, ind_3] = min(abs(dat3-sens_3_real));
[~, ind_4] = min(abs(dat4-sens_4_real));
[~, ind_5] = min(abs(dat5-sens_5_real));
[~, ind_6] = min(abs(dat6-sens_6_real));
[~, cam_1] = min(abs(camera_blue-camera_b_real));
[~, cam_2] = min(abs(camera_green-camera_g_real));
[~, cam_3] = min(abs(camera_red-camera_r_real));

[~, ind_pH_1] = min(abs(ppH-pH_sens1));
[~, ind_pH_2] = min(abs(ppH-pH_sens2));
[~, ind_pH_3] = min(abs(ppH-pH_sens3));
[~, ind_pH_4] = min(abs(ppH-pH_sens4));
[~, ind_pH_5] = min(abs(ppH-pH_sens5));
[~, ind_pH_6] = min(abs(ppH-pH_sens6));
[~, ind_pH_cam_1] = min(abs(ppH-pH_camera_b));
[~, ind_pH_cam_2] = min(abs(ppH-pH_camera_g));
[~, ind_pH_cam_3] = min(abs(ppH-pH_camera_r));
```

7. Calculating final pH using weights coefficients.

Then the formula for calculating the pH value:

$$pH = \frac{pH_1 * \left( \frac{\Delta sens1_{output}}{\Delta pH_1} \right) + \dots + pH_6 * \left( \frac{\Delta sens6_{output}}{\Delta pH_6} \right)}{\frac{\Delta sens1_{output}}{\Delta pH_1} + \dots + \left( \frac{\Delta sens6_{output}}{\Delta pH_6} \right)} \quad (22)$$

On average, the value obtained differs from randomly generated:

$$error = (\Delta pH_1 + \Delta pH_2 + \dots + \Delta pH_n)/n \quad (23)$$

Where  $\Delta pH$  – difference between obtained and given values, n is a number of measurements.

- for sensor using this formula for calculating the average error value - 0.7615%
- for camera using the same formula for calculating the average error value - 1.1706%
- for sensor using weight coefficients - 0.1147%
- for camera using weight coefficients - 0.2687%

Thus, since the average error for the camera is greater than for the spectral sensor, it can be concluded that a large number of sensors channels provides greater measurement accuracy, and the method of weighting factors will increase the accuracy. This implies it worth considering the spectral sensors as an alternative to the camera in the LOAR instrument, but practical test results need to be investigated (chapter 5.5).

### **4.3 Experiment to evaluate carbonate concentration with paper analytical device**

The aim of the experiment is to evaluate the use of Raspberry Pi camera in the LOAR instrument over a range of carbonate concentrations up to 300 mg per litre. This range was chosen based on the values of calcium carbonate concentration for Hull tap water, the value of which is close to the concentration of carbonates in water in caves. A range of PAD pH values from 4 to 5 was used to understand at what initial pH value bromocresol green will most effectively change its colour. It was expected that bromocresol green at pH 4.4 would give the highest measurement accuracy (was suggested by Samantha Richardson in private communication, as expected that PADs will be most efficient at this pH).

In this experiment, the Adafruit AD7262 board is connected to the Raspberry Pi (Raspberry Pi Zero was used in this experiment since good performance does not require here) and aligned to capture a light passed via the PAD reaction zone. The experimental setup used in this experiment is shown in Figure 80 and Figure 81. The setup consists of a microscope stand with LED backlighting (light is passed through the PAD device), Raspberry Pi, and optical Sensor AD7262 or camera mounted on the stand. The whole setup was covered in a black box to prevent provide constant and repeatable lighting conditions.

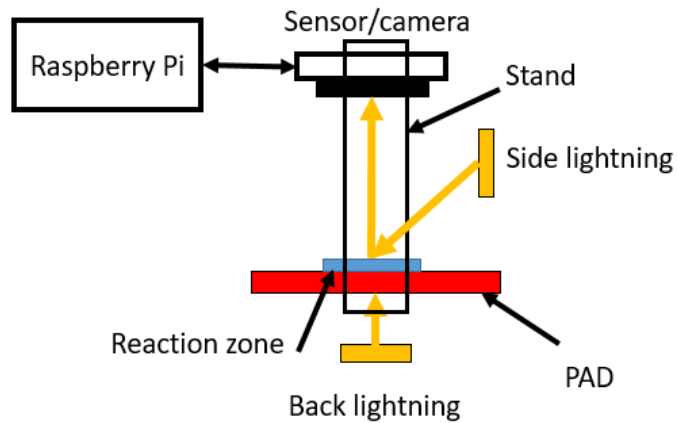


Figure 80. Experimental setup diagram

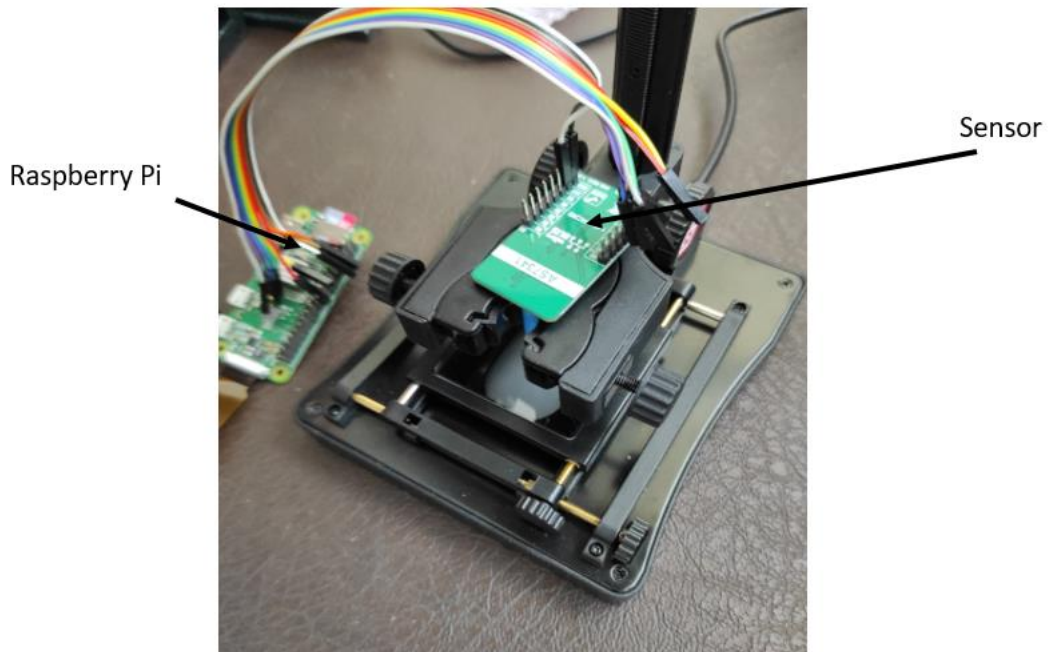


Figure 81. Experimental Setup

The experiment methodology is simple: PAD reaction zone is placed opposite the sensor in the transmission light mode. Next, raspberry sends a command to make a measurement, and the sensor returns the measurement result.

The PAD design is shown in Figure 82. The reaction zones have a diameter of 4mm.

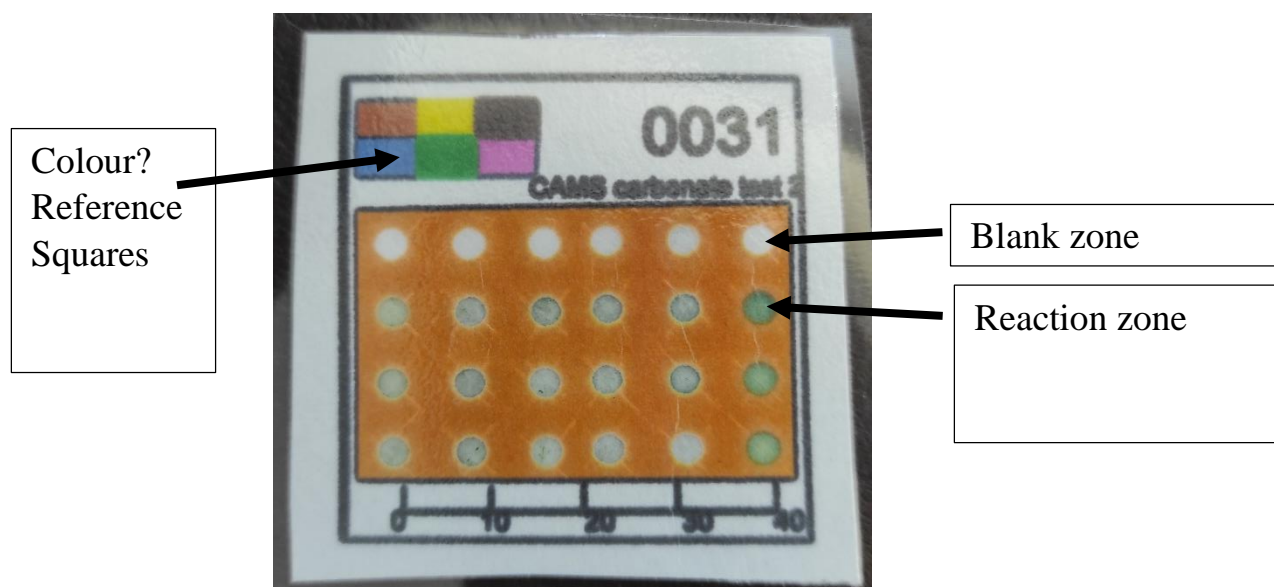


Figure 82. PAD image

PAD devices were prepared as described in chapter 4.2.4 (0.04 wt % BCG, in 0.1 M citrate buffer) using six different buffer pH values from 4 to 5 with step 0.2. PADs were dried at room temperature for 1-2 hours.

Four sample water solutions of different concentrations of carbonates were prepared (0, 100, 200, 300 mg per litre) using 0, 5, 10, 15 mg of calcium carbonate in 50 ml water, respectively.

Each PAD consists of six sets of different buffer pH values reaction zones. There are three PADs for each carbonate concentration value. Further, after measuring all the PAD, based on the results obtained, the average value and standard deviation are calculated for each concentration value. And then for each pH value, a graph of the dependence of colour intensity on the concentration of carbonates is plotted.

Three pads were immersed in each of these solutions for 15 seconds. The PADs were used within 2 days of preparation. Photos of each device were taken 15 minutes after immersion. Image analysis was performed using image processing software Image J (calculated average pixel intensity of reaction zones). To get normalized concentration values the difference between the average RGB pixel intensity of the PAD device and average pixel intensity of blank zone was divided by average intensity of the blue reference square.

The measurement results are shown in Figure 83.

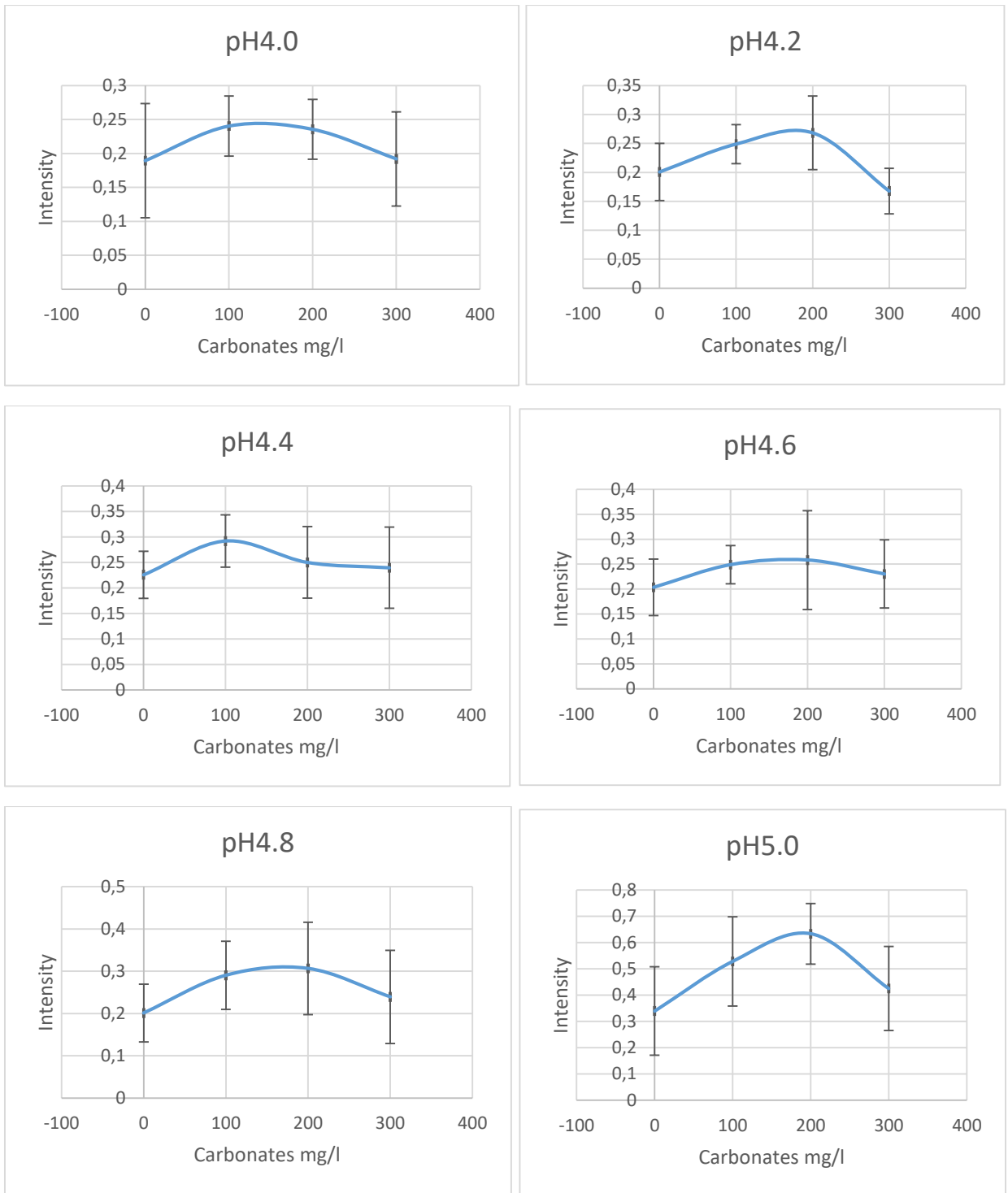


Figure 83. Coloure intensity measurement results for various buffer pH values  
 Figure 84 shows all results on the same axis to facilitate comparison.

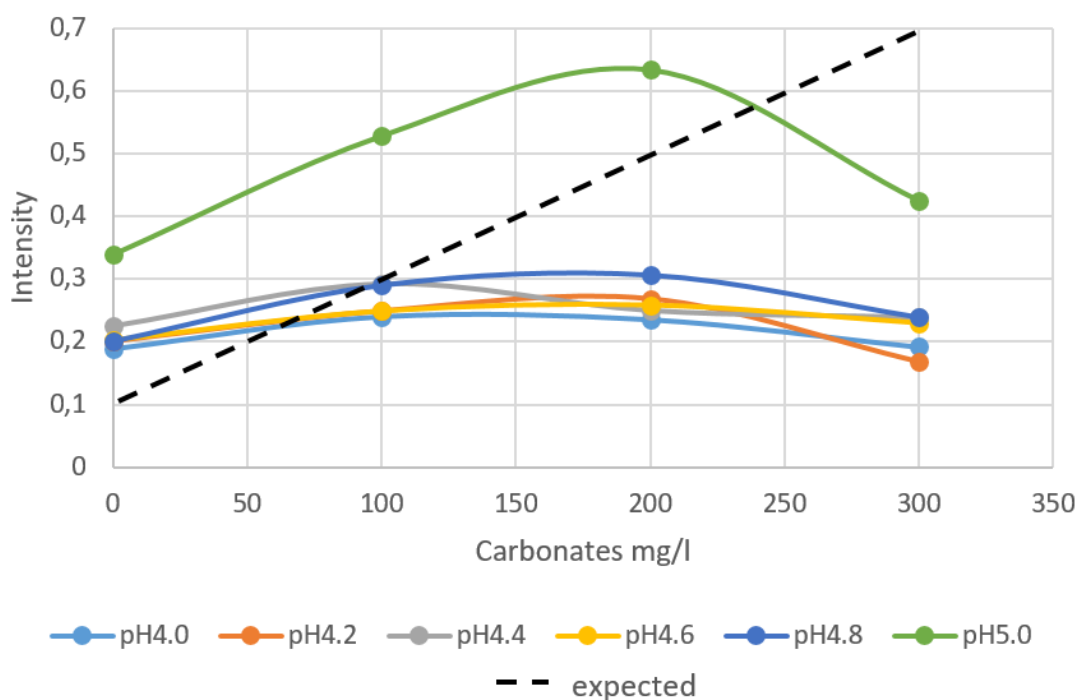


Figure 84. All measurement results on one plot

The results shown in Figure 84 indicate that for all buffer pHs the colour change for all concentrations is within the standard deviation (measurement variations are large with respect to the value changes, an increasing function was expected – dashed line on Figure 84), which means that the minimum detectable value of dissolved carbonates is above the tested range of 300 mg/l.

In this experiment, back lighting was used, so it is necessary to exclude its influence on the measurement and compare it with side lighting. The exact spectral characteristic of the LED embedded in the microscope stand is unknown, but it should not affect the measurement results since it remained constant for all samples.

#### 4.4 Comparison of side and back lighting.

Back lighting and side lighting are two ways to illuminate paper-based analytical devices for detection and analysis purposes.

Back lighting involves shining a light from behind the paper substrate, so that the light travels through the paper and illuminates any analytes that have been deposited on the paper. Back lighting can be achieved using a light source placed behind the paper and by using a transparent substrate that allows light to pass through.

Side lighting, on the other hand, involves illuminating the paper from the side, perpendicular to the plane of the paper. This technique is useful for detecting



colorimetric signals from the analytes. Side lighting can be achieved using a light source placed at the edge of the paper (see Figure 85).

Pictures of PADs obtained with back and side lighting are shown in Figure 85.

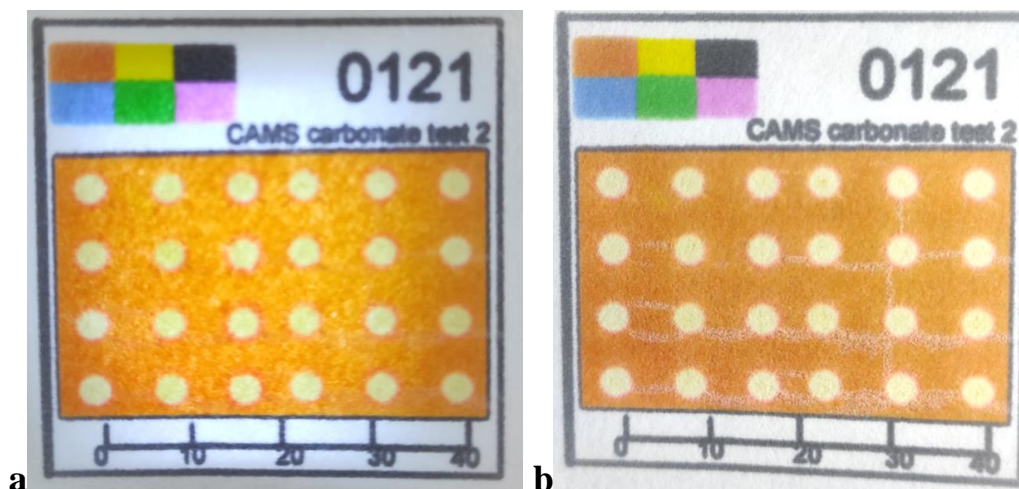


Figure 85. Images of PADs obtained at Back (a) and side (b) illumination conditions.

The standard deviation of the colour values for the clean (no carbonates in reaction zone) zones for back lighting is 2.6% and for side lighting is 2.4%. These values were obtained after processing images of 24 devices for each lighting conditions.

The results of the experiment show that the side lighting introduces slightly less error than the rear lighting. Perhaps this is due to the fact that the light passing through the PAD changes its spectral characteristic, which introduces an additional error. However, the difference is small indicating potential to use either approach in system construction.

#### **4.5 Experimental comparison of sensor and camera accuracy for measuring PAD device colour change**

The poor performance of the carbonate PADs described in section 4.3 makes it difficult to compare different types of optical sensors. In order to understand the relative accuracy of measurement using the camera and the spectral sensor, artificial (don't do any measurements) PAD devices have been developed that emulate changes in the colour of bromocresol green during carbonate measurement. These "artificial" devices recreate the colour change of BCG in the range from 3.5 to 6 pH following graph in Figure 25, but without attempting to measure carbonate concentration (they do not require a carbonate sample input). The colours for these devices were obtained by photographing (using Raspberry Pi camera) and averaging the intensity values of three RGB colour channels of known pH solutions using setup from chapter 4.3 and side lighting. The PADs were printed using a laser printer and typical paper. This method introduces its own error, but it

is assumed that the deviations in colour will be less than the preparation of PAD by described in chapter 3.2.4. this is caused by the appearance of dark spots and other difficulties in production (see chapter 4.3). These devices are shown in Figure 86.

The colours of these PADs were obtained using photos of different pH BCG solutions. Then the average value of all three channels is converted to the colour of artificial PADs. It should be mentioned that, ultimately, the PAD colours and the error in obtaining them, as well as the colours themselves, will not affect the results of this experiment. Artificial PAD is very little error compared to camera and sensor error. There is an error coming from the colour variation from device to device due to the non-repeatability of printing process, but this variation is the same for both camera and spectral sensor. Thus, by comparing standard deviation of the measurement results using the camera and a spectral sensor, it will be possible to conclude which of the devices introduce greater error.

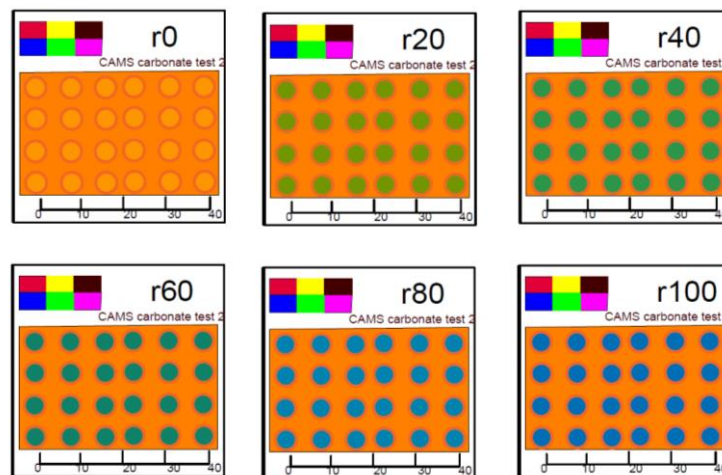


Figure 86. Artificial devices (not carbonate measuring)

The colour of six PAD devices that simulate the bromine-green colour at different pH from 3.5 to 6 with step 0.5 pH were measured using the camera and the sensor. The setup of the experiment is shown in the Figure 81 using the side lighting (using LED torch as a side light). The spectral sensors (Adafruit AS7262) were aligned manually (because automatic alignment was not implemented by the time when this experiment was conducted) using the setup from section 4.3.

The camera and the sensor were used to analyse these artificial devices. After calculating, the standard deviation of the reaction zone colour intensity (camera and spectral sensor were used to measure all PADs colours and after average standard deviation for all 6 colours was calculated to compare error introduced by them) for the camera was 3.06% and for the sensor 4.47%.

The purpose of this experiment was to determine the error of the camera and sensor. That is why the artificial PADs were used, since they almost do not have

their own error. It is possible that the higher error of the sensor is due to the principle of its operation (the joint error of the Gaussian filter and the light-sensing element) or the difficulties in obtaining the precise positioning required. Thus, no solid conclusion can be made based on these results alone.

#### **4.6 Calibration curve**

In order for the system to determine the carbonate concentration (or pH) of a sample, a calibration curve is required. It is a graphical tabulated representation of the relationship between the pH of a solution and the corresponding camera response.

The calibration curve is necessary for the interpretation of the data obtained during the measurement. By superimposing the obtained value on the curve, it is possible to determine the pH of the solution, and therefore the concentration of carbonates in water. In this experiment, the calibration curve is constructed specifically for pH values, since the concentration of carbonates that change the acidity of solutions in the same pH range would significantly exceed the carbonate concentration in natural water. This was done due to previously discussed limitations of the carbonate PADs. It is impossible to make a calibration curve in lower concentration range as discussed in section 4.3. But if there will be a way to make such a small concentration significantly change water pH these curves will be useful.

To create a calibration curve for a pH measurement system, a series of standard solutions with known pH values are prepared. A BCG is then added to each solution, and the resulting colour of the solution is measured using the pH measurement system (Jenway 3510 pH Meter,  $\pm 0.003$  specified pH accuracy). This solutions (with different Sodium Citrate and Citric Acid proportions to achieve different pH see Appendix F) was used for preparing a set of PADs. These PADs have been used for colour measuring with the camera. The obtained individual pH values and corresponding RGB colour changes are then plotted on a graph, resulting in a calibration curve that shows the relationship between pH and colour for the indicator being used.

Once the calibration curve has been created, it can be used to determine the pH of unknown solutions. To do this, the colour of the unknown solution is measured using the pH measurement system, and the corresponding pH value is determined by comparing the colour measurement to the calibration curve. This can be done manually with the graph or in software using a curve fit equation.

Calibration curves were constructed for the R G and B channels of the camera using experimental data (using setup from section 4.3 with side lightning, spectral sensor replaced with the camera). The red, green and blue channels of the

calibration curve for pH measurements are shown in Figure 87 (experimental points). The figure also shows the model-based curves (see Figure 79) which were obtained in chapter 3.2.3. These curves are shifted and scaled down in order to visually see their correlation with the data obtained. The offset is necessary due to the wide range of background illumination on the white areas of the paper (the model does not take into account the optical properties of the paper) as well as spots of BCG in the reaction zones. The scaling is needed due to the fact that the illumination intensity is different in each case.

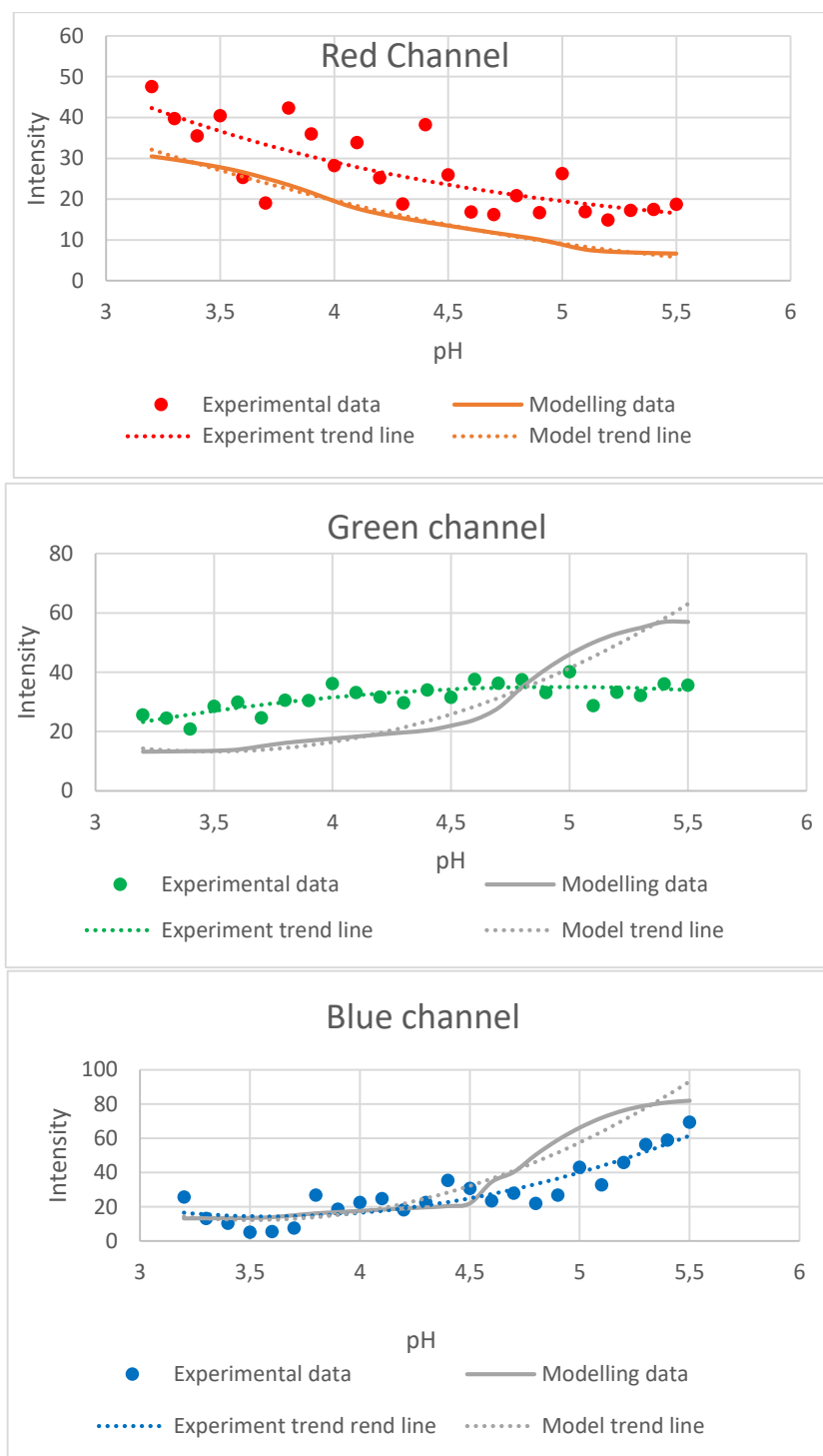


Figure 87. Calibration curves for pH measurements.

Trend curves are added to aid visualisation of the relationship between colour intensity and pH for each colour channel.

When comparing the variation of intensity vs pH for different channels on Figure 87, it is clear that the colour intensity of the blue channel (experimental) is most sensitive to changes in pH above 4, and the red channel expected to be more sensitive for pH below 4, but it turned out to be monotonous throughout the pH range. The blue channel shows very similar shaped curves for the model and experimental data. The main difference is an offset (used only for model-based curve to check if it follows experimental data, but it is will not be used for calibration). The red channel also follows the model, and the green channel turned out to be more uniform than expected.

Additionally, the isosbestic point was expected to fall in the green zone, meaning that at that particular pH value the changes in colour intensity for the green channel should be minimal. This point can be used to calibrate the values (by calculating offset) when external conditions change (illumination, humidity, etc.) that what changes the average colour intensity. The difference between the theoretical and the resulting measurement value at the isobestic point will be equal to the difference at any other point on the curve. Thus, knowing this difference, it is possible to calibrate the measurement results, eliminating the influence external conditions.

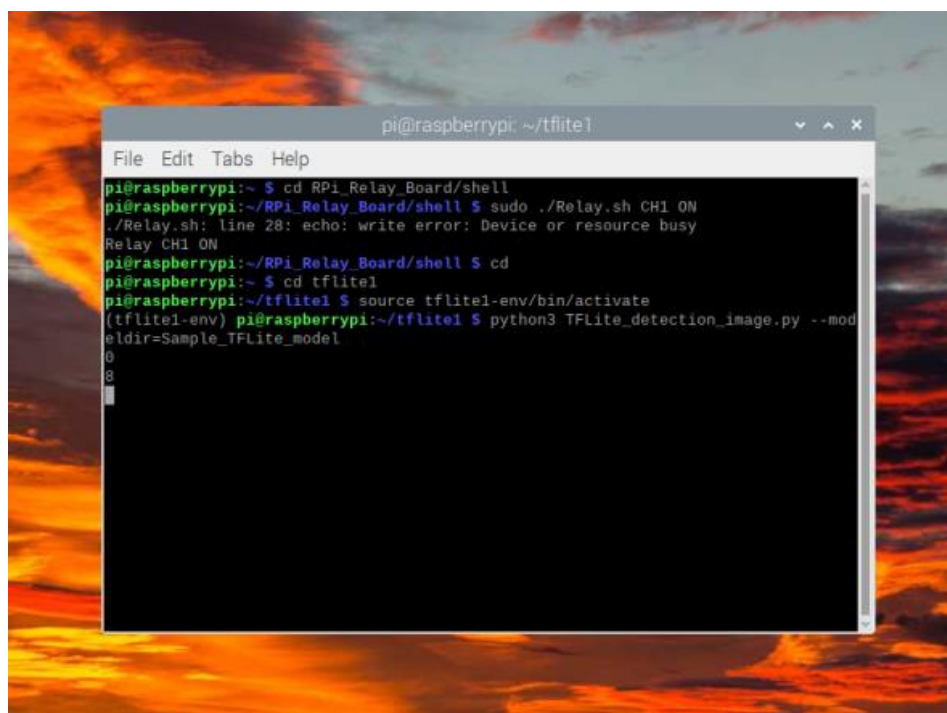
But the graph colour of the green channel changes too significantly, which does not allow calibration. This is due to the fact that the green channel is quite wide and covers spectral regions where the colour changes of the bromocresol green are quite significant.

Thus, it can be concluded that the PAD can be used to measure the pH of water, but, as mentioned in section 4.3, this PAD design does not allow measuring the specified concentrations of carbonates, since it was not possible to achieve a significant change in pH value.

Even taking into account the fact that no measurements of carbonates were carried out in this experiment, there is a fairly large spread the pH measurement in a given measurement range. The variability of the data is due to difficulties in the manufacture of solutions and their application to PAD. This is due to that BCG is slightly soluble in water and precipitates quickly. This leads to the formation of dark spots in the reaction zone, which makes it difficult to achieve high reliability and measurement accuracy.

## 5 Operational test

The final experiment involves a comprehensive assessment of the entire system operability. To do this, the system was built in accordance with Chapter 3 (Figure 35 and Figure 36). In this test, the system performs a full cycle of measurement, starting with dipping the PAD into water, detecting, analysing and ending with saving the measurement results in a database. The Raspberry Pi camera was used as an optical measuring device. Tap water was used as the measuring liquid, but it is also worth noting that the carbonate content was not measured (see chapter 4). This experiment was conducted under laboratory conditions. Figure 88 shows the commands that starts the analysis.

A screenshot of a terminal window on a Raspberry Pi. The window title is 'pi@raspberrypi: ~/tflite1'. The terminal shows the following commands and output:

```
pi@raspberrypi:~ $ cd RPi_Relay_Board/shell
pi@raspberrypi:~/RPi_Relay_Board/shell $ sudo ./Relay.sh CH1 ON
./Relay.sh: line 28: echo: write error: Device or resource busy
Relay CH1 ON
pi@raspberrypi:~/RPi_Relay_Board/shell $ cd
pi@raspberrypi:~ $ cd tflite1
pi@raspberrypi:~/tflite1 $ source tflite1-env/bin/activate
(tflite1-env) pi@raspberrypi:~/tflite1 $ python3 TFLite_detection_image.py --mod
eldir=Sample_TFLite_model
0
8
```

Figure 88. Start of the analysis

The system is fully operational (assuming the PADs are able to detect the required chemical species), as shown in the video [143].

After starting the system, the motor moves the PAD and dips it into the water tank (see Figure 89). After dipping, the motor continues to move the PAD until it is in the field of view of the camera (see Figure 90).

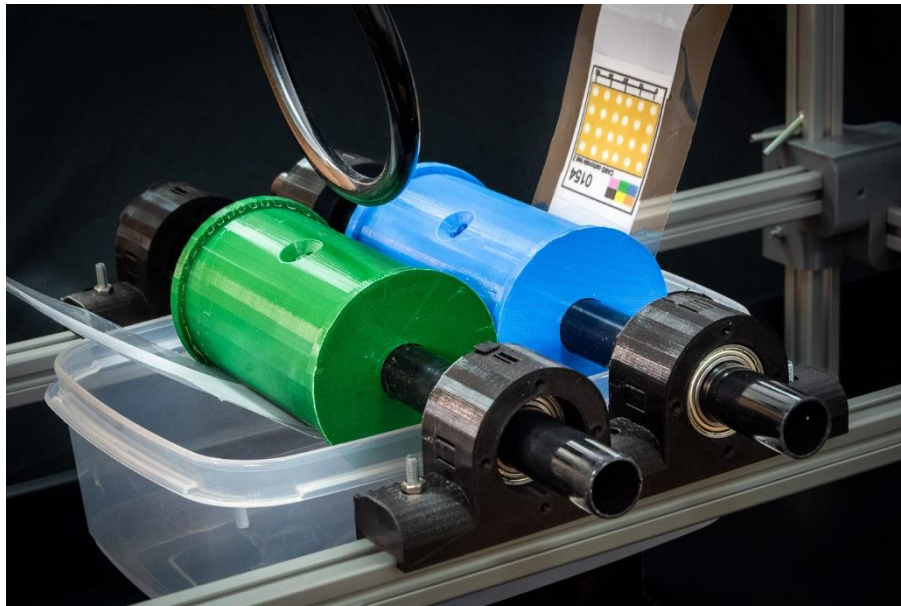


Figure 89. PAD before dipping.

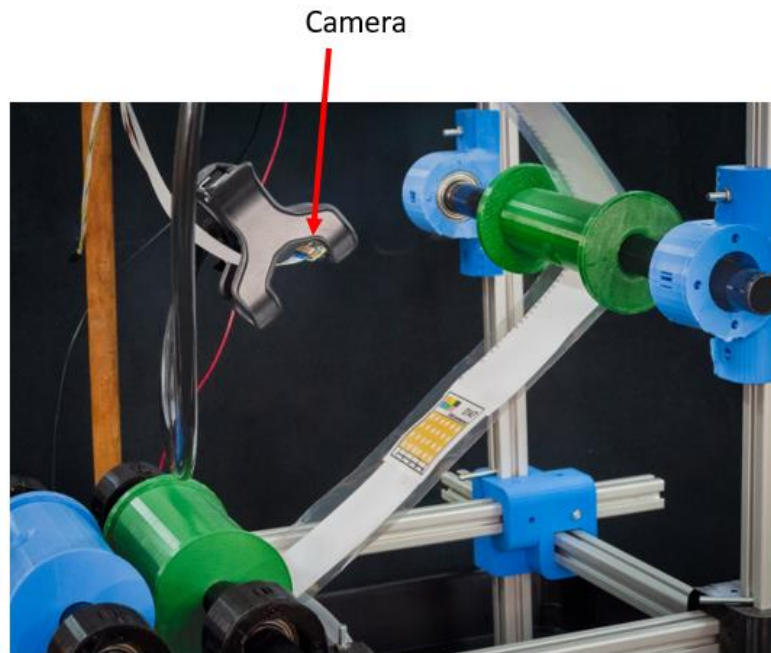


Figure 90. PAD analysis.

Then the system performs analysis and saves results (photo and analysis results). The result is shown in Figure 91, results saved in database are illustrated in Figure 92.

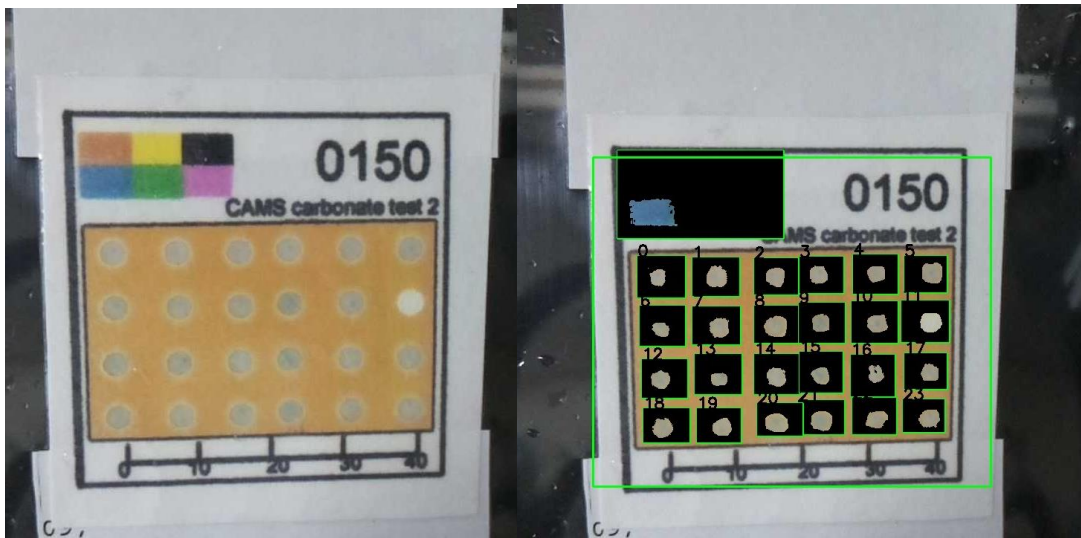


Figure 91. Pictures taken by the camera before and after analysis.

id	name	avrint	ref
13	17 /home/pi/tfllite1/images/img16.jpg	179.2711038961039;177.2014388489...	0.0
14	18 /home/pi/tfllite1/images/img17.jpg	162.11273792093704;172.185185185...	0.0
15	19 /home/pi/tfllite1/images/img18.jpg		0.0
16	20 /home/pi/tfllite1/images/img19.jpg	188.63606911447084;182.582524271...	79.0
17	21 /home/pi/tfllite1/images/img20.jpg	179.59151785714286;179.646744930...	79.02159973000337
18	22 /home/pi/tfllite1/images/img21.jpg	168.34584450402144;165.305584826...	0.0
19	23 /home/pi/tfllite1/images/img22.jpg		0.0
20	24 /home/pi/tfllite1/images/img23.jpg	182.4542772861357;179.7155599603...	78.88911290322581
21	25 /home/pi/tfllite1/images/img24.jpg	171.301043219076;171.13200379867...	81.3361762615494
22	26 /home/pi/tfllite1/images/img25.jpg	152.36868186323093;157.117647058...	0.0
23	27 /home/pi/tfllite1/images/img26.jpg	192.0099573257468;192.7016645326...	75.37157894736842
24	28 /home/pi/tfllite1/images/img27.jpg	112.10304878048781;169.674876847...	0.0
25	29 /home/pi/tfllite1/images/img28.jpg		0.0
26	30 /home/pi/tfllite1/images/img29.jpg		0.0
27	31 /home/pi/tfllite1/images/img30.jpg		0.0
28	32 /home/pi/tfllite1/images/img31.jpg	188.61904761904762;192.854508196...	68.76488785769529
29	33 /home/pi/tfllite1/images/img32.jpg	166.83333333333334;170.98375;173...	55.69885931558935
30	34 /home/pi/tfllite1/images/img33.jpg	172.73878627968338;177.445504087...	56.42150247413405
31	35 /home/pi/tfllite1/images/img34.jpg	171.82798833819243;176.216049382...	56.847457627118644
32	36 /home/pi/tfllite1/images/img35.jpg	176.75632911392404;182.896940418...	61.300534759358285
33	37 /home/pi/tfllite1/images/img36.jpg	192.45406824146983;184.205357142...	0.0
34	38 /home/pi/tfllite1/images/img37.jpg	187.06927710843374;184.577889447...	66.73747680890538
35	39 /home/pi/tfllite1/images/img38.jpg		0.0
36	40 /home/pi/tfllite1/images/img39.jpg		0.0
37	41 /home/pi/tfllite1/images/img40.jpg	162.39716312056737;159.447968285...	75.94045174537987

Figure 92. Result saved in SQLite database

The frequency of measurements can be adjusted, but currently uses a watchdog to periodically boot the Raspberry Pi after a set delay. Given that it is impossible to pre-determine the exact time taken by the Raspberry Pi to boot, this may introduce aperture jitter (as discussed in Chapter 3.7). To solve this problem a Real Time Clock (RTC) could be added to the system, with power-down timing set to ensure that the system can be ready to precisely time the sampling.



## 6 Conclusion

### 6.1 Project outcomes

This thesis represents the culmination of a four-year effort to develop an automated system for sensing natural geochemical fluxes. While the project has yielded significant progress towards this goal, in particular in developing the potentially widely applicable Lab on a Roll platform concept, it has also highlighted the need for improvement in the current method of paper-based analytical device production. Below is a list of the results that have been achieved during the work

- The electro-mechanics of a laboratory-based lab-on-roll prototype.
- Carbonate-measurement PAD designs and processes for manufacturing PAD rolls.
- The electronic hardware and associated control software for control of the laboratory prototype.
- Sensor hardware systems and analysis algorithms and software for automated measurement using the carbonate PADs.

During the testing of the system, it turned out that the accuracy of the measurement of dissolved carbonates does not correspond to the desired value, which imposes a limitation on the ability of the system to effectively capture fluctuations in the composition of water in caves (see Chapter 4.3 PADs are capable to capture only measurements much higher than the values for natural water or water in the cave. PAD devices require refinement and possibly a new approach to measurement, for example, the use of distance-based analytical devices [104]. Striving to improve the accuracy of these measurements is of paramount importance. Future efforts should focus on the development of improved methodologies, calibration methods and sensor technologies to ensure that the system provides reliable and accurate data. This issue may have already been addressed to some extent, but too late to integrate into this project, by ongoing work by Prof. Pamme's group [104].

However, even despite this problem, supported by the better performance for similar PADs for phosphorous [101], it is important to emphasize the achievement demonstrated by the automated sensing system as a whole. Its effectiveness in carrying out colorimetric measurements is an important milestone in the development of automated sensor systems. This capability opens up the possibility for many potential applications beyond the direct measurement of natural carbonates.

The initial project objectives included field testing at the Poole's Cavern site (see Chapter 2.1.5), however this was not achieved due to the impact of the COVID19 pandemic lockdowns on the rate at which development of both the instrument prototype and carbonate PADs could proceed.

Modelling of the uses of a camera and low costs spectral sensor devices indicated the sensors may deliver better accuracy than camera(see Chapter 4.2). However, the experiment in Chapter 5.5 showed that the camera makes a smaller error than the sensor. This may be due to the practical difficulties of aligning the sensors with the PADs. Also, the camera has more flexibility compared to the sensor. Use of a camera, with machine learning to identify PAD features and the relevant data/pixels from the image for further processing to obtain the chemical measurement, means that the system is not limited by the PAD shape, size, location and analysis method (e.g. colorimetry spots and distance-based), and can be used to analyse almost any paper devices based on optical detection methods within the camera's wavelength range. In addition, the system can be configured to simultaneously analyse pads of different types within a cluster (simultaneous measurement of various chemical species). To achieve this flexibility, it is just necessary to update the dataset for the object detection function.

In summary, this project has demonstrated the feasibility of in-situ automated sensing systems for improving our understanding of natural geochemical fluxes, including in challenging locations, such as caves.

## **6.2 Further work**

The results and achievements of this project open up wide opportunities for further research and development. The following is a potential plan for improving the system and expanding its application in environmental monitoring.

**1. Improving PAD production methods:** The main attention in future work should be paid to improving the production of PADs. The research of new methods with improved sensitivity and durability will be important. Fine-tuning of production processes to ensure consistency and reproducibility will give an even greater impetus to the study of geochemical flow processes and climate change.

**2. Field tests in Poole's Cavern:** To test the system's performance in real-world scenarios, comprehensive field tests must be conducted in Poole's Cavern or other appropriate cave conditions. This requires manufacture of a more robust prototype instrument and PAD rolls (see section 4). This step will provide invaluable information about the reliability of the system and adaptability to changing conditions. It will also serve as a confirmation of the usefulness of the system for monitoring geochemical flows of clean water.

**3. Advanced detection of analytes:** Extending the functionality of the system beyond carbonates opens up great opportunities for future research. Studying the possibility of measuring various water parameters, such as the content of phosphates or heavy metals, will significantly increase the versatility and usefulness of the system. This expansion makes it possible to use the system in the field of pollution monitoring, water quality assessment and resource management.

**4. Integration with data analytics:** Collected data from an automated sensing system can be integrated with advanced data analysis and machine learning techniques. Such integration will allow the system not only to detect changes in geochemical flows, but also to make forecasts and early warnings about potential environmental violations.

The development of such a system is a complex process that contains many stages, so the following two sections contain detailed recommendations for creating a system that will help avoid some difficulties.

### **6.3 Recommendations for the design of a LOAR platform**

The production process of the LOAR system is a complex process that requires careful planning and attention to detail. To speed up the process and improve the efficiency of the system, several key recommendations need to be considered.

#### **6.3.1 PAD and PAD roll production**

First of all, when manufacturing PADs for the LOAR system, careful preparation is necessary. This implies the advance preparation of the workspace and the availability of all solutions and a specially designated place for drying. Such preparation will optimize the workflow and minimize delays in the production process.

Throughout the entire PADs production process, it is extremely important to be vigilant when checking the reaction zones of paper devices. Sometimes dark spots may occur due to the presence of undissolved clots of bromocresol green.

Although it is not feasible to completely eliminate these stains, their appearance can be significantly reduced by shaking the solution with a sonicator immediately before dipping solution to paper.

One of the most important component of the production process is a wax printer, which can cause certain problems. At the time of writing this thesis, wax printers are no longer available, but refurbished devices can be found on the market. However, the use of repaired equipment can increase the risk of breakdowns, which underscores the need for regular maintenance and backup solutions to avoid interruptions in production.

Production of a PAD roll is challenging when done entirely by hand and potential leads to uneven roll thickness and skewed PAD positioning. Development of a mechanical rig to assist manufacture, for example to guide the paper into the laminator and cut the laminate to the required width, should be considered.

#### **6.3.2 LOAR instrument system**

For the prototype system, all fasteners were created on a 3D printer. It is important to consider the potential shrinkage of plastic parts as they cool down. To solve this

problem, leave small gaps and scale each part printed on a 3D printer to 103% of the intended size. Also it is necessary to take into account the heat released by stepper motors at rest, as this heat can lead to plastic deformation. Switching from 3D-printed parts to metal components can solve these problems by increasing the durability and stability of the system, but it can also increase costs and production times.

Sample time accuracy is important. The system should include an accurate RTC, possibly with its own battery (the system is unlikely to be able to access a time server from many in-situ locations). System wake-up and boot prior to sampling must be configured to allow the sample time to be guaranteed. To prevent variations on PAD separation, or PAD roll movement, from influencing sample time the PAD cluster should be moved accurately into position just above the sample prior to sampling, stopped, and then dipped in the sample at the exact sample time. Positioning can be sensed using alignment markers on the roll. There should be a guidance slots to position the roll accurately, like those used in printers and other paper-handling systems.

Water removal from the PAD roll after dipping was not developed and needs to be investigated. Use of automotive wiper blades, brushes, sponges and blow air, alone or in combination as possible approaches.

As the dynamics of carbonate fluxes are generally unknown, and may vary significantly, there is a risk of significant aliasing even with a tank-based low pass filter. Measurement of the water's conductivity at a far higher sample rate than the PADs is straightforward and would give some indication of the dynamics of the chemistry in the water. This would be helpful in assessing the PAD measurements. Other environmental parameters such as temperature and humidity should also be recorded.

It should also be mentioned that, since there is high humidity in the cave, it is necessary that all electronics be protected from moisture ingress. This can be achieved by placing the system (or only electronics) in a waterproof box

The user interface based on the Telegram app provided rapid development of some functionality, however, most of the evaluation and experimental work was performed via a command shell running on the Raspberry Pi. The next stage prototype should have a custom app for Android phones and tablets to provide users (not just developers) system configuration and data management functionality. This should allow geoscientists to operate the system in-situ without code changes being required to manage operations. Communication with the Android device is likely to be by short range radio such as Bluetooth, but other radio systems for sensor networking and through the ground communication should also be investigated.

## References

- [1] J. A.-K. Gideon Henderson, "The Life Scientific," ed, 2023.
- [2] R. Young and L. Norby, *Geological Monitoring*. Geological Society of America, 2009.
- [3] A. J. Wade *et al.*, "Hydrochemical processes in lowland rivers: insights from in situ, high-resolution monitoring," *Hydrol. Earth Syst. Sci.*, vol. 16, no. 11, pp. 4323-4342, 2012.
- [4] E. P. Joly, "Development of an autonomous lab-on-a-chip system with ion separation and conductivity detection for river water quality monitoring. (Thesis)," *University of Hull*, 2013.
- [5] A. M. Fallatah, "Development of lab-on-a-chip technology for the analysis of ions in natural waters. (Thesis)," *University of Hull*, 2015.
- [6] I. M. B. E. Joly, A. Fallatah, G. M. Greenway, S. J. Haswell, A. J. Wade and R. Skeffington, *Mixed-Signals, Sensors and Systems Test Workshop (IMS3TW)*, pp. 28-33, 2012.
- [7] J. H. I. Haddeland, H. Biemans, S. Eisner, M. Flörke, N. Hanasaki, M. Konzmann, F. Ludwig, Y. Masaki, J. Schewe, T. Stacke, Z. D. Tessler, Y. Wada and D. Wisser, *Proceedings of the National Academy of Sciences*, p. 111, 2014.
- [8] D. B. a. A. W. P. Whitehead, "Potential impacts of climate change on river water quality," 2008.
- [9] T. Nogueira and C. L. d. Lago, "Determination of Ca, K, Mg, Na, sulfate, phosphate, formate, acetate, propionate, and glycerol in biodiesel by capillary electrophoresis with capacitively coupled contactless conductivity detection," *Microchemical Journal*, vol. 99, no. 2, pp. 267-272, 2011/11/01/ 2011.
- [10] P. Kubán and P. C. Hauser, "A review of the recent achievements in capacitively coupled contactless conductivity detection," (in eng), *Anal Chim Acta*, vol. 607, no. 1, pp. 15-29, Jan 21 2008.
- [11] B. A. P. Buscher, U. R. Tjaden, and J. van der Greef, "Three-compartment electro dialysis device for on-line sample clean-up and enrichment prior to capillary electrophoresis," *Journal of Chromatography A*, vol. 788, no. 1, pp. 165-172, 1997/11/14/ 1997.
- [12] S. Park, T. Chung, and H. C. Kim, "Ion bridges in microfluidic systems. Microfluid Nanofluid 6:315-331," *Microfluidics and Nanofluidics*, vol. 6, pp. 315-331, 03/01 2009.
- [13] T. Myers and I. Bell, "Assessment of Microfluidic System Testability using Fault Simulation and Test Metrics," *J. Electronic Testing*, vol. 27, pp. 363-373, 06/01 2011.
- [14] J. V. Hinshaw, *Stalking the Wild Baseline*. LC-GC, 1993.
- [15] Saint-Gobain. (2015, 15.06.2023). *Comparative Peristaltic Pumps Tubing life*. Available: [www.tygon.com](http://www.tygon.com)
- [16] T. F. Q. Stocker, D. Plattner, G. K. Tignor, M. Allen, S. K. Doschung, J. Nauels, A. Xia, Y. Bex, V. Midgley, P. M., "Summary for Policymakers," in *Climate Change 2013 – The Physical Science Basis: Working Group I Contribution to the Fifth Assessment Report of the Intergovernmental Panel on Climate Change*, C. Intergovernmental Panel on Climate, Ed. Cambridge: Cambridge University Press, 2014, pp. 1-30.
- [17] P. A. Arkin, T. M. Smith, M. R. P. Sapiano, and J. Janowiak, "The observed sensitivity of the global hydrological cycle to changes in surface temperature," (in English), *Environmental Research Letters*, Article vol. 5, no. 3, p. 6, Jul-Sep 2010, Art. no. 035201.
- [18] F. Guo *et al.*, "Trends of temperature variability: Which variability and what health implications?," (in English), *Science of the Total Environment*, Review vol. 768, p. 8, May 2021, Art. no. 144487.
- [19] K. B. Mao *et al.*, "Global surface temperature change analysis based on MODIS data in recent twelve years," (in English), *Advances in Space Research*, Article vol. 59, no. 2, pp. 503-512, Jan 2017.
- [20] R. Lindsey, "If carbon dioxide hits a new high every year, why isn't every year hotter than the last?," 2020.
- [21] Z. Hausfather. (2017, 28.03.2020). *Analysis: Why scientists think 100% of global warming is due to humans*. Available: <https://www.carbonbrief.org/analysis-why-scientists-think-100-of-global-warming-is-due-to-humans>

- [22] J. Wang, X. Zhang, L. Su, H. Li, L. Zhang, and J. Wei, "Global warming effects on climate zones for wine grape in Ningxia region, China," *Theoretical & Applied Climatology*, Article vol. 140, no. 3/4, pp. 1527-1536, 2020.
- [23] S. Piao *et al.*, "Plant phenology and global climate change: Current progresses and challenges," *Global Change Biology*, vol. 25, no. 6, pp. 1922-1940, 2019.
- [24] R. T. Corlett and D. A. Westcott, "Will plant movements keep up with climate change?," *Trends in Ecology & Evolution*, vol. 28, no. 8, pp. 482-488, 2013/08/01/ 2013.
- [25] Y. Vitasse, C. Signarbieux, and Y. H. Fu, "Global warming leads to more uniform spring phenology across elevations," *Proceedings of the National Academy of Sciences*, vol. 115, no. 5, pp. 1004-1008, 2018.
- [26] D. V. Pio *et al.*, "Climate change effects on animal and plant phylogenetic diversity in southern Africa," *Global Change Biology*, Article vol. 20, no. 5, pp. 1538-1549, 2014.
- [27] C. W. Schmidt, "Pollen Overload Seasonal Allergies in a Changing Climate," *Environmental Health Perspectives*, Article vol. 124, no. 4, pp. A70-A75, 2016.
- [28] G. R. Quetin, A. A. Bloom, K. W. Bowman, and A. G. Konings, "Carbon Flux Variability From a Relatively Simple Ecosystem Model With Assimilated Data Is Consistent With Terrestrial Biosphere Model Estimates," *Journal of Advances in Modeling Earth Systems*, Article vol. 12, no. 3, pp. 1-17, 2020.
- [29] S. Down, "Chemical Weathering," 2020/6/3/, 2020.
- [30] C. Le Quéré *et al.*, "Global Carbon Budget 2018," *Earth Syst. Sci. Data*, vol. 10, no. 4, pp. 2141-2194, 2018.
- [31] Z. Liu, W. Dreybrodt, and H. Liu, "Atmospheric CO<sub>2</sub> sink: Silicate weathering or carbonate weathering?," *Applied Geochemistry*, vol. 26, pp. S292-S294, 2011/06/01/ 2011.
- [32] P. Friedlingstein *et al.*, "Global Carbon Budget 2019," *Earth Syst. Sci. Data*, vol. 11, no. 4, pp. 1783-1838, 2019.
- [33] Z. Liu, G. L. Macpherson, C. Groves, J. B. Martin, D. Yuan, and S. Zeng, "Large and active CO<sub>2</sub> uptake by coupled carbonate weathering," *Earth-Science Reviews*, vol. 182, pp. 42-49, 2018/07/01/ 2018.
- [34] W. K. Jones and W. B. White, "Chapter 72 - Karst," in *Encyclopedia of Caves (Third Edition)*, W. B. White, D. C. Culver, and T. Pipan, Eds.: Academic Press, 2019, pp. 609-618.
- [35] N. Goldscheider *et al.*, "Global distribution of carbonate rocks and karst water resources," *Hydrogeology Journal*, vol. 28, no. 5, pp. 1661-1677, 2020/08/01 2020.
- [36] D. A. Ruban, "Karst as Important Resource for Geopark-Based Tourism: Current State and Biases," *Resources*, vol. 7, no. 4, p. 82, 2018.
- [37] S. S. S. Cardoso and J. T. H. Andres, "Geochemistry of silicate-rich rocks can curtail spreading of carbon dioxide in subsurface aquifers," (in English), *Nature Communications*, Article vol. 5, p. 6, Dec 2014, Art. no. 5743.
- [38] S. Zeng *et al.*, "Comparisons on the effects of temperature, runoff, and land-cover on carbonate weathering in different karst catchments: insights into the future global carbon cycle," *Hydrogeology Journal*, vol. 29, no. 1, pp. 331-345, 2021/02/01 2021.
- [39] L. P. Knauth and M. J. Kennedy, "The late Precambrian greening of the Earth," *Nature*, Article vol. 460, no. 7256, pp. 728-732, 2009.
- [40] C. Duffy, C. O'Donoghue, M. Ryan, D. Styles, and C. Spillane, "Afforestation: Replacing livestock emissions with carbon sequestration," *Journal of Environmental Management*, vol. 264, p. 110523, 2020/06/15/ 2020.
- [41] W. Trust. (24.04.2020). *Woodland Trust Northern Forest Project* Available: <https://www.woodlandtrust.org.uk/about-us/what-we-do/we-plant-trees/the-northern-forest/>
- [42] B. W. Griscom *et al.*, "Natural climate solutions," *Proceedings of the National Academy of Sciences*, vol. 114, no. 44, pp. 11645-11650, 2017.
- [43] A. Hartmann, M. Luetscher, R. Wachter, P. Holz, E. Eiche, and T. Neumann, "Technical note: GUARD - An automated fluid sampler preventing sample alteration by contamination, evaporation and gas exchange, suitable for remote areas and harsh conditions," (in english), *Hydrology and earth system sciences discussions*, journal article vol. 22, pp. 4281-4293, 2018.

- [44] DFROBOT. (14.01.2024). *Analog pH Sensor/Meter Kit V2*. Available: <https://www.dfrobot.com/product-1782.html>
- [45] DFROBOT. (14.01.2024). *Analog Electrical Conductivity Sensor*. Available: <https://www.dfrobot.com/product-1123.html>
- [46] DFROBOT. (14.01.2024). *Analog Dissolved Oxygen Sensor*. Available: <https://www.dfrobot.com/product-1628.html>
- [47] K. S. More, C. Wolkersdorfer, N. Kang, and A. S. Elmaghraby, "Automated measurement systems in mine water management and mine workings – A review of potential methods," *Water Resources and Industry*, vol. 24, p. 100136, 2020/12/01/ 2020.
- [48] P. L. d. Almeida Jr, L. M. A. Lima, and L. F. d. Almeida, "A 3D-printed robotic system for fully automated multiparameter analysis of drinkable water samples," *Analytica Chimica Acta*, vol. 1169, p. 338491, 2021/07/18/ 2021.
- [49] O. Samuelsson, E. U. Lindblom, A. Björk, and B. Carlsson, "To calibrate or not to calibrate, that is the question," *Water Research*, vol. 229, p. 119338, 2023/02/01/ 2023.
- [50] H. Fu, X. Jian, W. Zhang, and F. Shang, "A comparative study of methods for determining carbonate content in marine and terrestrial sediments," *Marine and Petroleum Geology*, vol. 116, p. 104337, 2020/06/01/ 2020.
- [51] M. C. Carvalho, "Portable open-source autosampler for shallow waters," *HardwareX*, vol. 8, p. e00142, 2020/10/01/ 2020.
- [52] B. H. Vaughn, J. W. C. White, M. Delmotte, M. Trolier, O. Cattani, and M. Stievenard, "An automated system for hydrogen isotope analysis of water," *Chemical Geology*, vol. 152, no. 3, pp. 309-319, 1998/11/16/ 1998.
- [53] J. Tschmelak *et al.*, "Automated Water Analyser Computer Supported System (AWACSS): Part II: Intelligent, remote-controlled, cost-effective, on-line, water-monitoring measurement system," *Biosensors and Bioelectronics*, vol. 20, no. 8, pp. 1509-1519, 2005/02/15/ 2005.
- [54] L. Lin *et al.*, "CIRCA: Cloud-based intelligent robotic system for chemical analysis in streamlining and automating open-ended measurement tasks," *Microchemical Journal*, p. 109880, 2024/01/03/ 2024.
- [55] P. Kurzweil, "Electrochemical devices | Electrochemical devices: History of electrochemistry," in *Reference Module in Chemistry, Molecular Sciences and Chemical Engineering*: Elsevier, 2023.
- [56] N. A. Ab Mutalib and H. Suzuki, "Evolution in the development of next generation electrochemical microdevices via bipolar electrochemistry," *Current Opinion in Electrochemistry*, vol. 43, p. 101424, 2024/02/01/ 2024.
- [57] M. Torkamanzadeh *et al.*, "Best practice for electrochemical water desalination data generation and analysis," *Cell Reports Physical Science*, vol. 4, no. 11, p. 101661, 2023/11/15/ 2023.
- [58] B. P. Yalagandula, S. Mohanty, P. P. Goswami, and S. G. Singh, "Optimizations towards a nearly invariable WO<sub>3</sub>-functionalized electrochemical aptasensor for ultra-trace identification of arsenic in lake water," *Sensors and Actuators B: Chemical*, vol. 398, p. 134730, 2024/01/01/ 2024.
- [59] M. Cuartero, "Electrochemical sensors for in-situ measurement of ions in seawater," *Sensors and Actuators B: Chemical*, vol. 334, p. 129635, 2021/05/01/ 2021.
- [60] A. O. Idris, J. P. Mafa, N. Mabuba, and O. A. Arotiba, "Dealing with interference challenge in the electrochemical detection of As(III) —A complexometric masking approach," *Electrochemistry Communications*, vol. 64, pp. 18-20, 2016/03/01/ 2016.
- [61] J. Rainbow *et al.*, "Integrated Electrochemical Biosensors for Detection of Waterborne Pathogens in Low-Resource Settings," (in eng), *Biosensors (Basel)*, vol. 10, no. 4, Apr 13 2020.
- [62] HACH. (03.03.2024). *DR1900 Portable Spectrophotometer*. Available: <https://uk.hach.com/spectrophotometers/dr1900-portable-spectrophotometer/family-downloads?productCategoryId=25114239786>
- [63] D. Pearson *et al.*, "Water analysis via portable X-ray fluorescence spectrometry," *Journal of Hydrology*, vol. 544, pp. 172-179, 2017/01/01/ 2017.

- [64] X. Zhu *et al.*, "Assessment of a portable UV–Vis spectrophotometer's performance for stream water DOC and Fe content monitoring in remote areas," *Talanta*, vol. 224, p. 121919, 2021/03/01/ 2021.
- [65] J. C. L. Erve, M. Gu, Y. Wang, W. DeMaio, and R. E. Talaat, "Spectral Accuracy of Molecular Ions in an LTQ/Orbitrap Mass Spectrometer and Implications for Elemental Composition Determination," *Journal of the American Society for Mass Spectrometry*, vol. 20, no. 11, pp. 2058-2069, 2009/11/01/ 2009.
- [66] R. A. Crocombe, "Portable Spectroscopy," *Applied Spectroscopy*, vol. 72, no. 12, pp. 1701-1751, 2018/12/01 2018.
- [67] E. Instruments. (18.02.2024). *What is a spectrometer*.
- [68] H. Moeur, A. Zanella, and T. Poon, "An Introduction to UV-Vis Spectroscopy Using Sunscreens," *Journal of Chemical Education - J CHEM EDUC*, vol. 83, 05/01 2006.
- [69] F. Fanjul-Vélez, L. Arévalo-Díaz, and J. L. Arce-Diego, "Intra-class variability in diffuse reflectance spectroscopy: application to porcine adipose tissue," (in eng), *Biomed Opt Express*, vol. 9, no. 5, pp. 2297-2303, May 1 2018.
- [70] D. S. Hage, "Electrophoresis | Capillary Electrophoresis: Clinical Applications☆," in *Encyclopedia of Analytical Science (Third Edition)*, P. Worsfold, C. Poole, A. Townshend, and M. Miró, Eds. Oxford: Academic Press, 2019, pp. 346-357.
- [71] M. R. N. Monton and S. Terabe, "Sample enrichment techniques in capillary electrophoresis: Focus on peptides and proteins," *Journal of Chromatography B*, vol. 841, no. 1, pp. 88-95, 2006/09/01/ 2006.
- [72] "Electrophoresis," *Journal of Chromatography A*, vol. 650, no. 2, pp. B467-B492, 1993/12/10/ 1993.
- [73] S. Ghosal, "Electrokinetic Flow and Dispersion in Capillary Electrophoresis," *Annu. Rev. Fluid Mech.*, vol. 38, pp. 309-338, 12/16 2005.
- [74] W. Campbell, P. Song, and G. Barbier, "Nitrate reductase for nitrate analysis in water," *Environmental Chemistry Letters*, vol. 4, pp. 69-73, 06/01 2006.
- [75] V. A. Puhl *et al.*, "Enzymatic analysis in household intermittent slow sand filters as a tool for assessing biological clogging," *Journal of Water Process Engineering*, vol. 55, p. 104177, 2023/10/01/ 2023.
- [76] E. C. Reynoso, C. Romero-Guido, G. Rebollar-Pérez, and E. Torres, "Chapter 16 - Enzymatic biosensors for the detection of water pollutants," in *Nanomaterials for Biocatalysis*, G. R. Castro, A. K. Nadda, T. A. Nguyen, X. Qi, and G. Yasin, Eds.: Elsevier, 2022, pp. 463-511.
- [77] P. K. Robinson, "Enzymes: principles and biotechnological applications," (in eng), *Essays Biochem*, vol. 59, pp. 1-41, 2015.
- [78] A. Dev, A. K. Srivastava, and S. Karmakar, "Chapter 12 - New Generation Hybrid Nanobiocatalysts: The Catalysis Redefined," in *Handbook of Nanomaterials for Industrial Applications*, C. Mustansar Hussain, Ed.: Elsevier, 2018, pp. 217-231.
- [79] I. R. Ausri, Y. Zilberman, S. Schneider, and X. Tang, "Recent advances and challenges: Translational research of minimally invasive wearable biochemical sensors," *Biosensors and Bioelectronics: X*, vol. 15, p. 100405, 2023/12/01/ 2023.
- [80] L. Liu *et al.*, "Ultrasensitive biochemical sensors based on controllably grown films of high-density edge-rich multilayer WS<sub>2</sub> islands," *Sensors and Actuators B: Chemical*, vol. 353, p. 131081, 2022/02/15/ 2022.
- [81] S. N. Zulkifli, H. A. Rahim, and W. J. Lau, "Detection of contaminants in water supply: A review on state-of-the-art monitoring technologies and their applications," (in eng), *Sens Actuators B Chem*, vol. 255, pp. 2657-2689, Feb 2018.
- [82] Y. Kim and S. Amemiya, "Stripping Analysis of Nanomolar Perchlorate in Drinking Water with a Voltammetric Ion-Selective Electrode Based on Thin-Layer Liquid Membrane," *Analytical Chemistry*, vol. 80, no. 15, pp. 6056-6065, 2008/08/01 2008.
- [83] G. A. Crespo, "Recent Advances in Ion-selective membrane electrodes for in situ environmental water analysis," *Electrochimica Acta*, vol. 245, pp. 1023-1034, 2017/08/10/ 2017.



- [84] Ngamsom B. *et al.*, "Pre-concentration with electrospun membranes coupled with paper-based assays towards on-site monitoring of heavy metals in water," *microTAS*, 2020 2020.
- [85] A. H. Galama, N. A. Hoog, and D. R. Yntema, "Method for determining ion exchange membrane resistance for electrodialysis systems," *Desalination*, vol. 380, pp. 1-11, 2016/02/15/ 2016.
- [86] T. Xu, "Ion exchange membranes: State of their development and perspective," *Journal of Membrane Science*, vol. 263, no. 1, pp. 1-29, 2005/10/15/ 2005.
- [87] M. Elumalai, A. Ipatov, J. Guerreiro, and M. Prado, "Automated lab-on-chip for the specific detection of invasive species through environmental DNA," *Sensors and Actuators B: Chemical*, vol. 398, p. 134722, 2024/01/01/ 2024.
- [88] V. Karthik, B. Karuna, P. S. Kumar, A. Saravanan, and R. V. Hemavathy, "Development of lab-on-chip biosensor for the detection of toxic heavy metals: A review," *Chemosphere*, vol. 299, p. 134427, 2022/07/01/ 2022.
- [89] R. Pol, F. Céspedes, D. Gabriel, and M. Baeza, "Microfluidic lab-on-a-chip platforms for environmental monitoring," *TrAC Trends in Analytical Chemistry*, vol. 95, pp. 62-68, 2017/10/01/ 2017.
- [90] D. Chen *et al.*, "An integrated, self-contained microfluidic cassette for isolation, amplification, and detection of nucleic acids," (in eng), *Biomed Microdevices*, vol. 12, no. 4, pp. 705-19, Aug 2010.
- [91] M. M. Maw, J. Wang, F. Li, J. Jiang, Y. Song, and X. Pan, "Novel Electrokinetic Microfluidic Detector for Evaluating Effectiveness of Microalgae Disinfection in Ship Ballast Water," (in eng), *Int J Mol Sci*, vol. 16, no. 10, pp. 25560-75, Oct 26 2015.
- [92] J. Yang and D. Y. Kwok, "Analytical treatment of electrokinetic microfluidics in hydrophobic microchannels," *Analytica Chimica Acta*, vol. 507, no. 1, pp. 39-53, 2004/04/01/ 2004.
- [93] Y. Lu *et al.*, "AC Electrokinetics of Physiological Fluids for Biomedical Applications," *SLAS Technology*, vol. 20, no. 6, pp. 611-620, 2015/12/01/ 2015.
- [94] T. M. Squires, "Induced-charge electrokinetics: fundamental challenges and opportunities," *Lab on a Chip*, 10.1039/B906909G vol. 9, no. 17, pp. 2477-2483, 2009.
- [95] D. Yan, "Electrokinetic flow: characterization, control and application in microfluidic systems," 2007.
- [96] Y. Liu *et al.*, "Recent progress in microfluidic biosensors with different driving forces," *TrAC Trends in Analytical Chemistry*, vol. 158, p. 116894, 2023/01/01/ 2023.
- [97] M. Zhou, J. Li, S. Yuan, X. Yang, J. Lu, and B. Jiang, "A centrifugal microfluidic system for automated detection of multiple heavy metal ions by aptamer-based colorimetric assay," *Sensors and Actuators B: Chemical*, vol. 403, p. 135210, 2024/03/15/ 2024.
- [98] I. J. Michael, T. H. Kim, V. Sunkara, and Y. K. Cho, "Challenges and Opportunities of Centrifugal Microfluidics for Extreme Point-of-Care Testing," (in eng), *Micromachines (Basel)*, vol. 7, no. 2, Feb 19 2016.
- [99] W. Alahmad, A. Sahragard, and P. Varanusupakul, "An overview of the recent developments of microfluidic paper-based analytical devices for the detection of chromium species," *Microchemical Journal*, vol. 170, p. 106699, 2021/11/01/ 2021.
- [100] J. Rotchell. (29.03.2020). *Sullied Sediments*. Available: <https://northsearegion.eu/sullied-sediments/>
- [101] S. Richardson *et al.*, "Citizen-led sampling to monitor phosphate levels in freshwater environments using a simple paper microfluidic device," (in eng), *PLoS One*, vol. 16, no. 12, p. e0260102, 2021.
- [102] A. Abdollahi-Aghdam, M. R. Majidi, and Y. Omid, "Microfluidic paper-based analytical devices ( $\mu$ PADs) for fast and ultrasensitive sensing of biomarkers and monitoring of diseases," *BiolImpacts*, Article vol. 8, no. 4, pp. 237-240, 2018.
- [103] D. H. Zhang, C. C. Li, D. L. Ji, and Y. F. Wang, "Paper-Based Microfluidic Sensors for Onsite Environmental Detection: A Critical Review," (in English), *Critical Reviews in Analytical Chemistry*, Review; Early Access p. 18.
- [104] P. Giménez-Gómez, I. Hättstrand, S. Sjöberg, C. Dupraz, S. Richardson, and N. Pamme, "Distance-based paper analytical device for the determination of dissolved inorganic carbon

- concentration in freshwater," *Sensors and Actuators B: Chemical*, vol. 385, p. 133694, 2023/06/15/ 2023.
- [105] M. Deng *et al.*, "A paper-based colorimetric microfluidic sensor fabricated by a novel spray painting prototyping process for iron analysis," *Canadian Journal of Chemistry*, Article vol. 97, no. 5, pp. 373-377, 2019.
- [106] Y. Soda and E. Bakker, "Quantification of Colorimetric Data for Paper-Based Analytical Devices," *ACS Sensors*, vol. 4, no. 12, pp. 3093-3101, 2019/12/27 2019.
- [107] Y. Soda, K. J. Robinson, T. J. Cherubini, and E. Bakker, "Colorimetric absorbance mapping and quantitation on paper-based analytical devices," *Lab on a Chip*, 10.1039/D0LC00028K vol. 20, no. 8, pp. 1441-1448, 2020.
- [108] G. G. Morbioli, T. Mazzu-Nascimento, A. M. Stockton, and E. Carrilho, "Technical aspects and challenges of colorimetric detection with microfluidic paper-based analytical devices (mu PADS) - A review," (in English), *Analytica Chimica Acta*, Review vol. 970, pp. 1-22, Jun 2017.
- [109] A. Gilchrist and J. Nobbs, "Colorimetry, Theory," in *Encyclopedia of Spectroscopy and Spectrometry (Third Edition)*, J. C. Lindon, G. E. Tranter, and D. W. Koppenaal, Eds. Oxford: Academic Press, 2017, pp. 328-333.
- [110] W. Mäntele and E. Deniz, "UV-VIS absorption spectroscopy: Lambert-Beer reloaded," (in eng), *Spectrochim Acta A Mol Biomol Spectrosc*, vol. 173, pp. 965-968, Feb 15 2017.
- [111] J. R. Askim and K. S. Suslick, "8.04 - Colorimetric and Fluorometric Sensor Arrays for Molecular Recognition," in *Comprehensive Supramolecular Chemistry II*, J. L. Atwood, Ed. Oxford: Elsevier, 2017, pp. 37-88.
- [112] A. P. Holkem *et al.*, "A green and high throughput method for salt determination in crude oil using digital image-based colorimetry in a portable device," *Fuel*, vol. 289, p. 119941, 2021/04/01/ 2021.
- [113] N. A. Chappell, T. D. Jones, and W. Tych, "Sampling frequency for water quality variables in streams: Systems analysis to quantify minimum monitoring rates," *Water Research*, vol. 123, pp. 49-57, 2017/10/15/ 2017.
- [114] E. Coraggio, D. Han, C. Gronow, and T. Tryfonas, "Water Quality Sampling Frequency Analysis of Surface Freshwater: A Case Study on Bristol Floating Harbour," (in English), *Frontiers in Sustainable Cities*, Original Research vol. 3, 2022-January-31 2022.
- [115] R. L. L. da Silva, A. L. L. da Silveira, and G. L. da Silveira, "Spectral analysis in determining water quality sampling intervals," *Rbrh-Revista Brasileira De Recursos Hidricos*, vol. 24, 2019, Art. no. e46.
- [116] J. W. Kirchner, X. Feng, C. Neal, and A. J. Robson, "The fine structure of water-quality dynamics: the (high-frequency) wave of the future," *Hydrological Processes*, vol. 18, no. 7, pp. 1353-1359, 2004.
- [117] K. T. Lau, R. Shepherd, D. Diamond, and D. Diamond, "Solid State pH Sensor Based on Light Emitting Diodes (LED) As Detector Platform," (in eng), *Sensors (Basel, Switzerland)*, vol. 6, no. 8, pp. 848-859, 2006.
- [118] M. Shamsipur, F. Abbasitabar, V. Zare-Shahabadi, Shahabadi, and M. Akhond, "Broad-Range Optical pH Sensor Based on Binary Mixed-Indicator Doped Sol-Gel Film and Application of Artificial Neural Network," *Analytical Letters*, Article vol. 41, no. 17, pp. 3113-3123, 2008.
- [119] B. Tian, X. Ge, G. Pan, B. Fan, and Z. Luan, "Adsorption and flocculation behaviors of polydiallyldimethylammonium (PDADMA) salts: Influence of counterion," *International Journal of Mineral Processing*, vol. 79, no. 4, pp. 209-216, 2006/07/01/ 2006.
- [120] P. Vardevanyan, V. Élbakyan, M. Shahinyan, M. Minasyants, M. Parsadanyan, and N. Sahakyan, "Determination of the Isosbestic Point in the Absorption Spectra of DNA-Ethidium Bromide Complexes," *Journal of Applied Spectroscopy*, Article vol. 81, no. 6, pp. 1060-1063, 2015.
- [121] K. I. Post, "ams launches world's first digital multispectral sensor-on-chip leveraging breakthrough wafer-level filter technology," in *ams-OSRAM AG*, ed, 2017.
- [122] AMS-OSRAM, "AS7262 Product Document," ed, 2022.
- [123] T. Wilberforce, J. Thompson, and A.-G. Olabi, "Classification of Energy Storage Materials," in *Encyclopedia of Smart Materials*, A.-G. Olabi, Ed. Oxford: Elsevier, 2022, pp. 8-14.

- [124] S. W. Smith, *The Scientist and Engineer's Guide to Digital Signal Processing* (no. 29.03.2020). 2002.
- [125] F. P. Miller, A. F. Vandome, and J. McBrewster, *Nyquist-Shannon Sampling Theorem: Aliasing, Sine Wave, Signal Processing, Nyquist Rate, Nyquist Frequency, Sampling Rate, Shannon-Hartley Theorem, Whittaker-Shannon Interpolation Formula, Reconstruction from Zero Crossings*. Alphascript Publishing, 2010.
- [126] M. Xiao, Z. Han, S. Xu, and Z. Wang, "Temporal Variations of Water Chemistry in the Wet Season in a Typical Urban Karst Groundwater System in Southwest China," (in eng), *Int J Environ Res Public Health*, vol. 17, no. 7, Apr 7 2020.
- [127] N. H. Abdulghafoor and H. N. Abdullah, "REAL-TIME MOVING OBJECTS DETECTION AND TRACKING USING DEEP-STREAM TECHNOLOGY," (in English), *Journal of Engineering Science and Technology*, Article vol. 16, no. 1, pp. 194-208, Feb 2021.
- [128] R. X. Yang and Y. Y. Yu, "Artificial Convolutional Neural Network in Object Detection and Semantic Segmentation for Medical Imaging Analysis," (in English), *Frontiers in Oncology*, Review vol. 11, p. 9, Mar 2021, Art. no. 638182.
- [129] TensorFlow, "TensorFlow Developers," 2023.
- [130] D. Frajberg, C. Bernaschina, C. Marone, and P. Fraternali, "Accelerating Deep Learning Inference on Mobile Systems," in *Artificial Intelligence and Mobile Services - Aims 2019*, vol. 11516, D. Wang and L. J. Zhang, Eds. (Lecture Notes in Computer Science, Cham: Springer International Publishing Ag, 2019, pp. 118-134.
- [131] A. Zeroual, M. Amroune, M. Derdour, and A. Bentahar, *Using a Fine-tuning method for a Deep authentication in Mobile Cloud Computing based on Tensorflow lite framework* (2019 4th International Conference on Networking and Advanced Systems). New York: Ieee, 2019, pp. 84-88.
- [132] J. a. D. Redmon, Santosh and Girshick, Ross and Farhadi, Ali, "You Only Look Once: Unified, Real-Time Object Detection," *2016 IEEE Conference on Computer Vision and Pattern Recognition (CVPR)*, pp. 779-788, 2016.
- [133] G. Bradski, "The OpenCV Library," *Dr. Dobb's Journal of Software Tools*, 2000.
- [134] C. R. Harris *et al.*, "Array programming with NumPy," *Nature*, vol. 585, no. 7825, pp. 357-362, 2020/09/01 2020.
- [135] Adafruit. (02.11.2023). *adafruit motorkit*. Available: <https://docs.circuitpython.org/projects/motorkit/en/latest/>
- [136] Argparse. (02.11.2023). *argparse — Parser for command-line options, arguments and sub-commands*. Available: <https://docs.python.org/3/library/argparse.html>
- [137] Richardson S., AlHinai S., Gitaka J., Mayers W., Lorch M., and P. N., "Towards on-site monitoring of soil nutrients via a cafetiere-based extraction and paper-based analysis," *microTAS*, 2020 2020.
- [138] Camera-Module. (2024, 01.03.2024). *8MP Auto Focus Camera Module with Sony IMX179 sensor*. Available: <http://www.camera-module.com/product/8mpcameramodule/8MP-Auto-Focus-Camera-Module-Sony-IMX179-sensor.html>
- [139] AMS-OSRAM. (02.11.2023). *OSRAM DURIS® S 5, GW PSLM31.FM*. Available: <https://ams-osram.com/products/leds/white-leds/osram-duris-s-5-gw-pslm31-fm#Datasheets>
- [140] R. R. Farnood, "OPTICAL PROPERTIES OF PAPER : THEORY AND PRACTICE," 2018.
- [141] H. Mousavipazhouh, M. Azadfallah, and I. R. Jouybari, "ENCAPSULATION OF PRECIPITATED CALCIUM CARBONATE FILLERS USING CARBOXYMETHYL CELLULOSE/POLYALUMINIUM CHLORIDE: PREPARATION AND ITS INFLUENCE ON MECHANICAL AND OPTICAL PROPERTIES OF PAPER," *Maderas: Ciencia y Tecnología*, Article vol. 20, no. 4, pp. 703-714, 2018.
- [142] M. Ataefard, "The influence of paper whiteness, roughness and gloss on the optical density of colour digital printing," *Pigment & Resin Technology*, Article vol. 44, no. 4, pp. 232-238, 2015.
- [143] A. Iurkov. (2023). *LOAR*. Available: <https://drive.google.com/file/d/1vzqODZj3VIOA00YMF5QcuO6mejPZ4WgG/view?usp=drivesdk>

# Appendix A - Sensor Board Schematic

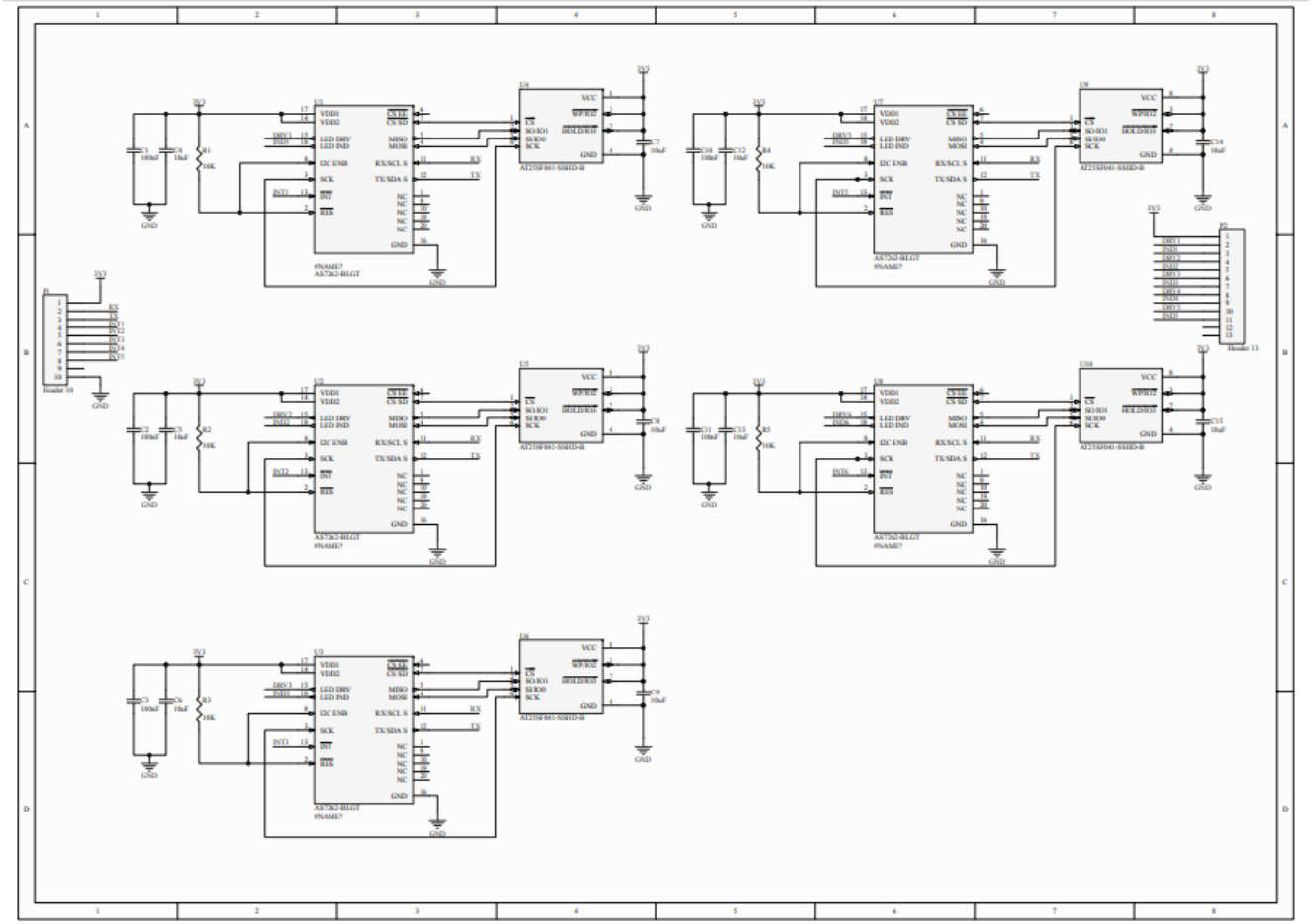


Figure 93. Sensor board schematic

## Appendix B – LED Board Schematic

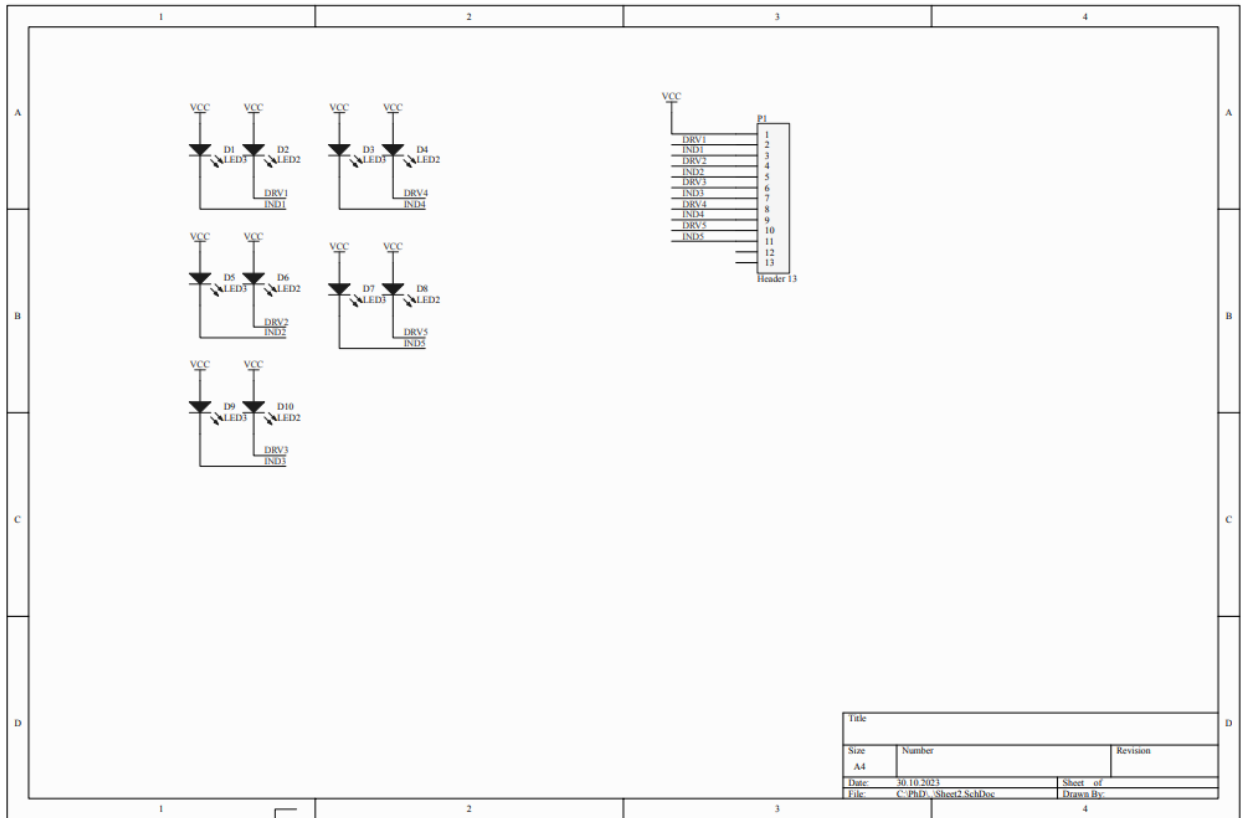


Figure 94. LED board schematic

## Appendix C – Analysis function

```
import os
import argparse
import cv2
import numpy as np
import sys
import glob
import importlib.util
from datetime import datetime
import time
import board
from adafruit_motorkit import MotorKit
import sqlite3
import TFLite_detection_webcam as TFcam

def analysis(image_name, labels, interpreter):

    parser = argparse.ArgumentParser()
    parser.add_argument('--modeldir', help='Folder the .tflite file is located
in',
                        required=True)
    parser.add_argument('--graph', help='Name of the .tflite file, if different
than detect.tflite',
                        default='detect.tflite')
    parser.add_argument('--labels', help='Name of the labelmap file, if different
than labelmap.txt',
                        default='labelmap.txt')
    parser.add_argument('--threshold', help='Minimum confidence threshold for
displaying detected objects',
                        default=0.4)
    parser.add_argument('--image', help='Name of the single image to perform
detection on. To run detection on multiple images, use --imagedir',
                        default=None)
    parser.add_argument('--imagedir', help='Name of the folder containing images
to perform detection on. Folder must contain only images.',
                        default=None)
    parser.add_argument('--edgetpu', help='Use Coral Edge TPU Accelerator to
speed up detection',
                        action='store_true')

    args = parser.parse_args()

    MODEL_NAME = args.modeldir
    GRAPH_NAME = args.graph
    LABELMAP_NAME = args.labels
    min_conf_threshold = float(args.threshold)
    use_TPU = args.edgetpu

    IM_NAME = image_name
```

```

IM_DIR = 'images'

if (not IM_NAME and not IM_DIR):
    IM_NAME = 'test1.jpg'

if use_TPU:
    if (GRAPH_NAME == 'detect.tflite'):
        GRAPH_NAME = 'edgetpu.tflite'

CWD_PATH = os.getcwd()

if IM_NAME:
    PATH_TO_IMAGES = os.path.join(CWD_PATH, IM_DIR, IM_NAME)
    print(PATH_TO_IMAGES)
    images = glob.glob(PATH_TO_IMAGES)

PATH_TO_CKPT = os.path.join(CWD_PATH, MODEL_NAME, GRAPH_NAME)

PATH_TO_LABELS = os.path.join(CWD_PATH, MODEL_NAME, LABELMAP_NAME)

if labels[0] == '???':
    del(labels[0])

interpreter.allocate_tensors()

input_details = interpreter.get_input_details()
output_details = interpreter.get_output_details()
height = input_details[0]['shape'][1]
width = input_details[0]['shape'][2]

floating_model = (input_details[0]['dtype'] == np.float32)

input_mean = 127.5
input_std = 127.5
outname = output_details[0]['name']

if ('StatefulPartitionedCall' in outname):
    boxes_idx, classes_idx, scores_idx = 1, 3, 0
else:
    boxes_idx, classes_idx, scores_idx = 0, 1, 2

object_list = []
slit_list = []
ref_all = 0
ref_num = 1
for image_path in images:

```

```

image = cv2.imread(image_path)
image_rgb = cv2.cvtColor(image, cv2.COLOR_BGR2RGB)
imH, imW, _ = image.shape
image_resized = cv2.resize(image_rgb, (width, height))
input_data = np.expand_dims(image_resized, axis=0)

if floating_model:
    input_data = (np.float32(input_data) - input_mean) / input_std

interpreter.set_tensor(input_details[0]['index'],input_data)
interpreter.invoke()

boxes = interpreter.get_tensor(output_details[boxes_idx]['index'])[0]
classes = interpreter.get_tensor(output_details[classes_idx]['index'])[0]
scores = interpreter.get_tensor(output_details[scores_idx]['index'])[0]

for i in range(len(scores)):
    if ((scores[i] > min_conf_threshold) and (scores[i] <= 1.0)):
        ymin = int(max(1,(boxes[i][0] * imH)))
        xmin = int(max(1,(boxes[i][1] * imW)))
        ymax = int(min(imH,(boxes[i][2] * imH)))
        xmax = int(min(imW,(boxes[i][3] * imW)))

        cv2.rectangle(image, (xmin,ymin), (xmax,ymax), (10, 255, 0), 2)

        object_name = labels[int(classes[i])]
        label = '%s: %d%%' % (object_name, int(scores[i]*100))
        object_list.append(object_name)
        labelSize, baseLine = cv2.getTextSize(label,
cv2.FONT_HERSHEY_SIMPLEX, 0.7, 2)
        label_ymin = max(ymin, labelSize[1] + 10)

        if object_name == 'ref' :
            minred = 255
            maxblue = 1
            ref_all = 0
            ref_num = 1
            for m in range (ymax-ymin):
                for n in range (xmax-xmin):
                    if image[m+ymin,n+xmin,2] < minred:
                        minred = image[m+ymin,n+xmin,2]
                    if image[m+ymin,n+xmin,0] > maxblue:
                        maxblue = image[m+ymin,n+xmin,0]
            for m in range (ymax-ymin):

```



```

        for n in range (xmax-xmin):
            if image[m+ymin,n+xmin,0]<maxblue-90 or
image[m+ymin,n+xmin,2]>minred+90:
                image[m+ymin,n+xmin] = (0, 0, 0)
            else:
                ref_all += image[m+ymin,n+xmin,2]
                ref_num += 1
                ref_avr = ref_all/ref_num

    if object_name == 'reactionzone' :
        slit_all = 0
        slit_num = 0
        image_ref = image[ymin+int((ymax-ymin)/2),xmin+int((xmax-
xmin)/2)]

        for m in range (ymax-ymin):
            for n in range (xmax-xmin):
                if image[m+ymin,n+xmin,0]>image_ref[0]+20 or
image[m+ymin,n+xmin,0]<image_ref[0]-20:
                    image[m+ymin,n+xmin] = (0, 0, 0)
                else:
                    slit_all += image[m+ymin,n+xmin,1]
                    slit_num += 1

            slit_list.append([ymin,xmin,slit_all/slit_num, label])

    for i in range(len(slit_list)):
        for j in range(0, len(slit_list) - i - 1):
            if slit_list[j][0] > slit_list[j + 1][0]+40 or (slit_list[j][0] <
slit_list[j + 1][0]+40 and slit_list[j][0] > slit_list[j + 1][0]-40 and
slit_list[j][1] > slit_list[j + 1][1] + 40):
                temp = slit_list[j]
                slit_list[j] = slit_list[j+1]
                slit_list[j+1] = temp

    for k in range(len(slit_list)):
        cv2.putText(image, str(k), (slit_list[k][1], slit_list[k][0]),
cv2.FONT_HERSHEY_SIMPLEX, 0.7, (0, 0, 0), 2) # Draw label text

    aftproc_image_name = image_name.split('/')
    print('images/aftproc' + aftproc_image_name[-1])
    if len(object_list) > 0:
        cv2.imwrite('images/aftproc' + aftproc_image_name[-1], image)

    cv2.destroyAllWindows()
    return (object_list, slit_list, ref_all/ref_num)

conn = sqlite3.connect('pads.db')

```

```

cur = conn.cursor()
cur.execute("""CREATE TABLE IF NOT EXISTS pad(
    id INTEGER PRIMARY KEY,
    name TEXT,
    avrredint INT,
    avrgreenint INT,
    avrblueint INT,
    ref INT);
""")
conn.commit()

kit = MotorKit(i2c=board.I2C())

PATH_TO_LABELS = '/home/pi/tflite1/Sample_TFLite_model/labelmap.txt'
with open(PATH_TO_LABELS, 'r') as f:
    labels = [line.strip() for line in f.readlines()]

PATH_TO_CKPT = '/home/pi/tflite1/Sample_TFLite_model/detect.tflite'
pkg = importlib.util.find_spec('tflite_runtime')
if pkg:
    from tflite_runtime.interpreter import Interpreter
else:
    from tensorflow.lite.python.interpreter import Interpreter

interpreter = Interpreter(model_path=PATH_TO_CKPT)

while True:

    print(cur.lastrowid)
    last_row = cur.execute('SELECT id FROM pad ORDER BY id DESC LIMIT
1').fetchall()[-1]

    print(last_row[0])
    TFcam.padder(last_row[0])

    time.sleep(0.5)
    image = '/home/pi/tflite1/images/img' + str(last_row[0]) + '.jpg'

    detected_objects, slit_list, ref= analysis(image, labels, interpreter)
    res = [i:detected_objects.count(i) for i in detected_objects]

    re = ""
    for a in slit_list:
        re = re + str(a[2]) + ";"
    sqllex = "INSERT INTO pad(id, name, avrint, ref) VALUES(NULL, '%s', '%s',
's')" %(image, re, str(ref))
    cur.execute(sqllex)

```

```
conn.commit()

for i in range(500):
    kit.stepper1.onestep()
    time.sleep(0.03)
```

## Appendix D – Object detection function

```
import os
import argparse
import cv2
import numpy as np
import sys
import time
from threading import Thread
import importlib.util
import board
from adafruit_motorkit import MotorKit

global stop_threads

def objectdetection():

    class VideoStream:
        """Camera object that controls video streaming from the Picamera"""
        def __init__(self, resolution=(1280,720), framerate=30):
            self.stream = cv2.VideoCapture(0)
            ret = self.stream.set(cv2.CAP_PROP_FOURCC,
cv2.VideoWriter_fourcc(*'MJPG'))
            ret = self.stream.set(3,resolution[0])
            ret = self.stream.set(4,resolution[1])

            (self.grabbed, self.frame) = self.stream.read()

            self.stopped = False

        def start(self):
            Thread(target=self.update, args=()).start()
            return self

        def update(self):
            while True:
                if self.stopped:
                    self.stream.release()
                    return
                (self.grabbed, self.frame) = self.stream.read()

        def read(self):
            return self.frame

        def stop(self):
            self.stopped = True

    parser = argparse.ArgumentParser()
    parser.add_argument('--modeldir', help='Folder the .tflite file is located
in',
```

```

        default='Sample_TFLite_model')
    parser.add_argument('--graph', help='Name of the .tflite file, if different
than detect.tflite',
        default='detect.tflite')
    parser.add_argument('--labels', help='Name of the labelmap file, if different
than labelmap.txt',
        default='labelmap.txt')
    parser.add_argument('--threshold', help='Minimum confidence threshold for
displaying detected objects',
        default=0.4)
    parser.add_argument('--resolution', help='Desired webcam resolution in WxH.
If the webcam does not support the resolution entered, errors may occur.',
        default='1280x720')
    parser.add_argument('--edgetpu', help='Use Coral Edge TPU Accelerator to
speed up detection',
        action='store_true')

args = parser.parse_args()

MODEL_NAME = args.modeldir
GRAPH_NAME = args.graph
LABELMAP_NAME = args.labels
min_conf_threshold = float(args.threshold)
resW, resH = args.resolution.split('x')
imW, imH = int(resW), int(resH)
use_TPU = args.edgetpu

pkg = importlib.util.find_spec('tflite_runtime')
if pkg:
    from tflite_runtime.interpreter import Interpreter
    if use_TPU:
        from tflite_runtime.interpreter import load_delegate
else:
    from tensorflow.lite.python.interpreter import Interpreter
    if use_TPU:
        from tensorflow.lite.python.interpreter import load_delegate

if use_TPU:

    if (GRAPH_NAME == 'detect.tflite'):
        GRAPH_NAME = 'edgetpu.tflite'

CWD_PATH = os.getcwd()

PATH_TO_CKPT = os.path.join(CWD_PATH,MODEL_NAME,GRAPH_NAME)

PATH_TO_LABELS = os.path.join(CWD_PATH,MODEL_NAME,LABELMAP_NAME)

```

```

with open(PATH_TO_LABELS, 'r') as f:
    labels = [line.strip() for line in f.readlines()]

if labels[0] == '???':
    del(labels[0])

if use_TPU:
    interpreter = Interpreter(model_path=PATH_TO_CKPT,
                             experimental_delegates=[load_delegate('libedget
pu.so.1.0')])
    print(PATH_TO_CKPT)
else:
    interpreter = Interpreter(model_path=PATH_TO_CKPT)

interpreter.allocate_tensors()

input_details = interpreter.get_input_details()
output_details = interpreter.get_output_details()
height = input_details[0]['shape'][1]
width = input_details[0]['shape'][2]

floating_model = (input_details[0]['dtype'] == np.float32)

input_mean = 127.5
input_std = 127.5

outname = output_details[0]['name']

if ('StatefulPartitionedCall' in outname):
    boxes_idx, classes_idx, scores_idx = 1, 3, 0
else:
    boxes_idx, classes_idx, scores_idx = 0, 1, 2

frame_rate_calc = 1
freq = cv2.getTickFrequency()

videostream = VideoStream(resolution=(imW,imH),framerate=30).start()
time.sleep(1)

global take_picture
take_picture = False
while True:

    t1 = cv2.getTickCount()

```

```

frame1 = videostream.read()
frame = frame1.copy()
frame_rgb = cv2.cvtColor(frame, cv2.COLOR_BGR2RGB)
frame_resized = cv2.resize(frame_rgb, (width, height))
input_data = np.expand_dims(frame_resized, axis=0)

if floating_model:
    input_data = (np.float32(input_data) - input_mean) / input_std

interpreter.set_tensor(input_details[0]['index'],input_data)
interpreter.invoke()

boxes = interpreter.get_tensor(output_details[boxes_idx]['index'])[0]
classes = interpreter.get_tensor(output_details[classes_idx]['index'])[0]
scores = interpreter.get_tensor(output_details[scores_idx]['index'])[0]

global stop_threads

if take_picture:
    cv2.imwrite('images/img' + str(picid) + '.jpg', frame)
    stop_threads = True
    cv2.destroyAllWindows()
    videostream.stop()
    break
for i in range(len(scores)):
    if ((scores[i] > min_conf_threshold) and (scores[i] <= 1.0)):

        ymin = int(max(1,(boxes[i][0] * imH)))
        xmin = int(max(1,(boxes[i][1] * imW)))
        ymax = int(min(imH,(boxes[i][2] * imH)))
        xmax = int(min(imW,(boxes[i][3] * imW)))

        cv2.rectangle(frame, (xmin,ymin), (xmax,ymax), (10, 255, 0), 2)

        object_name = labels[int(classes[i])]
        label = '%s: %d%%' % (object_name, int(scores[i]*100))
        labelSize, baseLine = cv2.getTextSize(label,
cv2.FONT_HERSHEY_SIMPLEX, 0.7, 2)
        label_ymin = max(ymin, labelSize[1] + 10)
        cv2.rectangle(frame, (xmin, label_ymin-labelSize[1]-10),
(xmin+labelSize[0], label_ymin+baseLine-10), (255, 255, 255), cv2.FILLED)
        cv2.putText(frame, label, (xmin, label_ymin-7),
cv2.FONT_HERSHEY_SIMPLEX, 0.7, (0, 0, 0), 2)
        if object_name == 'pad' and ymax < 700:
            print (ymin)
            print (ymax)

        take_picture = True

```

```

        cv2.putText(frame, 'FPS:
[0:.2f]'.format(frame_rate_calc),(30,50),cv2.FONT_HERSHEY_SIMPLEX,1,(255,255,0),2
,cv2.LINE_AA)
        cv2.imshow('Object detector', frame)

        t2 = cv2.getTickCount()
        time1 = (t2-t1)/freq
        frame_rate_calc= 1/time1

        if cv2.waitKey(1) == ord('q'):
            break

        if stop_threads:
            break

cv2.destroyAllWindows()
videostream.stop()

def motormove():
    kit = MotorKit(i2c=board.I2C())
    while True:
        kit.stepper1.onestep()
        time.sleep(0.03)
        if stop_threads:
            break
def padfinder(pic_id):
    global stop_threads
    global picid
    picid = pic_id
    stop_threads = False
    t1 = Thread(target=objectdetection)
    t2 = Thread(target=motormove)
    t1.start()
    t2.start()
    while True:
        if stop_threads:
            t1.join()
            t2.join()
            break

```



## Appendix E - System limitations MATLAB code

```
lifetime = 30; %PAD life time (days)
sample_int = 30; %Sample interval in minutes
gap = 10; %Gap between PAD group on roll cm
length_pad = 5; %Length of PAD group for one measurement cm
weight_pap = 80; %Weight per unit area of paper g/m2
weight_lam = 175; %Weight per unit area of laminate g/m2
wheel_weight = 100; %wheel weight g
pad_width = 8; %PAD width cm
d_core= 5; %Diameter of roll core cm
lam_thi = 0.125; %Thickness of laminate mm
thickness = 0.1; %Thickness of paper mm
n = 2; %Number of paper layers in PAD
box_length = 55; % Length (cm) of waterproof case

D = box_length - 20;

t=(thickness*n+lam_thi*2)/10;
di=sprintf('total thickness = %g cm' ,t);
disp(di);

L2 = ((D/2)*(D/2)-d_core*d_core/4)*pi/t;

di=sprintf('Length of sampling = %g cm' ,L2);
disp(di);

L=(length_pad+gap)*lifetime*sample_int;

num_samples = ceil(L2/(length_pad+gap));

di=sprintf('Total number of samples = %g' ,num_samples);
disp(di);

duration = num_samples*sample_int/24/60;

if (duration < lifetime)
di=sprintf('Total duration of sampling = %g days' ,duration);
disp(di);
else
di=sprintf('Total duration of sampling = %g days warning duration is grater than
lifetime of the PAD' ,duration);
disp(di);
end

di=sprintf('Maximum diameter of PAD roll on full roll = %g cm' ,D);
disp(di);

total_weight=(weight_pap*n+weight_lam*2)*L2*pad_width/10000+wheel_weight;

di=sprintf('Total weight of the roll with PADs = %g g' ,total_weight);
disp(di);
```

## Appendix F – Carbonates BCG buffer solution preparation method

To create the reagent for a carbonate PAD, the following essential components are required:

- **Laboratory Scales:**  
Laboratory scales are indispensable instruments for precise and accurate measurements of different substances. The ability to weigh the exact amounts of reagents and materials is crucial in ensuring the device's optimal performance.
- **Sonicator:**  
A sonicator, also known as an ultrasonic homogenizer, is necessary for the preparation of solutions. It uses ultrasonic waves to disperse, mix and dissolve substances, ensuring an even distribution of components inside the solution. The sonicator helps to eliminate any air bubbles or clumps, increasing the overall reliability of the analytical device.
- **pH Meter:**  
To determine the acidity or alkalinity of solutions incorporated into the device, a pH meter is fundamental. Accurate pH measurements are crucial for assessing the device's sensitivity and reliability, as certain reactions and processes are highly dependent on the pH level. The pH meter guarantees the optimization of the paper-based analytical device, enabling it to deliver precise and consistent results across different test scenarios.
- **Wax Printer:**  
The wax printer plays a key role in the fabrication of the paper-based analytical device. It allows to precisely set of hydrophobic barriers on the paper, defining the fluidic pathways and containment zones. These hydrophobic barriers ensure controlled fluid flow and prevent unwanted spreading, thereby enhancing the device's efficiency and accuracy.  
a wax printer.

The following is an instruction for preparing the solution, all numerical values of the reagents were obtained experimentally:

1. **Gather the Required Materials:**  
Ensure you have all the necessary materials ready, including sodium citrate, citric acid, BCG reagents, a volumetric flask (50 mL), MilliQ water, a sonicator, PDADMAC (poly(dimethyl diallyl ammonium chloride)), NaOH (sodium hydroxide), and HCl (hydrochloric acid).
2. **Weigh out Sodium Citrate and Citric Acid:**  
Using a laboratory scale, accurately weigh out 0.639 g of sodium citrate and 0.412 g of citric acid. These two components will form the main buffer system.

3. **Combine the Powders in the Volumetric Flask:**  
Carefully add the weighed sodium citrate and citric acid powders to the 50 mL volumetric flask. The volumetric flask provides accurate volume measurement, ensuring a precise buffer concentration.
4. **Weigh and Add BCG:**  
Next, weigh out 0.02 g of BCG and add this to the same volumetric flask containing the sodium citrate and citric acid. The BCG act as indicators for detecting specific pH ranges, allowing for accurate pH determination in the buffer solution.
5. **Fill with MilliQ Water:**  
Now, fill the volumetric flask to the 50 mL mark using MilliQ water. Gradually add the water to avoid splashing or overfilling. Ensure all the components are well-dissolved in the water for a homogenous buffer solution.
6. **Dissolve Using Sonicator if Necessary:**  
If the BCG was not fully dissolved during the previous step, utilize the sonicator to achieve complete dissolution.
7. **Add PDADMAC:**  
To enhance the stability and performance of the buffer solution, add 2.5 mL of PDADMAC to the mixture in the volumetric flask. PDADMAC serves as a stabilizing agent, contributing to the overall effectiveness of the buffer.
8. **Measure the pH and Adjust:**  
Using a pH meter, measure the pH of the solution. The desired pH value should be within the range of the buffer system's intended use. If the pH falls outside the desired range, carefully adjust it using either NaOH (sodium hydroxide) to increase pH or HCl (hydrochloric acid) to decrease pH. Make gradual adjustments and recheck the pH until the target value is achieved.
9. **Final Check and Storage:**  
Perform a final check to ensure that the buffer solution meets the desired pH and concentration requirements. If everything is satisfactory, the buffer solution is now ready for use. Store it in a suitable container with proper labeling and keep it in appropriate conditions to maintain its stability and effectiveness over time.

After preparing the BCG buffer solution using the meticulous steps outlined earlier, the next crucial stage involves pipetting the solution onto each reaction spot of the PAD. Follow these steps to ensure a successful application of the buffer:

1. **Pipette 5 $\mu$ L of BCG Buffer Solution:**  
Using a micropipette with precise volume control, carefully pipette 5 $\mu$ L of the BCG buffer solution onto each designated reaction spot of the device.

- This step ensures that the required volume of buffer is accurately dispensed to initiate the chemical reactions necessary for the device's intended purpose.
2. Check for Darker Spots of BCG:  
After pipetting the buffer solution, inspect the reaction spots for any darker patches or concentrated areas of BCG. If such spots are detected, it indicates uneven distribution of the reagents on the device, which could potentially affect the accuracy of the results.
  3. Discard the Problematic PADs:  
In the event of detecting darker spots or uneven BCG distribution, it is essential to discard the problematic devices, as they may not provide reliable and consistent results. Quality control is critical at this stage to ensure that only properly functioning devices move forward in the testing process.
  4. Sonicate the Buffer Solution (if necessary):  
For any discarded devices or if there are concerns about incomplete BCG mixing, it's important to address this issue promptly. If required, use the sonicator to thoroughly mix the buffer solution, ensuring an even distribution of BCG throughout the solution. The sonication process disperses any aggregated BCG particles, leading to a more homogeneous mixture.
  5. Dry the Devices:  
Once the pipetting and BCG mixing stages are complete, proceed to dry the devices before further use. Drying is a crucial step to stabilize the reagents and prevent unwanted interactions. There are two options for drying the devices:
    - a) Room Temperature Drying (1-2 Hours):  
Place the devices in a clean and dry environment at room temperature. Allow them to air-dry for 1 to 2 hours. This gradual drying process ensures gentle removal of the solvent and water content from the reaction spots.
    - b) Oven Drying (60°C for 10 Minutes):  
Alternatively, if time is limited or for faster drying, place the devices in an oven set to 60°C for approximately 10 minutes. Ensure proper ventilation during this process to prevent any undesirable effects due to excessive heat.
  6. Confirm Drying Completion:  
After the specified drying period, visually inspect the devices to ensure that all reaction spots are thoroughly dried. Proper drying ensures that the reagents remain stable and ready for subsequent steps in the experimental process.

## Appendix G - Mechanical design

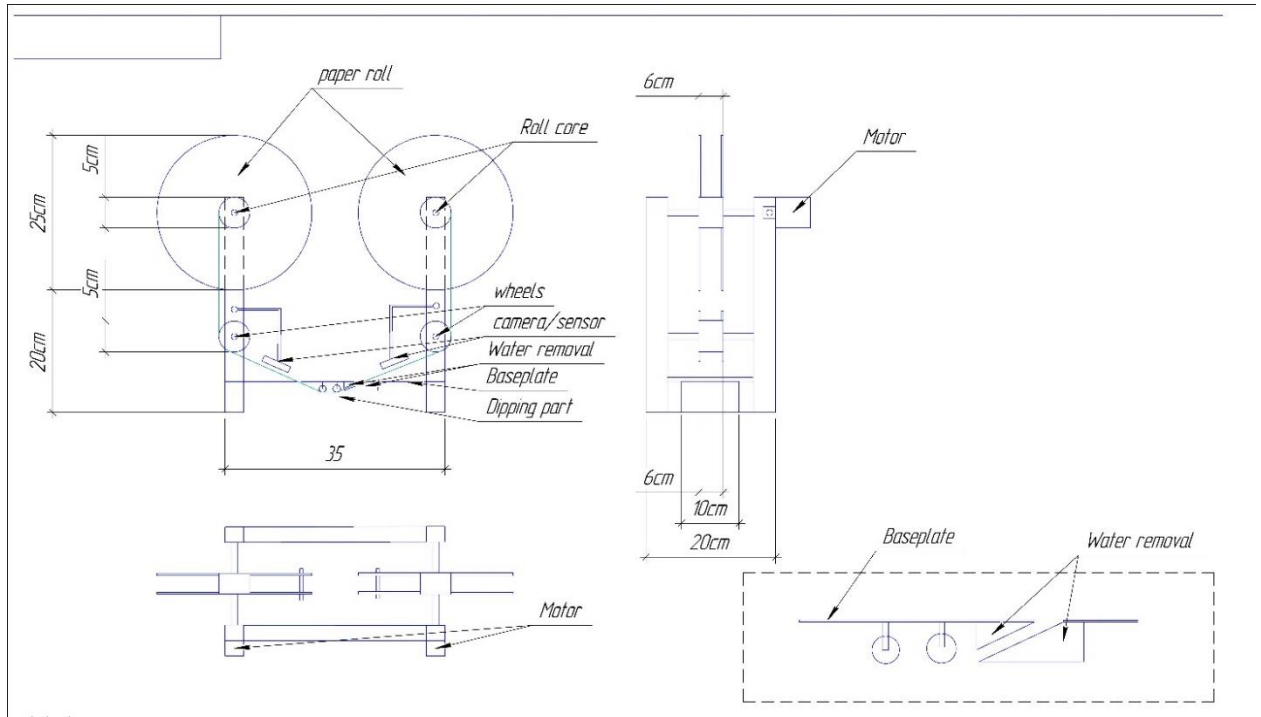


Figure 95. Mechanical design

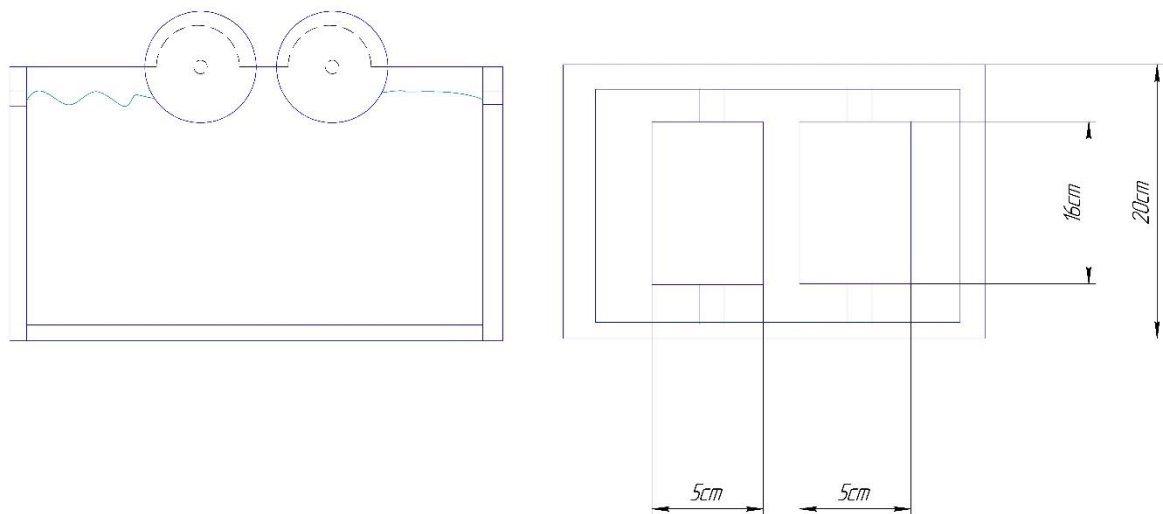


Figure 96. Water tank

## Appendix H - LTSpice filter implementation

In order to practically implement the described filtering processes, LTSpice software was used to simulate and analyse the behaviour of the system. The idea is creating an RC Antialiasing Filter (tank analogue) by utilizing a capacitor (C) with a value of 1 Farad and a resistor (R) of 1,500 Ohms, resulting in a cut-off frequency ( $f_c$ ) of 106.1  $\mu$ Hz.

To ensure accurate reconstruction, a Butterworth low-pass filter is used as the reconstruction filter. This filter is designed with the same cut-off frequency as the tank system and is realized as a 6th order filter. Its implementation involves utilizing three 2nd order low-pass LTSpice components, each designed to replicate the required characteristics. To configure these components accurately, standard filter design parameters were used, presented in the note to the TI application note SLOA049D entitled "Active low-pass filter Design", dated February 2023. These design parameters are taken from Table 9.1 "Butterworth Filter Table".

The developed Butterworth filter demonstrates a gain of 1 for each stage. The values of the quality factor (Q) for individual stages are carefully selected to ensure optimal filter performance. Schematic is shown in Figure 97. These Q values are assigned as follows:

Stage 1:  $Q = 0.5177$

Stage 2:  $Q = 0.7071$

Stage 3:  $Q = 1.9320$

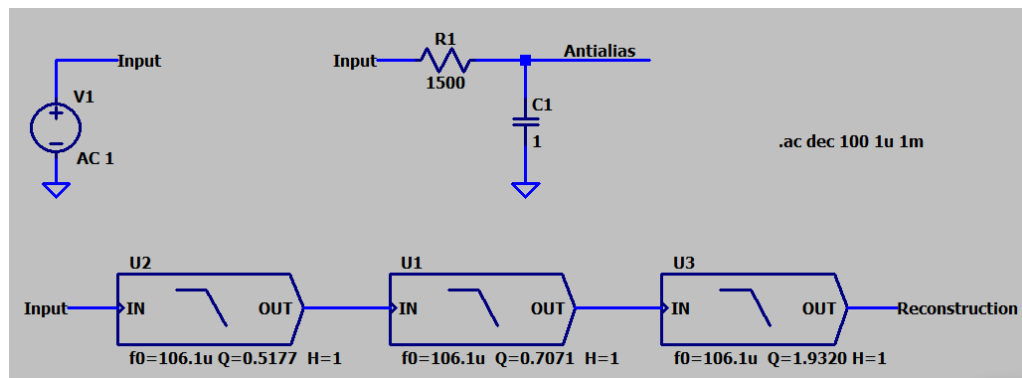


Figure 97. Filtering schematic

With these carefully defined parameters in mind, the next step involves confirming the functionality of the implemented filters. This is achieved by conducting an alternating current analysis, which allows to obtain the frequency response of the filters. It is noteworthy that the -3 dB point in the frequency response means the cut-off frequency, and, as expected, both the RC smoothing filter and the Butterworth reduction filter demonstrate a -3 dB point at a frequency of 106  $\mu$ Hz (Figure 98).

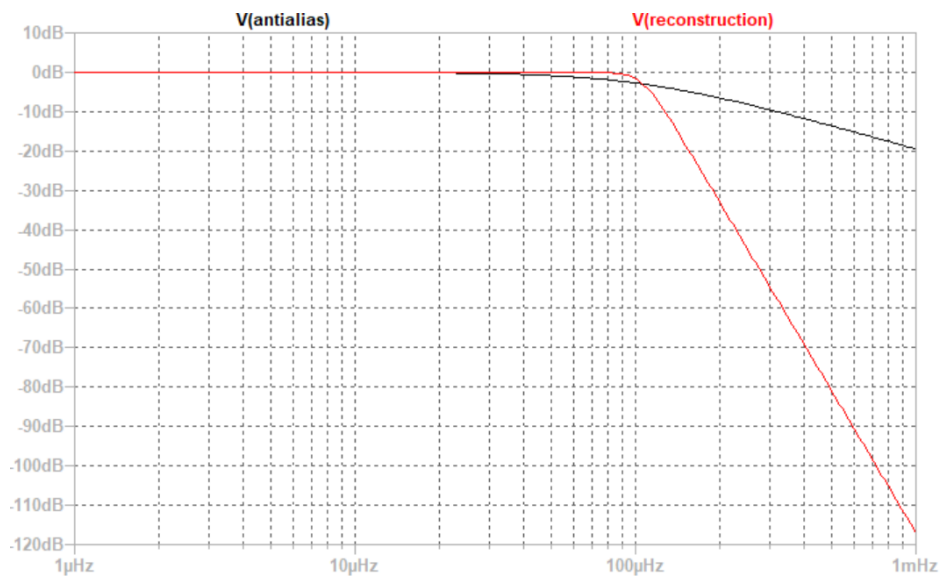


Figure 98. Filters response

By modelling the system and confirming its operation with LTspice, a practical understanding of the behaviour of filters and their impact on signal processing can be achieved. This approach bridges the gap between theoretical understanding and actual application, allowing to test the expected behaviour of filters under the described conditions.

### Simulate Sampling Without Anti-aliasing Filter

In order to clearly show the significance of the anti-aliasing filter, a simulation of the system where it is absent was carried out. The scheme is shown Figure 99 .

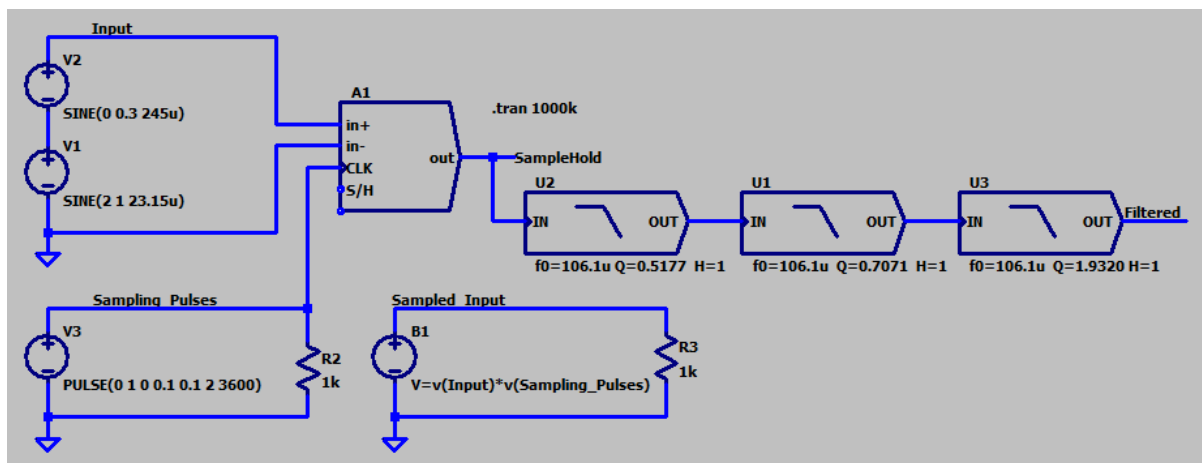


Figure 99. Schematic without anti-aliasing filter

In this scheme, concentration signals are simulated using voltage sources V1 and V2. These sources are used to simulate the behaviour of concentration signals as sine waves, with frequencies aligned to those defined in the example model—namely, 23.15  $\mu\text{Hz}$  and 240.0  $\mu\text{Hz}$ . Low frequency (non-aliasing) signal is at amplitude 1.0 V and high frequency (aliasing) signal at level 0.3 V. DC offset of

2.0 V added so that concentration signal does not become negative (which is possible for a voltage, but not physically meaningful as an analogy for concentration).

Sampling is implemented using LTspice “Sample” component (special functions behavioural device with sample and hold functionality). The output latches the input value when the CLK input goes true (alternative behaviour is available using the S/H input, but this is not needed here). LTspice logic signals default to 0V/1V false/true logic with a logic threshold of 0.5V. The sampling signal is a 1.0 V pulse waveform generated by source V3 with period 3600 s (1 hour) defined in the example model. The pulse duration is 2.0 s and the rise and fall times are 0.1s. The Sample component has a default output resistance of 1kΩ, as it is not loaded in this circuit this is not changed. It also has a default output voltage range of ±10 V, as this is not exceeded here this is not changed.

The sample pulses are not available directly from the Sample component so are obtained separately using behavioural voltage source B1 to implement  $x_s(t) = p(t)x(t)$ .

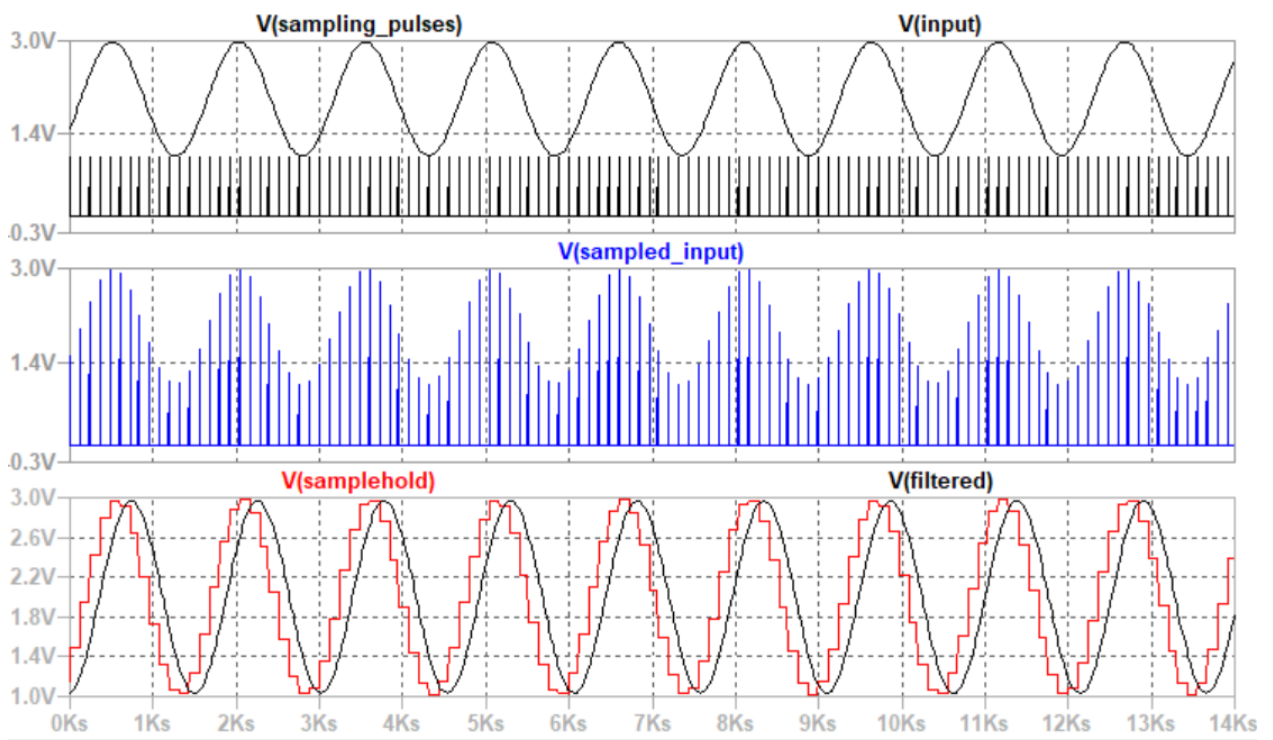


Figure 100. Results without the aliasing signal (source V2 set to 0.0 V amplitude).



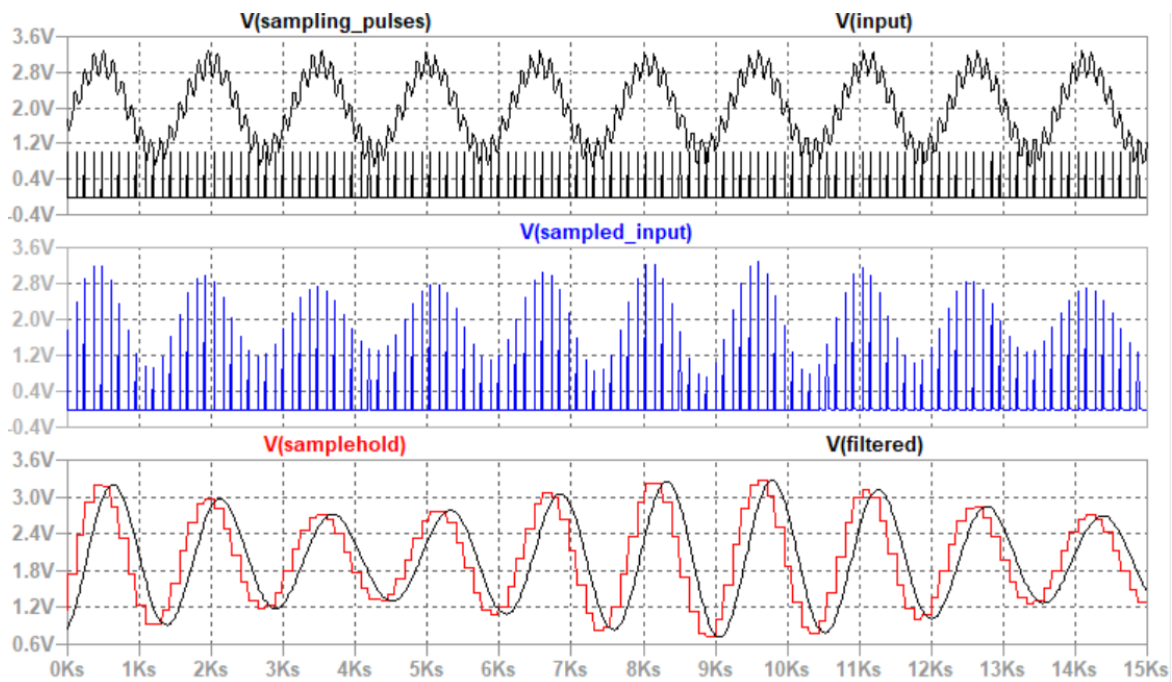


Figure 101. With the aliasing signal at 0.3V (30% of the amplitude of the non-aliasing signal)

The aliasing results in apparent variation of the amplitude of 12 hour (23.15  $\mu$ Hz) signal, which is actually constant (Figure 100 shows results without the aliasing signal, Figure 101 with the aliasing signal). If this was real data it would lead to potential misinterpretation. In this case the aliasing causes a regular variation, but the interactions in real concentration measurements would be more complex and difficult to attribute to specific aliasing signals.

A RC circuit can be added to model the tank (as defined in the example model).

Using the tank, the effect of the aliasing signal is reduced significantly, but not eliminated. In electronic systems higher order, sharper cut-off filters could be used, but this is not feasible with a tank. The scheme is shown in Figure 102 and results in Figure 103

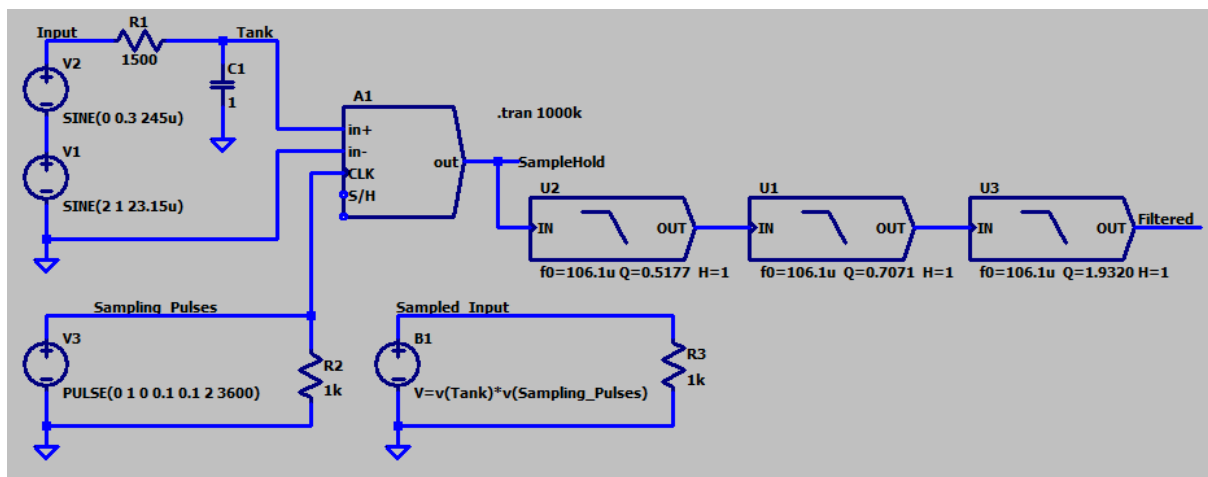


Figure 102. Schematic with anti-aliasing filter

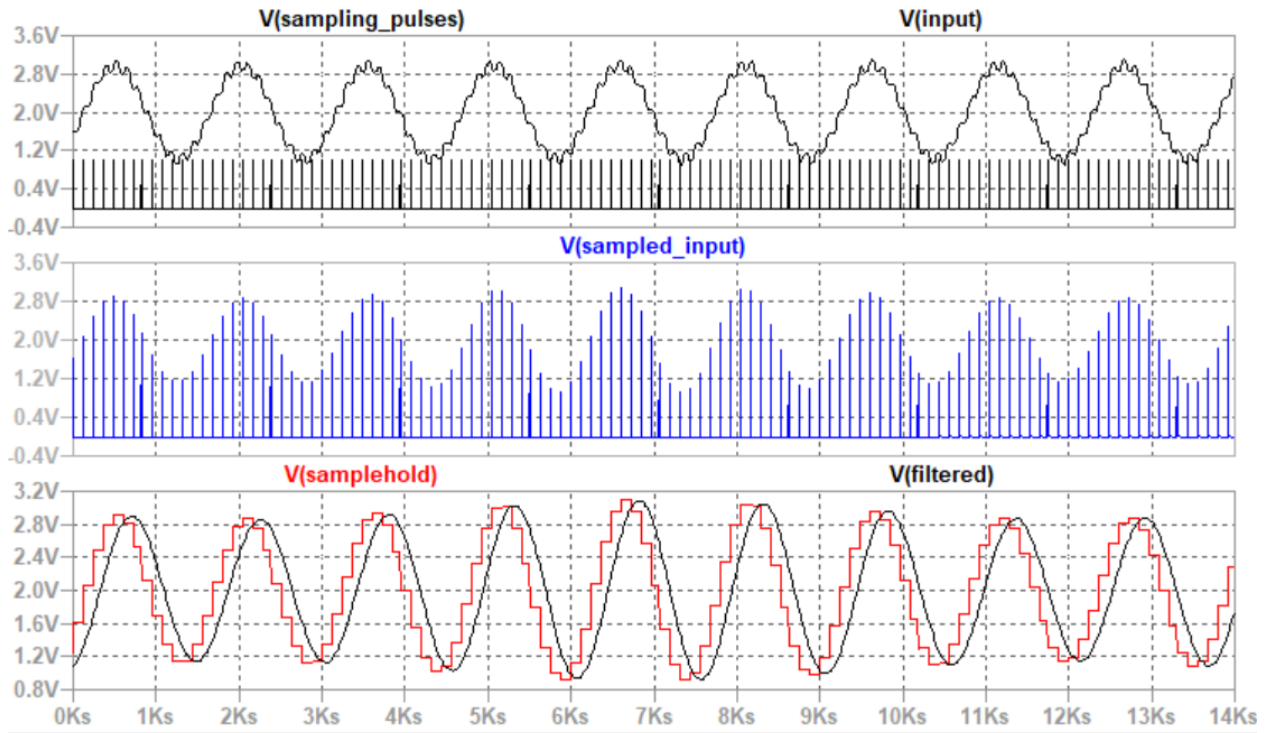


Figure 103. Results with the aliasing filter

## Appendix I – Automated measurement system (MATLAB)

```
clear; clc;
xx=imread('sample', 'jpeg');
%spatial resolution

x=imresize(xx,[312 416]);
x1=imresize(xx,[312 416]);

for m = 1:312
    for n = 1:416
        if ((x(m,n,1)>= 140)&&(x(m,n,2)>= 140)&&(x(m,n,3)>= 140))
            x(m,n,1) = 0;
            x(m,n,2) = 0;
            x(m,n,3) = 0;
        end
    end
end

y=x(:,:,1);
%y=rgb2gray(xx);
```

```
figure (1)
subplot(1,2,1), subimage(x);
subplot(1,2,2), subimage(y);
```

```
bw = im2bw(y,0.5);
% bwi = bwinv(bw);
bwi=bw;
[L,num] = bwlabel(bwi,4);
areas = bwareas(L,num);
bws1 = bwsublow(L,areas,max(areas)-1);
[L,num] = bwlabel(bws1,4);
areas = bwareas(L,num);
bws11 = bwsubhigh(L,areas,max(areas)+1);
figure (2)
subplot(1,2,1), subimage(bwi);
subplot(1,2,2), subimage(bws11);
% subplot(1,3,3), subimage(bws1);
```

```
bws = bwinv(bws11);
[L1,num1] = bwlabel(bws,4);
areas1 = bwareas(L1,num1);
bws1 = bwsublow(L1,areas1,max(areas1)-1);
```

```

figure (3)
subplot(1,2,1), subimage(bws);
subplot(1,2,2), subimage(bws1);

for m = 1:312
    for n = 1:416
        if ((bws1(m,n)== 1)|| (bws11(m,n)== 1))
            x1(m,n,1) = 0;
            x1(m,n,2) = 0;
            x1(m,n,3) = 0;
        end
    end
end
end

```

```

figure (3)
subplot(1,2,1), subimage(x1);
subplot(1,2,2), subimage(bws1);

```

```
po=rgb2gray(x1);
```

```

[L2,num2] = bwlabel(po,4);
areas2 = bwareas(L2,num2);
tt = bwsublow(L2,areas2,max(areas2)-1000);

```

```

figure (4)
subplot(1,2,1), subimage(x1);
subplot(1,2,2), subimage(tt);

```

```
[cir,num_cir] = bwlabel(tt,4);
```

```

int_blue(1) = 0;
pix_num(1) = 0;
int_avr(1)=0;
areas_cir = bwareas(cir,1);
cir_blue = bwsublow(cir,areas_cir,max(areas_cir)-500);
for m = 1:312
    for n = 1:416
        if (cir_blue(m,n)== 1)
            int_blue(1) = int_blue(1) + int32(x1(m,n,3));
            pix_num(1) = pix_num(1) + 1;
        end
    end
end
int_avr(1) = int_blue(1)/pix_num(1);

```

```

figure (5)
subplot(1,2,1), subimage(x1);
subplot(1,2,2), subimage(cir_blue);

```

```

int_blue(2) = 0;
pix_num(2) = 0;
int_avr(2)=0;
areas_cir = bwareas(cir,2);
cir_blue = bwsublow(cir,areas_cir,max(areas_cir)-500);
for m = 1:312
    for n = 1:416
        if (cir_blue(m,n)== 1)
            int_blue(2) = int_blue(2) + int32(x1(m,n,3));
            pix_num(2) = pix_num(2) + 1;

        end
    end
end
int_blue(2) = int_blue(2) - int_blue(1);
pix_num(2) = pix_num(2) - pix_num(1);
int_avr(2) = int_blue(2)/pix_num(2);

```

```

figure (6)
subplot(1,2,1), subimage(x1);
subplot(1,2,2), subimage(cir_blue);

```

```

int_blue(3) = 0;
pix_num(3) = 0;
int_avr(3)=0;
areas_cir = bwareas(cir,3);
cir_blue = bwsublow(cir,areas_cir,max(areas_cir)-500);
for m = 1:312
    for n = 1:416
        if (cir_blue(m,n)== 1)
            int_blue(3) = int_blue(3) + int32(x1(m,n,3));
            pix_num(3) = pix_num(3) + 1;

        end
    end
end
int_blue(3) = int_blue(3) - int_blue(2) - int_blue(1);
pix_num(3) = pix_num(3) - pix_num(2) - pix_num(1);
int_avr(3) = int_blue(3)/pix_num(3);

```

```

int_blue(4) = 0;
pix_num(4) = 0;
int_avr(4)=0;
areas_cir = bwareas(cir,4);
cir_blue = bwsublow(cir,areas_cir,max(areas_cir)-500);
for m = 1:312
    for n = 1:416
        if (cir_blue(m,n)== 1)

```

```

        int_blue(4) = int_blue(4) + int32(x1(m,n,3));
        pix_num(4) = pix_num(4) + 1;

    end

end

int_blue(4) = int_blue(4) - int_blue(3) - int_blue(2) - int_blue(1);
pix_num(4) = pix_num(4) - pix_num(3) - pix_num(2) - pix_num(1);
int_avr(4) = int_blue(4)/pix_num(4);

int_blue(5) = 0;
pix_num(5) = 0;
int_avr(5)=0;
areas_cir = bwareas(cir,5);
cir_blue = bwsublow(cir,areas_cir,max(areas_cir)-500);
for m = 1:312
    for n = 1:416
        if (cir_blue(m,n)== 1)
            int_blue(5) = int_blue(5) + int32(x1(m,n,3));
            pix_num(5) = pix_num(5) + 1;

        end

    end

end

int_blue(5) = int_blue(5) - int_blue(4) - int_blue(3) - int_blue(2) -
int_blue(1);
pix_num(5) = pix_num(5) - pix_num(4) - pix_num(3) - pix_num(2) - pix_num(1);
int_avr(5) = int_blue(5)/pix_num(5);

int_blue(6) = 0;
pix_num(6) = 0;
int_avr(6)=0;
areas_cir = bwareas(cir,6);
cir_blue = bwsublow(cir,areas_cir,max(areas_cir)-500);
for m = 1:312
    for n = 1:416
        if (cir_blue(m,n)== 1)
            int_blue(6) = int_blue(6) + int32(x1(m,n,3));
            pix_num(6) = pix_num(6) + 1;

        end

    end

end

int_blue(6) = int_blue(6) - int_blue(5) - int_blue(4) - int_blue(3) - int_blue(2)
- int_blue(1);
pix_num(6) = pix_num(6) - pix_num(5) - pix_num(4) - pix_num(3) - pix_num(2) -
pix_num(1);
int_avr(6) = int_blue(6)/pix_num(6);

```

```

int_blue(7) = 0;
pix_num(7) = 0;
int_avr(7)=0;
areas_cir = bwareas(cir,7);
cir_blue = bwsublow(cir,areas_cir,max(areas_cir)-500);
for m = 1:312
    for n = 1:416
        if (cir_blue(m,n)== 1)
            int_blue(7) = int_blue(7) + int32(x1(m,n,3));
            pix_num(7) = pix_num(7) + 1;

        end
    end
end
int_blue(7) = int_blue(7) - int_blue(6) - int_blue(5) - int_blue(4) - int_blue(3)
- int_blue(2) - int_blue(1);
pix_num(7) = pix_num(7) - pix_num(6) - pix_num(5) - pix_num(4) - pix_num(3) -
pix_num(2) - pix_num(1);
int_avr(7) = int_blue(7)/pix_num(7);

int_blue(8) = 0;
pix_num(8) = 0;
int_avr(8)=0;
areas_cir = bwareas(cir,8);
cir_blue = bwsublow(cir,areas_cir,max(areas_cir)-500);
for m = 1:312
    for n = 1:416
        if (cir_blue(m,n)== 1)
            int_blue(8) = int_blue(8) + int32(x1(m,n,3));
            pix_num(8) = pix_num(8) + 1;

        end
    end
end
int_blue(8) = int_blue(8) - int_blue(7) - int_blue(6) - int_blue(5) - int_blue(4)
- int_blue(3) - int_blue(2) - int_blue(1);
pix_num(8) = pix_num(8) - pix_num(7) - pix_num(6) - pix_num(5) - pix_num(4) -
pix_num(3) - pix_num(2) - pix_num(1);
int_avr(8) = int_blue(8)/pix_num(8);

```

## Appendix J – Camera and sensor comparison MATLAB code

```
clear;clc;

clear;

clc;

pH5_9 = xlsread('pH5_9.xlsx');
pH5_17 = xlsread('pH5_17.xlsx');
pH4_9 = xlsread('pH4_9.xlsx');
pH4_6 = xlsread('pH4_6.xlsx');
pH4_13 = xlsread('pH4_13.xlsx');
pH3_8 = xlsread('pH3_8.xlsx');
pH3_5 = xlsread('pH3_5.xlsx');
pH2_94 = xlsread('pH2_94.xlsx');

pH5_9(:,3) = 5.9;
pH5_17(:,3) = 5.17;
pH4_9(:,3) = 4.9;
pH4_6(:,3) = 4.6;
pH4_13(:,3) = 4.13;
pH3_8(:,3) = 3.8;
pH2_94(:,3) = 2.94;

pHH = cat(1,pH5_9,pH5_17,pH4_9,pH4_6,pH4_13,pH3_8,pH2_94);
pHH2(:,1) = pHH(:,3);
pHH2(:,3) = pHH(:,1);

figure (1)
surf (pHH2);

x=400:0.1:700;

led = xlsread('LED.xlsx');
```



```

%led =
[350,400,450,475,500,540,590,625,675,725,800;0,0,1,0.3,0.4,0.56,0.48,0.5,0.3,0.1,
0];
% figure (1)
% plot(led(:,1),led(:,2))

led_wave = led(:,1);
led_int = led(:,2);

led_int = interp1 (led_wave,led_int,x,'PCHIP');

% sens_1 = normpdf(x,450,17);
% sens_2 = normpdf(x,500,17);
% sens_3 = normpdf(x,550,17);
% sens_4 = normpdf(x,570,17);
% sens_5 = normpdf(x,600,17);
% sens_6 = normpdf(x,650,17);
%
% sens_1 = sens_1/max(sens_1);
% sens_2 = sens_2/max(sens_2);
% sens_3 = sens_3/max(sens_3);
% sens_4 = sens_4/max(sens_4);
% sens_5 = sens_5/max(sens_5);
% sens_6 = sens_6/max(sens_6);

sens_1 = xlsread('sens_1.xlsx');
sens_2 = xlsread('sens_2.xlsx');
sens_3 = xlsread('sens_3.xlsx');
sens_4 = xlsread('sens_4.xlsx');
sens_5 = xlsread('sens_5.xlsx');
sens_6 = xlsread('sens_6.xlsx');

camera_blue = xlsread('camera_blue.xlsx');

```

```

camera_green = xlsread('camera_green.xlsx');
camera_red = xlsread('camera_red.xlsx');

camera_b_int = interp1 (camera_blue(:,1),camera_blue(:,2),x, 'PCHIP');
camera_g_int = interp1 (camera_green(:,1),camera_green(:,2),x, 'PCHIP');
camera_r_int = interp1 (camera_red(:,1),camera_red(:,2),x, 'PCHIP');

camera_b_int = camera_b_int./100;
camera_g_int = camera_g_int./100;
camera_r_int = camera_r_int./100;

```

figure (2)

```

plot(x, [camera_b_int' camera_g_int' camera_r_int']);

```

```

sens_1_int = interp1 (sens_1(:,1),sens_1(:,2),x, 'PCHIP');
sens_2_int = interp1 (sens_2(:,1),sens_2(:,2),x, 'PCHIP');
sens_3_int = interp1 (sens_3(:,1),sens_3(:,2),x, 'PCHIP');
sens_4_int = interp1 (sens_4(:,1),sens_4(:,2),x, 'PCHIP');
sens_5_int = interp1 (sens_5(:,1),sens_5(:,2),x, 'PCHIP');
sens_6_int = interp1 (sens_6(:,1),sens_6(:,2),x, 'PCHIP');

```

figure (3)

```

plot(x, [sens_1_int' sens_2_int' sens_3_int' sens_4_int' sens_5_int'
sens_6_int']);

```

```

y(1,:) = interp1 (pH5_9(:,1),pH5_9(:,2),x, 'PCHIP');
y(2,:) = interp1 (pH5_17(:,1),pH5_17(:,2),x, 'PCHIP');
y(3,:) = interp1 (pH4_9(:,1),pH4_9(:,2),x, 'PCHIP');
y(4,:) = interp1 (pH4_6(:,1),pH4_6(:,2),x, 'PCHIP');
y(5,:) = interp1 (pH4_13(:,1),pH4_13(:,2),x, 'PCHIP');
y(6,:) = interp1 (pH3_8(:,1),pH3_8(:,2),x, 'PCHIP');
y(7,:) = interp1 (pH3_5(:,1),pH3_5(:,2),x, 'PCHIP');
y(8,:) = interp1 (pH2_94(:,1),pH2_94(:,2),x, 'PCHIP');

```

```

figure (4)
plot(x, [y(1,:) y(2,:) y(3,:) y(4,:) y(5,:) y(6,:) y(7,:) y(8,:)]);

for i = 1:8
    a = y(i,:);
    sens_1_resp = sens_1_int.*led_int./(1.-a/2);
    sens_2_resp = sens_2_int.*led_int./(1.-a/2);
    sens_3_resp = sens_3_int.*led_int./(1.-a/2);
    sens_4_resp = sens_4_int.*led_int./(1.-a/2);
    sens_5_resp = sens_5_int.*led_int./(1.-a/2);
    sens_6_resp = sens_6_int.*led_int./(1.-a/2);

    camera_b_resp = camera_b_int.*led_int./((1.-a/2));
    camera_g_resp = camera_g_int.*led_int./((1.-a/2));
    camera_r_resp = camera_r_int.*led_int./((1.-a/2));

    %integration
    sens_out (i,1) = trapz (x,sens_1_resp);
    sens_out (i,2) = trapz (x,sens_2_resp);
    sens_out (i,3) = trapz (x,sens_3_resp);
    sens_out (i,4) = trapz (x,sens_4_resp);
    sens_out (i,5) = trapz (x,sens_5_resp);
    sens_out (i,6) = trapz (x,sens_6_resp);

    camera (i,1) = trapz (x,camera_b_resp);
    camera (i,2) = trapz (x,camera_g_resp);
    camera (i,3) = trapz (x,camera_r_resp);
%plot(x, [sens_1' sens_2' sens_3' sens_4' sens_5' sens_6']);

```

```
end
```

```
pH = [5.9,5.17,4.9,4.6,4.13,3.8,3.5,2.94];
```

```
% figure (2)
```

```
% plot (pH, sens_out(:,6))
```

```
abc = interp1 (sens_out(:,1),pH,30,'PCHIP');
```

```
%sens_out = [7.59759647537725 6.36251084936502 4.40371172219997 2.54053684286316  
0.797209119073164 2.94946485193930;6.07480268334696 5.99325865031792  
5.04705432514710 3.13030691781745 1.14805786885976  
3.46563220751126;4.40782019353861 5.78167996781363 7.01252417737779  
5.11071466624264 2.57172331735265 5.01891636735292;3.79328004732161  
5.74015477313616 8.37399629348841 6.65040843038503 3.94118169308427  
6.25159322688878;3.11926824032261 5.63545455830493 10.4937061795234  
9.33383469182735 6.69689762391016 8.30993655933348;2.77359488784079  
5.65846388237607 12.6760494758835 12.3416969331000 10.4547740297629  
10.9275437375146;2.62685677222606 5.57379202347552 14.1870299837303  
14.5237236119761 13.2006752844683 12.5487381988550;2.50403431050539  
5.45022024876547 15.1525653110024 16.1700692915935 15.6606541485262  
14.1925405263400];  
pH = [5.9,5.17,4.9,4.6,4.13,3.8,3.5,2.94];
```

```
%camera = [11.4242529103293 13.0940814301681 6.41193701499344;9.88757963698167  
13.5651949519029 7.20238607183284;8.53415746595782 16.1896011031989  
10.0760464536801;8.20244709351965 18.3253708118310  
12.6224581964116;7.96232541248830 21.8714456132951  
17.2817500420481;8.20448846914528 26.1347019565169  
23.4992994816168;8.41874977635325 29.0269177349441  
27.8443235524540;8.56640691553001 31.1397775306127 31.8310772595067];
```

```
ppH = 3.2:0.1:5.5;
```

```
dat1 = interp1 (pH,sens_out(:,1),ppH,'PCHIP');
```

```
dat2 = interp1 (pH,sens_out(:,2),ppH,'PCHIP');
```

```
dat3 = interp1 (pH,sens_out(:,3),ppH,'PCHIP');
```

```
dat4 = interp1 (pH,sens_out(:,4),ppH,'PCHIP');
```

```

dat5 = interp1 (pH,sens_out(:,5),ppH,'PCHIP');
dat6 = interp1 (pH,sens_out(:,6),ppH,'PCHIP');

camera_blue = interp1 (pH,camera(:,1),ppH,'PCHIP');
camera_green = interp1 (pH,camera(:,2),ppH,'PCHIP');
camera_red = interp1 (pH,camera(:,3),ppH,'PCHIP');

camera_blue = camera_blue./2
camera_green = camera_green./2
camera_red = camera_red./2

figure (1)
plot (ppH, [dat1' dat2' dat3' dat4' dat5' dat6'])

figure (2)
plot (ppH, [camera_blue' camera_green' camera_red'])

av_error = 0;
av_wheight_error = 0;
av_error_cam = 0;
av_wheight_error_cam = 0;

for i = 1:10000
    pH_val = 2.2*rand+3.25;
    %pH_val = [4.12555065153409];
    sens_1 = interp1 (ppH,dat1,pH_val,'PCHIP');
    sens_2 = interp1 (ppH,dat2,pH_val,'PCHIP');
    sens_3 = interp1 (ppH,dat3,pH_val,'PCHIP');
    sens_4 = interp1 (ppH,dat4,pH_val,'PCHIP');
    sens_5 = interp1 (ppH,dat5,pH_val,'PCHIP');
    sens_6 = interp1 (ppH,dat6,pH_val,'PCHIP');
    camera_b = interp1 (ppH,camera_blue,pH_val,'PCHIP');

```

```

camera_g = interp1 (ppH,camera_green,pH_val, 'PCHIP');
camera_r = interp1 (ppH,camera_red,pH_val, 'PCHIP');

sens_1_real = sens_1 + sens_1*(0.5 - rand)*0.02;
sens_2_real = sens_2 + sens_2*(0.5 - rand)*0.02;
sens_3_real = sens_3 + sens_3*(0.5 - rand)*0.02;
sens_4_real = sens_4 + sens_4*(0.5 - rand)*0.02;
sens_5_real = sens_5 + sens_5*(0.5 - rand)*0.02;
sens_6_real = sens_6 + sens_6*(0.5 - rand)*0.02;
camera_b_real = camera_b + camera_b*(0.5 - rand)*0.02;
camera_g_real = camera_g + camera_g*(0.5 - rand)*0.02;
camera_r_real = camera_r + camera_r*(0.5 - rand)*0.02;

pH_sens1 = interp1 (dat1,ppH,sens_1_real, 'PCHIP');
pH_sens2 = interp1 (dat2,ppH,sens_2_real, 'PCHIP');
pH_sens3 = interp1 (dat3,ppH,sens_3_real, 'PCHIP');
pH_sens4 = interp1 (dat4,ppH,sens_4_real, 'PCHIP');
pH_sens5 = interp1 (dat5,ppH,sens_5_real, 'PCHIP');
pH_sens6 = interp1 (dat6,ppH,sens_6_real, 'PCHIP');
pH_camera_b = interp1 (camera_blue,ppH,camera_b_real, 'PCHIP');
pH_camera_g = interp1 (camera_green,ppH,camera_g_real, 'PCHIP');
pH_camera_r = interp1 (camera_red,ppH,camera_r_real, 'PCHIP');

pH_av = (pH_sens1 + pH_sens2 + pH_sens3 + pH_sens4 + pH_sens5 + pH_sens6)/6;

if pH_val < 4.5
    pH_camera_av = (pH_camera_g + pH_camera_r)/2;
else
    pH_camera_av = (pH_camera_b + pH_camera_g + pH_camera_r)/3;
end

[~, ind_1] = min(abs(dat1-sens_1_real));

```

```

[~, ind_2] = min(abs(dat2-sens_2_real));
[~, ind_3] = min(abs(dat3-sens_3_real));
[~, ind_4] = min(abs(dat4-sens_4_real));
[~, ind_5] = min(abs(dat5-sens_5_real));
[~, ind_6] = min(abs(dat6-sens_6_real));
[~, cam_1] = min(abs(camera_blue-camera_b_real));
[~, cam_2] = min(abs(camera_green-camera_g_real));
[~, cam_3] = min(abs(camera_red-camera_r_real));

[~, ind_pH_1] = min(abs(ppH-pH_sens1));
[~, ind_pH_2] = min(abs(ppH-pH_sens2));
[~, ind_pH_3] = min(abs(ppH-pH_sens3));
[~, ind_pH_4] = min(abs(ppH-pH_sens4));
[~, ind_pH_5] = min(abs(ppH-pH_sens5));
[~, ind_pH_6] = min(abs(ppH-pH_sens6));
[~, ind_pH_cam_1] = min(abs(ppH-pH_camera_b));
[~, ind_pH_cam_2] = min(abs(ppH-pH_camera_g));
[~, ind_pH_cam_3] = min(abs(ppH-pH_camera_r));

pH_wheight_1 = abs((dat1(ind_1)-dat1(ind_1 - 1))/(ppH(ind_pH_1 - 1)-
ppH(ind_pH_1)));
pH_wheight_2 = abs((dat2(ind_2)-dat2(ind_2 - 1))/(ppH(ind_pH_2 - 1)-
ppH(ind_pH_2)));
pH_wheight_3 = abs((dat3(ind_3)-dat3(ind_3 - 1))/(ppH(ind_pH_3 - 1)-
ppH(ind_pH_3)));
pH_wheight_4 = abs((dat4(ind_4)-dat4(ind_4 - 1))/(ppH(ind_pH_4 - 1)-
ppH(ind_pH_4)));
pH_wheight_5 = abs((dat5(ind_5)-dat5(ind_5 - 1))/(ppH(ind_pH_5 - 1)-
ppH(ind_pH_5)));
pH_wheight_6 = abs((dat6(ind_6)-dat6(ind_6 - 1))/(ppH(ind_pH_6 - 1)-
ppH(ind_pH_6)));
pH_wheight_cam_1 = abs((camera_blue(cam_1)-camera_blue(cam_1 -
1))/(ppH(ind_pH_cam_1 - 1)-ppH(ind_pH_cam_1)));
pH_wheight_cam_2 = abs((camera_green(cam_2)-camera_green(cam_2 -
1))/(ppH(ind_pH_cam_2 - 1)-ppH(ind_pH_cam_2)));

```

```

    pH_wheight_cam_3 = abs((camera_red(cam_3)-camera_red(cam_3 -
1)))/(ppH(ind_pH_cam_3 - 1)-ppH(ind_pH_cam_3));

    pH_av_wheight = (pH_sens1*pH_wheight_1 + pH_sens2*pH_wheight_2 +
pH_sens3*pH_wheight_3 + pH_sens4*pH_wheight_4 + pH_sens5*pH_wheight_5 +
pH_sens6*pH_wheight_6)/(pH_wheight_1 + pH_wheight_2 + pH_wheight_3 + pH_wheight_4
+ pH_wheight_5 + pH_wheight_6);

    if pH_val < 4.5

        pH_av_wheight_cam = (pH_camera_g*pH_wheight_cam_2 +
pH_camera_r*pH_wheight_cam_3)/(pH_wheight_cam_2 + pH_wheight_cam_3);

    else

        pH_av_wheight_cam = (pH_camera_b*pH_wheight_cam_1 +
pH_camera_g*pH_wheight_cam_2 + pH_camera_r*pH_wheight_cam_3)/(pH_wheight_cam_1 +
pH_wheight_cam_2 + pH_wheight_cam_3);

    end

    pH_vv(1,i) = pH_val;
    pH_av_error(1,i) = pH_av;
    pH_av_wheight_error(1,i) = pH_av_wheight;
    pH_av_cam_error(1,i) = pH_camera_av;
    pH_av_wheight_cam_error(1,i) = pH_av_wheight_cam;
    error = abs((pH_val - pH_av)/pH_val*100);
    wheight_error = abs((pH_val - pH_av_wheight)/pH_val*100);
    error_cam = abs((pH_val - pH_camera_av)/pH_val*100);
    wheight_error_cam = abs((pH_val - pH_av_wheight_cam)/pH_val*100);
    av_error = av_error + error;
    av_wheight_error = av_wheight_error + wheight_error;

    av_error_cam = av_error_cam + error_cam;
    av_wheight_error_cam = av_wheight_error_cam + wheight_error_cam;

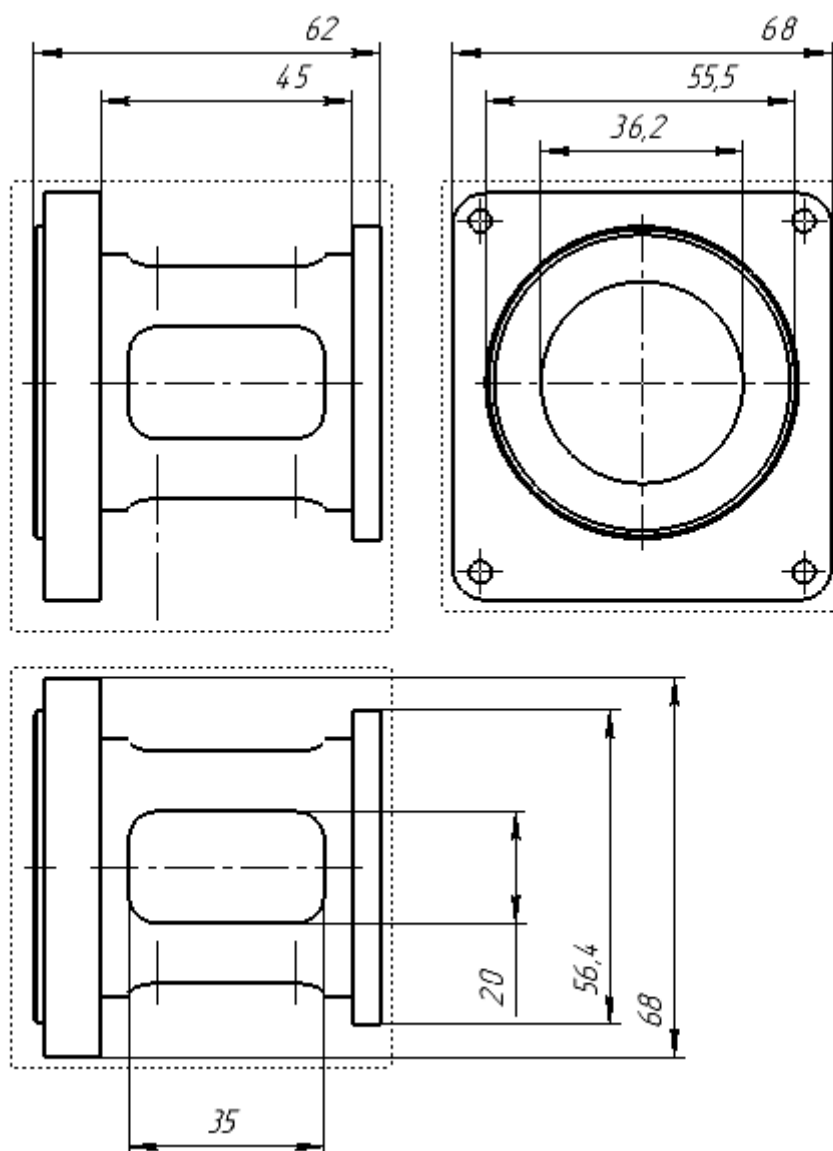
end

av_error = av_error/10000;
av_wheight_error = av_wheight_error/10000;
av_error_cam = av_error_cam/10000;
av_wheight_error_cam = av_wheight_error_cam/10000;

```



## Appendix K – Mounting



**Appendix L – Motor coupling**

